Silesian University of Technology

Modelling of thermal fields in metamaterials using radial basis function-based meshless methods

by

Olaf Popczyk

supervised by

Dr. Grzegorz Dziatkiewicz
Assoc. Prof. in Computational Mechanics

A thesis submitted in partial fulfillment of the requirements for the degree of *Doctor of Philosophy*

June 2022

Abstract

Heat flow is one of the most fundamental and common phenomena in nature, which makes it one of the most intensively used phenomena by a mankind. Nevertheless, due to the significant dissipative nature of heat flow, many very promising applications of this phenomenon remain in the realm of research and discussion. If the dissipative nature of the heat flow could be overcome and the heat flow could be manipulated, thermal cloaking or shielding could be performed, as well as inversion or concentration of the heat flow. It would open up great opportunities in science, industry, military and many other fields. For hundreds of years, manipulation of the heat flux was unattainable until the appearance of thermal metamaterials, which, thanks to their structure, characterised by a strong spatial variability of thermophysical parameters, made it possible to fulfil the dream of controlling the heat flux. This is the driving force behind research like this.

The complex structure of metamaterials requires advanced methods for their analysis. For many methods, it is not entirely clear if they are suitable for this. This thesis decided to check whether the radial basis function-based Kansa method is suitable for this purpose. As part of the research, heat conduction problems in a material with spatially variable distributions of thermophysical parameters were investigated. The study considered the coefficient and pseudospectral formulation of the non-symmetric Kansa's method for solving elliptic, parabolic and hyperbolic problems. For the time-dependent problems, two approaches were used: the method of lines combined with the time integration schemes known from the structural dynamics and the spacetime approach in which time is treated as a coordinate. An extensive study of the applicability of the Kansa method has been conducted for various combinations of the above approaches for one- and two-dimensional problems. The thesis proposes a group of algorithms for finding a good value of the multiquadric radial basis function shape parameter, one of the most important research problems within the radial basis function-based methods for solving partial differential equations. The work also carried out the process of designing a thermal metamaterial device for heat flux inversion and concentration as well as thermal shielding and cloaking using gradient optimisation.

The thesis shows that the Kansa method is suitable for solving the considered class of problems for most combinations of the aforementioned approaches. The spacetime approach has worked only for some of the problems considered in the work. It is worth noting that this approach, despite its enormous potential, does not receive wide attention from the scientific community, which makes it an interesting topic for further research. The proposed group of algorithms for finding a good shape parameter value turned out to be very effective for the considered class of problems. Designing a thermal metamaterial device was not successful in the case of inversion, the desired effect was not achieved, however, it is an extremely demanding case from a numerical point of view, and it is certainly a good direction for further research. On the other hand, designing was successful in three other cases of the heat flux manipulation: shielding, cloaking and concentration.

Acknowledgements

I would like to thank my supervisor, Dr. Grzegorz Dziatkiewicz for his great knowledge, patience, meticulousness and commitment without which this thesis would not have arisen. His enormous enthusiasm for mechanics, heat transfer and numerical methods made me interested in these fields of science like no other.

Contents

List of Figures

Nomenclature

Symbol	Meaning
Latin italic	
c	Radial basis function coefficient
E_∞	Value of the infinity norm of error vector
f	Objective function
L	Length of a domain
m	Spatial filter multiplier
p	Multiquadric radial basis function exponent
q	Heat flux
r	Filter radius
$r_{\min}$	Minimum distance between collocation points
s	Regularization constant
t	Time
u	Temperature
u_∞	Ambient temperature
u_0	Initial temperature
x	x coordinate
y	y coordinate
z	z coordinate
Latin bold	
$\boldsymbol{A}$	Interpolation matrix
$\bar{\boldsymbol{A}}$	Interpolation matrix after imposing boundary conditions
$\boldsymbol{b}$	Right-hand side vector

$\bar{\boldsymbol{b}}$	Right-hand side vector after imposing boundary conditions
$\boldsymbol{c}$	Radial basis function coefficient vector
$\boldsymbol{D}$	Thermal damping matrix
$\boldsymbol{E}$	Error vector
$\boldsymbol{G}$	Filter matrix
$\boldsymbol{I}$	Identity matrix
$\boldsymbol{K}$	Thermal stiffness matrix
$\boldsymbol{M}$	Thermal mass matrix
$\boldsymbol{P}$	Condition algorithm input matrix
$\boldsymbol{q}$	Heat flux vector
$\boldsymbol{u}$	Temperature vector
$\boldsymbol{W}$	Objective function weight matrix
$\bar{\boldsymbol{W}}$	Filter weight matrix
$\boldsymbol{Y}$	Output matrix
$\boldsymbol{x}$	Position vector in the Cartesian coordinate system

Greek italic

α	Heat transfer coefficient
β	Spacetime scaling parameter
γ	Specific heat capacity
Γ	Boundary of the domain
δ	Distance between the collocation points
Δt	Time step size
Δx	Space step size in x-direction
Δy	Space step size in y-direction
ε	Shape parameter
ζ	Heat flux manipulation parameter
κ	Thermal conductivity
κ_1	Fast mode thermal conductivity
ξ_u	Local relative error of the temperature

ξ_q	Local relative error of the heat flux
$\bar{\xi}_u$	Global relative error of the temperature
$\bar{\xi}_q$	Global relative error of the heat flux
Ξ_u	Global relative error of the time-varying temperature
Ξ_q	Global relative error of the time-varying heat flux
ψ	Diagonal matrix operator
ρ	Density
ϱ	Artificial density
σ	Singular value of a matrix
τ	Relaxation time
τ_1	Second relaxation time (thermalization time)
φ	Multiquadric radial basis function
ω	Harmonic spatial distribution frequency
Ω	Domain
$\bar{\Omega}$	Interior of the domain

Greek bold

$\boldsymbol{\alpha}$	Heat transfer coefficient matrix
$\boldsymbol{\gamma}$	Specific heat capacity matrix
$\boldsymbol{\chi}$	Position vector in the spacetime
$\boldsymbol{\kappa}$	Thermal conductivity vector / matrix
$\boldsymbol{\lambda}$	Lagrange multipliers vector
$\boldsymbol{\rho}$	Density matrix
$\boldsymbol{\varrho}$	Artificial density vector
$\boldsymbol{\phi}$	Radial basis function matrix

Other italic

∇	Nabla operator
$\mathcal{L}$	Condition algorithm function
ℓ	Lagrangian
$\bar{\ell}$	Lagrangian after first filtration

$\breve{\ell}$	Lagrangian after second filtration

Other bold

$\mathbf{0}$	Zero vector
$\mathbf{1}$	All-ones vector
$\boldsymbol{\mathcal{A}}$	Interpolation matrix for the spacetime formulation
$\bar{\boldsymbol{\mathcal{A}}}$	Interpolation matrix for the spacetime formulation after imposing boundary conditions
$\mathfrak{b}$	Right-hand side vector for the spactime formulation
$\bar{\mathfrak{b}}$	Right-hand side vector for the spactime formulation after imposing boundary conditions
$\boldsymbol{\mathcal{D}}$	Pseudospectral differentiation operator
$\boldsymbol{\mathcal{W}}$	Spacetime scaling matrix

Indices and other denotations

$\dot{(\cdot)}$	First-order time derivative
$\ddot{(\cdot)}$	Second-order time derivative
$(\cdot)_{,x}$	First-order spatial derivative in x direction
$(\cdot)_{,xx}$	Second-order spatial derivative in x direction
$(\cdot)_{,y}$	First-order spatial derivative in y direction
$(\cdot)_{,yy}$	Second-order spatial derivative in y direction
$(\cdot)_{,z}$	First-order spatial derivative in z direction
$(\cdot)_{,zz}$	Second-order spatial derivative in z direction
$(\cdot)_{,\bar{n}}$	First-order normal derivative
$\|\|\cdot\|\|$	Second Euclidean norm

1. Introduction

Heat transfer Heat transfer is one of the most fundamental phenomena in nature. In terms of importance in everyday life, it can be put on a par with the phenomenon of motion, current flow or gravity [32]. The first substantial description of the heat flow was proposed by Isaac Newton in 1701 [118]. In his work, he stated that the heat flux q transferred out of the body is proportional to the heat transfer coefficient α and the difference between the body temperature u and the ambient temperature u_∞:

$$q = \alpha \left(u - u_\infty \right), \tag{1.1}$$

Equation 1.1 is known today as Newton's law of cooling and is until today the fundamental law governing convective heat flow. Despite its great importance, Newton's law did not describe the most fundamental mechanism of heat flow, namely thermal conduction. It took more than 120 years to explain this mechanism. This was done by Joseph Fourier who in 1822 published a paper in which he stated that the heat flux $\boldsymbol{q}$ passing through the locally isotropic medium is proportional to the thermal conductivity κ and the local gradient of temperature u [55]:

$$\boldsymbol{q} = -\kappa \nabla u. \tag{1.2}$$

Equation 1.2 is known today as Fourier's law. Combining the Fourier's law with the law of conservation of internal energy for heat conduction process without an internal heat source or sink:

$$\gamma \rho \frac{\partial u}{\partial t} + \nabla \cdot \boldsymbol{q} = 0, \tag{1.3}$$

leads to the following parabolic heat equation:

$$\gamma \rho \frac{\partial u}{\partial t} = \nabla \cdot \left(\kappa \nabla u \right), \tag{1.4}$$

where ρ is the density of the medium, γ is the specific heat capacity. Despite their age, Fourier's law and heat equation are still fundamental models governing heat flow and are the starting points for introducing new heat transport theories. Fourier's model indicates a parabolic model of the temperature evolution. It implies that a sudden temperature disturbance is felt simultaneously by the whole part of a medium; in other words, the propagation speed of thermal disturbance is infinite, which is non-physical. This issue is irrelevant in most traditional engineering problems [4], however, it is extremely important in some specialized cases, such as, for example, bioheat transfer [111] or phase transformations [153]. For this reason, researchers began to pay attention to this paradox from the late 1940s [20, 115, 165]. Cattaneo, Morse, and Vernotte noted that a certain

amount of time is needed to accelerate thermal energy carriers for heat conduction under the imposition of sudden temperature disturbances. Therefore, they stated that a time delay called relaxation time τ should exist between the heat flux and the temperature gradient:

$$\boldsymbol{q}\left(t+\tau\right)=-\kappa\nabla u\left(t\right). \tag{1.5}$$

Through first-order approximation of Equation 1.5, the Cattaneo-Vernotte model is obtained:

$$\tau\frac{\partial \boldsymbol{q}}{\partial t}+\boldsymbol{q}=-\kappa\nabla u, \tag{1.6}$$

The combination of the Cattaneo-Vernotte model with the law of conservation of internal energy given by Equation 1.3 leads to the Cattaneo-Vernotte equation:

$$\gamma\rho\left(\tau\frac{\partial^2 u}{\partial t^2}+\frac{\partial u}{\partial t}\right)=\nabla\cdot\left(\kappa\nabla u\right). \tag{1.7}$$

They proposed a modification of the Fourier model, which makes the heat flow model hyperbolic. The presence of the second-order time derivative in Cattaneo-Vernotte equation makes it hyperbolic. This has a fundamental impact on both its solution and the way of solving it. Although the Cattaneo-Vernotte model avoids the paradox of infinite speed of thermal disturbance propagation, it is far from ideal and has certain limitations. For example, the heat waves' overlap predicted by the Cattaneo-Vernotte model could lead to the local temperature lower than 0 K [10, 92, 77]. Additionally, some experiments [1, 2, 140, 83, 117] indicate that the temperature profile strongly deviates from the Cattaneo-Vernotte model in the case of significant thermal disturbance. Therefore, researchers developed a series of unsteady non-Fourier heat conduction models beyond the Cattaneo-Vernotte model. In analogy to the relaxation relation between strain and stress in viscoelastic materials, Joseph and Preziosi proposed the Jefferey's type model for heat conduction [85]:

$$\tau\frac{\partial \boldsymbol{q}}{\partial t}+\boldsymbol{q}=-\kappa\nabla u-\kappa_1\frac{\partial}{\partial t}\left(\nabla u\right). \tag{1.8}$$

The second term on the right-hand side of Equation 1.8 suggests that additional mode of heat waves could exist and propagate with a different speed from the primary heat wave. κ_1 is defined as the thermal conductivity corresponding to the "fast mode" of heat wave. Özişik and Tzou [121, 160] stated that the interaction of microscopic particles causes macroscopic response delay. If the disturbance is a temperature gradient, then the heat flux evolution will be delayed. If the disturbance is a heat flux, then the temperature response will be delayed. In this way the relaxation of both heat flux and temperature gradient should be taken into account, which leads to the Dual Phase Lagging model [112]:

$$\boldsymbol{q}\left(t+\tau\right)=-\kappa\nabla u\left(t+\tau_1\right). \tag{1.9}$$

The Dual Phase Lagging model is quite a general model and can be simplified to specific models for specific values of τ and τ_1. For example, if $\tau_1 = 0$ then the Dual Phase Lagging is simplified to the Cattaneo-Vernotte model while if $\tau_1 = 0$ and $\tau = 0$ then

the Dual Phase Lagging is simplified to the Fourier model. The above list of the most important models of conductive heat transfer is far from complete, however, it presents those that are currently the most widely used. At this point, the question arises: which of these models will be the basic model used in the work? It was decided that it would be the Cattaneo-Vernotte model. But why was this model chosen despite the awareness of the limitations of this model? There are many reasons, but the two most important of them are the fact that for the considered problems the Cattaneo-Vernotte model will not meet the above mentioned limitations and because this model is the foundation for other hyperbolic heat conduction models such as Dual Phase Lagging, and it does not differ from them on the essentials - they are all hyperbolic. It is also worth emphasizing that there are very few publications in which the Cattaneo-Vernotte equation would be solved utilizing the method that is used in thesis - the Kansa method.

Kansa method The heat equation is 199 years old at the time of writing this thesis. Despite this, its general analytical solution remains unknown. The situation in which the equation describing one of the most fundamental laws of physics remains analytically unsolved is quite peculiar. This is due to the fact that the heat equation is a partial differential equation, most of which do not have closed analytical solutions. Such a situation concerns not only the heat flow but also many other fundamental physical phenomena. The gravity of the situation has naturally led to a significant development in techniques for approximate solving of partial differential equations in the last hundred years. Currently, the four most important methods for solving partial differential equations are the finite difference method [73], the finite element method [179], the finite volume method [166], and the boundary element method [90]. Why these four methods? The answer is quite prosaic, these methods have been known for many years and therefore are well researched and widely implemented in scientific and commercial software. For example, the finite difference method was invented by Leonhard Euler as early as 1768 [149]. The common feature of the above-mentioned methods is a mesh - a set of points connected with each other in a specific way. At these points, the system of algebraic equations - which is a discretized form of the considered partial differential equation - is solved. The mentioned common feature is also one of the biggest drawback of these methods. This is because creating a high-quality mesh is a very difficult and time-consuming task when the analysed geometry is complex [21]. The importance of this problem has led to the development of a whole new group of methods specifically designed to deal with this particular problem - meshless methods. As the name suggests, meshless methods do not use a mesh but a cloud of unconnected points. Meshless methods make solving partial differential equation-based problems with complex geometry so much easier that they are viewed as next generation computational techniques [37]. One of the most popular meshless methods is the Kansa method. As already known from the abstract, this method is used in the presented research. The Kansa method was introduced in 1990 by Edward Kansa [88, 89]. The Kansa method is a method for approximate solving partial differential equations problems which is based on the so-called radial basis functions. It can achieve outstanding accuracy [29], is easy-to-use and easy-to-implement. Among the many radial basis functions, the multiquadric one is especially popular [145], not without reason, as this combination has many significant advantages. The Kansa method has found application to a wide range of problems for which a brief selective overview is presented below. Dubal et al. [43] utilized the multiquadric approximation scheme to solve a three-dimensional elliptic partial differential equation describing the time-evolution of in-

teracting black holes and the production of gravitational waves. Moridis and Kansa [114] combined the numerical inversion of Laplace Transforms to integrate partial differential equations in time, with an exponentially-convergent grid-free multiquadrics spatial approximation scheme for the spatial terms. Sharan et al. [150] have used the multiquadric approximation scheme to solve elliptic partial differential equations with Dirichlet and/or Neumann boundary conditions. Despite the excellent results of researchers using the Kansa method to solve partial differential equation-based problems, until 1998, there was no evidence of the convergence of this method [172]. This fact changed with the publication of Franke's and Schaback's work [56]. They gave a convergence proof and error bound of collocation-based radial basis functions techniques for partial differential equations with constant coefficients. Their analysis was based on the fact that the Kansa approach can be considered as a special case of the general Hermite-Birkhoff interpolation problem. Zerroukat et al. [173] used the multiquadrics scheme to solve the heat transfer problem, later Zerroukat et al. [172] utilized the Kansa method to solve linear advection-diffusion equations by using the thin-plate splines and gave the stability proof. Dong and Cheung [42] used the multiquadric collocation method to solve elastic inclusion problems. Chantasiriwan [23] utilized the Kansa method to solve the heat conduction problem with stochastic initial and boundary conditions. Sarra [142] performed a numerical study of the accuracy and stability of symmetric and asymmetric radial basis function collocation methods for hyperbolic partial differential equations. Zheng and Li [177] utilized the Kansa method to investigate acoustic wave propagations. Chen et al. [30] made the first attempt to apply the Kansa method in the solution of the time-fractional diffusion equations, in which the multiquadrics and thin-plate spline serve as the radial basis function. Simonenko et al. [152] utilized the Kansa method to solve elastostatic problems. Pang et al. [123] applied the Kansa method to the space-fractional advection-dispersion equations. Dehghan and Shirzad [40] proposed two numerical methods to solve the elliptic stochastic partial differential equations in two and three dimensions obtained by Gaussian noises using radial basis functions collocation and pseudo-spectral collocation methods. Reutskiy [137] utilized a meshless radial basis function method for 2D steady-state heat conduction problems in anisotropic and inhomogeneous media. Sarra and Cogar [144] examined the evaluation algorithms for the radial basis function method. Fallah et al. [48] used the Kansa approach for solving seepage problems. Haq and Hussain [68] used the Kansa method to solve time-fractional higher-order partial differential equations with constant and variable coefficients. Jankowska and Karageorghis [84] used the Kansa approach for the numerical solution of second and fourth-order nonlinear boundary-value problems in two dimensions. Liu and Chang [108] performed energy regularization of the multiquadric radial basis function method. They used the Kansa method to solve the Cauchy problems of diffusion-convection-reaction equations. Verma and Kumar [164] used the phase lag bio-heat model, an extension of the Cattaneo-Vernotte model to solve the problem of heat distribution in skin tissue with constant and sinusoidal heat flux at the skin surface. Ang [9] utilized radial basis function method for the Cattaneo–Vernotte equation in anisotropic media with spatially varying and temperature dependent properties. Lin et al. [107] used a meshless radial basis function based method for modelling dual phase lag heat transfer in irregular domains. As can be seen, the spectrum of applications of the Kansa method is extremely wide. It is worth paying special attention to the last three cited publications, they share a common denominator. These publications consider hyperbolic heat flow solved using the radial basis function-based meshless methods. These publications are one of the few dealing with the subject, which shows that this area of science is so

far poorly researched and many questions remain unanswered. On the other hand, the extremely recent publication dates of these publications show that this topic is beginning to gain momentum, therefore it seems that the beginning of the 1920s will be a period of increased interest in this area of research. In conclusion, one can risk a statement that the subject of this work fits perfectly into the current scientific trends.

Shape parameter The significant advantages of the Kansa method presented in the previous paragraph, such as high accuracy, ease of implementation, the lack of a grid and ease of use, give the impression that it is a method without disadvantages. However, it is not so. It turns out that this method is associated with an unresolved problem, a problem so significant that prevents its application to the challenging real-world problems [169]. Most of the most commonly used radial basis functions contain the so-called shape parameter which has a fundamental impact on the interpolation matrix and, consequently, on the entire numerical procedure. It turns out that currently there is no algorithm that would allow for its optimal determination. For this reason, the problem of choosing the proper value of shape parameter has been the subject of great scientific debate. The first attempts to find a good shape parameter value were made even before the Kansa method was invented because multiquadric radial basis functions were used for interpolation of scattered data. Hardy [69] suggested the use of $\varepsilon = 0.815\Delta x$, where Δx is the distance between equispaced nodes. On the other hand, Franke [57] recommended $\varepsilon = 1.25\sqrt{2}\Delta x$. Rippa [139] proposed a leave-one-out cross-validation algorithm to estimate the interpolation error and use it to compute a quasi-optimal value of the shape parameter. Rippa's algorithm was a breakthrough, it is now one of the most popular algorithms for searching a good value of shape parameter. Wang and Liu [168] studied the effect of shape parameters on the numerical accuracy of the radial point interpolation meshless method. A range of suitable shape parameters is obtained from the analysis of the condition number of the main system matrix, error of energy and irregularity of node distribution. However, it is observed that the widely used shape parameters for multiquadric and reciprocal multiquadric radial basis functions are not close to their optimums obtained in performed numerical experiments. Trahan and Wyatt [157] said that a good radial basis function shape parameter represents the best possible compromise between the inherent ill-conditioning of the radial basis function coefficient matrix and the smoothest possible interpolate. In the application presented in their paper, the famous Rippa technique may be unsuitable for choosing the good shape parameter, especially for time-dependent problems, where the quasi-optimal shape parameter value should be determined at every time step. Larsson and Fornberg [100] explored theoretically and numerically the behaviour of the interpolants in the limit of nearly flat radial basis functions. The approaches that determine the optimal radial basis function shape parameter value are explained through approximate expansions of the interpolation error. Fasshauer and Zhang [52] introduced the approximate moving least squares algorithm. In this method, leave-one-out cross-validation algorithm was applied to optimise the shape parameter and good number of iterations. The approximate moving least squares algorithm was used for radial basis function pseudo-spectral methods to solve the partial differential equation. Huang et al. [79] experimentally derived a formula for a good value of the shape parameter $\varepsilon = \log(a/3b\Delta x)$, where a and b are constants that depend on the problem. Further, Fornberg and Zuev [54] proposed the approach in which the shape parameter varies spatially, improving accuracy and numerical conditioning. Ferreira et al. [53] used the cross-validation technique to optimise the shape parameter for the radial basis func-

tions in the mixed radial basis function-pseudospectral mode. Bayona et al. [11] also used the radial basis function-finite difference method's mixed mode. The local approximation error of radial basis function-finite difference formulas serves as the tool for estimating the optimal shape parameter that minimizes the solution error. Huang et al. [80] applied the increasingly flat radial basis function. They determined the optimal shape parameter for the elliptic partial differential equations solution using the root-mean-square error measure calculated using the exact solutions of presented examples. Boyd and Gildersleeve [15] used numerical experiments to examine the condition numbers of the interpolation matrix for many species of radial basis functions. Davydov and Oanh [36] formulated a new multilevel algorithm that effectively finds a near-optimal shape parameter, which helps to reduce the solution error significantly. Sarra [143] applied the extended precision floating-point arithmetic to improve the accuracy of radial basis function-based methods efficiently. Among other methods of determining the good value of the radial basis function shape parameter are the golden section algorithm [159], the method based on the convergence analysis [59], the strategy with trigonometric, exponential and random variable shape parameter [170], the local optimisation algorithm [141], the extended Rippa's algorithm [161], the global genetic algorithm optimisation method for the single [46] and variable [3] shape parameter value approach, the application of the principle of a minimum of the total potential energy [82], the sample solution approach [29] and the particle swarm optimisation method [94]. As was shown above, the stability of the radial basis function method is often related to the ill-conditioning of the main matrix [81]. However, it is rare to find the method of determining the good value of the shape parameter using the measure of ill-conditioning. One of the few articles on this topic is the paper of Haq and Hussain [67] in which the time-fractional Black-Scholes equations were solved using the Kansa method. They formulated an algorithm for determining the quasi-optimal shape parameter value based on Zhang et al.'s paper [175]. This paper proposed a case-independent shape parameter selection strategy. In the proposed strategy, for a finite precision computation, the upper limit of the condition number is predetermined. Therefore, the shape parameter can be chosen where the condition number oscillates in the early stage. The authors solved equations modelled the transmission line model, the long straight cable channel model, and the grounding metal box model. This idea seems to be very interesting, which, combined with the fact that it is relatively poorly researched, caused that as a part of the thesis an algorithm of this class for searching a good value of the shape parameter was proposed.

Metamaterials The issues of the heat flow model and numerical methods have already been discussed, so it is worth moving on to discussing the application of the Cattaneo-Vernotte model in conjunction with the Kansa method. In recent years, the gaze of materials science community has been intensely directed towards an extremely interesting material group - metamaterials. Metamaterials are artificially engineered composite materials that derive their properties from internal micro- and nanostructures, rather than the chemical composition found in natural materials [93]. As a result, metamaterial structures enable properties and capabilities, which are generally not possible to create using conventional material discovery or chemical manufacturing technologies. The spectrum of potential applications of metamaterials is enormous, among them it is worth mentioning: medical devices [122], screening of personnel for hidden objects [135], viruses detection [14], vibration suppression [178], sound isolation [72], acoustic waveguiding [120], seismic shielding [16], high-frequency battlefield communications [95], negative refractive

index devices [151], high gain antennas [136], superlenses [50] and many others. The presented applications of metamaterials are impressive, however, they seem insignificant when compared with one application - the possibility of creating an invisibility cloak. This possibility arose thanks to metamaterials. A cloaking device is a stealth technology that can cause objects to be partially or wholly invisible from the point of view of a certain physical field. Initially, the researcher's attention was focused mainly on electromagnetic [148, 125, 96, 109, 60, 97] and optical [101, 19, 6, 162, 58, 45, 8, 31, 174, 7, 25, 26] invisibility which were based on the theory of transformation optics [125, 101, 104, 102]. Promising results in these areas meant that the research on cloaking was soon extended for such scientific fields as elastodynamic [17, 87] and acoustic [24, 176, 105, 180, 35] cloaking. It didn't take long for the idea of cloaking with metamaterials to be adapted to the heat flow as well. In the case of thermal cloaking, it is necessary to consider the problem of controlling the direction of the heat flow, which is not easy due to the Fourier law and the strong dissipation of the heat flow process. Below is a brief overview of important advances in thermal metamaterials cloaking development. Inspired by transformation optics, heat flux manipulation based on a coordinate transformation was first studied by Fan, et al. [49] and Chen et al. [27]. Li et al. [103] adopted the coordinate transformation method for the steady heat conduction equation, based on which a bifunctional spherical cloak working for both static electric field and heat flux was numerically demonstrated. Guenneau et al. [62] proposed a systematic theoretical extension of transformation optics to the field of thermal conduction and proposed a practical method to simplify the highly inhomogeneous anisotropic and singular parameters for a transient cylindrical thermal invisibility cloak. Later, Schittny et al. [147] experimentally demonstrated that Guenneau method. Narayana et al. [116] experimentally proposed to simplify the thermal invisibility cloak with homogeneous anisotropic materials working in a steady-state. Han et al. [66] theoretically verified the Narayana et al. findings. As inspired by the successful demonstration of a static magnetic cloak [60], an alternative way to realize a thermal cloak with homogeneous isotropic structures that is similar to the previous scattering-cancellation plasmonic cloaking approach for electromagnetic waves [5, 44] has been experimentally demonstrated by Xu et al. [171] in three dimensions, and Han et al. [63] in two dimensions, respectively. The development of thermal metamaterials and thermal cloaking has also led to development of other thermal devices with interesting functionalities such as a thermal concentrator [116, 78, 39, 65, 163], rotator [116, 39, 61] and thermal camouflage [64, 70]. As can seen the development of thermal metamaterials and thermal cloaking is extremely dynamic, in addition, it is worth adding that thermal cloaking is more perspective than optical cloaking. This is due to the fact that the bottlenecks of current optical cloaking technology mainly arise from the phase preservation in transformation optics, thermal cloaking has no such limitations as the concept of phase is inherently not involved in heat diffusion. As can be easily guessed, thermal cloaking would find unimaginably wide applications, especially in the military industry [134] and in electronics it would allow to create an isothermal region in multilayer printed circuit boards to protect the heat sensitive device [38]. It is for these reasons that thermal metamaterials were chosen as the materials through which the heat flow will be simulated in this thesis using the Kansa method.

Aim of the work The aim of the work consists of several goals. The main aim of the study is the application of the Kansa method for solving elliptic, parabolic and hyperbolic problems of heat flow in a material with spatially variable thermophysical parameters. In

addition to the main goal, it was also important to formulate algorithms for finding a good value of the shape parameter which are effective from the computational point of view. The last of the main goals was to apply the Kansa method to design the thermal metamaterial device for manipulating heat flux using gradient optimisation.

Hypothesis The most important hypothesis put forward in the thesis is the following. The Kansa method with developed formulations is suitable for solving the problems of elliptical, parabolic and hyperbolic heat flow in thermal metamaterials with spatially variable thermophysical parameters and the method is appropriate for the effective design of a metamaterial device by gradient optimisation.

Structure of the work The thesis is divided into five chapters:

- **Introduction** This chapter is an introduction to the thesis in which the considered problems are outlined, as well as a literature review and the objectives and hypothesis of the work are presented.
- **Governing equations and computational methods** This chapter presents the governing equations and computational methods used in the work. Thesis shows the application of collocation methods in conjunction with the Kansa method for solving the initial-boundary value problem. An important element of this chapter is the discussion on the algorithms for finding the good value of the shape parameter.
- **Validation and verification of developed methods and algorithms** This chapter examines whether the created solver has been correctly implemented, whether the Kansa method is suitable for solving the problems considered in the thesis, and whether the proposed algorithms for finding a good shape parameter value are effective.
- **Optimal design for heat flux manipulation** In this chapter, the problem of designing a metamaterial device is formulated in the form of an optimisation problem. Several types of device were considered for different variants of the heat flux manipulation: inversion, concentration, shielding, and cloaking.
- **Conclusions** This chapter collects all conclusions drawn on the basis of the research and presents recommendations for future research.
- **Appendix** This chapter contains a short description of the implementation of the finite difference method solver used in the work.

Author's publications created in the course of research In the course of research on the problems considered in the work, the author published several articles closely related to the thesis theme. In [132], the problems of two-dimensional hyperbolic heat flow in a material with spatially variable thermophysical parameters in irregular domains and time-dependent Neumann boundary conditions were analysed. [127] was the first author's work on analysis of the algorithms for finding good value of the shape parameter, this research was continued in [130] and [133]. [128] considered the problems of one-dimensional heat flow for exponential spatial distributions of thermophysical parameters. In [126], heat flow was analysed in materials whose thermophysical parameter distributions were modelled using the Heaviside function. In [129] and [131], one and two-dimensional cases of hyperbolic heat flow in a material with spatially variable thermophysical parameters were considered.

2. Governing equations and computational methods

2.1 Statement of the initial-boundary value problem of heat flow in inhomogeneous medium

The basic equation that is solved in the thesis is the Cattaneo-Vernotte Equation 1.7 for an inhomogeneous medium:

$$\gamma\left(\boldsymbol{x}\right)\rho\left(\boldsymbol{x}\right)\left(\tau\frac{\partial^2 u}{\partial t^2}+\frac{\partial u}{\partial t}\right)=\nabla\cdot\left(\kappa\left(\boldsymbol{x}\right)\nabla u\right). \tag{2.1}$$

The above equation is solved in the time domain $t\in\left(0,\,T\right\rangle$ where T is the length of the observation interval and the space domain $\boldsymbol{x}\in\bar{\Omega}\subset\mathbb{R}^d$ where $d\geq 1$. Since the Cattaneo-Vernotte model is hyperbolic, it is necessary to impose two initial conditions, one for the initial temperature field:

$$u\left(\boldsymbol{x},t=0\right)=u_0\left(\boldsymbol{x}\right), \tag{2.2}$$

and one for the time derivative of the initial temperature field:

$$\dot{u}\left(\boldsymbol{x},t=0\right)=\dot{u_0}\left(\boldsymbol{x}\right). \tag{2.3}$$

Three types of boundary conditions were used [22]:

- Dirichlet boundary condition

$$u\left(\boldsymbol{x}_b,t\right)=u_b\left(\boldsymbol{x}_b,t\right), \tag{2.4}$$

  where u_b is the boundary temperature function and $\boldsymbol{x}_b$ is the boundary point,

- Neumann boundary condition

$$-\kappa\left(\boldsymbol{x}_b\right)\frac{\partial u\left(\boldsymbol{x}_b,t\right)}{\partial\bar{n}}=q_b\left(\boldsymbol{x}_b,t\right)+\tau\frac{\partial q_b\left(\boldsymbol{x}_b,t\right)}{\partial t}, \tag{2.5}$$

  where $\partial/\partial\bar{n}$ is the derivative in the normal direction and q_b is the boundary heat flux in the normal direction,

- Robin boundary condition

$$-\kappa\left(\boldsymbol{x}_b\right)\frac{\partial u\left(\boldsymbol{x}_b,t\right)}{\partial\bar{n}}=\alpha\left(\boldsymbol{x}_b\right)\left(u_\infty\left(\boldsymbol{x}_b\right)-u\left(\boldsymbol{x}_b,t\right)\right)-\alpha\left(\boldsymbol{x}_b\right)\tau\frac{\partial u\left(\boldsymbol{x}_b,t\right)}{\partial t}. \tag{2.6}$$

  where u_∞ is the ambient temperature and α is the heat transfer coefficient.

Cattaneo-Vernotte Equation 2.1 together with the initial and the boundary conditions creates the initial-boundary value problem which is considered in the work. Special cases of the Cattaneo-Vernotte Equation 2.1 were also considered. When relaxation time $\tau = 0$, Equation 2.1 simplifies to the unsteady-state parabolic heat equation for an inhomogeneous medium:

$$\gamma(\boldsymbol{x})\,\rho(\boldsymbol{x})\,\frac{\partial u}{\partial t} = \nabla\cdot(\kappa(\boldsymbol{x})\,\nabla u)\,, \tag{2.7}$$

for which the initial condition given by Equation 2.3 does not apply. When $\dot{u} = 0$, Equation 2.1 simplifies to the steady-state elliptic heat equation for an inhomogeneous medium:

$$\nabla\cdot(\kappa(\boldsymbol{x})\,\nabla u) = 0. \tag{2.8}$$

for which the initial conditions given by Equations 2.2 and 2.3 do not apply while the boundary conditions given by Equations 2.4 - 2.6 become time independent. At the end of this section, it is worth emphasizing once again that the heat flow problems solved in the thesis, governed by a hyperbolic, parabolic or elliptical model, were considered for materials with spatially variable thermophysical parameters: density $\rho(\boldsymbol{x})$, specific heat capacity $\gamma(\boldsymbol{x})$ and thermal conductivity $\kappa(\boldsymbol{x})$.

2.2 Collocation methods

There is no known general closed solution of the described initial-boundary value problem. For this reason, numerical methods have to be employed to construct a solution approximately. In the thesis, it will be done using the collocation method, while in this section, it will be shown how to do it. The starting point for considering the collocation method is to rewrite the Cattaneo-Vernotte Equation 2.1 in the Cartesian coordinate system and denote the temporal derivative by a dot and the spatial derivative by a comma:

$$\begin{aligned}\gamma(\boldsymbol{x})\,\rho(\boldsymbol{x})\,(\tau\ddot{u}+\dot{u}) = \\ \kappa_{,x}(\boldsymbol{x})\,u_{,x} + \kappa_{,y}(\boldsymbol{x})\,u_{,y} + \kappa_{,z}(\boldsymbol{x})\,u_{,z} + \kappa(\boldsymbol{x})\,(u_{,xx}+u_{,yy}+u_{,zz})\,.\end{aligned} \tag{2.9}$$

This form of the Cattaneo-Vernotte equation is very useful for further considerations, because it is written in the Cartesian coordinate system that will be used at work.

2.2.1 Spatial collocation method for solving the initial-boundary value problem

Let's start by introducing the two-dimensional domain in which the problem will be solved, it is shown in Figure 2.1. The presented formulation is also valid for n-dimensional domains.

As shown in Figure 2.1, the domain Ω consists of the interior $\bar{\Omega}$ and the boundary Γ which consists of boundaries Γ_D, Γ_N, Γ_R on which the Dirichlet, Neumann, and Robin boundary conditions are imposed, respectively. The above can be written as:

$$\Omega = \bar{\Omega}\cup\Gamma, \tag{2.10}$$

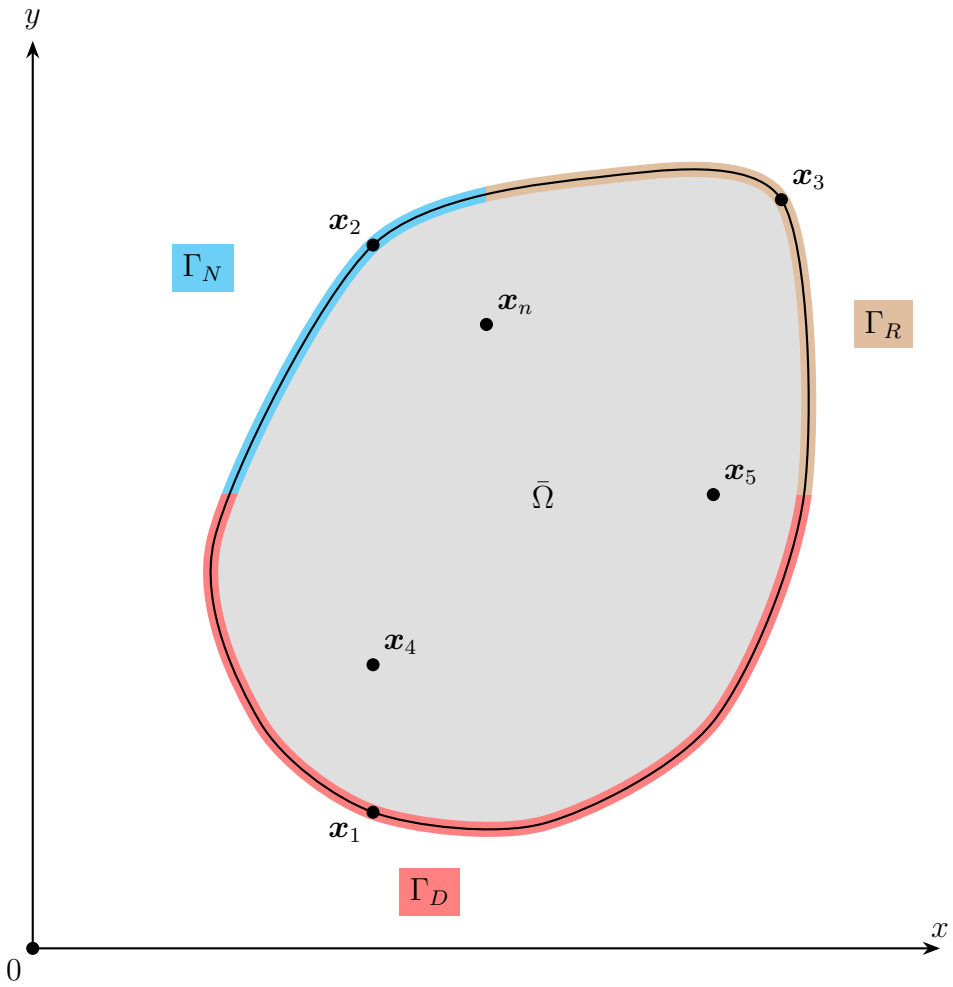

Figure 2.1: Two-dimensional domain Ω with distinguished interior $\bar{\Omega}$, boundary Γ and collocation points $\boldsymbol{x}$

$$\Gamma = \Gamma_D \cup \Gamma_N \cup \Gamma_R, \tag{2.11}$$

$$\Gamma_D \cap \Gamma_N \cap \Gamma_R = \varnothing. \tag{2.12}$$

Cattaneo-Vernotte Equation 2.9 must be satisfied at every moment in time and every point in the interior $\bar{\Omega}$, while Equations 2.4 - 2.6 describing the Dirichlet, Neumann and Robin boundary conditions must be satisfied at every moment in time and every point belonging to the Γ_D, Γ_N, Γ_R boundaries respectively. In the collocation method, it is assumed that the introduced equations are satisfied only in a discrete set $\boldsymbol{X} \in \Omega$ of n collocation points [106, 91]:

$$\boldsymbol{X} = \begin{bmatrix} \boldsymbol{x}_1 \\ \boldsymbol{x}_2 \\ \vdots \\ \boldsymbol{x}_n \end{bmatrix} \tag{2.13}$$

where

$$\boldsymbol{x_i} = \begin{bmatrix} x_i \\ y_i \\ z_i \end{bmatrix}. \tag{2.14}$$

The total number of collocation points n consists of n_I points belonging to the interior and n_D, n_N, n_R belonging to the boundaries on which the Dirichlet, Neumann and Robin boundary conditions were imposed, respectively:

$$n = n_I + n_D + n_N + n_R. \tag{2.15}$$

The proposed variant of the collocation method is called the mixed collocation [106, 91], because the set $\boldsymbol{X}$ contains both the interior collocation points and boundary collocation points. Therefore, Equation 2.9 is satisfied only at the collocation points in the interior $\bar{\Omega}$ at any time moment, while the boundary conditions 2.4 - 2.6 are satisfied at any time moment and only at the collocation points on the boundary Γ_D, Γ_N, Γ_R, respectively. Using the language of mathematics it can be stated that:

$$\forall\,(\boldsymbol{x}_i, t) \in \left(\bar{\Omega} \times (0,\, T\rangle\right) : \boldsymbol{\gamma\rho}\,(\tau\ddot{\boldsymbol{u}} + \dot{\boldsymbol{u}}) = \\ \boldsymbol{\kappa}_{,x}\boldsymbol{u}_{,x} + \boldsymbol{\kappa}_{,y}\boldsymbol{u}_{,y} + \boldsymbol{\kappa}_{,z}\boldsymbol{u}_{,z} + \boldsymbol{\kappa}\left(\boldsymbol{u}_{,xx} + \boldsymbol{u}_{,yy} + \boldsymbol{u}_{,zz}\right), \tag{2.16}$$

$$\forall\,(\boldsymbol{x}_i, t) \in (\Gamma_D \times (0,\, T\rangle) : \boldsymbol{u} = \boldsymbol{u}_b, \tag{2.17}$$

$$\forall\,(\boldsymbol{x}_i, t) \in (\Gamma_N \times (0,\, T\rangle) : -\boldsymbol{\kappa}\boldsymbol{u}_{,\bar{n}} = (\boldsymbol{q}_b + \tau\dot{\boldsymbol{q}}_b), \tag{2.18}$$

$$\forall\,(\boldsymbol{x}_i, t) \in (\Gamma_R \times (0,\, T\rangle) : -\boldsymbol{\kappa}\boldsymbol{u}_{,\bar{n}} = \boldsymbol{\alpha}\,(\boldsymbol{u}_\infty - \boldsymbol{u}) - \boldsymbol{\alpha}\tau\dot{\boldsymbol{u}}, \tag{2.19}$$

where vectors and matrices related to Equation 2.16 are as follows:

$$\dot{\boldsymbol{u}} = \begin{bmatrix} \dot{u}\,(\boldsymbol{x}_1, t) \\ \dot{u}\,(\boldsymbol{x}_2, t) \\ \vdots \\ \dot{u}\,(\boldsymbol{x}_{n_I}, t) \end{bmatrix}, \quad \ddot{\boldsymbol{u}} = \begin{bmatrix} \ddot{u}\,(\boldsymbol{x}_1, t) \\ \ddot{u}\,(\boldsymbol{x}_2, t) \\ \vdots \\ \ddot{u}\,(\boldsymbol{x}_{n_I}, t) \end{bmatrix}, \tag{2.20}$$

$$\boldsymbol{u}_{,x} = \begin{bmatrix} u_{,x}\,(\boldsymbol{x}_1, t) \\ u_{,x}\,(\boldsymbol{x}_2, t) \\ \vdots \\ u_{,x}\,(\boldsymbol{x}_{n_I}, t) \end{bmatrix}, \quad \boldsymbol{u}_{,y} = \begin{bmatrix} u_{,y}\,(\boldsymbol{x}_1, t) \\ u_{,y}\,(\boldsymbol{x}_2, t) \\ \vdots \\ u_{,y}\,(\boldsymbol{x}_{n_I}, t) \end{bmatrix}, \quad \boldsymbol{u}_{,z} = \begin{bmatrix} u_{,z}\,(\boldsymbol{x}_1, t) \\ u_{,z}\,(\boldsymbol{x}_2, t) \\ \vdots \\ u_{,z}\,(\boldsymbol{x}_{n_I}, t) \end{bmatrix}, \tag{2.21}$$

$$\boldsymbol{u}_{,xx} = \begin{bmatrix} u_{,xx}\,(\boldsymbol{x}_1, t) \\ u_{,xx}\,(\boldsymbol{x}_2, t) \\ \vdots \\ u_{,xx}\,(\boldsymbol{x}_{n_I}, t) \end{bmatrix}, \quad \boldsymbol{u}_{,yy} = \begin{bmatrix} u_{,yy}\,(\boldsymbol{x}_1, t) \\ u_{,yy}\,(\boldsymbol{x}_2, t) \\ \vdots \\ u_{,yy}\,(\boldsymbol{x}_{n_I}, t) \end{bmatrix}, \quad \boldsymbol{u}_{,zz} = \begin{bmatrix} u_{,zz}\,(\boldsymbol{x}_1, t) \\ u_{,zz}\,(\boldsymbol{x}_2, t) \\ \vdots \\ u_{,zz}\,(\boldsymbol{x}_{n_I}, t) \end{bmatrix}, \tag{2.22}$$

$$\boldsymbol{\gamma} = \begin{bmatrix} \gamma(\boldsymbol{x}_1) & 0 & \cdots & 0 \\ 0 & \gamma(\boldsymbol{x}_2) & \cdots & 0 \\ \vdots & \vdots & \ddots & \vdots \\ 0 & 0 & \cdots & \gamma(\boldsymbol{x}_{n_I}) \end{bmatrix}, \tag{2.23}$$

$$\boldsymbol{\rho} = \begin{bmatrix} \rho(\boldsymbol{x}_1) & 0 & \cdots & 0 \\ 0 & \rho(\boldsymbol{x}_2) & \cdots & 0 \\ \vdots & \vdots & \ddots & \vdots \\ 0 & 0 & \cdots & \rho(\boldsymbol{x}_{n_I}) \end{bmatrix}, \tag{2.24}$$

$$\boldsymbol{\kappa} = \begin{bmatrix} \kappa(\boldsymbol{x}_1) & 0 & \cdots & 0 \\ 0 & \kappa(\boldsymbol{x}_2) & \cdots & 0 \\ \vdots & \vdots & \ddots & \vdots \\ 0 & 0 & \cdots & \kappa(\boldsymbol{x}_{n_I}) \end{bmatrix}, \tag{2.25}$$

$$\boldsymbol{\kappa}_{,x} = \begin{bmatrix} \kappa_{,x}(\boldsymbol{x}_1) & 0 & \cdots & 0 \\ 0 & \kappa_{,x}(\boldsymbol{x}_2) & \cdots & 0 \\ \vdots & \vdots & \ddots & \vdots \\ 0 & 0 & \cdots & \kappa_{,x}(\boldsymbol{x}_{n_I}) \end{bmatrix}, \tag{2.26}$$

$$\boldsymbol{\kappa}_{,y} = \begin{bmatrix} \kappa_{,y}(\boldsymbol{x}_1) & 0 & \cdots & 0 \\ 0 & \kappa_{,y}(\boldsymbol{x}_2) & \cdots & 0 \\ \vdots & \vdots & \ddots & \vdots \\ 0 & 0 & \cdots & \kappa_{,y}(\boldsymbol{x}_{n_I}) \end{bmatrix}, \tag{2.27}$$

$$\boldsymbol{\kappa}_{,z} = \begin{bmatrix} \kappa_{,z}(\boldsymbol{x}_1) & 0 & \cdots & 0 \\ 0 & \kappa_{,z}(\boldsymbol{x}_2) & \cdots & 0 \\ \vdots & \vdots & \ddots & \vdots \\ 0 & 0 & \cdots & \kappa_{,z}(\boldsymbol{x}_{n_I}) \end{bmatrix}, \tag{2.28}$$

to Dirichlet boundary condition 2.17 as follows:

$$\boldsymbol{u} = \begin{bmatrix} u(\boldsymbol{x}_1, t) \\ u(\boldsymbol{x}_2, t) \\ \vdots \\ u(\boldsymbol{x}_{n_D}, t) \end{bmatrix}, \tag{2.29}$$

$$\boldsymbol{u}_b = \begin{bmatrix} u_b(\boldsymbol{x}_1, t) \\ u_b(\boldsymbol{x}_2, t) \\ \vdots \\ u_b(\boldsymbol{x}_{n_D}, t) \end{bmatrix}, \tag{2.30}$$

to Neumann boundary condition 2.18 as follows:

$$\boldsymbol{u}_{,n} = \begin{bmatrix} u_{,n}\left(\boldsymbol{x}_1, t\right) \\ u_{,n}\left(\boldsymbol{x}_2, t\right) \\ \vdots \\ u_{,n}\left(\boldsymbol{x}_{n_N}, t\right) \end{bmatrix}, \quad \boldsymbol{q}_b = \begin{bmatrix} q_b\left(\boldsymbol{x}_1, t\right) \\ q_b\left(\boldsymbol{x}_2, t\right) \\ \vdots \\ q_b\left(\boldsymbol{x}_{n_N}, t\right) \end{bmatrix}, \quad \dot{\boldsymbol{q}}_b = \begin{bmatrix} \dot{q}_b\left(\boldsymbol{x}_1, t\right) \\ \dot{q}_b\left(\boldsymbol{x}_2, t\right) \\ \vdots \\ \dot{q}_b\left(\boldsymbol{x}_{n_N}, t\right) \end{bmatrix}, \tag{2.31}$$

$$\boldsymbol{\kappa} = \begin{bmatrix} \kappa\left(\boldsymbol{x}_1\right) & 0 & \cdots & 0 \\ 0 & \kappa\left(\boldsymbol{x}_2\right) & \cdots & 0 \\ \vdots & \vdots & \ddots & \vdots \\ 0 & 0 & \cdots & \kappa\left(\boldsymbol{x}_{n_N}\right) \end{bmatrix}, \tag{2.32}$$

and to Robin boundary condition 2.19 as follows:

$$\boldsymbol{u}_{\infty} = \begin{bmatrix} u_{\infty}\left(\boldsymbol{x}_1\right) \\ u_{\infty}\left(\boldsymbol{x}_2\right) \\ \vdots \\ u_{\infty}\left(\boldsymbol{x}_{n_R}\right) \end{bmatrix}, \quad \boldsymbol{\alpha} = \begin{bmatrix} \alpha\left(\boldsymbol{x}_1\right) & 0 & \cdots & 0 \\ 0 & \alpha\left(\boldsymbol{x}_2\right) & \cdots & 0 \\ \vdots & \vdots & \ddots & \vdots \\ 0 & 0 & \cdots & \alpha\left(\boldsymbol{x}_{n_R}\right) \end{bmatrix}, \tag{2.33}$$

$$\boldsymbol{\kappa} = \begin{bmatrix} \kappa\left(\boldsymbol{x}_1\right) & 0 & \cdots & 0 \\ 0 & \kappa\left(\boldsymbol{x}_2\right) & \cdots & 0 \\ \vdots & \vdots & \ddots & \vdots \\ 0 & 0 & \cdots & \kappa\left(\boldsymbol{x}_{n_R}\right) \end{bmatrix}. \tag{2.34}$$

Time advancement will be presented only later, however, for the sake of consistency, it is worth introducing the vectors of initial conditions:

$$\boldsymbol{u}_0 = \begin{bmatrix} u_0\left(\boldsymbol{x}_1, 0\right) \\ u_0\left(\boldsymbol{x}_2, 0\right) \\ \vdots \\ u_0\left(\boldsymbol{x}_{n_I}, 0\right) \end{bmatrix}, \quad \dot{\boldsymbol{u}}_0 = \begin{bmatrix} \dot{u}_0\left(\boldsymbol{x}_1, 0\right) \\ \dot{u}_0\left(\boldsymbol{x}_2, 0\right) \\ \vdots \\ \dot{u}_0\left(\boldsymbol{x}_{n_I}, 0\right) \end{bmatrix}. \tag{2.35}$$

The solution of the considered initial-boundary value problem boils down to solving the system of differential-algebraic Equations 2.16 - 2.19. In order to solve such a system, it is necessary to transform it into a system of algebraic equations by approximation of terms containing spatial and temporal derivatives. In the case of the Neumann boundary conditions, it is necessary to approximate the terms containing spatial derivatives while in the case of the Robin boundary conditions, it is necessary to approximate the terms containing spatial and temporal derivatives. In turn, in order to approximate Equation 2.16, the method of lines will be used [146]. Method of lines consists in transforming a partial differential equation into a set of ordinary differential equations. The result is a system of time-dependent ordinary differential equations. In the considered initial-boundary value problem, the partial differential equation Equation 2.16 undergoes transformation, as a result of which the following ordinary differential equation is obtained:

$$\boldsymbol{M}\ddot{\boldsymbol{u}} + \boldsymbol{D}\dot{\boldsymbol{u}} + \boldsymbol{K}\boldsymbol{u} = \boldsymbol{0}, \tag{2.36}$$

where $\boldsymbol{M}$ is the thermal mass matrix, $\boldsymbol{D}$ is the thermal damping matrix, and $\boldsymbol{K}$ is the thermal stiffness matrix and $\mathbf{0}$ is a zero vector of the appropriate size. Naturally, the above names of the matrices were created through the analogy to mechanical vibrations [179]. Determining the thermal mass matrix $\boldsymbol{M}$ and thermal damping matrix $\boldsymbol{D}$ is simple in the considered problem because it will only require the multiplication of a priori known matrices containing thermophysical parameters, which will be presented later. However, the calculation of the thermal stiffness matrix $\boldsymbol{K}$ is much more difficult because it requires an approximation of the spatial derivatives terms in the right-hand side of Equation 2.16:

$$-\boldsymbol{K}\boldsymbol{u} \approx \boldsymbol{\kappa}_{,x}\boldsymbol{u}_{,x} + \boldsymbol{\kappa}_{,y}\boldsymbol{u}_{,y} + \boldsymbol{\kappa}_{,z}\boldsymbol{u}_{,z} + \boldsymbol{\kappa}\left(\boldsymbol{u}_{,xx} + \boldsymbol{u}_{,yy} + \boldsymbol{u}_{,zz}\right). \tag{2.37}$$

This step will be done using the Kansa method however it will be discussed in detail later in the work. In the special case when the relaxation time is equal to zero $\tau = 0$, the thermal mass matrix $\boldsymbol{M}$ is also equal to zero. Consequently, Equation 2.36 simplifies to:

$$\boldsymbol{D}\dot{\boldsymbol{u}} + \boldsymbol{K}\boldsymbol{u} = \mathbf{0}, \tag{2.38}$$

In turn, when the problem is steady, the thermal mass matrix $\boldsymbol{M}$ and thermal damping matrix $\boldsymbol{D}$ are equal to zero. Consequently, Equation 2.36 simplifies to:

$$\boldsymbol{K}\boldsymbol{u} = \mathbf{0}. \tag{2.39}$$

After approximating the spatial derivatives terms, it becomes possible to use the time integration scheme which approximates Equation 2.36 or 2.38 in time to the form that allows to determining the state variable vector in the next $(k+1)$ time step based on the values from the current (k) and previous $(k-1,\ k-2\ \ldots\ )$ time steps:

$$\boldsymbol{A}\boldsymbol{u}_{k+1} = \boldsymbol{b}\left(\boldsymbol{u}_k, \dot{\boldsymbol{u}}_k, \ddot{\boldsymbol{u}}_k, \boldsymbol{u}_{k-1}, \dot{\boldsymbol{u}}_{k-1}, \ddot{\boldsymbol{u}}_{k-1} \ldots\right), \tag{2.40}$$

where $\boldsymbol{A}$ is the main matrix:

$$\boldsymbol{A} = \begin{bmatrix} A_{1,1} & A_{1,2} & \cdots & A_{1,n_I} \\ A_{2,1} & A_{2,2} & \cdots & A_{2,n_I} \\ \vdots & \vdots & \ddots & \vdots \\ A_{n_I,1} & A_{n_I,2} & \cdots & A_{n_I,n_I} \end{bmatrix}, \tag{2.41}$$

and $\boldsymbol{b}$ is right-hand side vector:

$$\boldsymbol{b} = \begin{bmatrix} b_1 \\ b_2 \\ \vdots \\ b_{n_I} \end{bmatrix}. \tag{2.42}$$

The time integration scheme application is omitted when the problem is steady and Equation 2.39 is being considered. The next step is to impose the boundary conditions which is done by extending the system of Equations 2.40 describing the interior points with equations describing the boundary points. After that, the following equation is then obtained:

$$\bar{\boldsymbol{A}}\boldsymbol{u}_{k+1} = \bar{\boldsymbol{b}}, \tag{2.43}$$

where $\bar{\boldsymbol{A}}$ is the main matrix after imposing boundary conditions and $\bar{\boldsymbol{b}}$ is right-hand side vector after imposing boundary conditions. Solving the system of Equation 2.43 gives the solution at the next time step. As can be seen, the classical approach in the unsteady-state case is a time-marching procedure. If the problem is steady and described by Equation 2.39 then there is no time-marching anymore and consequently Equation 2.43 is simplified to the following form:

$$\bar{\boldsymbol{A}}\boldsymbol{u} = \bar{\boldsymbol{b}}. \tag{2.44}$$

The presented approach to collocation will be called classical in the thesis.

2.2.2 Spacetime collocation method for solving the initial-boundary value problem

The previous section presents the spatial collocation method in which only space is collocated and consequently Equations 2.9 - 2.6 must be satisfied at any moment. However, it is possible to develop this approach and collocate the time as well. If time is also taken as a coordinate then the considered domain Ω becomes a part of the Galilean spacetime Ω_{ST}:

$$\Omega \subset \Omega_{\mathrm{ST}} = \mathbb{R}^3 \times \mathbb{R}_{\geq 0}, \tag{2.45}$$

and the collocation points have four coordinates:

$$\boldsymbol{\chi_i} = \begin{bmatrix} \boldsymbol{x}_i \\ t_i \end{bmatrix} = \begin{bmatrix} x_i \\ y_i \\ z_i \\ t_i \end{bmatrix}. \tag{2.46}$$

This approach has a number of consequences, first of all, the coordinate system becomes a four-dimensional spacetime coordinate system. Due to the obvious difficulties related to drawing four-dimensional figures, a three-dimensional version will be presented in which a two-dimensional space is considered in conjunction with the third dimension which is time. Figure 2.2 shows the three-dimensional spacetime domain with collocation points used in the work.

The most important observation about Figure 2.2 is that in the spacetime the initial-boundary problem is treated as a boundary-value problem. As for the boundaries Γ_D, Γ_N, Γ_R become spacetime boundaries, and there is one new boundary Γ_0 associated with the initial conditions due to the fact that in the spacetime approach the initial conditions become the Dirichlet boundary condition at $\boldsymbol{\chi}\,(t=0)$.Similar to the classical approach, the domain Ω consists of the interior $\bar{\Omega}$ and the boundary Γ which consists of boundaries Γ_D, Γ_N, Γ_R, and Γ_0. The above can be written as:

$$\Omega = \bar{\Omega} \cup \Gamma, \tag{2.47}$$

$$\Gamma = \Gamma_D \cup \Gamma_N \cup \Gamma_R \cup \Gamma_0, \tag{2.48}$$

$$\Gamma_D \cap \Gamma_N \cap \Gamma_R \cap \Gamma_0 = \varnothing. \tag{2.49}$$

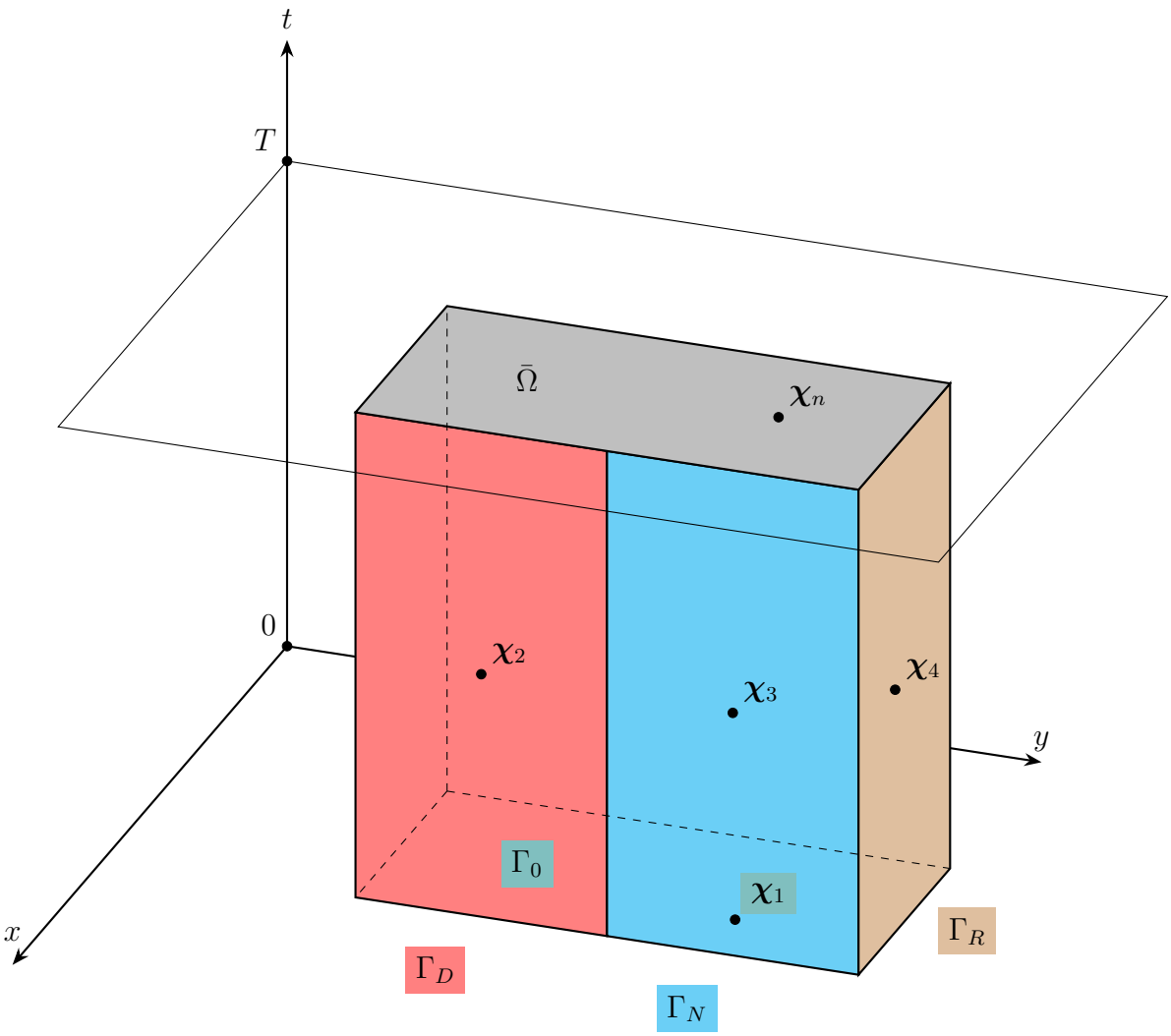

Figure 2.2: Three-dimensional spacetime domain Ω with distinguished interior $\bar{\Omega}$, boundary Γ and collocation points $\boldsymbol{\chi}$

The total number of collocation points n consists of n_I points belonging to the interior and n_D, n_N, n_R belonging to the boundaries on which the Dirichlet, Neumann and Robin boundary conditions were imposed, respectively and n_0 belonging to the boundary on which the initial conditions were imposed:

$$n = n_I + n_D + n_N + n_R + n_0. \tag{2.50}$$

In the case of the collocation approach, it is assumed that Equation 2.9 is satisfied only at the collocation points in the interior $\bar{\Omega}$, the initial conditions are satisfied only at the collocation points on the boundary Γ_0, while the boundary conditions 2.4 - 2.6 are satisfied only at the collocation points on the boundary Γ_D, Γ_N, Γ_R, respectively:

$$\forall \boldsymbol{\chi}_i \in \bar{\Omega} : \boldsymbol{\gamma}\boldsymbol{\rho}\left(\tau\ddot{\boldsymbol{u}} + \dot{\boldsymbol{u}}\right) = \boldsymbol{\kappa}_{,x}\boldsymbol{u}_{,x} + \boldsymbol{\kappa}_{,y}\boldsymbol{u}_{,y} + \boldsymbol{\kappa}_{,z}\boldsymbol{u}_{,z} + \boldsymbol{\kappa}\left(\boldsymbol{u}_{,xx} + \boldsymbol{u}_{,yy} + \boldsymbol{u}_{,zz}\right), \tag{2.51}$$

$$\forall \boldsymbol{\chi}_i \in \Gamma_0 : \boldsymbol{u} = \boldsymbol{u}_0 \wedge \dot{\boldsymbol{u}} = \dot{\boldsymbol{u}}_0, \tag{2.52}$$

$$\forall \boldsymbol{\chi}_i \in \Gamma_D : \boldsymbol{u} = \boldsymbol{u}_b, \tag{2.53}$$

$$\forall \boldsymbol{\chi}_i \in \Gamma_N : -\boldsymbol{\kappa}\boldsymbol{u}_{,\bar{n}} = \left(\boldsymbol{q}_b + \tau \dot{\boldsymbol{q}}_b\right), \tag{2.54}$$

$$\forall \boldsymbol{\chi}_i \in \Gamma_R : -\boldsymbol{\kappa}\boldsymbol{u}_{,\bar{n}} = \boldsymbol{\alpha}\left(\boldsymbol{u}_\infty - \boldsymbol{u}\right) - \boldsymbol{\alpha}\tau\dot{\boldsymbol{u}}, \tag{2.55}$$

where vectors and matrices have the same form as in the classical approach, given by Equation 2.29 - 2.35 with the one difference that instead of the $(\boldsymbol{x}_i, t)$ argument there is $(\boldsymbol{\chi}_i)$ argument, for example:

$$\boldsymbol{u} = \begin{bmatrix} u\left(\boldsymbol{\chi}_1\right) \\ u\left(\boldsymbol{\chi}_2\right) \\ \vdots \\ u\left(\boldsymbol{\chi}_n\right) \end{bmatrix}. \tag{2.56}$$

In the spacetime approach, in contrast to the classical approach and the method of lines, the partial differential Equation 2.16 is not approximated to the set of ordinary differential equations, but directly to the system of linear equations:

$$\boldsymbol{\mathcal{A}}\boldsymbol{u} = \mathfrak{b}, \tag{2.57}$$

where $\boldsymbol{\mathcal{A}}$ is the main matrix:

$$\boldsymbol{\mathcal{A}} = \begin{bmatrix} \mathcal{A}_{1,1} & \mathcal{A}_{1,2} & \cdots & \mathcal{A}_{1,n_I} \\ \mathcal{A}_{2,1} & \mathcal{A}_{2,2} & \cdots & \mathcal{A}_{2,n_I} \\ \vdots & \vdots & \ddots & \vdots \\ \mathcal{A}_{n_I,1} & \mathcal{A}_{n_I,2} & \cdots & \mathcal{A}_{n_I,n_I} \end{bmatrix}, \tag{2.58}$$

and $\mathfrak{b}$ is right-hand side vector:

$$\mathfrak{b} = \begin{bmatrix} \mathfrak{b}_1 \\ \mathfrak{b}_2 \\ \vdots \\ \mathfrak{b}_{n_I} \end{bmatrix}. \tag{2.59}$$

The last step is to impose the initial and boundary conditions which is done by extending the system of Equations 2.57 with equations of boundary conditions for boundary collocation points. After that, the following equation is then obtained:

$$\bar{\boldsymbol{\mathcal{A}}}\boldsymbol{u} = \bar{\mathfrak{b}}. \tag{2.60}$$

Solving Equation 2.60 gives the solution at all points of the spacetime domain. The spacetime approach appears to be structurally much simpler, but is much more computationally expensive because it operates on much larger matrices which is more expensive than operating on smaller matrices in conjunction with time advancement.

2.3 Approximation of unknown fields and their spatial and temporal derivatives using the Kansa method

The Kansa method is a numerical method for solving partial differential equations based on the approximation of unknown fields using radial basis functions [51]. Radial basis function is a real-valued function φ whose value at a given point $\boldsymbol{x}_i$ or $\boldsymbol{\chi}_i$ depends only on the distance from the selected point $\boldsymbol{x}_j$ or $\boldsymbol{\chi}_j$ so-called center. Thus, every radial basis function satisfies:

$$\varphi\left(\boldsymbol{x}_i, \boldsymbol{x}_j\right) = \varphi\left(||\boldsymbol{x}_i - \boldsymbol{x}_j||\right), \tag{2.61}$$

in case of the classical approach and

$$\varphi\left(\boldsymbol{\chi}_i, \boldsymbol{\chi}_j\right) = \varphi\left(||\boldsymbol{\mathcal{W}}\left(\boldsymbol{\chi}_i - \boldsymbol{\chi}_j\right)||\right), \tag{2.62}$$

in case of the spacetime approach. $||\cdot||$ is the second Euclidean norm and $\boldsymbol{\mathcal{W}}$ is spacetime scaling matrix:

$$\boldsymbol{\mathcal{W}} = \begin{bmatrix} 1 & 0 & 0 & 0 \\ 0 & 1 & 0 & 0 \\ 0 & 0 & 1 & 0 \\ 0 & 0 & 0 & \beta \end{bmatrix}, \tag{2.63}$$

where β is a spacetime scaling parameter, the measure of which is the distance per time, i.e. velocity. Figure 2.3 shows distance between two points in a two-dimensional Cartesian coordinate system and in a two-dimensional spacetime coordinate system in which one dimension is spatial and one is temporal.

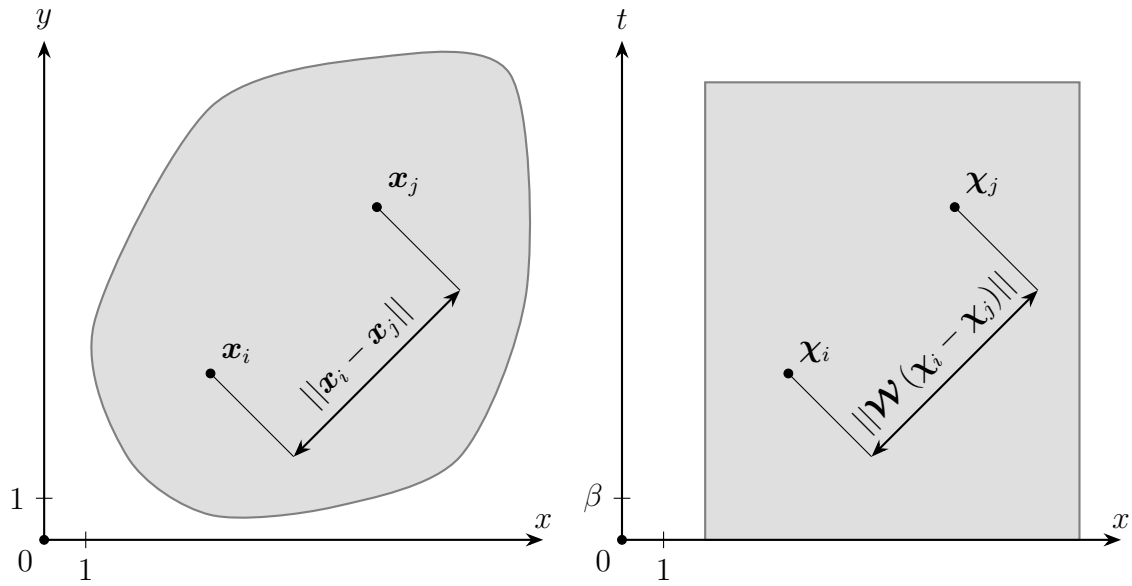

Figure 2.3: The distance between two points in a two-dimensional Cartesian coordinate system on the left and a two-dimensional spacetime coordinate system in which one dimension is spatial and one is temporal on the right

There are many radial base functions such as Gaussian, Laguerre-Gaussian, Poisson radial, Matérn, truncated power and many more, however, in this work it was decided to use the general multiquadric radial basis function [51]. For the classical approach it is as follows:

$$\varphi\left(\boldsymbol{x}_i, \boldsymbol{x}_j\right) = \left(||\boldsymbol{x}_i - \boldsymbol{x}_j||^2 + \varepsilon^2\right)^p, \tag{2.64}$$

while for spacetime as follows [28, 98]:

$$\varphi\left(\boldsymbol{x}_i, \boldsymbol{x}_j\right) = \left(||\boldsymbol{\mathcal{W}}\left(\boldsymbol{\chi}_i - \boldsymbol{\chi}_j\right)|| + \varepsilon^2\right)^p = \left(||\boldsymbol{x}_i - \boldsymbol{x}_j||^2 + \beta^2\left(t_i - t_j\right)^2 + \varepsilon^2\right)^p, \tag{2.65}$$

where ε is a shape parameter and p is a multiquadric radial basis function exponent. In this study, the most commonly used value of $p = 0.5$ was used [51], considerations on other values can be found in [132]. The shape parameter ε is of fundamental importance for the radial basis function approximation, therefore its value must be carefully selected. Due to the consistency of the work, the algorithms for selecting its value will be presented later in the thesis. In the Kansa method, it is assumed that the value of an unknown variable u at a given point $\boldsymbol{x}_i$ can be expressed as a linear combination of radial basis functions using the set of centres [51]:

$$u\left(\boldsymbol{x}_i\right) = \sum_{j=1}^{n} \varphi\left(\boldsymbol{x}_i, \boldsymbol{x}_j\right) c_j, \tag{2.66}$$

where c_j are coefficients in a linear combination. Writing Equation 2.66 for all collocation points of the computational domain leads to a $n \times n$ system of linear equations, which can be written in a matrix form:

$$\boldsymbol{u} = \boldsymbol{\phi}\boldsymbol{c}, \tag{2.67}$$

where $\boldsymbol{c}$ is the coefficients vector:

$$\boldsymbol{c} = \begin{bmatrix} c_1 \\ c_2 \\ \vdots \\ c_n \end{bmatrix}. \tag{2.68}$$

and $\boldsymbol{\phi}$ is the radial basis functions matrix:

$$\boldsymbol{\phi} = \begin{bmatrix} \varphi\left(||\boldsymbol{x}_1 - \boldsymbol{x}_1||\right) & \varphi\left(||\boldsymbol{x}_1 - \boldsymbol{x}_2||\right) & \cdots & \varphi\left(||\boldsymbol{x}_1 - \boldsymbol{x}_n||\right) \\ \varphi\left(||\boldsymbol{x}_2 - \boldsymbol{x}_1||\right) & \varphi\left(||\boldsymbol{x}_2 - \boldsymbol{x}_2||\right) & \cdots & \varphi\left(||\boldsymbol{x}_2 - \boldsymbol{x}_n||\right) \\ \vdots & \vdots & \ddots & \vdots \\ \varphi\left(||\boldsymbol{x}_n - \boldsymbol{x}_1||\right) & \varphi\left(||\boldsymbol{x}_n - \boldsymbol{x}_2||\right) & \cdots & \varphi\left(||\boldsymbol{x}_n - \boldsymbol{x}_n||\right) \end{bmatrix}, \tag{2.69}$$

in case of the classical approach and:

$$\boldsymbol{\phi} = \begin{bmatrix} \varphi\left(||\boldsymbol{\chi}_1 - \boldsymbol{\chi}_1||\right) & \varphi\left(||\boldsymbol{\chi}_1 - \boldsymbol{\chi}_2||\right) & \cdots & \varphi\left(||\boldsymbol{\chi}_1 - \boldsymbol{\chi}_n||\right) \\ \varphi\left(||\boldsymbol{\chi}_2 - \boldsymbol{\chi}_1||\right) & \varphi\left(||\boldsymbol{\chi}_2 - \boldsymbol{\chi}_2||\right) & \cdots & \varphi\left(||\boldsymbol{\chi}_2 - \boldsymbol{\chi}_n||\right) \\ \vdots & \vdots & \ddots & \vdots \\ \varphi\left(||\boldsymbol{\chi}_n - \boldsymbol{\chi}_1||\right) & \varphi\left(||\boldsymbol{\chi}_n - \boldsymbol{\chi}_2||\right) & \cdots & \varphi\left(||\boldsymbol{\chi}_n - \boldsymbol{\chi}_n||\right) \end{bmatrix}, \tag{2.70}$$

in case of the spacetime approach. In the presented approach the set of collocation points coincide with the set of centres. It is worth emphasizing that there are approaches in which the collocation points and the centres do not coincide [51]. Solving the initial-boundary value problem described by Equation 2.9 using the classical or spacetime approach requires approximating terms containing derivatives. The foundation of solving this problem is differentiating Equation 2.67 with respect to the appropriate spatial or temporal coordinate:

$$\boldsymbol{u}_{,v} = \boldsymbol{\phi}_{,v}\boldsymbol{c}, \tag{2.71}$$

where:

$$v = \{x, y, z, xx, yy, zz\}, \tag{2.72}$$

$$\boldsymbol{\phi}_{,v} = \begin{bmatrix} \varphi_{,v}\left(||\boldsymbol{x}_1 - \boldsymbol{x}_1||\right) & \varphi_{,v}\left(||\boldsymbol{x}_1 - \boldsymbol{x}_2||\right) & \cdots & \varphi_{,v}\left(||\boldsymbol{x}_1 - \boldsymbol{x}_n||\right) \\ \varphi_{,v}\left(||\boldsymbol{x}_2 - \boldsymbol{x}_1||\right) & \varphi_{,v}\left(||\boldsymbol{x}_2 - \boldsymbol{x}_2||\right) & \cdots & \varphi_{,v}\left(||\boldsymbol{x}_2 - \boldsymbol{x}_n||\right) \\ \vdots & \vdots & \ddots & \vdots \\ \varphi_{,v}\left(||\boldsymbol{x}_n - \boldsymbol{x}_1||\right) & \varphi_{,v}\left(||\boldsymbol{x}_n - \boldsymbol{x}_2||\right) & \cdots & \varphi_{,v}\left(||\boldsymbol{x}_n - \boldsymbol{x}_n||\right) \end{bmatrix}, \tag{2.73}$$

in case of the classical approach and:

$$v = \{x, y, z, t, xx, yy, zz, tt\}, \tag{2.74}$$

$$\boldsymbol{\phi}_{,v} = \begin{bmatrix} \varphi_{,v}\left(||\boldsymbol{\chi}_1 - \boldsymbol{\chi}_1||\right) & \varphi_{,v}\left(||\boldsymbol{\chi}_1 - \boldsymbol{\chi}_2||\right) & \cdots & \varphi_{,v}\left(||\boldsymbol{\chi}_1 - \boldsymbol{\chi}_n||\right) \\ \varphi_{,v}\left(||\boldsymbol{\chi}_2 - \boldsymbol{\chi}_1||\right) & \varphi_{,v}\left(||\boldsymbol{\chi}_2 - \boldsymbol{\chi}_2||\right) & \cdots & \varphi_{,v}\left(||\boldsymbol{\chi}_2 - \boldsymbol{\chi}_n||\right) \\ \vdots & \vdots & \ddots & \vdots \\ \varphi_{,v}\left(||\boldsymbol{\chi}_n - \boldsymbol{\chi}_1||\right) & \varphi_{,v}\left(||\boldsymbol{\chi}_n - \boldsymbol{\chi}_2||\right) & \cdots & \varphi_{,v}\left(||\boldsymbol{\chi}_n - \boldsymbol{\chi}_n||\right) \end{bmatrix}, \tag{2.75}$$

in case of the spacetime approach. Determination of the spatial derivatives terms using Equation 2.71 in the classical approach and Equation 2.67 leads to the system of ordinary differential equations, i.e. as in the method of lines. On the other hand, application of Equation 2.67 and the determination of the spatial and temporal derivatives terms using this equation in the spacetime approach leads to the system of algebraic equations. The approach presented so far uses the linear combination coefficients $\boldsymbol{c}$, which means that in order to obtain an unknown field $\boldsymbol{u}$ it is necessary to use Equation 2.67. For this reason, this approach is called the coefficient approach in work. It turns out that it is possible to determine the spatial and temporal derivatives terms in a different way [51] - a way to get an immediately unknown field $\boldsymbol{u}$ without having to perform the intermediate step of using Equation 2.67. Assuming that [51]:

$$\det \boldsymbol{\phi} \neq 0, \tag{2.76}$$

one can transform Equation 2.67 to the following form:

$$\boldsymbol{c} = \boldsymbol{\phi}^{-1}\boldsymbol{u}. \tag{2.77}$$

which after substituting to Equation 2.71 gives:

$$\boldsymbol{u}_{,v} = \boldsymbol{\phi}_{,v}\boldsymbol{\phi}^{-1}\boldsymbol{u}. \tag{2.78}$$

To distinguish the coefficient approach from this approach, the following differential operator is introduced:

$$\boldsymbol{\mathcal{D}}_{,v} = \boldsymbol{\phi}_{,v}\boldsymbol{\phi}^{-1}, \tag{2.79}$$

which after substituting to Equation 2.78 gives:

$$\boldsymbol{u}_{,v} = \boldsymbol{\mathcal{D}}_{,v}\boldsymbol{u}. \tag{2.80}$$

The approach presented above is called the pseudospectral approach. The advantage of the coefficient approach is that the obtained linear combination coefficients allow for an easy and accurate interpolation of the results beyond the collocation points. In turn, an important advantage of the pseudospectral approach is that the temperature field is obtained directly. An attentive reader has probably already noticed that the methodology presented above allows using as many as four approaches of the Kansa method:

- Classical coefficient approach,
- Classical pseudospectral approach,
- Spacetime coefficient approach,
- Spacetime pseudospectral approach.

All four approaches represents the non-symmetric Kansa method and will be covered in the thesis. These four approaches to the Kansa method are not the only approaches to this method that are quite numerous [51]. The above considerations are complemented by showing how to fill the matrix cells containing the derivatives of the radial basis functions given by Equations 2.64 and 2.65. Radial basis functions were differentiated with respect to the coordinates of the collocation points. The first- and second-order spatial derivatives of the radial basis function given by Equation 2.64 in the three-dimensional Cartesian coordinate system are as follows:

$$\varphi_{,x} = 2p\left(x_i - x_j\right)\left(\left(x_i - x_j\right)^2 + \left(y_i - y_j\right)^2 + \left(z_i - z_j\right)^2 + \varepsilon^2\right)^{p-1}, \tag{2.81}$$

$$\varphi_{,y} = 2p\left(y_i - y_j\right)\left(\left(x_i - x_j\right)^2 + \left(y_i - y_j\right)^2 + \left(z_i - z_j\right)^2 + \varepsilon^2\right)^{p-1}, \tag{2.82}$$

$$\varphi_{,z} = 2p\left(z_i - z_j\right)\left(\left(x_i - x_j\right)^2 + \left(y_i - y_j\right)^2 + \left(z_i - z_j\right)^2 + \varepsilon^2\right)^{p-1}, \tag{2.83}$$

$$\begin{aligned}\varphi_{,xx} = {} & 2p\left(\left(2p-1\right)\left(x_i - x_j\right)^2 + \left(y_i - y_j\right)^2 + \left(z_i - z_j\right)^2 + \varepsilon^2\right)\cdot \\ & \left(\left(x_i - x_j\right)^2 + \left(y_i - y_j\right)^2 + \left(z_i - z_j\right)^2 + \varepsilon^2\right)^{p-2},\end{aligned} \tag{2.84}$$

$$\begin{aligned}\varphi_{,yy} = {} & 2p\left(\left(2p-1\right)\left(y_i - y_j\right)^2 + \left(z_i - z_j\right)^2 + \left(x_i - x_j\right)^2 + \varepsilon^2\right)\cdot \\ & \left(\left(x_i - x_j\right)^2 + \left(y_i - y_j\right)^2 + \left(z_i - z_j\right)^2 + \varepsilon^2\right)^{p-2},\end{aligned} \tag{2.85}$$

$$\begin{aligned}\varphi_{,zz} = &2p\left((2p-1)\left(z_i-z_j\right)^2+\left(x_i-x_j\right)^2+\left(y_i-y_j\right)^2+\varepsilon^2\right)\cdot\\ &\left(\left(x_i-x_j\right)^2+\left(y_i-y_j\right)^2+\left(z_i-z_j\right)^2+\varepsilon^2\right)^{p-2}.\end{aligned} \tag{2.86}$$

In the case of the spacetime coordinate system, the first and second spatial and temporal derivatives of the radial basis function given by Equation 2.65 are as follows:

$$\varphi_{,x} = 2p\left(x_i-x_j\right)\left(\left(x_i-x_j\right)^2+\left(y_i-y_j\right)^2+\left(z_i-z_j\right)^2+\beta^2\left(t_i-t_j\right)^2+\varepsilon^2\right)^{p-1}, \tag{2.87}$$

$$\varphi_{,y} = 2p\left(y_i-y_j\right)\left(\left(x_i-x_j\right)^2+\left(y_i-y_j\right)^2+\left(z_i-z_j\right)^2+\beta^2\left(t_i-t_j\right)^2+\varepsilon^2\right)^{p-1}, \tag{2.88}$$

$$\varphi_{,z} = 2p\left(z_i-z_j\right)\left(\left(x_i-x_j\right)^2+\left(y_i-y_j\right)^2+\left(z_i-z_j\right)^2+\beta^2\left(t_i-t_j\right)^2+\varepsilon^2\right)^{p-1}, \tag{2.89}$$

$$\varphi_{,t} = 2p\beta^2\left(t_i-t_j\right)\left(\left(x_i-x_j\right)^2+\left(y_i-y_j\right)^2+\left(z_i-z_j\right)^2+\beta^2\left(t_i-t_j\right)^2+\varepsilon^2\right)^{p-1}, \tag{2.90}$$

$$\begin{aligned}\varphi_{,xx} = &2p\left((2p-1)\left(x_i-x_j\right)^2+\left(y_i-y_j\right)^2+\left(z_i-z_j\right)^2+\beta^2\left(t_i-t_j\right)^2+\varepsilon^2\right)\cdot\\ &\left(\left(x_i-x_j\right)^2+\left(y_i-y_j\right)^2+\left(z_i-z_j\right)^2+\beta^2\left(t_i-t_j\right)^2+\varepsilon^2\right)^{p-2},\end{aligned} \tag{2.91}$$

$$\begin{aligned}\varphi_{,yy} = &2p\left((2p-1)\left(y_i-y_j\right)^2+\left(z_i-z_j\right)^2+\left(x_i-x_j\right)^2+\beta^2\left(t_i-t_j\right)^2+\varepsilon^2\right)\cdot\\ &\left(\left(x_i-x_j\right)^2+\left(y_i-y_j\right)^2+\left(z_i-z_j\right)^2+\beta^2\left(t_i-t_j\right)^2+\varepsilon^2\right)^{p-2},\end{aligned} \tag{2.92}$$

$$\begin{aligned}\varphi_{,zz} = &2p\left((2p-1)\left(z_i-z_j\right)^2+\left(x_i-x_j\right)^2+\left(y_i-y_j\right)^2+\beta^2\left(t_i-t_j\right)^2+\varepsilon^2\right)\cdot\\ &\left(\left(x_i-x_j\right)^2+\left(y_i-y_j\right)^2+\left(z_i-z_j\right)^2+\beta^2\left(t_i-t_j\right)^2+\varepsilon^2\right)^{p-2},\end{aligned} \tag{2.93}$$

$$\begin{aligned}\varphi_{,tt} = &2p\left((2p-1)\beta^2\left(t_i-t_j\right)^2+\left(x_i-x_j\right)^2+\left(y_i-y_j\right)^2+\left(z_i-z_j\right)^2+\varepsilon^2\right)\cdot\\ &\left(\left(x_i-x_j\right)^2+\left(y_i-y_j\right)^2+\left(z_i-z_j\right)^2+\beta^2\left(t_i-t_j\right)^2+\varepsilon^2\right)^{p-2}.\end{aligned} \tag{2.94}$$

At this point, all the most important tools to approximate spatial derivatives (and additionally time derivatives for the spacetime approach) in Equation 2.16

$$\boldsymbol{\gamma\rho}\left(\tau\ddot{\boldsymbol{u}}+\dot{\boldsymbol{u}}\right) = \boldsymbol{\kappa}_{,x}\boldsymbol{u}_{,x}+\boldsymbol{\kappa}_{,y}\boldsymbol{u}_{,y}+\boldsymbol{\kappa}_{,z}\boldsymbol{u}_{,z}+\boldsymbol{\kappa}\left(\boldsymbol{u}_{,xx}+\boldsymbol{u}_{,yy}+\boldsymbol{u}_{,zz}\right),$$

are presented.

2.3.1 Classical approach

Coefficient approach In the classical coefficient approach, the terms containing spatial derivatives $\boldsymbol{\phi}_{,x}$, $\boldsymbol{\phi}_{,xx}$, $\boldsymbol{\phi}_{,y}$, $\boldsymbol{\phi}_{,yy}$, $\boldsymbol{\phi}_{,z}$, $\boldsymbol{\phi}_{,zz}$ are approximated using Equation 2.71 while the terms containing temporal derivatives $\dot{\boldsymbol{u}}$, $\ddot{\boldsymbol{u}}$ by differentiating Equation 2.67 over time:

$$\dot{\boldsymbol{u}} = \boldsymbol{\phi}\dot{\boldsymbol{c}}, \tag{2.95}$$

$$\ddot{\boldsymbol{u}} = \boldsymbol{\phi}\ddot{\boldsymbol{c}}, \tag{2.96}$$

which after substitution to Equation 2.16 leads to:

$$\boldsymbol{\gamma}\boldsymbol{\rho}\boldsymbol{\phi}\left(\tau\ddot{\boldsymbol{c}} + \dot{\boldsymbol{c}}\right) = \left(\boldsymbol{\kappa}_{,x}\boldsymbol{\phi}_{,x} + \boldsymbol{\kappa}_{,y}\boldsymbol{\phi}_{,y} + \boldsymbol{\kappa}_{,z}\boldsymbol{\phi}_{,z} + \boldsymbol{\kappa}\left(\boldsymbol{\phi}_{,xx} + \boldsymbol{\phi}_{,yy} + \boldsymbol{\phi}_{,zz}\right)\right)\boldsymbol{c}, \tag{2.97}$$

which can be written in a manner characteristic for the mechanical vibrations presented earlier in Equation 2.36:

$$\boldsymbol{M}_c\ddot{\boldsymbol{c}} + \boldsymbol{D}_c\dot{\boldsymbol{c}} + \boldsymbol{K}_c\boldsymbol{c} = \boldsymbol{0}, \tag{2.98}$$

or when $\tau = 0$ as:

$$\boldsymbol{D}_c\dot{\boldsymbol{c}} + \boldsymbol{K}_c\boldsymbol{c} = \boldsymbol{0}. \tag{2.99}$$

The c index in the matrices indicates that the coefficient approach is used. These matrices can be computed as follows:

$$\boldsymbol{M}_c = \tau\boldsymbol{\gamma}\boldsymbol{\rho}\boldsymbol{\phi}, \tag{2.100}$$

$$\boldsymbol{D}_c = \boldsymbol{\gamma}\boldsymbol{\rho}\boldsymbol{\phi}, \tag{2.101}$$

$$\boldsymbol{K}_c = -\left(\boldsymbol{\kappa}_{,x}\boldsymbol{\phi}_{,x} + \boldsymbol{\kappa}_{,y}\boldsymbol{\phi}_{,y} + \boldsymbol{\kappa}_{,z}\boldsymbol{\phi}_{,z} + \boldsymbol{\kappa}\left(\boldsymbol{\phi}_{,xx} + \boldsymbol{\phi}_{,yy} + \boldsymbol{\phi}_{,zz}\right)\right). \tag{2.102}$$

Pseudospectral approach In the classical pseudospectral approach, the terms containing spatial derivatives $\boldsymbol{\phi}_{,x}$, $\boldsymbol{\phi}_{,xx}$, $\boldsymbol{\phi}_{,y}$, $\boldsymbol{\phi}_{,yy}$, $\boldsymbol{\phi}_{,z}$, $\boldsymbol{\phi}_{,zz}$ are approximated using Equation 2.80 which after substitution to Equation 2.16 leads to:

$$\boldsymbol{\gamma}\boldsymbol{\rho}\left(\tau\ddot{\boldsymbol{u}} + \dot{\boldsymbol{u}}\right) = \left(\boldsymbol{\kappa}_{,x}\boldsymbol{\mathcal{D}}_{,x} + \boldsymbol{\kappa}_{,y}\boldsymbol{\mathcal{D}}_{,y} + \boldsymbol{\kappa}_{,z}\boldsymbol{\mathcal{D}}_{,z} + \boldsymbol{\kappa}\left(\boldsymbol{\mathcal{D}}_{,xx} + \boldsymbol{\mathcal{D}}_{,yy} + \boldsymbol{\mathcal{D}}_{,zz}\right)\right)\boldsymbol{u}, \tag{2.103}$$

which can be written in a manner characteristic for the mechanical vibrations presented earlier in Equation 2.36:

$$\boldsymbol{M}_u\ddot{\boldsymbol{u}} + \boldsymbol{D}_u\dot{\boldsymbol{u}} + \boldsymbol{K}_u\boldsymbol{u} = \boldsymbol{0}. \tag{2.104}$$

or when $\tau = 0$ as:

$$\boldsymbol{D}_u\dot{\boldsymbol{u}} + \boldsymbol{K}_u\boldsymbol{u} = \boldsymbol{0}. \tag{2.105}$$

The u index in the matrices indicates that the pseudospectral approach is used. These matrices can be computed as follows:

$$\boldsymbol{M}_u = \tau\boldsymbol{\gamma}\boldsymbol{\rho}, \tag{2.106}$$

$$\boldsymbol{D}_u = \boldsymbol{\gamma}\boldsymbol{\rho}, \tag{2.107}$$

$$\boldsymbol{K}_u = -\left(\boldsymbol{\kappa}_{,x}\boldsymbol{\mathcal{D}}_{,x} + \boldsymbol{\kappa}_{,y}\boldsymbol{\mathcal{D}}_{,y} + \boldsymbol{\kappa}_{,z}\boldsymbol{\mathcal{D}}_{,z} + \boldsymbol{\kappa}\left(\boldsymbol{\mathcal{D}}_{,xx} + \boldsymbol{\mathcal{D}}_{,yy} + \boldsymbol{\mathcal{D}}_{,zz}\right)\right). \tag{2.108}$$

Alternative way of calculating thermal stiffness matrix The approaches presented above require the knowledge of both thermophysical parameters and some of their derivatives, precisely, spatial derivatives of the thermal conductivity in the x, y, z directions. The values of these distributions are stored in the matrices $\boldsymbol{\gamma}$, $\boldsymbol{\rho}$, $\boldsymbol{\kappa}$, $\boldsymbol{\kappa}_{,x}$, $\boldsymbol{\kappa}_{,y}$, $\boldsymbol{\kappa}_{,z}$. Unfortunately, in some practical problems, the values of thermophysical parameters may be given by discontinuous spatial functions or the distribution function is not known explicitly. In this thesis such a problem will be encountered later in the work when the optimisation process is considered. It may cause significant problems in determining the thermal conductivity derivatives $\boldsymbol{\kappa}_{,x}$, $\boldsymbol{\kappa}_{,y}$, $\boldsymbol{\kappa}_{,z}$. Calculating them using the classical numerical differentiation operation can be burdened with a huge numerical error. Consequently, it is necessary to find an alternative way of solving this issue. The Kansa method allows to circumvent this problem. Let's start with rewriting Equation 2.16:

$$\boldsymbol{\gamma\rho}\left(\tau\ddot{\boldsymbol{u}}+\dot{\boldsymbol{u}}\right)=\boldsymbol{\kappa}_{,x}\boldsymbol{u}_{,x}+\boldsymbol{\kappa}_{,y}\boldsymbol{u}_{,y}+\boldsymbol{\kappa}_{,z}\boldsymbol{u}_{,z}+\boldsymbol{\kappa}\left(\boldsymbol{u}_{,xx}+\boldsymbol{u}_{,yy}+\boldsymbol{u}_{,zz}\right),$$

in a different form in which the product rule of differentiation did not apply:

$$\boldsymbol{\gamma\rho}\left(\tau\ddot{\boldsymbol{u}}+\dot{\boldsymbol{u}}\right)=\left(\boldsymbol{\kappa}\boldsymbol{u}_{,x}\right)_{,x}+\left(\boldsymbol{\kappa}\boldsymbol{u}_{,y}\right)_{,y}+\left(\boldsymbol{\kappa}\boldsymbol{u}_{,z}\right)_{,z}. \tag{2.109}$$

Using differential operators given by Equation 2.80 leads to:

$$\boldsymbol{\gamma\rho}\left(\tau\ddot{\boldsymbol{u}}+\dot{\boldsymbol{u}}\right)=\left(\boldsymbol{\kappa}\boldsymbol{\mathcal{D}}_{,x}\boldsymbol{u}\right)_{,x}+\left(\boldsymbol{\kappa}\boldsymbol{\mathcal{D}}_{,y}\boldsymbol{u}\right)_{,y}+\left(\boldsymbol{\kappa}\boldsymbol{\mathcal{D}}_{,z}\boldsymbol{u}\right)_{,z}, \tag{2.110}$$

and using it second time leads to:

$$\boldsymbol{\gamma\rho}\left(\tau\ddot{\boldsymbol{u}}+\dot{\boldsymbol{u}}\right)=\boldsymbol{\mathcal{D}}_{,x}\boldsymbol{\kappa}\boldsymbol{\mathcal{D}}_{,x}\boldsymbol{u}+\boldsymbol{\mathcal{D}}_{,y}\boldsymbol{\kappa}\boldsymbol{\mathcal{D}}_{,y}\boldsymbol{u}+\boldsymbol{\mathcal{D}}_{,z}\boldsymbol{\kappa}\boldsymbol{\mathcal{D}}_{,z}\boldsymbol{u}, \tag{2.111}$$

which can be written as:

$$\boldsymbol{\gamma\rho}\left(\tau\ddot{\boldsymbol{u}}+\dot{\boldsymbol{u}}\right)=\left(\boldsymbol{\mathcal{D}}_{,x}\boldsymbol{\kappa}\boldsymbol{\mathcal{D}}_{,x}+\boldsymbol{\mathcal{D}}_{,y}\boldsymbol{\kappa}\boldsymbol{\mathcal{D}}_{,y}+\boldsymbol{\mathcal{D}}_{,z}\boldsymbol{\kappa}\boldsymbol{\mathcal{D}}_{,z}\right)\boldsymbol{u}, \tag{2.112}$$

From the above equation it follows that the stiffness matrix for the pseudospectral formulation is now as follows:

$$\boldsymbol{K}_u=-\left(\boldsymbol{\mathcal{D}}_{,x}\boldsymbol{\kappa}\boldsymbol{\mathcal{D}}_{,x}+\boldsymbol{\mathcal{D}}_{,y}\boldsymbol{\kappa}\boldsymbol{\mathcal{D}}_{,y}+\boldsymbol{\mathcal{D}}_{,z}\boldsymbol{\kappa}\boldsymbol{\mathcal{D}}_{,z}\right), \tag{2.113}$$

while the substitution of Equation 2.67 to Equation 2.113 allows determining the stiffness matrix for the coefficient formulation:

$$\boldsymbol{K}_c=-\left(\boldsymbol{\phi}_{,x}\boldsymbol{\phi}^{-1}\boldsymbol{\kappa}\boldsymbol{\phi}_{,x}+\boldsymbol{\phi}_{,y}\boldsymbol{\phi}^{-1}\boldsymbol{\kappa}\boldsymbol{\phi}_{,y}+\boldsymbol{\phi}_{,z}\boldsymbol{\phi}^{-1}\boldsymbol{\kappa}\boldsymbol{\phi}_{,z}\right). \tag{2.114}$$

2.3.2 Spacetime approach

Coefficient approach In the spacetime coefficient approach, the terms containing spatial and temporal derivatives $\boldsymbol{\phi}_{,x}$, $\boldsymbol{\phi}_{,xx}$, $\boldsymbol{\phi}_{,y}$, $\boldsymbol{\phi}_{,yy}$, $\boldsymbol{\phi}_{,z}$, $\boldsymbol{\phi}_{,zz}$, $\boldsymbol{\phi}_{,t}$, $\boldsymbol{\phi}_{,tt}$ are approximated using Equation 2.71 which after substitution to Equation 2.16 leads to:

$$\boldsymbol{\gamma\rho}\left(\tau\boldsymbol{\phi}_{,tt}+\boldsymbol{\phi}_{,t}\right)\boldsymbol{c}=\left(\boldsymbol{\kappa}_{,x}\boldsymbol{\phi}_{,x}+\boldsymbol{\kappa}_{,y}\boldsymbol{\phi}_{,y}+\boldsymbol{\kappa}_{,z}\boldsymbol{\phi}_{,z}+\boldsymbol{\kappa}\left(\boldsymbol{\phi}_{,xx}+\boldsymbol{\phi}_{,yy}+\boldsymbol{\phi}_{,zz}\right)\right)\boldsymbol{c}, \tag{2.115}$$

which can be written in a manner presented earlier in Equation 2.57:

$$\boldsymbol{\mathcal{A}}_c\boldsymbol{c}=\boldsymbol{\mathfrak{b}}_c. \tag{2.116}$$

The c index in the matrices indicates that the coefficient approach is used. These matrices can be computed as follows:

$$\boldsymbol{\mathcal{A}}_c=\boldsymbol{\gamma\rho}\left(\tau\boldsymbol{\phi}_{,tt}+\boldsymbol{\phi}_{,t}\right)-\left(\boldsymbol{\kappa}_{,x}\boldsymbol{\phi}_{,x}+\boldsymbol{\kappa}_{,y}\boldsymbol{\phi}_{,y}+\boldsymbol{\kappa}_{,z}\boldsymbol{\phi}_{,z}+\boldsymbol{\kappa}\left(\boldsymbol{\phi}_{,xx}+\boldsymbol{\phi}_{,yy}+\boldsymbol{\phi}_{,zz}\right)\right), \tag{2.117}$$

$$\boldsymbol{\mathfrak{b}}_c=\boldsymbol{0}. \tag{2.118}$$

Pseudospectral approach In the spacetime pseudospectral approach, the terms containing spatial and temporal derivatives $\boldsymbol{\phi}_{,x}$, $\boldsymbol{\phi}_{,xx}$, $\boldsymbol{\phi}_{,y}$, $\boldsymbol{\phi}_{,yy}$, $\boldsymbol{\phi}_{,z}$, $\boldsymbol{\phi}_{,zz}$, $\boldsymbol{\phi}_{,t}$, $\boldsymbol{\phi}_{,tt}$ are approximated using Equation 2.80 which after substitution to Equation 2.16 leads to:

$$\boldsymbol{\gamma}\boldsymbol{\rho}\left(\tau\boldsymbol{\mathcal{D}}_{,tt}+\boldsymbol{\mathcal{D}}_{,t}\right)\boldsymbol{u}= \\ \left(\boldsymbol{\kappa}_{,x}\boldsymbol{\mathcal{D}}_{,x}+\boldsymbol{\kappa}_{,y}\boldsymbol{\mathcal{D}}_{,y}+\boldsymbol{\kappa}_{,z}\boldsymbol{\mathcal{D}}_{,z}+\boldsymbol{\kappa}\left(\boldsymbol{\mathcal{D}}_{,xx}+\boldsymbol{\mathcal{D}}_{,yy}+\boldsymbol{\mathcal{D}}_{,zz}\right)\right)\boldsymbol{u}, \quad (2.119)$$

which can be written in a manner presented earlier in Equation 2.57:

$$\boldsymbol{\mathcal{A}}_u\boldsymbol{u}=\mathfrak{b}_u. \quad (2.120)$$

The u index in the matrices indicates that the pseudospectral approach is used. These matrices can be computed as follows:

$$\boldsymbol{\mathcal{A}}_u=\boldsymbol{\gamma}\boldsymbol{\rho}\left(\tau\boldsymbol{\mathcal{D}}_{,tt}+\boldsymbol{\mathcal{D}}_{,t}\right)- \\ \left(\boldsymbol{\kappa}_{,x}\boldsymbol{\mathcal{D}}_{,x}+\boldsymbol{\kappa}_{,y}\boldsymbol{\mathcal{D}}_{,y}+\boldsymbol{\kappa}_{,z}\boldsymbol{\mathcal{D}}_{,z}+\boldsymbol{\kappa}\left(\boldsymbol{\mathcal{D}}_{,xx}+\boldsymbol{\mathcal{D}}_{,yy}+\boldsymbol{\mathcal{D}}_{,zz}\right)\right), \quad (2.121)$$

$$\mathfrak{b}_u=\mathbf{0}. \quad (2.122)$$

The zero vector on the right-hand side of the above equation results from the fact that the problem under consideration is, from a mathematical point of view, a sourceless boundary value problem and since there is no source term in it, the right-hand side of the above equation is equal to the zero vector.

Alternative way of calculating stiffness part of interpolation matrix As in the classical approach, also in the spacetime approach, it is possible to formulate the interpolation matrix without the knowledge of the thermophysical parameters derivatives. The procedure is the same as in the case of the classical approach, after its application, the interpolation matrix for the spacetime coefficient approach is as follows:

$$\boldsymbol{\mathcal{A}}_c=\boldsymbol{\gamma}\boldsymbol{\rho}\left(\tau\boldsymbol{\phi}_{,tt}+\boldsymbol{\phi}_{,t}\right)-\left(\boldsymbol{\phi}_{,x}\boldsymbol{\phi}^{-1}\boldsymbol{\kappa}\boldsymbol{\phi}_{,x}+\boldsymbol{\phi}_{,y}\boldsymbol{\phi}^{-1}\boldsymbol{\kappa}\boldsymbol{\phi}_{,y}+\boldsymbol{\phi}_{,z}\boldsymbol{\phi}^{-1}\boldsymbol{\kappa}\boldsymbol{\phi}_{,z}\right), \quad (2.123)$$

while for the spacetime pseudospectral approach as follows:

$$\boldsymbol{\mathcal{A}}_u=\boldsymbol{\gamma}\boldsymbol{\rho}\left(\tau\boldsymbol{\mathcal{D}}_{,tt}+\boldsymbol{\mathcal{D}}_{,t}\right)-\left(\boldsymbol{\mathcal{D}}_{,x}\boldsymbol{\kappa}\boldsymbol{\mathcal{D}}_{,x}+\boldsymbol{\mathcal{D}}_{,y}\boldsymbol{\kappa}\boldsymbol{\mathcal{D}}_{,y}+\boldsymbol{\mathcal{D}}_{,z}\boldsymbol{\kappa}\boldsymbol{\mathcal{D}}_{,z}\right). \quad (2.124)$$

2.4 Initial and boundary conditions, time integration schemes

So far, the collocation method for the approximate solution of Equation 2.1 has been presented and the approximation of terms containing spatial (and temporal in the case of spacetime) derivatives using the Kansa method has been introduced. Unfortunately, these steps are not sufficient to solve the problem, however, this section will present most of the remaining steps that still need to be performed to solve the problem. As already mentioned, in the classical approach Equation 2.16:

$$\boldsymbol{\gamma}\boldsymbol{\rho}\left(\tau\ddot{\boldsymbol{u}}+\dot{\boldsymbol{u}}\right)=\boldsymbol{\kappa}_{,x}\boldsymbol{u}_{,x}+\boldsymbol{\kappa}_{,y}\boldsymbol{u}_{,y}+\boldsymbol{\kappa}_{,z}\boldsymbol{u}_{,z}+\boldsymbol{\kappa}\left(\boldsymbol{u}_{,xx}+\boldsymbol{u}_{,yy}+\boldsymbol{u}_{,zz}\right)$$

is approximated to the form of Equation 2.36:

$$\boldsymbol{M}\ddot{\boldsymbol{u}} + \boldsymbol{D}\dot{\boldsymbol{u}} + \boldsymbol{K}\boldsymbol{u} = \boldsymbol{0},$$

while in the spacetime approach to the form of Equation 2.57:

$$\boldsymbol{\mathcal{A}}\boldsymbol{u} = \mathfrak{b},$$

using the Kansa method. In the case of the classical approach, at this point, it is necessary to apply the time integration scheme, impose initial and boundary conditions, and solve the system of linear equations. However, in the case of the spacetime approach, it is only necessary to impose initial and boundary conditions and solve the system of linear equations because the problem is treated as a boundary problem.

2.4.1 Classical approach

2.4.1.1 Time integration schemes and initial conditions

Since the problem is hyperbolic, two initial conditions needs to be imposed:

$$\boldsymbol{u}\left(\boldsymbol{x}_i, t = 0\right) = \boldsymbol{u}_0, \tag{2.125}$$

$$\dot{\boldsymbol{u}}\left(\boldsymbol{x}_i, t = 0\right) = \dot{\boldsymbol{u}}_0. \tag{2.126}$$

where $\boldsymbol{x}_i \in \bar{\Omega}$. The initial conditions in the pseudospectral approach are imposed according to the two equations above, however for the coefficient approach it is necessary to transform them using Equation 2.67:

$$\boldsymbol{c}_0 = \boldsymbol{\phi}^{-1}\boldsymbol{u}_0, \tag{2.127}$$

$$\dot{\boldsymbol{c}}_0 = \boldsymbol{\phi}^{-1}\dot{\boldsymbol{u}}_0. \tag{2.128}$$

Vectors $\boldsymbol{c}_0$ and $\dot{\boldsymbol{c}}_0$ or $\boldsymbol{u}_0$ and $\dot{\boldsymbol{u}}_0$ are applied through the time integration schemes. As already mentioned, the goal of the time integration scheme is to approximate one of Equations 2.98, 2.104, 2.99, 2.105:

$$\boldsymbol{M}_c\ddot{\boldsymbol{c}} + \boldsymbol{D}_c\dot{\boldsymbol{c}} + \boldsymbol{K}_c\boldsymbol{c} = \boldsymbol{0},$$

$$\boldsymbol{M}_u\ddot{\boldsymbol{u}} + \boldsymbol{D}_u\dot{\boldsymbol{u}} + \boldsymbol{K}_u\boldsymbol{u} = \boldsymbol{0},$$

$$\boldsymbol{D}_c\dot{\boldsymbol{c}} + \boldsymbol{K}_c\boldsymbol{c} = \boldsymbol{0},$$

$$\boldsymbol{D}_u\dot{\boldsymbol{u}} + \boldsymbol{K}_u\boldsymbol{u} = \boldsymbol{0},$$

to one of the following:

$$\boldsymbol{A}_c\boldsymbol{c}_{k+1} = \boldsymbol{b}_c, \tag{2.129}$$

$$\boldsymbol{A}_u\boldsymbol{u}_{k+1} = \boldsymbol{b}_u, \tag{2.130}$$

It allows to determine the field variable vector in the next $(k+1)$ time step based on the values from the current (k) and the previous $(k-1,\ k-2\ \ldots\ )$ time steps. Two schemes were used in the work: the implicit Euler method [18] and the Houbolt method [76]. In this section, the vectors $\ddot{\boldsymbol{u}}$, $\dot{\boldsymbol{u}}$, $\boldsymbol{u}$ are used. However, all equations are also valid for vectors $\ddot{\boldsymbol{c}}$, $\dot{\boldsymbol{c}}$, $\boldsymbol{c}$, so they can be used in both the coefficient and pseudospectral approach.

Implicit Euler method for parabolic heat equation In the implicit Euler method for the parabolic heat equation, Equation 2.38 is approximated in time by:

$$\boldsymbol{D}\dot{\boldsymbol{u}}_k + \boldsymbol{K}\boldsymbol{u}_{k+1} = \boldsymbol{0}. \tag{2.131}$$

Vector $\dot{\boldsymbol{u}}_k$ can be approximated using the finite differences:

$$\dot{\boldsymbol{u}}_k = \frac{\boldsymbol{u}_{k+1} - \boldsymbol{u}_k}{\Delta t}, \tag{2.132}$$

which after substitution to Equation 2.131 leads to:

$$\left(\frac{1}{\Delta t}\boldsymbol{D} + \boldsymbol{K}\right)\boldsymbol{u}_{k+1} = \left(\frac{1}{\Delta t}\boldsymbol{D}\right)\boldsymbol{u}_k \tag{2.133}$$

Equation 2.133 is the implicit Euler scheme for the parabolic heat equation. Naturally, in this scheme, no starting procedure is needed, the initial conditions are imposed through the vector $\boldsymbol{u}_0$ by simply putting $k = 0$:

$$\left(\frac{1}{\Delta t}\boldsymbol{D} + \boldsymbol{K}\right)\boldsymbol{u}_1 = \left(\frac{1}{\Delta t}\boldsymbol{D}\right)\boldsymbol{u}_0. \tag{2.134}$$

Implicit Euler method for hyperbolic Cattaneo-Vernotte equation In the implicit Euler method for the hyperbolic Cattaneo-Vernotte model, Equation 2.36 is approximated in time by:

$$\boldsymbol{M}\ddot{\boldsymbol{u}}_k + \boldsymbol{D}\dot{\boldsymbol{u}}_k + \boldsymbol{K}\boldsymbol{u}_{k+1} = \boldsymbol{0}. \tag{2.135}$$

Vectors $\dot{\boldsymbol{u}}_k$, $\ddot{\boldsymbol{u}}_k$ can be approximated using the finite differences:

$$\dot{\boldsymbol{u}}_k = \frac{\boldsymbol{u}_{k+1} - \boldsymbol{u}_{k-1}}{2\Delta t}, \tag{2.136}$$

$$\ddot{\boldsymbol{u}}_k = \frac{\boldsymbol{u}_{k+1} - 2\boldsymbol{u}_k + \boldsymbol{u}_{k-1}}{(\Delta t)^2}, \tag{2.137}$$

which after substitution to Equation 2.135 leads to:

$$\boldsymbol{M}\left(\frac{\boldsymbol{u}_{k+1} - 2\boldsymbol{u}_k + \boldsymbol{u}_{k-1}}{(\Delta t)^2}\right) + \boldsymbol{D}\left(\frac{\boldsymbol{u}_{k+1} - \boldsymbol{u}_{k-1}}{2\Delta t}\right) + \boldsymbol{K}\boldsymbol{u}_{k+1} = \boldsymbol{0}, \tag{2.138}$$

and after rearrangement to:

$$\left(\frac{1}{(\Delta t)^2}\boldsymbol{M} + \frac{1}{2\Delta t}\boldsymbol{D} + \boldsymbol{K}\right)\boldsymbol{u}_{k+1} = \left(\frac{2}{(\Delta t)^2}\boldsymbol{M}\right)\boldsymbol{u}_k + \left(-\frac{1}{(\Delta t)^2}\boldsymbol{M} + \frac{1}{2\Delta t}\boldsymbol{D}\right)\boldsymbol{u}_{k-1}. \tag{2.139}$$

Equation 2.139 is the implicit Euler scheme for the hyperbolic Cattaneo-Vernotte equation. Obviously, it can only be used for the second and subsequent time advancements. It cannot be used in the first time advancement because vector $\boldsymbol{u}_{k-1}$ is outside the time domain. Accordingly, a starting procedure is required. Let's solve Equation 2.136 for $\boldsymbol{u}_{k-1}$:

$$\boldsymbol{u}_{k-1} = \boldsymbol{u}_{k+1} - 2\Delta t \dot{\boldsymbol{u}}_k \tag{2.140}$$

substitute it to Equation 2.139:

$$\left(\frac{1}{(\Delta t)^2}\boldsymbol{M} + \frac{1}{2\Delta t}\boldsymbol{D} + \boldsymbol{K}\right)\boldsymbol{u}_{k+1} = \left(\frac{2}{(\Delta t)^2}\boldsymbol{M}\right)\boldsymbol{u}_k + \left(-\frac{1}{(\Delta t)^2}\boldsymbol{M} + \frac{1}{2\Delta t}\boldsymbol{D}\right)\left(\boldsymbol{u}_{k+1} - 2\Delta t\dot{\boldsymbol{u}}_k\right), \tag{2.141}$$

rearrange:

$$\left(\frac{2}{(\Delta t)^2}\boldsymbol{M} + \boldsymbol{K}\right)\boldsymbol{u}_{k+1} = \left(\frac{2}{(\Delta t)^2}\boldsymbol{M}\right)\boldsymbol{u}_k + \left(\frac{2}{\Delta t}\boldsymbol{M} - \boldsymbol{D}\right)\dot{\boldsymbol{u}}_k, \tag{2.142}$$

and put $k = 0$:

$$\left(\frac{2}{(\Delta t)^2}\boldsymbol{M} + \boldsymbol{K}\right)\boldsymbol{u}_1 = \left(\frac{2}{(\Delta t)^2}\boldsymbol{M}\right)\boldsymbol{u}_0 + \left(\frac{2}{\Delta t}\boldsymbol{M} - \boldsymbol{D}\right)\dot{\boldsymbol{u}}_0, \tag{2.143}$$

Equation 2.143 is the starting procedure of the implicit Euler method. It allows to impose the initial conditions through the vectors $\boldsymbol{u}_0$, $\dot{\boldsymbol{u}}_0$.

Houbolt method for hyperbolic Cattaneo-Vernotte equation Hyperbolic problems are characterized by solutions with a great variability over time, much greater than, for example, in the case of parabolic problems. Therefore, lower-order methods such as the Euler method can be insufficient. For this reason, it was also decided to use a method tailored to hyperbolic problems - the Houbolt method [76]. In the Houbolt method, Equation 2.36 is approximated by :

$$\boldsymbol{M}\ddot{\boldsymbol{u}}_{k+1} + \boldsymbol{D}\dot{\boldsymbol{u}}_{k+1} + \boldsymbol{K}\boldsymbol{u}_{k+1} = \boldsymbol{0}, \tag{2.144}$$

while $\dot{\boldsymbol{u}}_{k+1}$, $\ddot{\boldsymbol{u}}_{k+1}$ are approximated by:

$$\dot{\boldsymbol{u}}_{k+1} = \frac{11\boldsymbol{u}_{k+1} - 18\boldsymbol{u}_k + 9\boldsymbol{u}_{k-1} - 2\boldsymbol{u}_{k-2}}{6\Delta t} \tag{2.145}$$

$$\ddot{\boldsymbol{u}}_{k+1} = \frac{2\boldsymbol{u}_{k+1} - 5\boldsymbol{u}_k + 4\boldsymbol{u}_{k-1} - \boldsymbol{u}_{k-2}}{(\Delta t)^2} \tag{2.146}$$

which after substitution to Equation 2.144 leads to:

$$\left(\frac{2}{(\Delta t)^2}\boldsymbol{M}+\frac{11}{6\Delta t}\boldsymbol{D}+\boldsymbol{K}\right)\boldsymbol{u}_{k+1}=\left(\frac{5}{(\Delta t)^2}\boldsymbol{M}+\frac{3}{\Delta t}\boldsymbol{D}\right)\boldsymbol{u}_k+\left(-\frac{4}{(\Delta t)^2}\boldsymbol{M}-\frac{3}{2\Delta t}\boldsymbol{D}\right)\boldsymbol{u}_{k-1}+\left(\frac{1}{(\Delta t)^2}\boldsymbol{M}+\frac{1}{3\Delta t}\boldsymbol{D}\right)\boldsymbol{u}_{k-2} \tag{2.147}$$

Equation 2.147 is the Houbolt scheme. Similar to the implicit Euler scheme, it can only be used for the third and subsequent time advancements. It cannot be used in the first and second time advancement because vectors $\boldsymbol{u}_{k-1}$ and $\boldsymbol{u}_{k-2}$ are outside the time domain. Also in this scheme, a starting procedure is needed. Let's approximate vectors $\dot{\boldsymbol{u}}_k$, $\ddot{\boldsymbol{u}}_k$ using the finite differences [156]:

$$\dot{\boldsymbol{u}}_k=\frac{2\boldsymbol{u}_{k+1}+3\boldsymbol{u}_k-6\boldsymbol{u}_{k-1}+\boldsymbol{u}_{k-2}}{6\Delta t}, \tag{2.148}$$

$$\ddot{\boldsymbol{u}}_k=\frac{\boldsymbol{u}_{k+1}-2\boldsymbol{u}_k+\boldsymbol{u}_{k-1}}{(\Delta t)^2}, \tag{2.149}$$

solve it for $\boldsymbol{u}_{k-1}$, $\boldsymbol{u}_{k-2}$:

$$\boldsymbol{u}_{k-1}=(\Delta t)^2\,\ddot{\boldsymbol{u}}_k+2\boldsymbol{u}_k-\boldsymbol{u}_{k+1}, \tag{2.150}$$

$$\boldsymbol{u}_{k-2}=6\,(\Delta t)^2\,\ddot{\boldsymbol{u}}_k+6\Delta t\dot{\boldsymbol{u}}_k+9\boldsymbol{u}_k-8\boldsymbol{u}_{k+1}, \tag{2.151}$$

substitute to Equation 2.147:

$$\left(\frac{2}{(\Delta t)^2}\boldsymbol{M}+\frac{11}{6\Delta t}\boldsymbol{D}+\boldsymbol{K}\right)\boldsymbol{u}_{k+1}= \tag{2.152}$$

$$\left(\frac{5}{(\Delta t)^2}\boldsymbol{M}+\frac{3}{\Delta t}\boldsymbol{D}\right)\boldsymbol{u}_k+\left(-\frac{4}{(\Delta t)^2}\boldsymbol{M}-\frac{3}{2\Delta t}\boldsymbol{D}\right)\left((\Delta t)^2\,\ddot{\boldsymbol{u}}_k+2\boldsymbol{u}_k-\boldsymbol{u}_{k+1}\right)+\left(\frac{1}{(\Delta t)^2}\boldsymbol{M}+\frac{1}{3\Delta t}\boldsymbol{D}\right)\left(6\,(\Delta t)^2\,\ddot{\boldsymbol{u}}_k+6\Delta t\dot{\boldsymbol{u}}_k+9\boldsymbol{u}_k-8\boldsymbol{u}_{k+1}\right), \tag{2.153}$$

rearrange:

$$\left(\frac{6}{(\Delta t)^2}\boldsymbol{M}+\frac{3}{\Delta t}\boldsymbol{D}+\boldsymbol{K}\right)\boldsymbol{u}_{k+1}=\left(\frac{6}{(\Delta t)^2}\boldsymbol{M}+\frac{3}{\Delta t}\boldsymbol{D}\right)\boldsymbol{u}_k+\left(\frac{6}{\Delta t}\boldsymbol{M}+2\boldsymbol{D}\right)\dot{\boldsymbol{u}}_k+\left(2\boldsymbol{M}+\frac{1}{2}\Delta t\boldsymbol{D}\right)\ddot{\boldsymbol{u}}_k, \tag{2.154}$$

and put $k = 0$:

$$\left(\frac{6}{(\Delta t)^2}\boldsymbol{M} + \frac{3}{\Delta t}\boldsymbol{D} + \boldsymbol{K}\right)\boldsymbol{u}_1 = \left(\frac{6}{(\Delta t)^2}\boldsymbol{M} + \frac{3}{\Delta t}\boldsymbol{D}\right)\boldsymbol{u}_0 + \left(\frac{6}{\Delta t}\boldsymbol{M} + 2\boldsymbol{D}\right)\dot{\boldsymbol{u}}_0 + \left(2\boldsymbol{M} + \frac{1}{2}\Delta t\boldsymbol{D}\right)\ddot{\boldsymbol{u}}_0. \tag{2.155}$$

Equation 2.155 is the starting procedure of the Houbolt method. It allows to impose the initial conditions through the vectors $\boldsymbol{u}_0$, $\dot{\boldsymbol{u}}_0$, $\ddot{\boldsymbol{u}}_0$. Naturally, the vector $\ddot{\boldsymbol{u}}_0$ is not an initial condition, however, it can be easily determined by solving Equation 2.144 for $\ddot{\boldsymbol{u}}_{k+1}$ and putting $k = -1$:

$$\ddot{\boldsymbol{u}}_0 = -\boldsymbol{M}^{-1}\left(\boldsymbol{D}\dot{\boldsymbol{u}}_0 + \boldsymbol{K}\boldsymbol{u}_0\right). \tag{2.156}$$

After the time integration scheme is applied, it is possible to proceed to the imposition of boundary conditions.

2.4.1.2 Boundary conditions

Once Equation 2.129 or 2.130:

$$\boldsymbol{A}_c\boldsymbol{c}_{k+1} = \boldsymbol{b}_c,$$

$$\boldsymbol{A}_u\boldsymbol{u}_{k+1} = \boldsymbol{b}_u,$$

has been obtained, it is possible to proceed to the imposition of the boundary conditions. It consists in replacing the equations corresponding to the boundary points in the system of Equations 2.129 or 2.130 with the equations corresponding to the given boundary conditions. This procedure is repeated at every time step after the time integration scheme is used. The forms of the matrix equations describing the boundary conditions depend on the type of boundary condition and the approach. In the case of the Dirichlet boundary condition for the coefficient approach, it is as follows:

$$\boldsymbol{\phi}\boldsymbol{c} = \boldsymbol{u}_b, \tag{2.157}$$

and for the pseudospectral approach as follows:

$$\boldsymbol{I}\boldsymbol{u} = \boldsymbol{u}_b, \tag{2.158}$$

where $\boldsymbol{I}$ is the identity matrix. In the case of the Neumann boundary condition for the coefficient approach, it is as follows:

$$-\boldsymbol{\kappa}\boldsymbol{\phi}_{,\bar{n}}\boldsymbol{c} = \left(\boldsymbol{q}_b + \tau\dot{\boldsymbol{q}}_b\right), \tag{2.159}$$

and for the pseudospectral approach as follows:

$$-\boldsymbol{\kappa}\boldsymbol{\mathcal{D}}_{,\bar{n}}\boldsymbol{u} = \left(\boldsymbol{q}_b + \tau\dot{\boldsymbol{q}}_b\right). \tag{2.160}$$

Obtaining the boundary condition equation for the Robin boundary condition is slightly more complex than for the Dirichlet and Neumann boundary conditions. Let's start by writing Equation 2.19 for the coefficient approach:

$$-\boldsymbol{\kappa}\boldsymbol{\phi}_{,\bar{n}}\boldsymbol{c} = \boldsymbol{\alpha}\left(\boldsymbol{u}_{\infty} - \boldsymbol{\phi}\boldsymbol{c}\right) - \boldsymbol{\alpha}\tau\dot{\boldsymbol{u}}. \tag{2.161}$$

Assuming the implicit scheme:

$$\boldsymbol{c} = \boldsymbol{c}_{k+1}, \tag{2.162}$$

and the forward approximation in time:

$$\dot{\boldsymbol{u}} \approx \boldsymbol{\phi}\frac{\boldsymbol{c}_{k+1} - \boldsymbol{c}_k}{\Delta t}, \tag{2.163}$$

leads to:

$$-\boldsymbol{\kappa}\boldsymbol{\phi}_{,\bar{n}}\boldsymbol{c}_{k+1} = \boldsymbol{\alpha}\left(\boldsymbol{u}_{\infty} - \boldsymbol{\phi}\boldsymbol{c}_{k+1}\right) - \boldsymbol{\alpha}\tau\boldsymbol{\phi}\frac{\boldsymbol{c}_{k+1} - \boldsymbol{c}_k}{\Delta t}, \tag{2.164}$$

and after rearrangements to:

$$\left(-\boldsymbol{\kappa}\boldsymbol{\phi}_{,\bar{n}} + \boldsymbol{\alpha}\boldsymbol{\phi}\left(\frac{\tau}{\Delta t} + 1\right)\right)\boldsymbol{c}_{k+1} = \boldsymbol{\alpha}\left(\boldsymbol{u}_{\infty} + \frac{\tau}{\Delta t}\boldsymbol{\phi}\boldsymbol{c}_k\right). \tag{2.165}$$

Using the same procedure for the pseudospectral approach gives:

$$\left(-\boldsymbol{\kappa}\boldsymbol{\mathcal{D}}_{,\bar{n}} + \boldsymbol{\alpha}\left(\frac{\tau}{\Delta t} + 1\right)\right)\boldsymbol{c}_{k+1} = \boldsymbol{\alpha}\left(\boldsymbol{u}_{\infty} + \frac{\tau}{\Delta t}\boldsymbol{u}_k\right). \tag{2.166}$$

After imposing the boundary conditions, one of the following equations is obtained:

$$\bar{\boldsymbol{A}}_c\boldsymbol{c}_{k+1} = \bar{\boldsymbol{b}}_c, \tag{2.167}$$

$$\bar{\boldsymbol{A}}_u\boldsymbol{u}_{k+1} = \bar{\boldsymbol{b}}_u. \tag{2.168}$$

2.4.2 Spacetime approach - initial and boundary conditions

As already mentioned in the introduction, the consequence of using the spacetime approach is that the initial conditions are treated as Dirichlet boundary conditions. Therefore, it is reasonable to discuss and impose them together with the boundary conditions. Once Equation 2.116 or 2.120 has been obtained:

$$\boldsymbol{\mathcal{A}}_c\boldsymbol{c} = \mathfrak{b}_c.$$

$$\boldsymbol{\mathcal{A}}_u\boldsymbol{u} = \mathfrak{b}_u.$$

it is possible to proceed to the imposition of the initial conditions and the boundary conditions. The procedure is the same as for the classical approach, i.e. it consists of replacing the equations corresponding to the initial or boundary points in the system of Equations 2.116 or 2.120 with the equations corresponding to the given initial or boundary

conditions. The forms of the matrix equations describing the initial and boundary conditions are listed below. In the case of the Dirichlet boundary condition for the coefficient approach, it is as follows:

$$\boldsymbol{\phi c} = \boldsymbol{u}_b, \tag{2.169}$$

and for pseudospectral approach as follows:

$$\boldsymbol{I u} = \boldsymbol{u}_b, \tag{2.170}$$

In the case of the Neumann boundary condition for the coefficient approach, it is as follows:

$$-\boldsymbol{\kappa \phi}_{,\bar{n}} \boldsymbol{c} = \left(\boldsymbol{q}_b + \tau \dot{\boldsymbol{q}}_b\right), \tag{2.171}$$

and for pseudospectral approach as follows:

$$-\boldsymbol{\kappa \mathcal{D}}_{,\bar{n}} \boldsymbol{u} = \left(\boldsymbol{q}_b + \tau \dot{\boldsymbol{q}}_b\right). \tag{2.172}$$

Obtaining the system of equations for the Robin boundary conditions is slightly more complex than for the Dirichlet and Neumann boundary conditions. In order to obtain it, let's write Equation 2.19 for the coefficient approach:

$$-\boldsymbol{\kappa \phi}_{,\bar{n}} \boldsymbol{c} = \boldsymbol{\alpha}\left(\boldsymbol{u}_\infty - \boldsymbol{\phi c}\right) - \boldsymbol{\alpha} \tau \boldsymbol{\phi}_{,t} \boldsymbol{c}, \tag{2.173}$$

and rearrange it:

$$\left(-\boldsymbol{\kappa \phi}_{,\bar{n}} + \boldsymbol{\alpha}\left(\boldsymbol{\phi} + \boldsymbol{\phi}_{,t} \tau\right)\right) \boldsymbol{c} = \boldsymbol{\alpha u}_\infty. \tag{2.174}$$

Using the same procedure for the pseudospectral approach gives: and rearrange it:

$$\left(-\boldsymbol{\kappa \mathcal{D}}_{,\bar{n}} + \boldsymbol{\alpha}\left(\boldsymbol{I} + \boldsymbol{\mathcal{D}}_{,t} \tau\right)\right) \boldsymbol{u} = \boldsymbol{\alpha u}_\infty. \tag{2.175}$$

Now let's move on to the initial conditions which, as a reminder, are imposed in the same way as the Dirichlet boundary conditions. In the following considerations, $\boldsymbol{\chi}_0$ and $\boldsymbol{\chi}_{-1}$ stands for:

$$\boldsymbol{\chi}_0 = \begin{bmatrix} x \\ y \\ z \\ 0 \end{bmatrix}, \quad \boldsymbol{\chi}_{-1} = \begin{bmatrix} x \\ y \\ z \\ -\Delta t \end{bmatrix}. \tag{2.176}$$

The problem is hyperbolic, thus, two initial conditions needs to be imposed:

$$\boldsymbol{u}\left(\boldsymbol{\chi}_0\right) = \boldsymbol{u}_0, \tag{2.177}$$

$$\dot{\boldsymbol{u}}\left(\boldsymbol{\chi}_0\right) = \dot{\boldsymbol{u}}_0. \tag{2.178}$$

Imposing the first condition of these two is easy, for the coefficient approach the equation describing the condition is as follows:

$$\boldsymbol{\phi c} = \boldsymbol{u}_0, \tag{2.179}$$

and for pseudospectral approach as follows:

$$\boldsymbol{I}\boldsymbol{u} = \boldsymbol{u}_0, \tag{2.180}$$

The imposition of the second initial condition described by Equation 2.178 is a bit more difficult because the lack of a time integration scheme, makes it impossible to impose it directly. Instead, it should be imposed through imposing the value of the temperature field at ghost time $-\Delta t$:

$$\boldsymbol{u}\left(\boldsymbol{\chi}_{-1}\right) = \boldsymbol{u}_{-1}. \tag{2.181}$$

The value of the vector $\boldsymbol{u}_{-1}$ can be determined by approximation of the value of the derivative vector $\dot{\boldsymbol{u}}_0$ using the first-order finite difference:

$$\dot{\boldsymbol{u}}_0 = \frac{\boldsymbol{u}_0 - \boldsymbol{u}_{-1}}{\Delta t}, \tag{2.182}$$

which after rearrangement leads to:

$$\boldsymbol{u}_{-1} = \boldsymbol{u}_0 - \dot{\boldsymbol{u}}_0 \Delta t. \tag{2.183}$$

Finally, the equations for the coefficient approach are as follows:

$$\boldsymbol{\phi}\boldsymbol{c} = \boldsymbol{u}_0 - \dot{\boldsymbol{u}}_0 \Delta t, \tag{2.184}$$

and for pseudospectral approach as follows:

$$\boldsymbol{I}\boldsymbol{u} = \boldsymbol{u}_0 - \dot{\boldsymbol{u}}_0 \Delta t. \tag{2.185}$$

After imposing the initial and the boundary conditions, one of the following equations is obtained:

$$\bar{\boldsymbol{\mathcal{A}}}_c \boldsymbol{c} = \bar{\mathfrak{b}}_c, \tag{2.186}$$

$$\bar{\boldsymbol{\mathcal{A}}}_u \boldsymbol{u} = \bar{\mathfrak{b}}_u, \tag{2.187}$$

thus it is possible to proceed to the solution of this system of linear equations.

2.5 Solving the system of linear equations

After obtaining one of systems of Equations 2.167, 2.168, 2.186, 2.187:

$$\bar{\boldsymbol{A}}_c \boldsymbol{c}_{k+1} = \bar{\boldsymbol{b}}_c,$$

$$\bar{\boldsymbol{A}}_u \boldsymbol{u}_{k+1} = \bar{\boldsymbol{b}}_u,$$

$$\bar{\boldsymbol{\mathcal{A}}}_c \boldsymbol{c} = \bar{\mathfrak{b}}_c,$$

$$\bar{\boldsymbol{\mathcal{A}}}_u \boldsymbol{u} = \bar{\mathfrak{b}}_u,$$

it is necessary to solve it. Since the numeric computing environment MATLAB was used in the research, the *mldivide* [113] algorithm was used to solve the systems of linear equations. It is a very complex and very well tested algorithm, the source code and structure of which are known. Solving the system of linear equations is the last step of the procedure for solving the initial-boundary value problem considered in the work.

2.6 An algorithm for searching the good value of the shape parameter

As mentioned earlier, the shape parameter ε is of fundamental importance for the radial basis function approximation, and consequently its value must be carefully selected. The algorithms of its selection that were used in the work are presented below. A question arises why this sub-section is presented now and not earlier in the paper, since the shape parameter ε already appears earlier in Equation 2.64 and 2.65 and has an influence on further equations. This is due to the fact that the algorithms that will be presented use the equations that were presented in the previous sections and were not known at the time of the first mention of the shape parameter ε.

2.6.1 Shape parameter

The shape parameter ε has already been mentioned in Equations 2.64 and 2.65, however, has not received a decent explanation for this point. In order to explain the meaning of the shape parameter ε, let's take a closer look at Equation 2.64:

$$\varphi\left(\boldsymbol{x}_i, \boldsymbol{x}_j\right) = \left(||\boldsymbol{x}_i - \boldsymbol{x}_j||^2 + \varepsilon^2\right)^p .$$

As can be seen, the shape parameter ε is a parameter occurring in the multiquadric radial basis function and influencing its value and shape, this function is in turn an interpolating function in the Kansa method, which means that the shape parameter ε is a parameter that determines the nature of the interpolation matrix. However, a question arises: why is this parameter called the "shape parameter"? To explain this, let's evaluate the values of multiquadric function described by Equation 2.64 for points in the two-dimensional domain $\boldsymbol{x}_i \in \langle -1, 1\rangle \times \langle -1, 1\rangle \subset \mathbb{R}^2$ and the following center:

$$\boldsymbol{x}_j = \begin{bmatrix} 0 \\ 0 \end{bmatrix},$$

and for the exponent equal to $p = 0.5$. Figures 2.4 and 2.5 show the distribution of the discussed multiquadric radial basis function for the shape parameter $\varepsilon = 1$ and $\varepsilon = 0.01$, respectively.

Figures 2.4 and 2.5 clearly show that the shape parameter ε value has a dominant influence on the shape of the surface, which is a graphical representation of the multiquadric radial basis function φ. As already mentioned, the shape parameter ε has a profound influence on the interpolation matrix and consequently on the numerical stability and the accuracy of the method. This means that the shape parameter ε is a parameter of fundamental importance in the Kansa method. Therefore, a question arises: if the shape parameter ε is so important, is there a known algorithm that allows to find its optimal value? The answer is no. However, there are many algorithms - some of which have been mentioned in the literature review - that allow to find a shape parameter ε value that leads to results of satisfactory accuracy, such algorithms are called algorithms for finding the "good" value of shape parameter - $\varepsilon_{\text{good}}$.

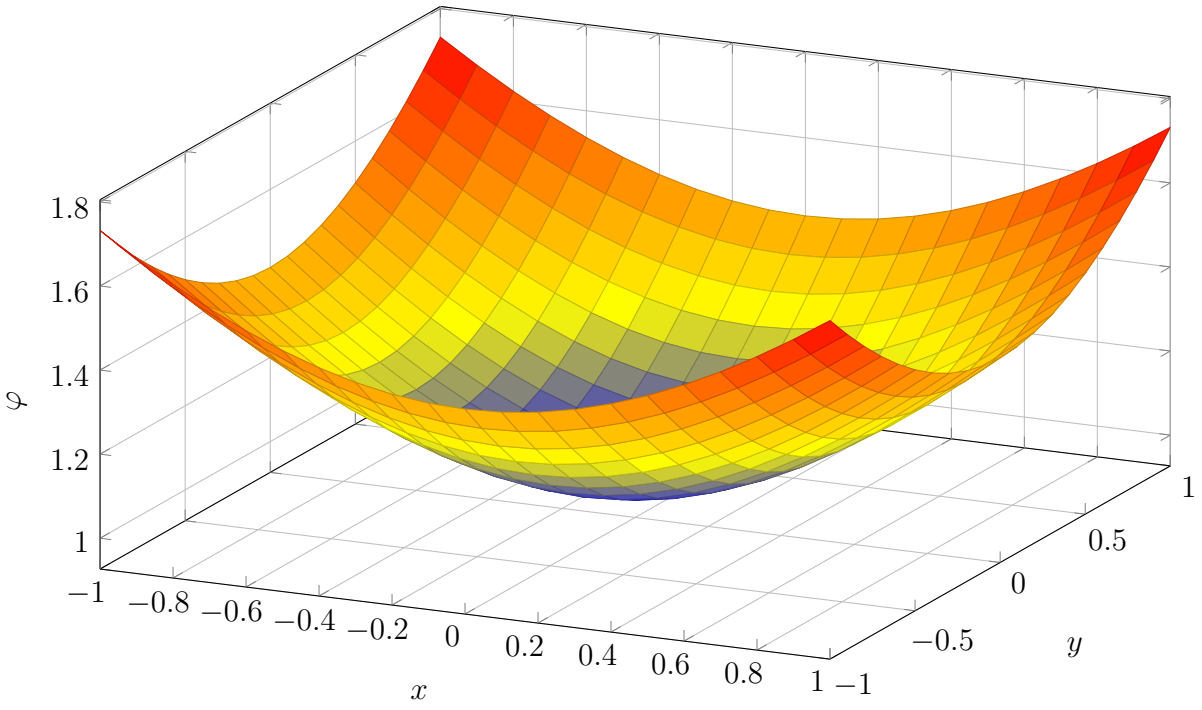

Figure 2.4: Multiquadric radial basis function graph for the shape parameter $\varepsilon = 1$

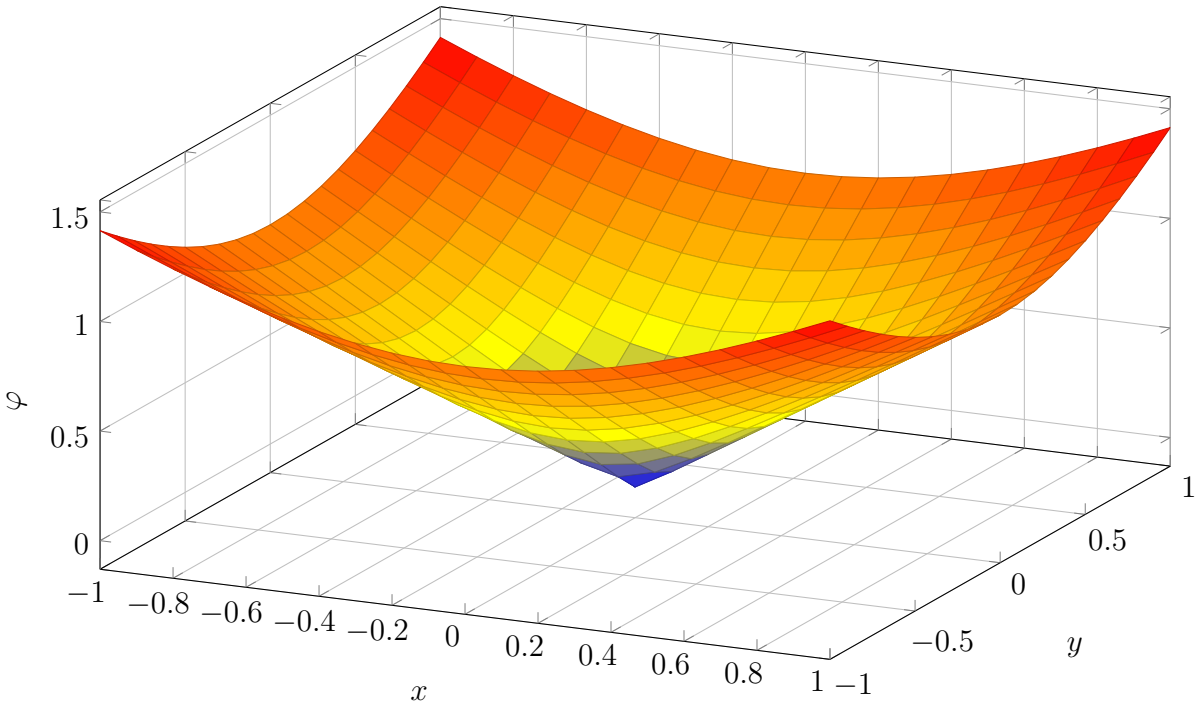

Figure 2.5: Multiquadric radial basis function graph for the shape parameter $\varepsilon = 0.01$

2.6.2 Rippa's algorithm

Currently one of the most popular and the most well-established algorithm for finding a good value of the shape parameter is the Rippa's algorithm [139]. For this reason, this algorithm is taken as the reference algorithm in the thesis and is briefly discussed below. The Rippa's algorithm is an algorithm consisting of several steps. First, it is necessary to select a range of searching for a good shape paramater value. In the next step, the considered partial differential equation-based problem should be solved for the first shape parameter value from this range using the Kansa method in order to obtain the coefficient vector $\boldsymbol{c}$. Next, it is necessary to determine the error estimation vector, the elements of which can be determined using Rippa's formula:

$$E_i = \frac{c_i}{(\boldsymbol{\phi}_{ii})^{-1}}, \tag{2.188}$$

for $i = 1, 2 \ldots n$ where n is length of vector $\boldsymbol{c}$. Then one must find the infinity norm of this vector:

$$E_\infty = \max |\boldsymbol{E}| . \tag{2.189}$$

The procedure should be repeated for all other values in the range in which a good shape parameter value is sought. According to the Rippa's algorithm, a good value of shape parameter $\varepsilon_{\text{good}}$ is one for which E_∞ reaches the minimum:

$$E_\infty (\varepsilon_{\text{good}}) = \min (E_\infty) . \tag{2.190}$$

Figure 2.6 shows an example of the log-log graph of the function $E_\infty (\varepsilon)$ with the indicated good value of the shape parameter $\varepsilon_{\text{good}}$.

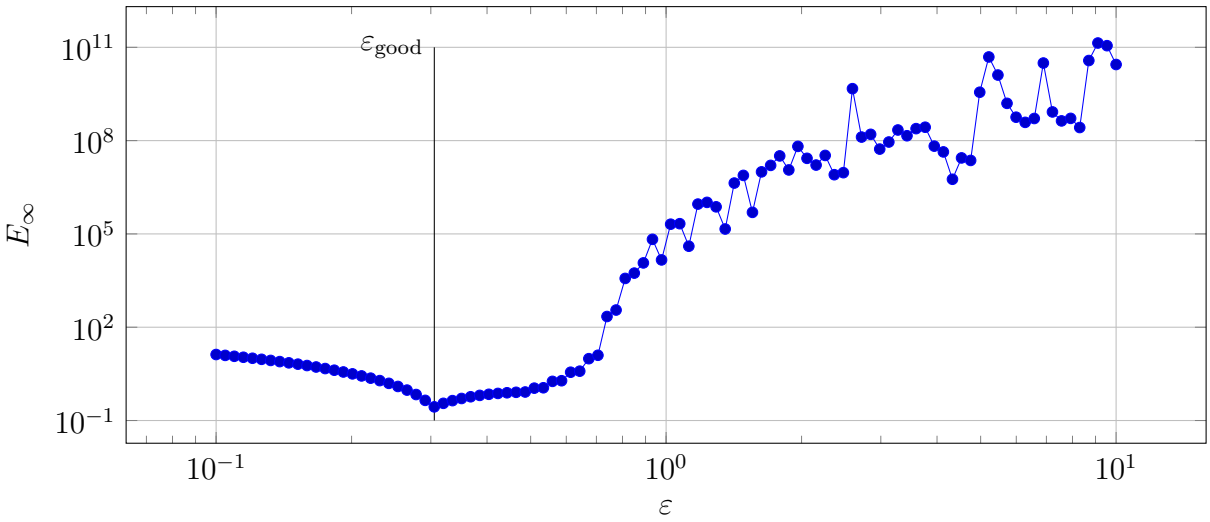

Figure 2.6: An example of the graph of the function $E_\infty (\varepsilon)$

It is worth paying attention to an important issue at this point, namely, finding the vector $\boldsymbol{E}$ requires solving the considered partial differential equation-based problem. This means that a full numerical simulation of the analysed problem should be repeatedly performed for different values of the shape parameter, which is numerically expensive.

2.6.3 Condition number algorithm

In this work, an algorithm based on the analysis of the interpolation matrix condition number will be examined. This algorithm will be referred to in the work as condition algorithm. This algorithm gained the author's special attention due to its enormous potential and, at the same time, low popularity among researchers. To the best of the author's knowledge, there are only two articles where this algorithm was mentioned [175, 67]. The condition algorithm is based on the well-known fact that for the solution of the partial differential equation-based problems with the Kansa method increasing the value of the shape parameter increases the accuracy of the solution [99, 100, 79]. On the other hand, increasing the value of the shape parameter too much makes the simulation unstable and, consequently, its results lose their accuracy significantly. Why is this happening? To explain it well, one should start with the introduction of two fundamental concepts - the ill-conditioned matrix and the condition number of the matrix. The ill-conditioned matrix is a matrix for which small changes in the values of the matrix elements cause significant changes in the results of operations using this matrix, for example when solving a system of linear equations. To understand what condition number is, it is necessary to first get acquainted with the concept of a singular value of the matrix and the so-called singular value decompsition. In this decomposition, matrix $\boldsymbol{A}$ is decomposed into the following three matrices [155, 158, 75]:

$$\boldsymbol{A} = \boldsymbol{U}\boldsymbol{\Sigma}\boldsymbol{V}^T, \tag{2.191}$$

where $\boldsymbol{U}$ and $\boldsymbol{V}$ are orthogonal matrices and $\boldsymbol{\Sigma}$ is a diagonal matrix whose elements $\sigma_i = \boldsymbol{\Sigma}_{ii}$ are singular values of the matrix $\boldsymbol{A}$:

$$\boldsymbol{\Sigma} = \begin{bmatrix} \sigma_1 & 0 & \cdots & 0 \\ 0 & \sigma_2 & \cdots & 0 \\ \vdots & \vdots & \ddots & \vdots \\ 0 & 0 & \cdots & \sigma_n \end{bmatrix}, \tag{2.192}$$

for $i = 1, 2 \ldots n$ is the number of rows in the matrix $\boldsymbol{A}$. Importantly, each complex matrix can be so decomposed. An overview of the methods for the singular value decomposition can be found in [155, 158, 75]. The condition number of a matrix is defined as the ratio of the largest singular value of that matrix to its smallest singular value [12]:

$$\mathrm{cond}\,(\boldsymbol{A}) = \frac{\sigma_{\max}}{\sigma_{\min}}, \tag{2.193}$$

and is a measure of how much ill-conditioned the matrix is, the higher it is, the more ill-conditioned the matrix is. After introducing these concepts, one can return to the question posed earlier: why excessive increase of the shape parameter causes instability of the simulation? This is because increasing the shape parameter increases the condition number of the interpolation matrix in the Kansa method and as a result makes it ill-conditioned. Summarizing the above considerations, the value of the shape parameter should be as high as possible, however, it cannot exceed a certain threshold value because this will cause the interpolation matrix to be ill-conditioned. As a consequence, another question arises: how to find this threshold value? The answer is not easy, however, one of the first thoughts that may come to mind is: maybe just follow how the condition number of the interpolation matrix changes as a function of the shape parameter and when the

threshold value is exceeded, something will happen that can be easily observed and based on this threshold value can be determined? The interpolation matrix may be, in classical formulation, impractical in determination because it is a combination of the $\boldsymbol{M}$, $\boldsymbol{D}$, and $\boldsymbol{K}$ matrices resulting from the application of the time integration scheme. Therefore, it is proposed to use the matrix $\boldsymbol{P}$ instead of the interpolation matrix directly. In the classical approach it can be determined as follows:

$$\boldsymbol{P} = \frac{\boldsymbol{M}}{\Delta t^2} + \frac{\boldsymbol{D}}{\Delta t} + \boldsymbol{K}, \tag{2.194}$$

and in the spacetime approach as follows :

$$\boldsymbol{P} = \boldsymbol{\mathcal{A}}. \tag{2.195}$$

Let's define the $\mathcal{L}(\varepsilon)$ function as follows:

$$\mathcal{L}(\varepsilon) = \mathrm{cond}(\boldsymbol{P}). \tag{2.196}$$

Figure 2.7 shows an example of the log-log graph of the function $\mathcal{L}(\varepsilon)$.

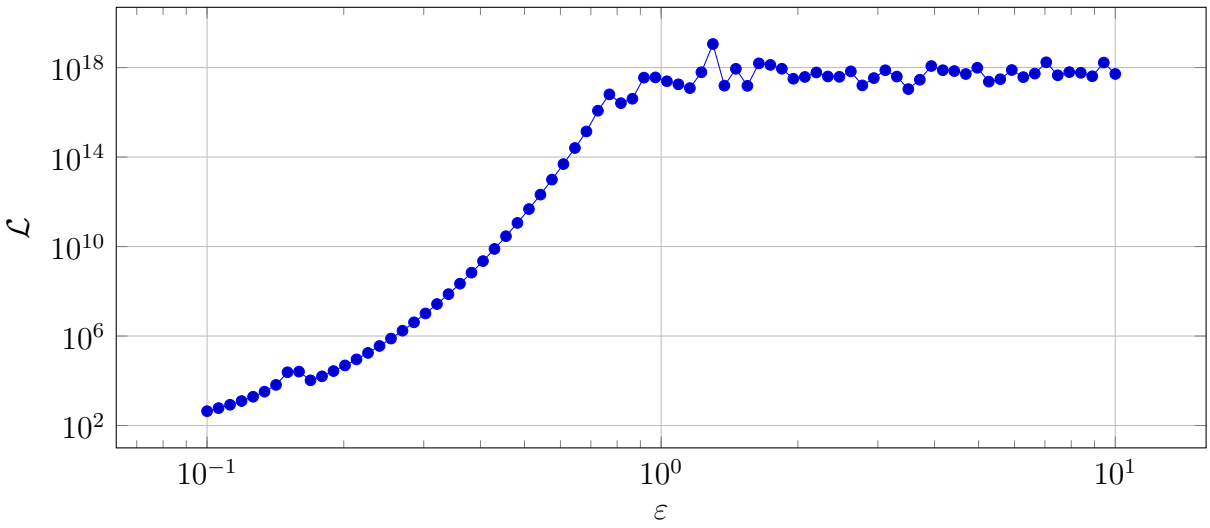

Figure 2.7: An example of the graph of the function $\mathcal{L}(\varepsilon)$

It turns out that for the class of problems considered in the thesis, the graph of the function $\mathcal{L}(\varepsilon)$ usually has the shape shown in Figure 2.7. It is clear that the presented graph can be divided into two parts, a smooth monotonic part and an oscillating part. It is proposed that a good value of the shape parameter is one for which there is a transition from the smooth region to the oscillating region. Figure 2.8 shows the previously shown example of the $\mathcal{L}(\varepsilon)$ function along with the marked value of the shape parameter separating the smooth part from the oscillating part which, according to the proposed algorithm, it is a good value of the shape parameter denoted by $\varepsilon_{\mathrm{good}}$.

The fundamental issue in this algorithm is how to detect the transition from the smooth part to the oscillatory part. It was proposed to study changes in the monotonicity of the function $\mathcal{L}(\varepsilon)$. If there are three monotonicity changes in a row - it is considered that oscillations begin there and consequently it is the value of shape parameter for which the smooth part is separated from the oscillatory part. Why three monotonicity changes? This decision was made on the basis of hundreds of simulations that were performed

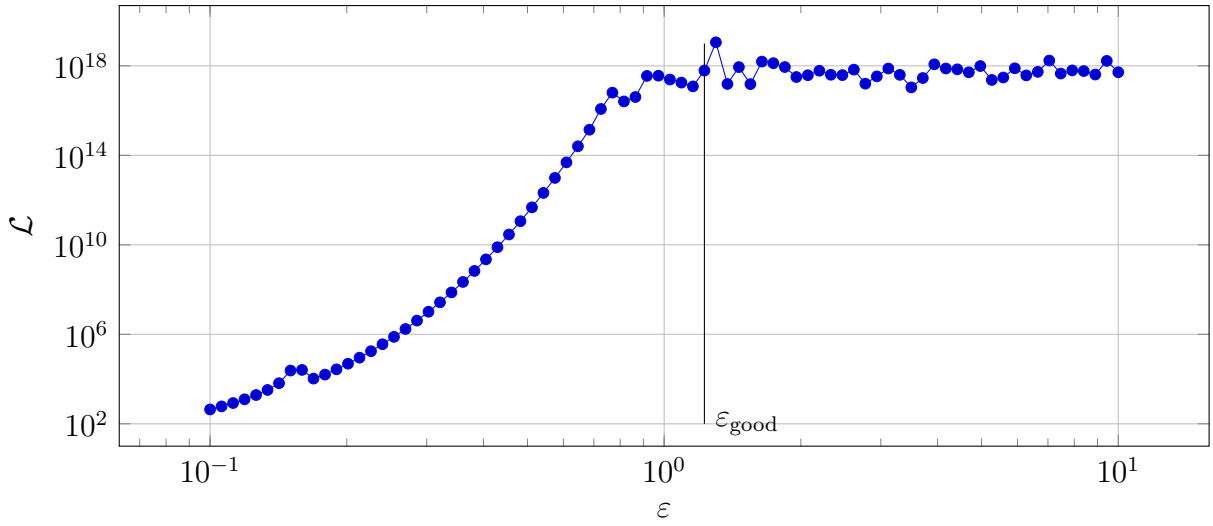

Figure 2.8: An example of the graph of the function $\mathcal{L}(\varepsilon)$ with the marked value of shape parameter separating the smooth region from the oscillating region

for different values. The value three turned out to be the most effective for the class of problems under consideration. Algorithm 1 presents a pseudo-code describing the proposed approach.

Another important question arises at this point. How to choose the range of searching for the transition from smooth to oscillatory region? The following approach was used in the work. First, an algorithm was used for a wide range of shape parameter, for example 10^{-6} to 10^{6} using several dozen logarithmically distributed values. This allows for a rough estimate of the transition location. Then an algorithm was applied for the region surrounding this value, this time using several hundred logarithmically distributed points.

Algorithm 1: The pseudocode describing the proposed condition algorithm. $\boldsymbol{\varepsilon}$ is a vector of the shape parameter values

input : $\boldsymbol{X}, \boldsymbol{\varepsilon}, \boldsymbol{\gamma}, \boldsymbol{\rho}, \boldsymbol{\kappa}, \boldsymbol{\kappa}_{,x}, \boldsymbol{\kappa}_{,y}, \boldsymbol{\kappa}_{,z}, \Delta t, \tau$
output: $\varepsilon_{\text{good}}$

for $i = 1 : length(\boldsymbol{\varepsilon})$ **do**
  $[\boldsymbol{\phi}, \boldsymbol{\phi}_{,x}, \boldsymbol{\phi}_{,xx}, \boldsymbol{\phi}_{,y}, \boldsymbol{\phi}_{,yy}, \boldsymbol{\phi}_{,z}, \boldsymbol{\phi}_{,zz}, \boldsymbol{\phi}_{,t}, \boldsymbol{\phi}_{,tt}] \leftarrow \text{RBF}\ (\boldsymbol{X},\ \boldsymbol{\varepsilon}\,(i))$
  if *classical approach* **then**
    $\boldsymbol{M} = \boldsymbol{M}\,(\boldsymbol{\gamma}, \boldsymbol{\rho}, \boldsymbol{\phi}, \tau)$
    $\boldsymbol{D} = \boldsymbol{D}\,(\boldsymbol{\gamma}, \boldsymbol{\rho}, \boldsymbol{\phi})$
    $\boldsymbol{K} = \boldsymbol{K}\,(\boldsymbol{\phi}, \boldsymbol{\phi}_{,x}, \boldsymbol{\phi}_{,xx}, \boldsymbol{\phi}_{,y}, \boldsymbol{\phi}_{,yy}, \boldsymbol{\phi}_{,z}, \boldsymbol{\phi}_{,zz}, \boldsymbol{\kappa}, \boldsymbol{\kappa}_{,x}, \boldsymbol{\kappa}_{,y}, \boldsymbol{\kappa}_{,z})$
    $\mathcal{L}_i = \text{cond}\left(\dfrac{\boldsymbol{M}}{\Delta t^2} + \dfrac{\boldsymbol{D}}{\Delta t} + \boldsymbol{K}\right)$
  end
  if *spacetime approach* **then**
    $\boldsymbol{\mathcal{A}} = \boldsymbol{\mathcal{A}}\,(\boldsymbol{\gamma}, \boldsymbol{\rho}, \tau, \boldsymbol{\phi}, \boldsymbol{\phi}_{,x}, \boldsymbol{\phi}_{,xx}, \boldsymbol{\phi}_{,y}, \boldsymbol{\phi}_{,yy}, \boldsymbol{\phi}_{,z}, \boldsymbol{\phi}_{,zz}, \boldsymbol{\phi}_{,t}, \boldsymbol{\phi}_{,tt}, \boldsymbol{\kappa}, \boldsymbol{\kappa}_{,x}, \boldsymbol{\kappa}_{,y}, \boldsymbol{\kappa}_{,z})$
    $\mathcal{L}_i = \text{cond}\,(\boldsymbol{\mathcal{A}})$
  end
  if $i > 4$ **then**
    $a = \mathcal{L}_{i-3} - \mathcal{L}_{i-4}$
    $b = \mathcal{L}_{i-2} - \mathcal{L}_{i-3}$
    $c = \mathcal{L}_{i-1} - \mathcal{L}_{i-2}$
    $d = \mathcal{L}_i - \mathcal{L}_{i-1}$
    if $sign\,(a) = sign\,(c)$ *and* $sign\,(b) = sign\,(d)$ *and* $sign\,(b) \neq sign\,(c)$ **then**
      $\varepsilon_{\text{good}} = \boldsymbol{\varepsilon}_{i-4}$
      break
    end
  end
end

2.6.4 Oscillation algorithm

The foundation of the condition algorithm, the study of the transition from the smooth region to the oscillatory region seems to be a concept that can be applied to a wider group of functions, not only the $\mathcal{L}\,(\varepsilon)$ function. This is due to the fact that probably many simulation parameters are strongly disturbed when the simulation loses its stability. This opens up the field for further research in this area and the search for functions that are alternative to the $\mathcal{L}\,(\varepsilon)$ function. Algorithms based on this idea, but not related to the function $\mathcal{L}\,(\varepsilon)$, will be called oscillation algorithms in this work. It is proposed that the function alternative to $\mathcal{L}\,(\varepsilon)$ can be the $E_\infty\,(\varepsilon)$ function from the Rippa's algorithm. An example of the use of such a modified Rippa's algorithm is presented in Figure 2.9, which shows the same distribution of the $E_\infty\,(\varepsilon)$ function as in Figure 2.6. However, the good value of the shape parameter is the one that separates the smooth part from the oscillatory part instead of the value for which the function $E_\infty\,(\varepsilon)$ reaches the minimum.

It is worth noting that there is no suggestion that the modified Rippa's algorithm is better than the original one, but it is only indicated that there is a relatively easy-to-implement alternative that may be better for some classes of problems and worse for

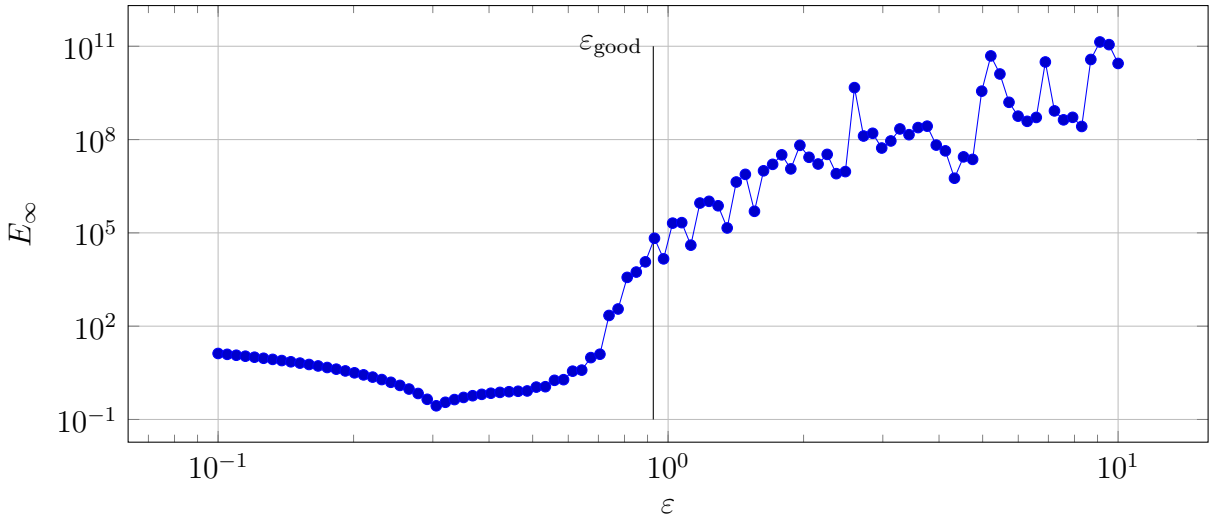

Figure 2.9: An example of the graph of the function $E_\infty(\varepsilon)$ with the marked value of shape parameter separating the smooth region from the oscillating region

others. At the end of this section, it is worth noting that in this paper the problems were considered, where for a given problem and a given cloud of collocation points a good value of the shape parameter is sought. However, there is a different approach in which the optimal distribution of collocation points is sought for a given problem, and only for such a selected distribution, a good value of the shape parameter is determined [145]. However, this approach is not considered at work.

2.7 Flowcharts describing the algorithms for solving initial-boundary value problem

This chapter covered all the steps necessary to solve the initial-boundary value problem under consideration. However, it is worth presenting these algorithms graphically in order to show all the essential steps in a clear and lucid way. Figures 2.10 and 2.11 show the flowcharts describing the algorithms for solving considered initial-boundary value problems using classical and spacetime approach, respectively.

The algorithms described in Figures 2.10 and 2.11 are simplified, however they show all the elements of the actual procedures. For the elliptic problem in the classical approach, after calculating the thermal stiffness matrix $\boldsymbol{K}$, one goes directly (and once) to solving the systems of linear equations. On the other hand, for the parabolic problem, computation of thermal mass matrix $\boldsymbol{M}$ is omitted.

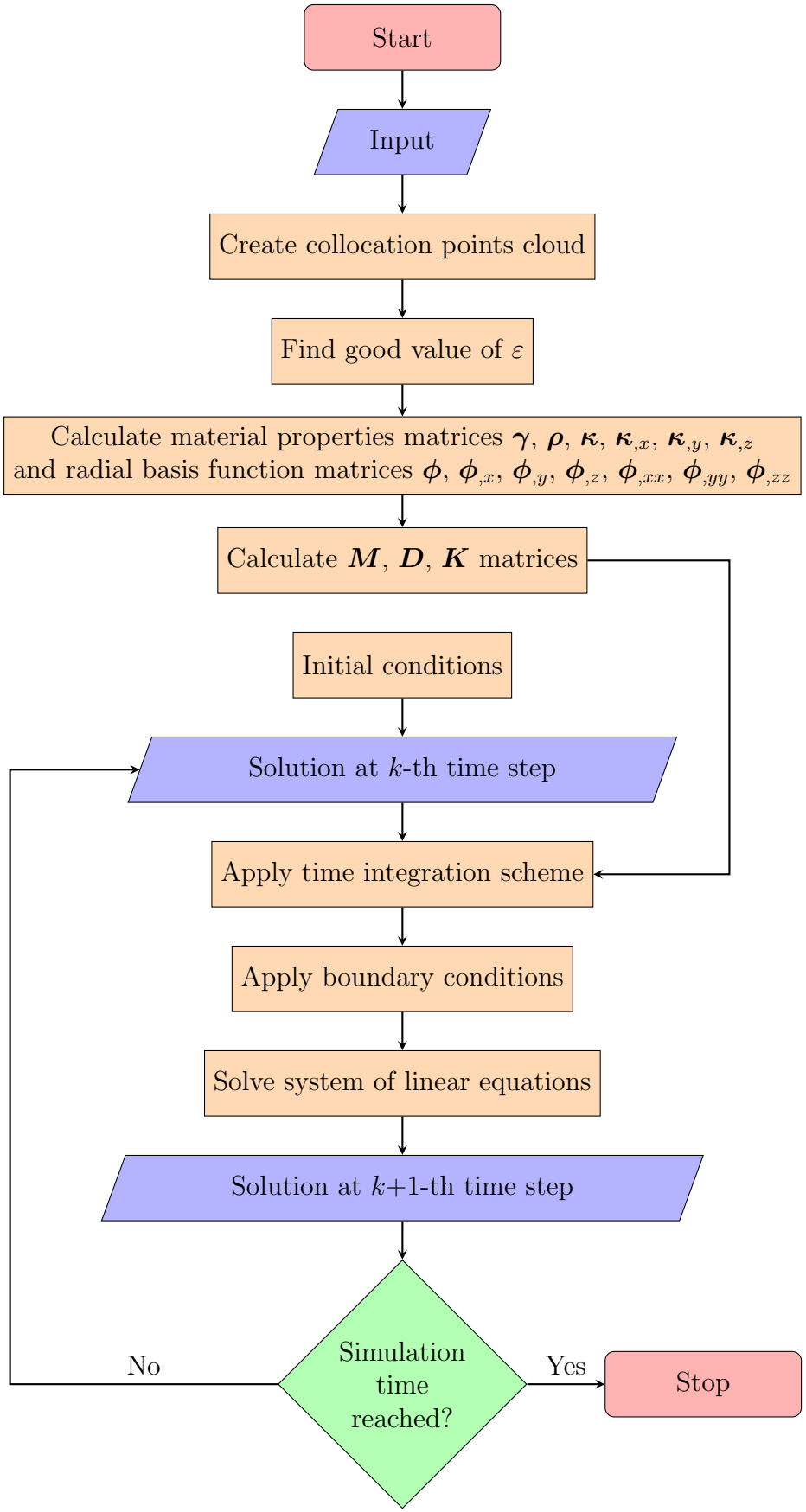

Figure 2.10: Flowchart describing the classical Kansa method algorithm for solving the considered initial-boundary value problem

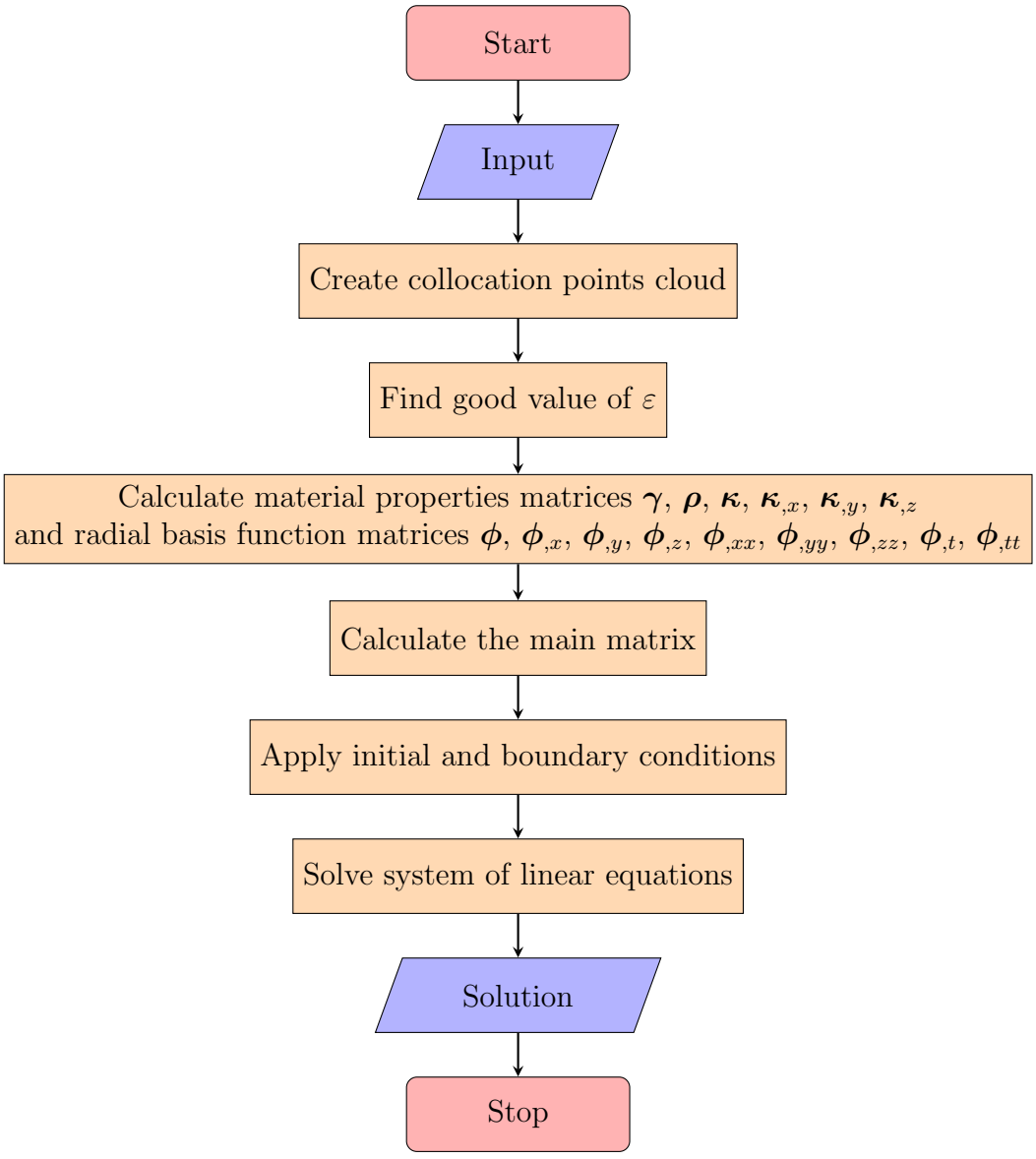

Figure 2.11: Flowchart describing the spacetime Kansa method algorithm for solving the considered initial-boundary value problem

3. Validation and verification of the developed methods and algorithms

Before the Kansa method will be used for practical, real-world problems, it was necessary to perform the validation whether the Kansa method in the presented formulations is suitable for the considered class of problems and the verification of the solver implementation. This was done by comparing the solution obtained using the Kansa method with the reference solutions obtained using other methods. The implementation of the algorithm for solving the considered initial-boundary value problem was made by the author using MATLAB 2022a numeric computing environment. For many of the considered problems, the reference solution was the solution obtained using the finite difference method solver, the implementation of which was also made by the author in the same environment as the Kansa method solver. The description of the finite difference method used in this work can be found in appendix.

3.1 Error measures

Firstly, the error measures used to evaluate the quality of the obtained solutions will be presented. The crucial thing is the way in which the solution under consideration is compared with the reference solution. Therefore, it is necessary to introduce certain error measures that will allow to examine in a quantitative manner the deviation of the considered solution from the reference solution. Two measures were used - local and global. The local measure is a measure that allows for the determination of an error at a specific point $\boldsymbol{x}$ of the computational domain. It means that this error measure evaluated for the entire computational domain is not a single number but a vector containing the error measure values at every point of the domain. This measure is primarily useful for graphical representation of error fields which are curves or surfaces depending on the dimension of the problem. A relative error was adopted as a local measure [119]:

$$\xi_u\left(\boldsymbol{x}\right) = \left| \frac{u_n\left(\boldsymbol{x}\right) - u_r\left(\boldsymbol{x}\right)}{u_r\left(\boldsymbol{x}\right)} \right|, \tag{3.1}$$

$$\xi_q\left(\boldsymbol{x}\right) = \left| \frac{q_n\left(\boldsymbol{x}\right) - q_r\left(\boldsymbol{x}\right)}{q_r\left(\boldsymbol{x}\right)} \right|, \tag{3.2}$$

where $u_n\left(\boldsymbol{x}\right)$ and $q_n\left(\boldsymbol{x}\right)$ are the temperature and heat flux values of the numerical solution at the point $\boldsymbol{x}$, while $u_r\left(\boldsymbol{x}\right)$ and $q_r\left(\boldsymbol{x}\right)$ are the temperature and heat flux values of the reference solutions at the point $\boldsymbol{x}$. The second measure used is the global measure. The

global measure is a measure that determines the error in the entire computational domain expressed by a single value, mean relative error was adopted as a global measure:

$$\bar{\xi}_u = \frac{1}{n}\sum_{i=1}^{n} \xi_u\left(\boldsymbol{x}_i\right) \tag{3.3}$$

$$\bar{\xi}_q = \frac{1}{n}\sum_{i=1}^{n} \xi_q\left(\boldsymbol{x}_i\right) \tag{3.4}$$

In the case where this error measure is calculated for the steady-state solution or for the given time step of the unsteady-state solution, $\bar{\xi}$ symbol is used. If it is calculated for all time steps of the unsteady-state solution, Ξ symbol is used. When calculating the error measure Ξ, the solution for the first time step is not taken into account in order not to artificially improve the error measure value.

3.2 Default numerical setup and general insights

Unless stated otherwise, the simulation parameters were as follows:

- the length of the domain $L = 1\,\mathrm{m}$,
- the initial temperature was $u_0 = 300\,\mathrm{K}$,
- the temporal derivative of the initial temperature was $\dot{u}_0 = 0$,
- the exponent in the multiquadric function was equal to $p = 0.5$,
- the relaxation time for hyperbolic problems was equal to $\tau = 5\,\mathrm{s}$,
- the spacetime scaling parameter was equal to $\beta = \sqrt{\frac{\Delta x}{\Delta t}}$, where Δx will be explained for the specific problems,
- the condition algorithm was used for finding a good value of the shape parameter.

The boundary conditions, alongside their full names, were also abbreviated in the graphs:

- Dirichlet boundary condition is also called the first-type boundary condition, so its designation is '1',
- Neumann boundary condition is also called the second-type boundary condition, so its designation is '2',
- Robin boundary condition is also called the third-type boundary condition, so its designation is '3'.

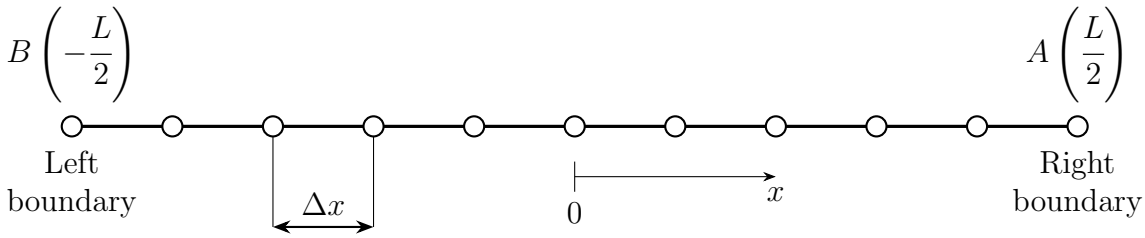

Figure 3.1: The one-dimensional computational domain used in the work

3.3 One-dimensional problems

If the problem is one-dimensional, the Cattaneo-Vernotte Equation 2.9 simplifies to the one-dimensional Cattaneo-Vernotte equation in the form of:

$$\gamma\left(\boldsymbol{x}\right)\rho\left(\boldsymbol{x}\right)\left(\tau\ddot{u}+\dot{u}\right)=\kappa_{,x}\left(\boldsymbol{x}\right)u_{,x}+\kappa\left(\boldsymbol{x}\right)u_{,xx}. \tag{3.5}$$

Problems described by Equation 3.5 were simulated in the computational domain of which a simplified sketch is shown in Figure 3.1.

The distributions of thermophysical parameters in the above domain are given by the following harmonic functions:

$$\kappa\left(x\right)=\frac{\kappa_{\max}+\kappa_{\min}}{2}+\frac{\kappa_{\max}-\kappa_{\min}}{2}\cos\left(\omega\pi\frac{x}{L}\right), \tag{3.6}$$

$$\rho\left(x\right)=\frac{\rho_{\max}+\rho_{\min}}{2}+\frac{\rho_{\max}-\rho_{\min}}{2}\cos\left(\omega\pi\frac{x}{L}\right), \tag{3.7}$$

$$\gamma\left(x\right)=\frac{\gamma_{\max}+\gamma_{\min}}{2}+\frac{\gamma_{\max}-\gamma_{\min}}{2}\cos\left(\omega\pi\frac{x}{L}\right), \tag{3.8}$$

where:

- $\kappa_{\min}=1\,\mathrm{W}\cdot\mathrm{m}^{-1}\cdot\mathrm{K}^{-1}$,
- $\kappa_{\max}=10\,\mathrm{W}\cdot\mathrm{m}^{-1}\cdot\mathrm{K}^{-1}$,
- $\rho_{\min}=1\,\mathrm{kg}\cdot\mathrm{m}^{-3}$,
- $\rho_{\max}=10\,\mathrm{kg}\cdot\mathrm{m}^{-3}$,
- $\gamma_{\min}=1\,\mathrm{J}\cdot\mathrm{kg}^{-1}\cdot\mathrm{K}^{-1}$,
- $\gamma_{\max}=10\,\mathrm{J}\cdot\mathrm{kg}^{-1}\cdot\mathrm{K}^{-1}$,
- $\omega=2$.

The values of the parameters related to the boundary conditions were as follows:

- when the Dirichlet boundary condition was used, the temperature on the left boundary was equal to $u_b=300\,\mathrm{K}$, while on the right boundary to $u_b=400\,\mathrm{K}$,

- when the Neumann boundary condition was used, the heat flux on the left boundary was equal to $q_b = 100\,\mathrm{W}\cdot\mathrm{m}^{-2}$, while on the right boundary to $q_b = -100\,\mathrm{W}\cdot\mathrm{m}^{-2}$
- when the Robin boundary condition was used, the ambient temperature on the left boundary was equal to $u_\infty = 300\,\mathrm{K}$, while on the right boundary to $u_\infty = 400\,\mathrm{K}$ and the heat transfer coefficient was equal to $\alpha = 10\,\mathrm{W}\cdot\mathrm{m}^{-2}\cdot\mathrm{K}^{-1}$.

In the one-dimensional problem, the Neumann boundary condition was not applied to the left and right boundaries at the same time because it would violate the conservation of energy principle.

3.3.1 Steady-state elliptic problem

If the problem is steady, the one-dimensional Cattaneo-Vernotte Equation 3.5 simplifies to the one-dimensional steady-state elliptic heat equation:

$$\kappa_{,x}\left(\boldsymbol{x}\right)u_{,x} + \kappa\left(\boldsymbol{x}\right)u_{,xx} = 0 \iff \left(\kappa\left(\boldsymbol{x}\right)u_{,x}\right)_{,x} = 0, \tag{3.9}$$

for which there is an analytical solution that will be used as a reference solution, it is as follows:

$$u_{,x}\left(x\right) = \frac{D_1}{\kappa\left(x\right)}, \tag{3.10}$$

$$u\left(x\right) = D_1\int\frac{dx}{\kappa\left(x\right)} + D_2, \tag{3.11}$$

where for the harmonic distribution of the thermal conductivity given by Equation 3.6:

$$I = \int\frac{dx}{\kappa\left(x\right)} = \frac{2L}{\omega\pi\sqrt{\kappa_{\max}\kappa_{\min}}}\left(\arctan\left(\tan\left(\omega\frac{\pi}{2}\frac{x}{L}\right)\sqrt{\frac{\kappa_{\min}}{\kappa_{\max}}}\right) + k\pi\right), \tag{3.12}$$

where

$$k = \begin{cases} \dots & \\ -2 & \text{if } \omega\dfrac{x}{L} \in \langle -5,\,-3) \\ -1 & \text{if } \omega\dfrac{x}{L} \in \langle -3,\,-1) \\ 0 & \text{if } \omega\dfrac{x}{L} \in \langle -1,\,1\rangle \\ 1 & \text{if } \omega\dfrac{x}{L} \in (1,\,3\rangle \\ 2 & \text{if } \omega\dfrac{x}{L} \in (3,\,5\rangle \\ \dots & \end{cases}. \tag{3.13}$$

The necessity to use Eequation 3.13 is due to the fact that the cyclometric function arctan gives values only in the range $\left\langle -\frac{\pi}{2},\,\frac{\pi}{2}\right\rangle$, which would lead to erroneous results if

$\omega \frac{x}{L} \notin \langle -1, 1 \rangle$. Constants of integration D_1, D_2 can be calculated based on the boundary conditions. For example, when imposing the Dirichlet boundary conditions on both boundaries, the constants of integration are a solution of the following system of linear equations:

$$\begin{bmatrix} I(-L/2) & 1 \\ 1 & I(L/2) \end{bmatrix} \begin{bmatrix} D_1 \\ D_2 \end{bmatrix} = \begin{bmatrix} u_b(-L/2) \\ u_b(L/2) \end{bmatrix}. \tag{3.14}$$

3.3.1.1 Convergence study

First, the convergence study was conducted. As part of it, a series of simulations was performed for the number of collocation points n in the range from 10 to 50. Such a small number of collocation points is due to the fact that the multiquadric radial basis function is a high-order interpolation function and such a small number of collocation points should result in a high accuracy of the solution. For each simulation, the good value of the shape parameter was individually selected. After each simulation, the value of the error measure $\bar{\xi}_u$ was calculated with respect to the analytical solution 3.11. The simulations were carried out using both coefficient and pseudospectral approach for various combinations of boundary conditions. Figures 3.2 - 3.6 show the values of error measure $\bar{\xi}_u$ versus the number of collocation points n calculated with respect to the analytical solution for various boundary-value problems.

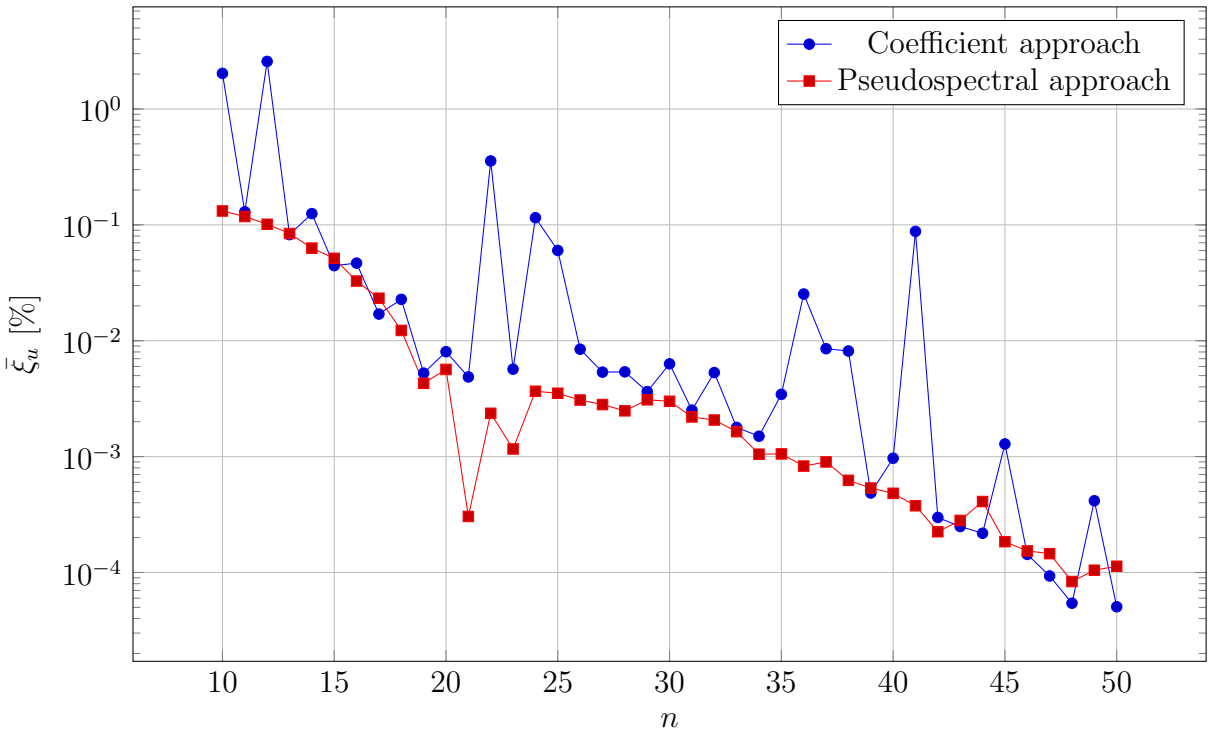

Figure 3.2: Error measure $\bar{\xi}_u$ versus the number of collocation points n obtained during one-dimensional convergence study for the Dirichlet-Dirichlet boundary conditions

The results presented in the Figures 3.2 - 3.6 are in line with expectations - the multiquadric scheme is a high-order interpolation scheme, so the accuracy of the results is satisfactory even with a small number of collocation points. Even about 20 collocation points allowed to achieve an error measure $\bar{\xi}_u$ value below 10^{-2} %. Therefore, it was

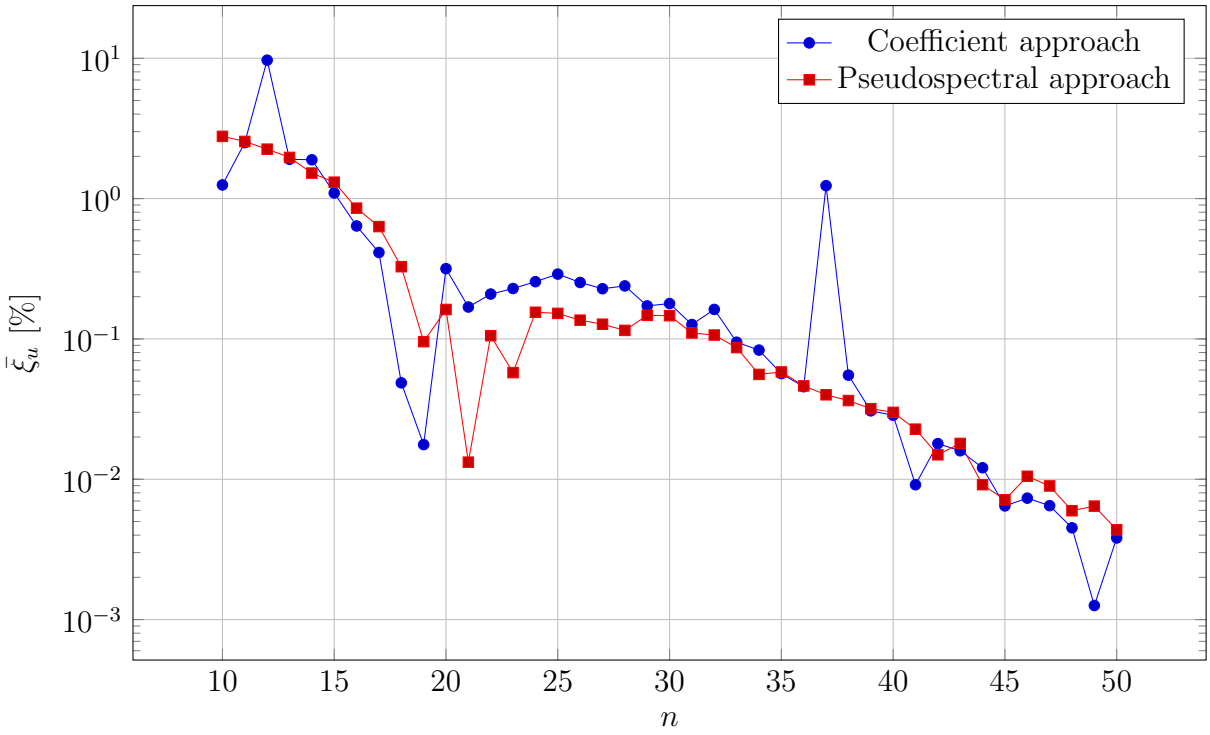

Figure 3.3: Error measure $\bar{\xi}_u$ versus the number of collocation points n obtained during one-dimensional convergence study for the Robin-Robin boundary conditions

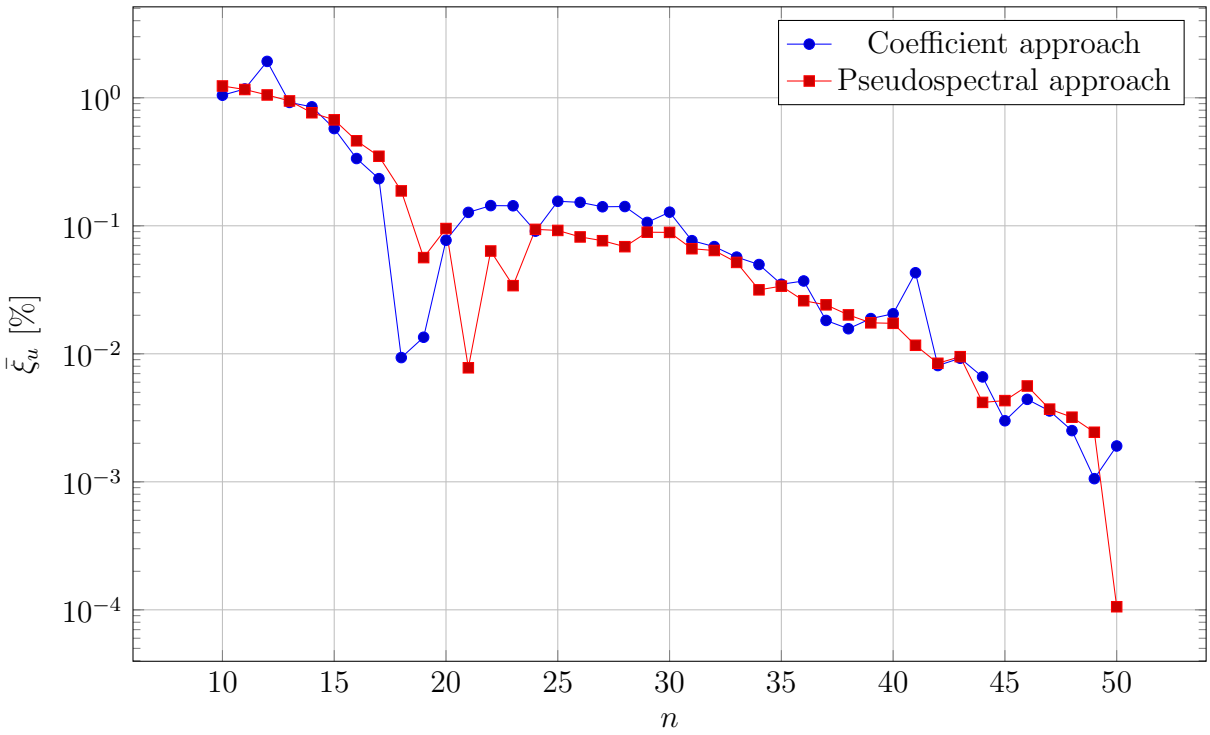

Figure 3.4: Error measure $\bar{\xi}_u$ versus the number of collocation points n obtained during one-dimensional convergence study for the Dirichlet-Neumann boundary conditions

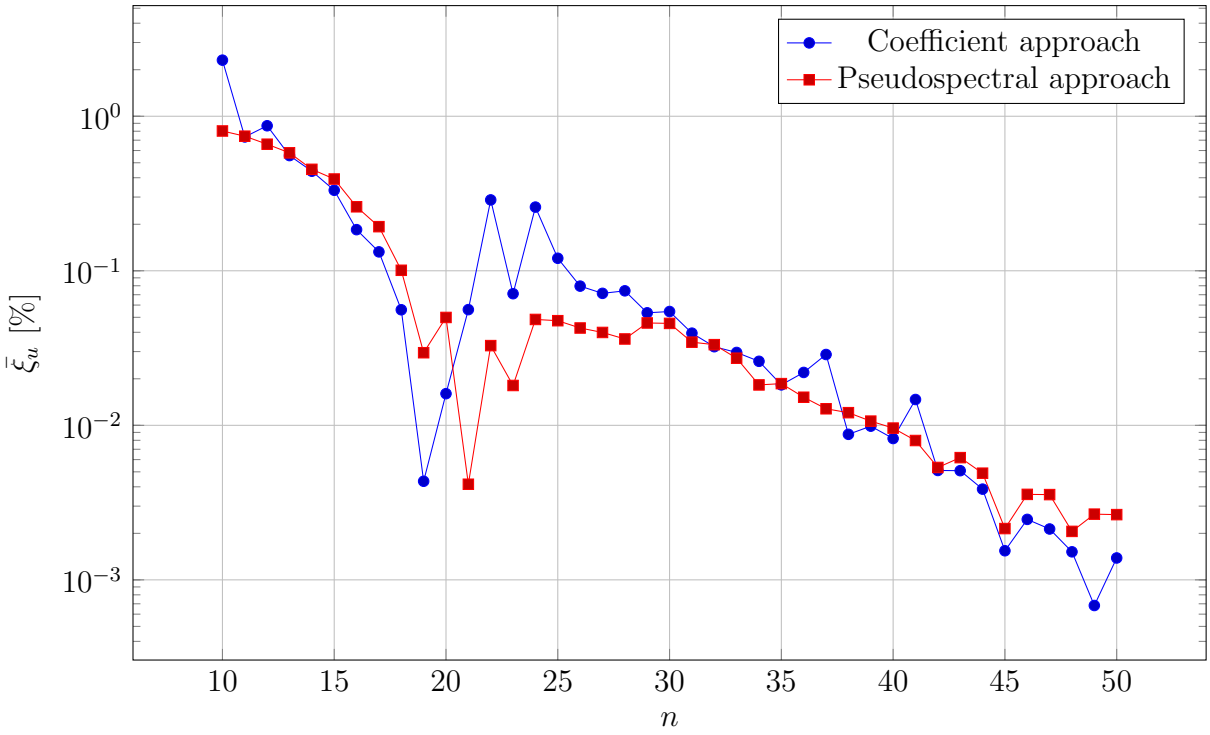

Figure 3.5: Error measure $\bar{\xi}_u$ versus the number of collocation points n obtained during one-dimensional convergence study for the Robin-Dirichlet boundary conditions

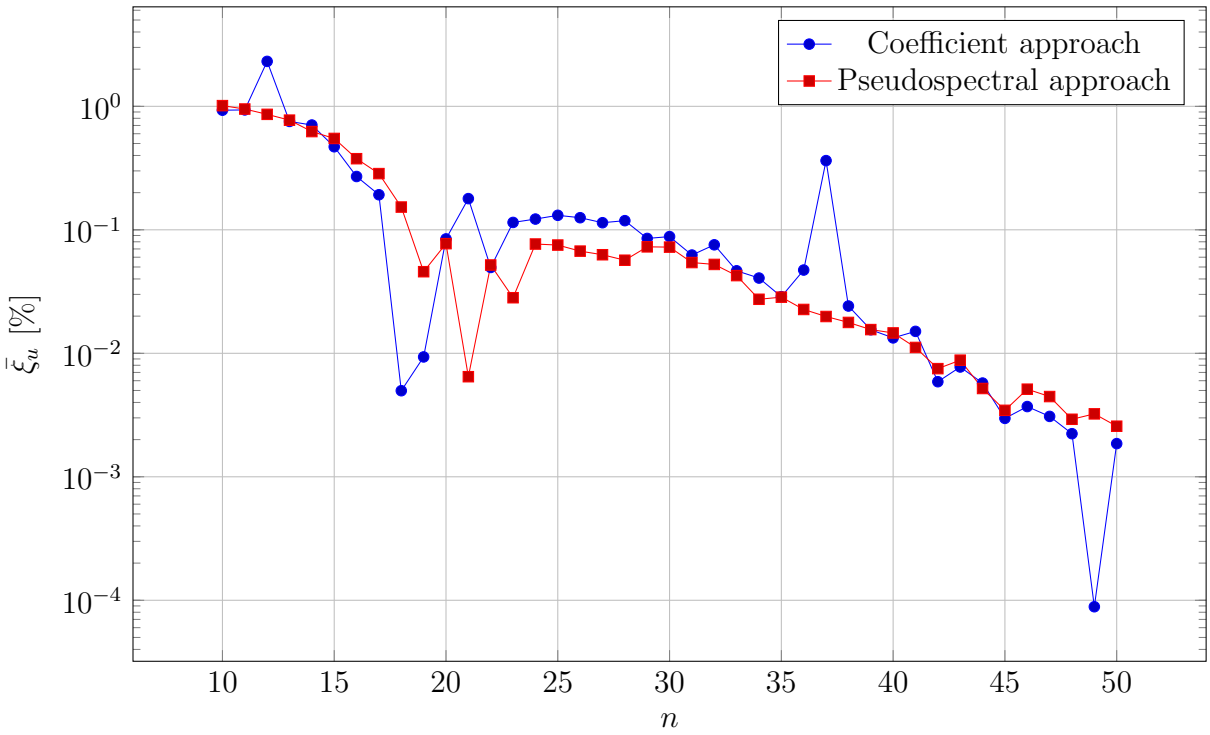

Figure 3.6: Error measure $\bar{\xi}_u$ versus the number of collocation points n obtained during one-dimensional convergence study for the Neumann-Robin boundary conditions

decided that the number of collocation points in the next one-dimensional simulations will be equal to 21. An issue that must be noted is that the presented solutions are not smooth but oscillating and at some points there are even peaks. This nature of the solution results from the fact that for each simulation the shape parameter value was individually selected with the use of the condition algorithm. However, it is worth noting that for the simulation with the number of collocation points above 20, even for the shape parameter value corresponding to the solution peak, the accuracy was very high, the error measure $\bar{\xi}_u$ values did not exceed 0.5%. When it comes to comparing the accuracy between the coefficient and pseudospectral approaches, the results are very similar, but it seems that for this problem class the pseudospectral approach gives slightly more accurate results.

3.3.1.2 One-dimensional elliptic problem no. 1

After performing the convergence study, it is possible to proceed to problem no. 1 in which the accuracy of the method for this class of problems will be closely examined. A series of simulations using different approaches and combinations of boundary conditions were performed and the global error measures $\bar{\xi}_u$ and $\bar{\xi}_q$ were calculated with respect to the analytical solution after each simulation. Figure 3.7 shows the values of error measures $\bar{\xi}_u$ and $\bar{\xi}_q$ calculated for the Kansa method solution with respect to the analytical solution for various approaches and combinations of the boundary conditions. Figures 3.8 - 3.12 show the comparisons between solutions obtained using Kansa method and analytical solution for various combinations of the boundary conditions.

Low values of error measures $\bar{\xi}_u$ and good agreement of the Kansa method solutions with the reference solutions show that the Kansa method is suitable for solving the considered class of problems and the solver is correctly implemented. The accuracy for the coefficient and pseudospectral approaches are very similar. The values of error measures $\bar{\xi}_q$ are also low, however are even two orders of magnitude greater than the values of error measure $\bar{\xi}_u$. This is due to the fact that the heat flux field is calculated using the obtained temperature field after the simulation is completed using the differentiation operator:

$$\boldsymbol{q} = -\boldsymbol{\kappa}\boldsymbol{\phi}_{,x}\boldsymbol{c}. \tag{3.15}$$

or:

$$\boldsymbol{q} = -\boldsymbol{\kappa}\boldsymbol{\mathcal{D}}_{,x}\boldsymbol{u}. \tag{3.16}$$

This operation is burdened with a numerical error, which in this case is strongly amplified because the interpolation matrices are characterized by very high condition number values, which results from the method of selecting the shape parameter value. It should be expected that in more complex problems that will be presented in the paper, this effect may be even stronger. This problem can be minimized by the use of regularization [41], which, however, will not be done in the work but seems to be a reasonable topic for further research. Finally, it is worth noting that the heat flux fields are characterized by a rapid change of values near the boundary, which is most likely due to the fact that a different equation is solved on the border than in the interior. Additionally, the flux field for the coefficient and pseudospectral approaches are almost symmetrical with respect to each other in relation to the line drawn by the points of the analytical solution. The explanation for this is unknown.

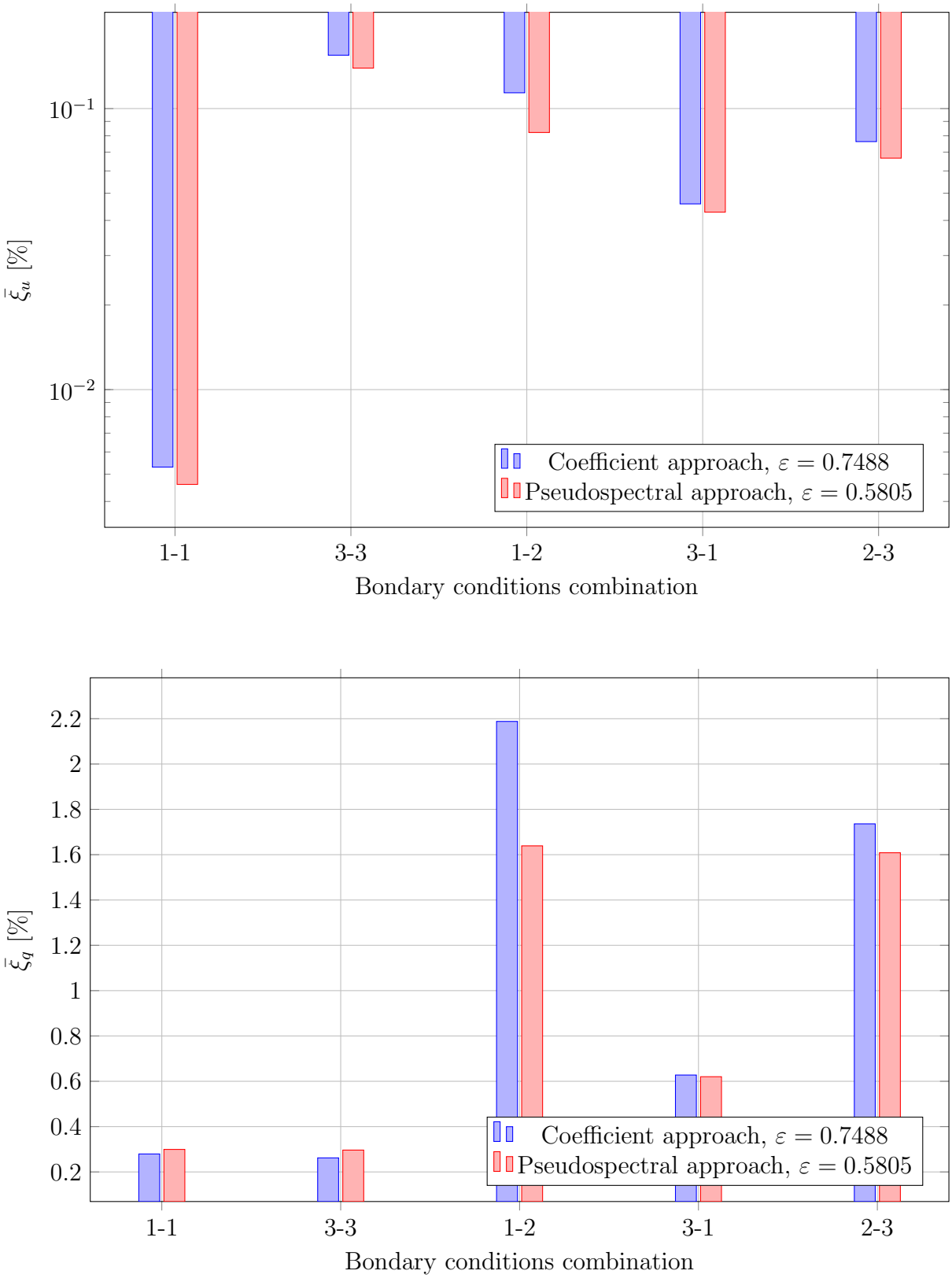

Figure 3.7: Error measures $\bar{\xi}_u$ and $\bar{\xi}_q$ for the one-dimensional elliptic problem no. 1 obtained using various approaches and combinations of boundary conditions

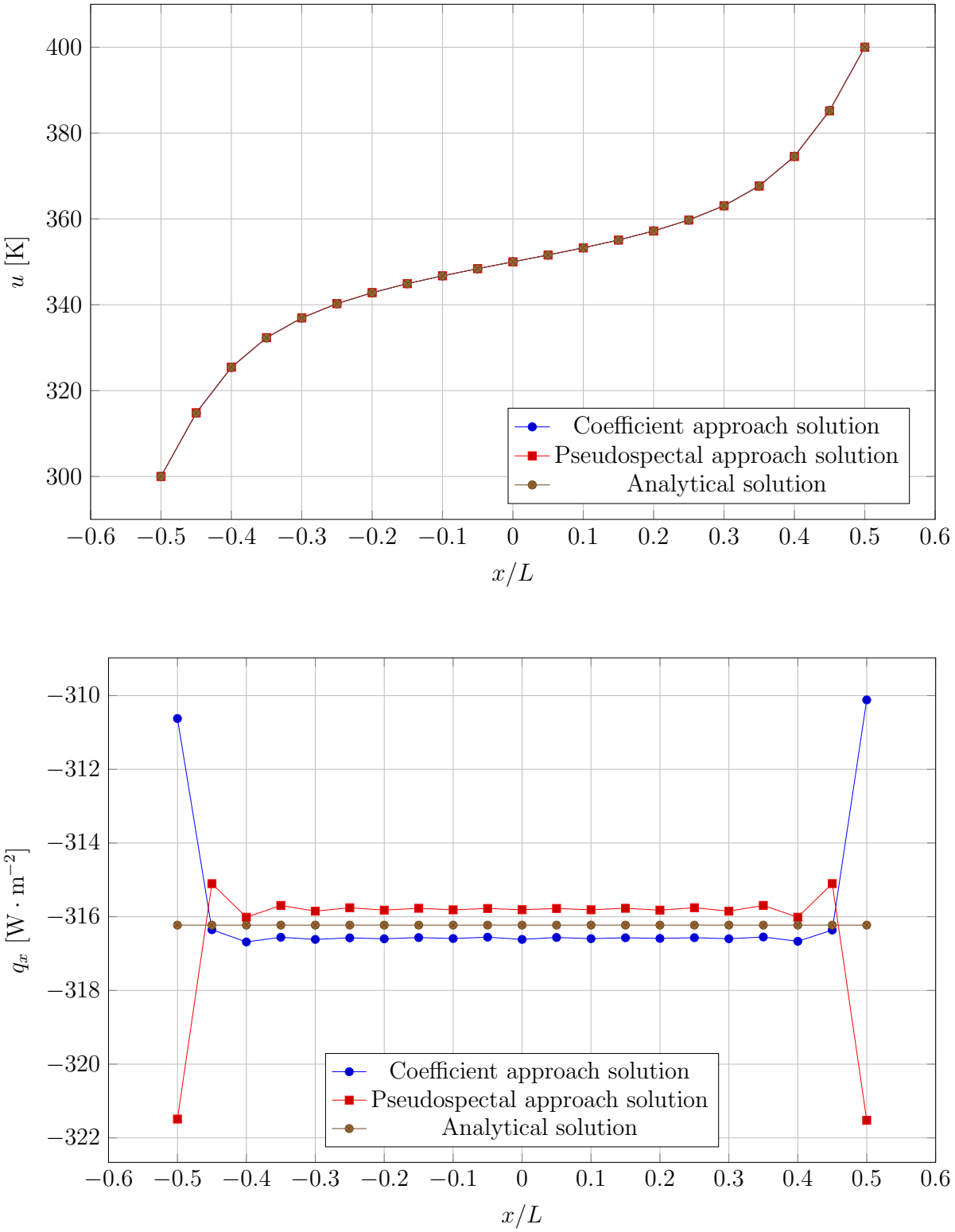

Figure 3.8: Comparison between the Kansa method solutions and the analytical solution for the one-dimensional elliptic problem no. 1 obtained using the Dirichlet-Dirichlet boundary conditions

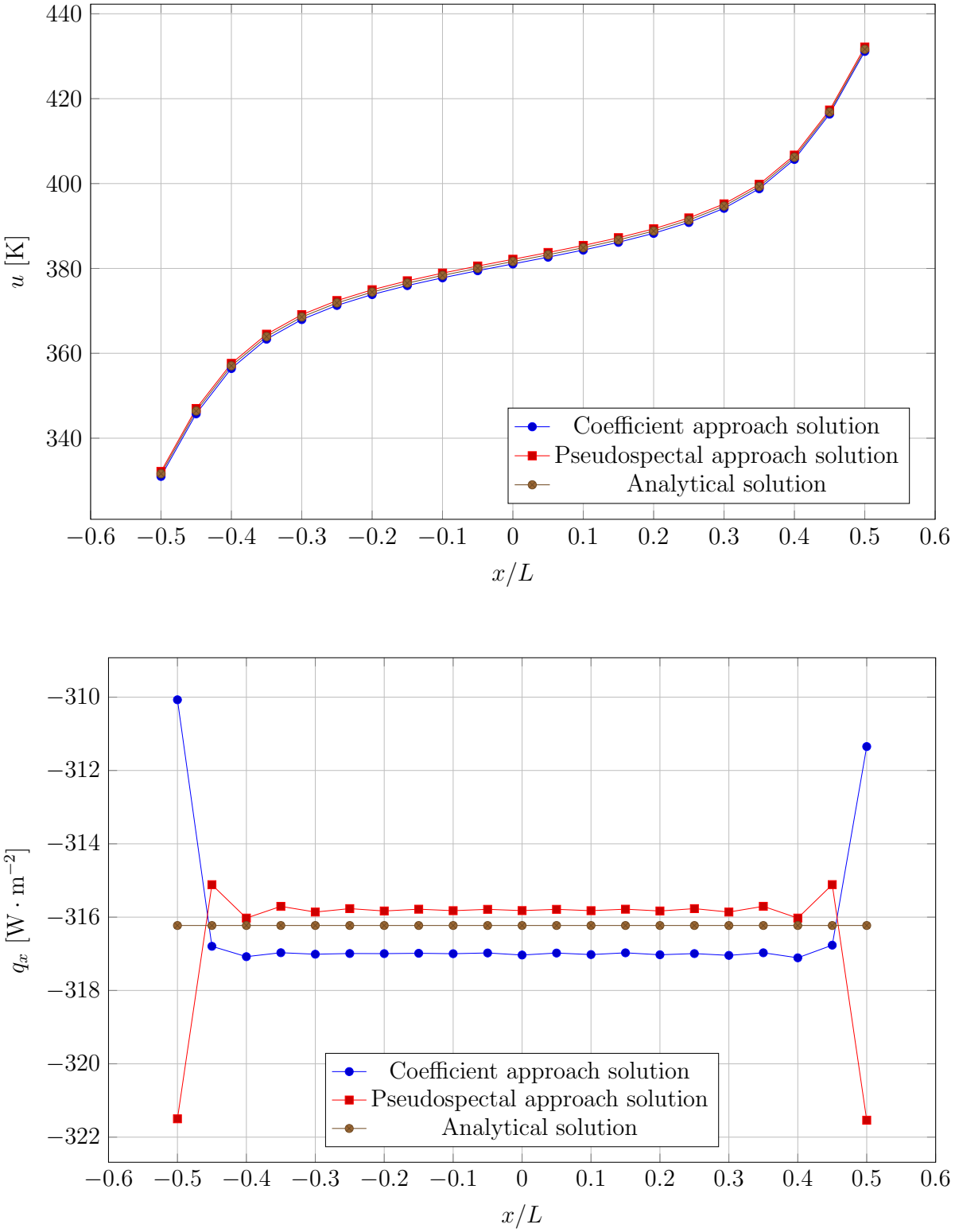

Figure 3.9: Comparison between the Kansa method solutions and the analytical solution for the one-dimensional elliptic problem no. 1 obtained using the Robin-Robin boundary conditions

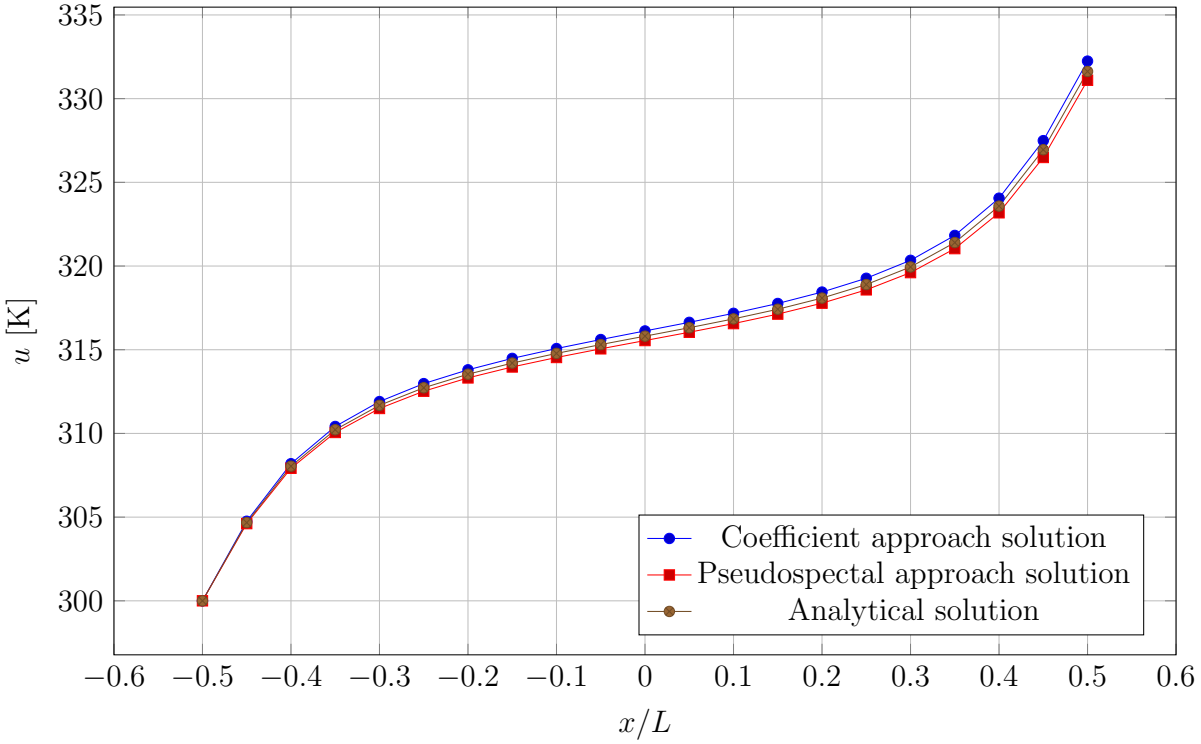

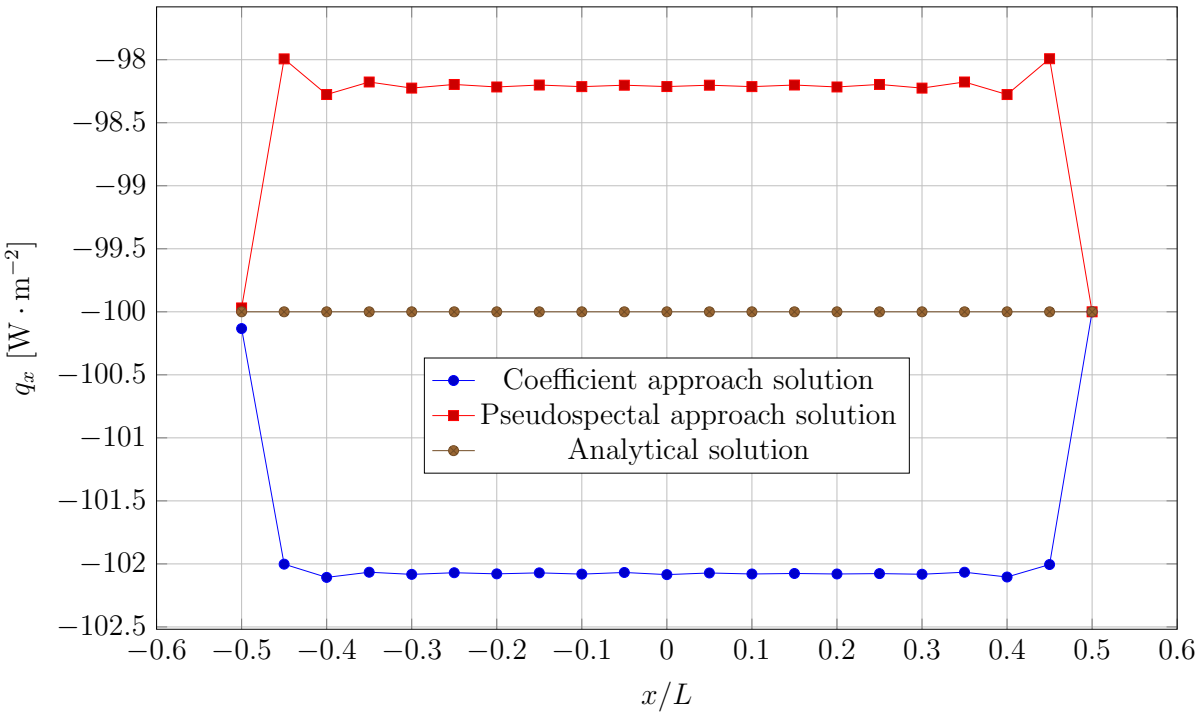

Figure 3.10: Comparison between the Kansa method solutions and the analytical solution for the one-dimensional elliptic problem no. 1 obtained using the Dirichlet-Neumann boundary conditions

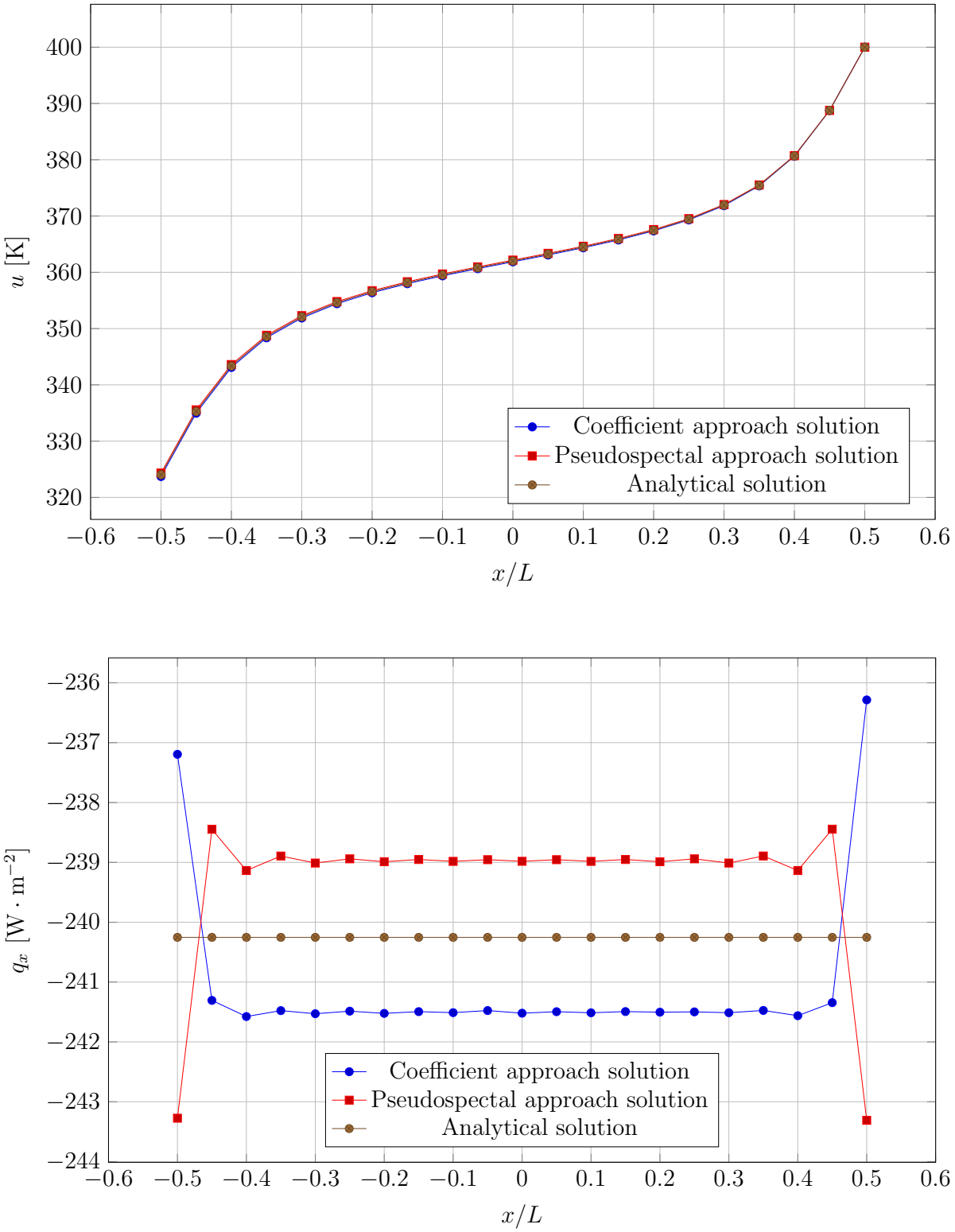

Figure 3.11: Comparison between the Kansa method solutions and the analytical solution for the one-dimensional elliptic problem no. 1 obtained using the Robin-Dirichlet boundary conditions

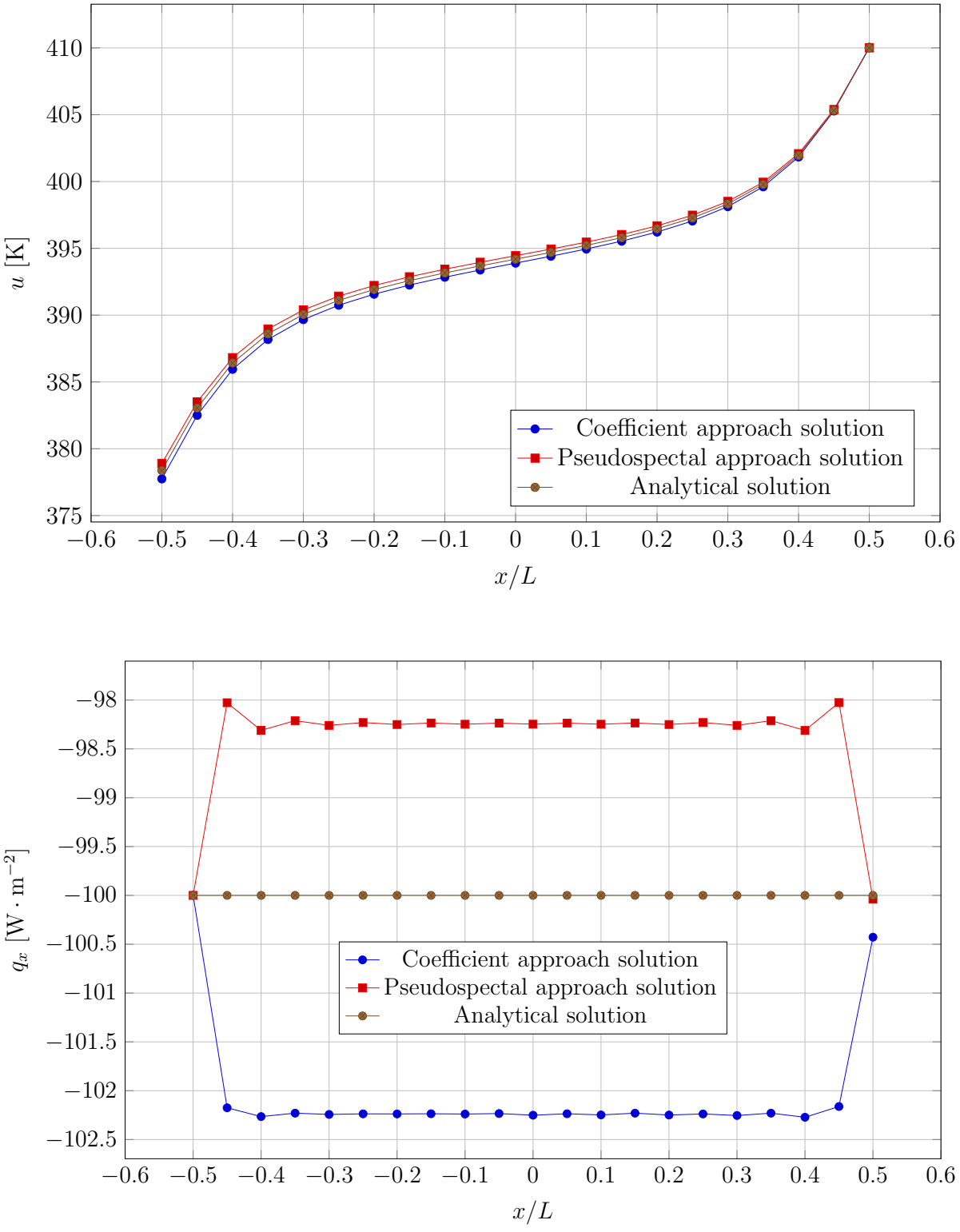

Figure 3.12: Comparison between the Kansa method solutions and the analytical solution for the one-dimensional elliptic problem no. 1 obtained using the Neumann-Robin boundary conditions

3.3.2 Unsteady-state parabolic problem

If the relaxation time $\tau = 0$, the one-dimensional Cattaneo-Vernotte Equation 3.5 simplifies to the one-dimensional parabolic heat equation:

$$\gamma\left(\boldsymbol{x}\right)\rho\left(\boldsymbol{x}\right)\dot{u} = \kappa_{,x}\left(\boldsymbol{x}\right)u_{,x} + \kappa\left(\boldsymbol{x}\right)u_{,xx}. \tag{3.17}$$

The reference solution for this problem was the finite difference method solution. In the case of the problem governed by the parabolic heat equation, similar studies were carried out as for the problem governed by the elliptic heat equation. A series of simulations for different approaches and combinations of boundary conditions were performed and the error measures values Ξ_u and Ξ_q were calculated with respect to the finite difference method solution after each simulation. Time step size was equal to $\Delta t = 0.1\,\mathrm{s}$ while the number of time advancements was equal to 50. The number of time advancements was chosen arbitrarily in such a way that the simulation ended long before reaching the steady state, so as not to artificially improve the value of the error measures. Figure 3.13 shows the values of error measure Ξ_u and Ξ_q calculated for the Kansa method solution with respect to the finite difference method solution for various approaches and combinations of the boundary conditions. Figures 3.14 - 3.18 show the evolution of temperature and heat flux at the point $x = 0$ for various combinations of boundary conditions and approaches obtained using the Kansa method and finite difference method.

Low values of error measures Ξ_u and good agreement of the Kansa method solutions with the reference solutions show that the Kansa method is suitable for solving the considered class of problems and the solver is correctly implemented. However, it is worth noting that the classical approach is slightly more accurate than the spacetime approach, while the accuracy of the pseudospectral approach is slightly better in conjunction with the classical approach and slightly worse in conjunction with the spacetime approach. All solutions are less accurate than their steady-state equivalents. The value of error measures Ξ_q are much higher than Ξ_u, which is similar to the steady-state case and consequently the same conclusions can be drawn.

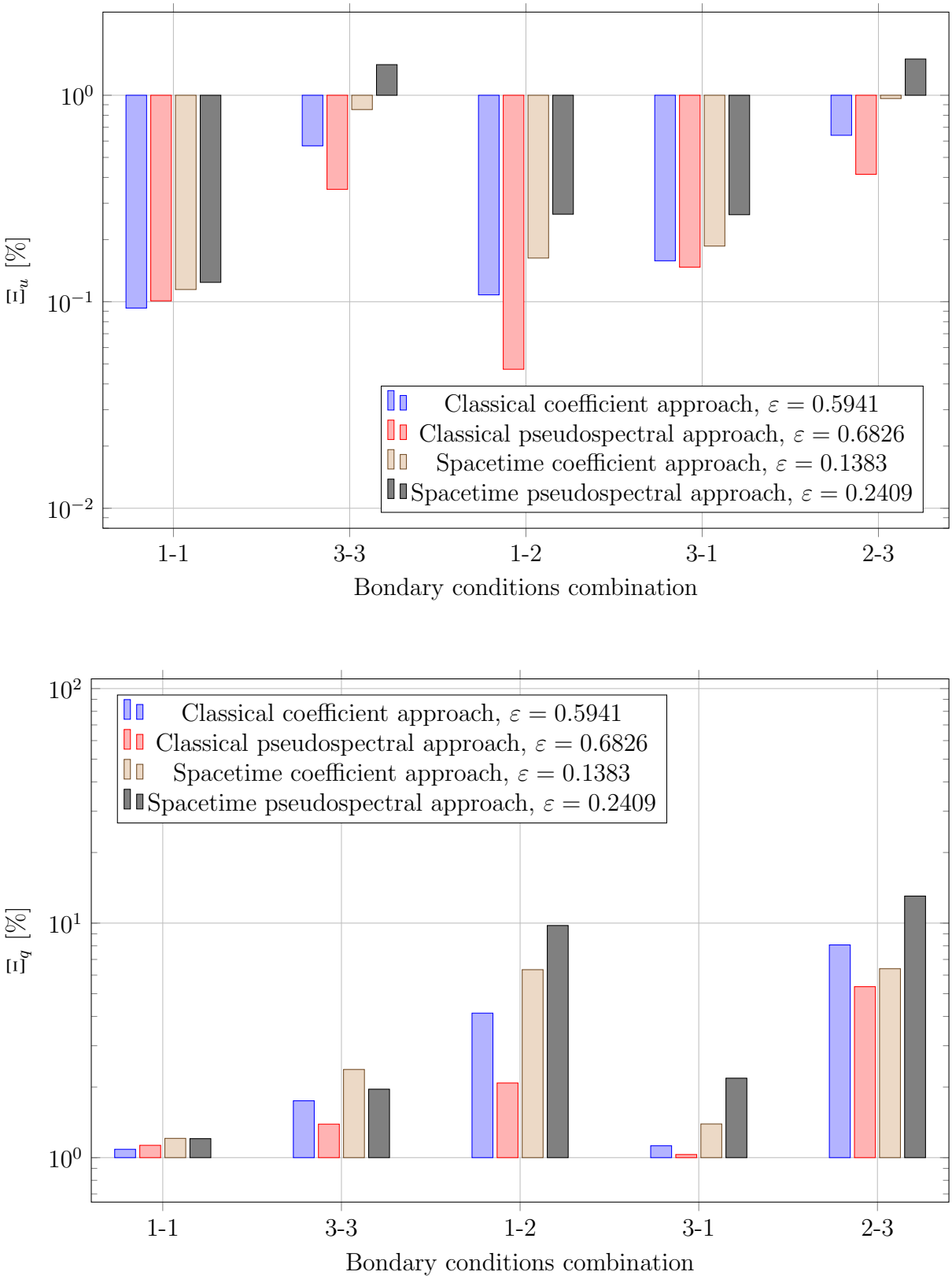

Figure 3.13: Error measures Ξ_u and Ξ_q for the one-dimensional parabolic problem obtained using various approaches and combinations of boundary conditions

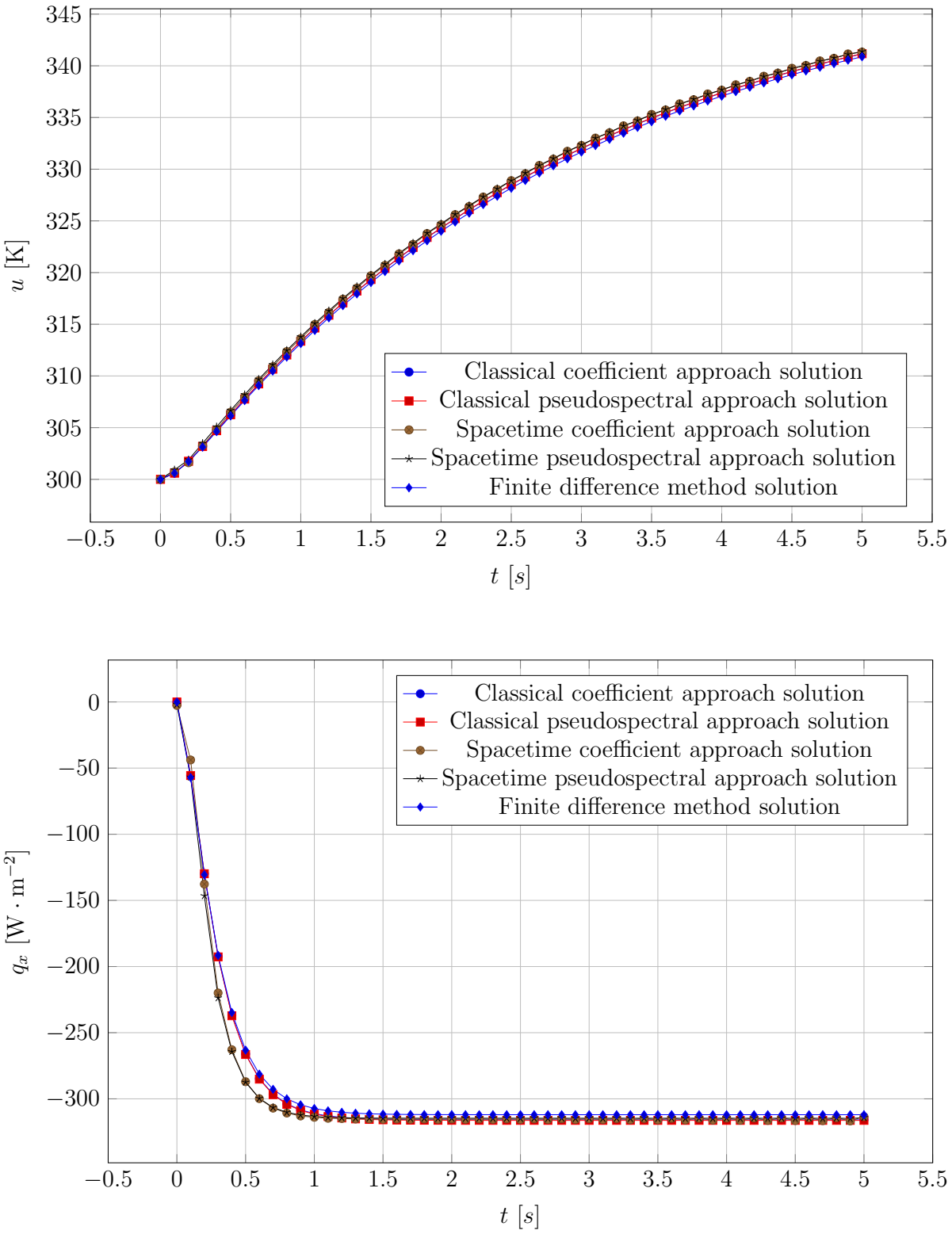

Figure 3.14: The evolution of temperature and heat flux for the one-dimensional parabolic problem at the point $x = 0$ obtained using the Dirichlet-Dirichlet boundary conditions

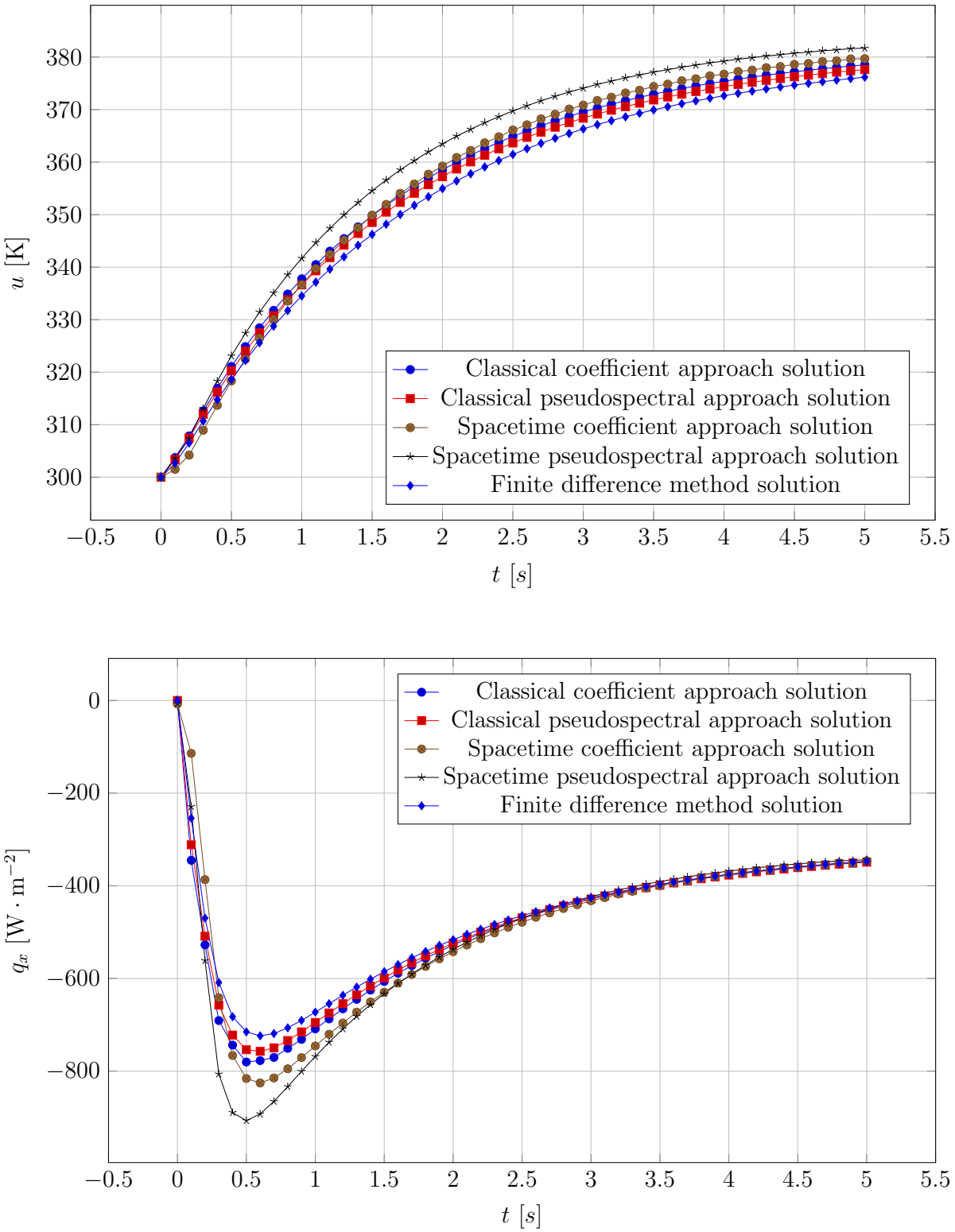

Figure 3.15: The evolution of temperature and heat flux for the one-dimensional parabolic problem at the point $x = 0$ obtained using the Robin-Robin boundary conditions

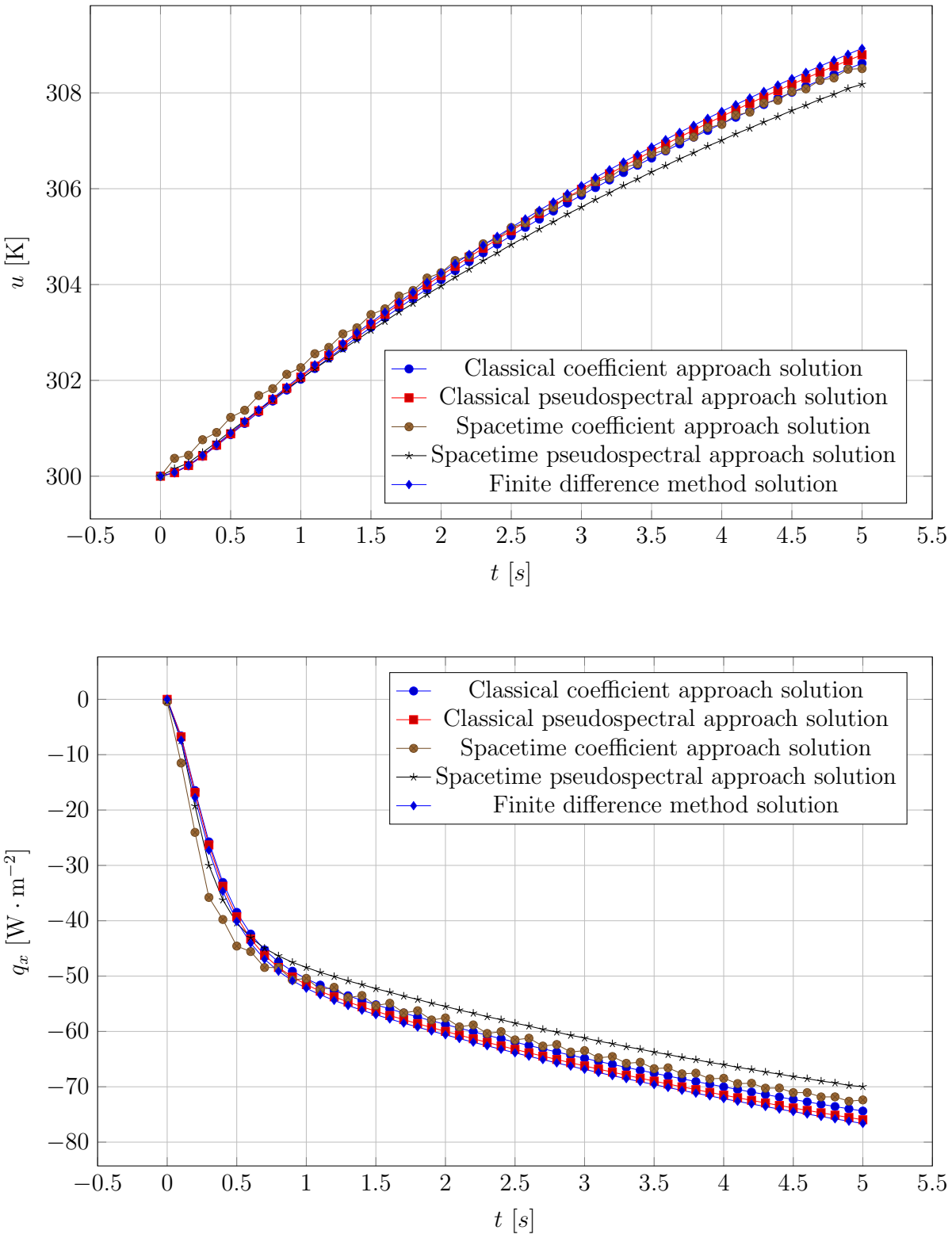

Figure 3.16: The evolution of temperature and heat flux for the one-dimensional parabolic problem at the point $x = 0$ obtained using the Dirichlet-Neumann boundary conditions

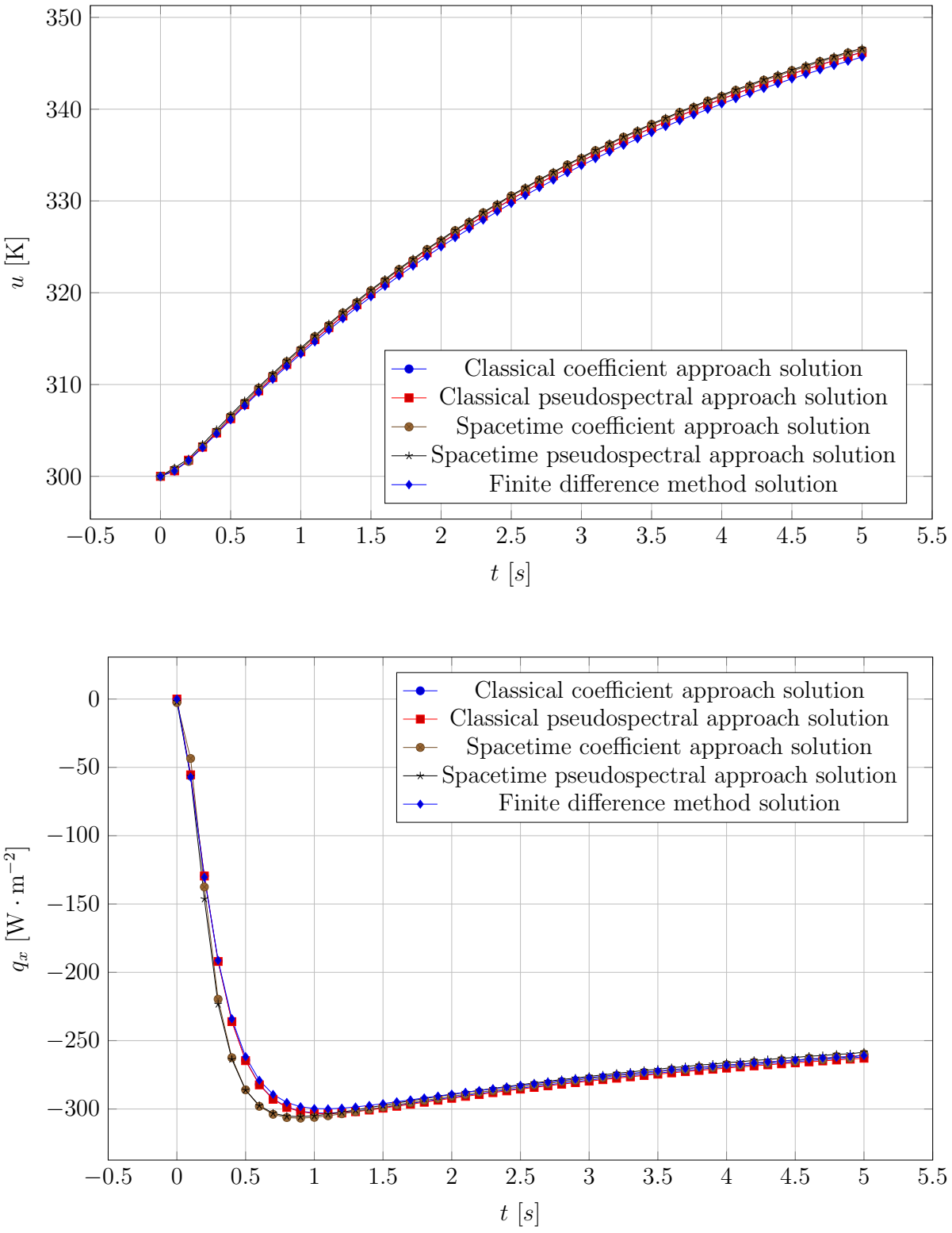

Figure 3.17: The evolution of temperature and heat flux for the one-dimensional parabolic problem at the point $x = 0$ obtained using the Robin-Dirichlet boundary conditions

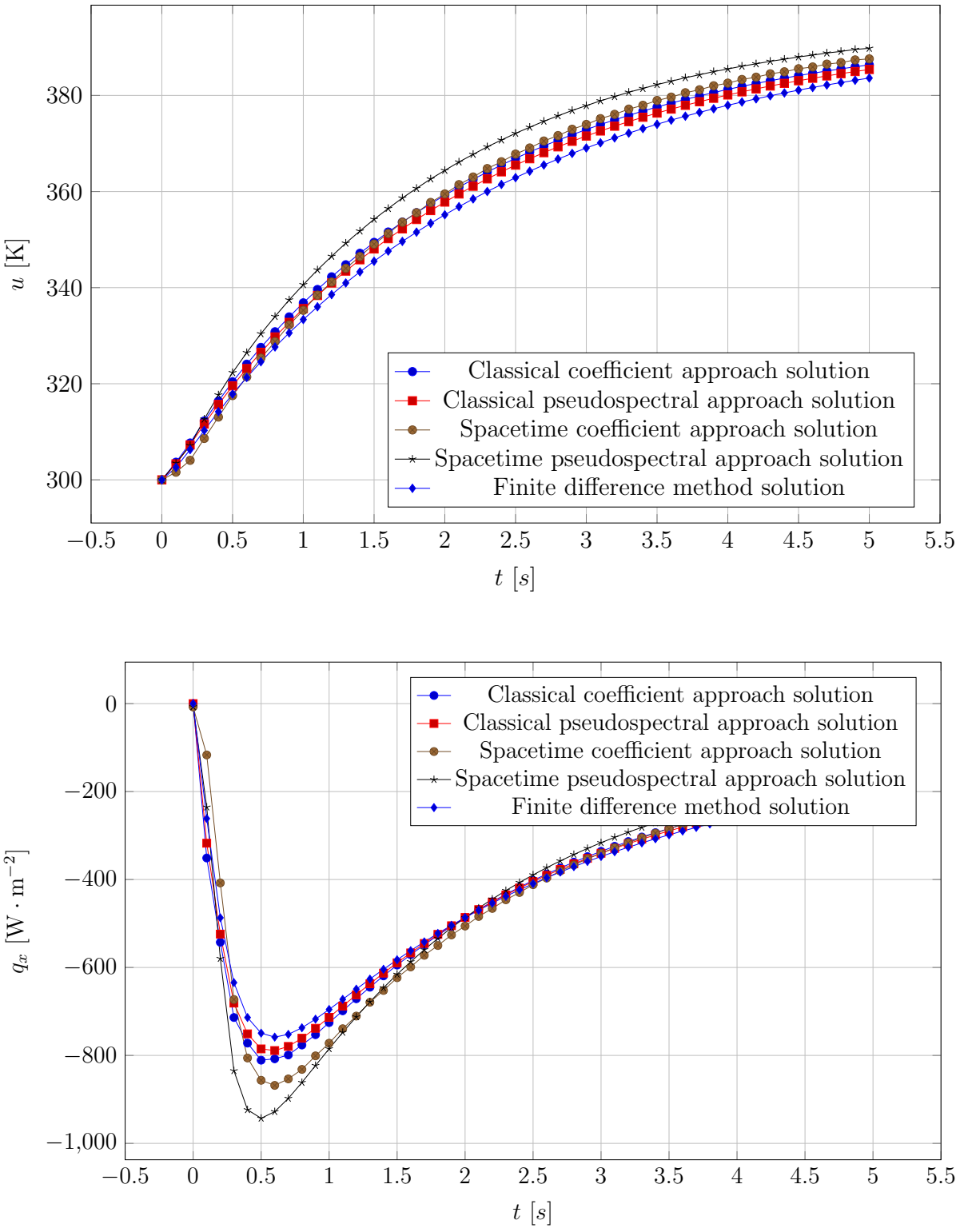

Figure 3.18: The evolution of temperature and heat flux for the one-dimensional parabolic problem at the point $x = 0$ obtained using the Neumann-Robin boundary conditions

3.3.3 Unsteady-state hyperbolic problem

Let's move on to the most general problem in this section, namely the one-dimensional hyperbolic problem which is described by Equation 3.5:

$$\gamma\left(\boldsymbol{x}\right)\rho\left(\boldsymbol{x}\right)\left(\tau\ddot{u}+\dot{u}\right)=\kappa_{,x}\left(\boldsymbol{x}\right)u_{,x}+\kappa\left(\boldsymbol{x}\right)u_{,xx}.$$

The reference solution for this problem was the finite difference method solution. The classical and spacetime approaches were examined separately.

3.3.3.1 Classical approach

In a first step, the classical approach was examined. A series of simulations for different approaches and combinations of boundary conditions were performed and the error measures values Ξ_u and Ξ_q were calculated with respect to the finite difference method solution after each simulation. When calculating the error measures, the solutions obtained using the same time inegration scheme were compared. Time step size was equal to $\Delta t = 0.5\,\mathrm{s}$ while the number of time advancements was equal to 100. The number of time advancements was chosen arbitrarily in such a way that the simulation ended long before reaching the steady state, so as not to artificially improve the value of the error measures. Figure 3.19 shows the values of error measures Ξ_u and Ξ_q calculated for the Kansa method solution with respect to the finite difference method solution for various combinations of the boundary conditions, approaches, and time integration schemes. Figures 3.20 - 3.24 show the evolution of temperature and heat flux at the point $x = 0$ obtained using Kansa method and finite difference method for Euler and Houbolt time integration scheme and for various combinations of the boundary conditions.

Low values of error measures Ξ_u and good agreement of the Kansa method solutions with the reference solutions show that the Kansa method is suitable for solving the considered class of problems and the solver is correctly implemented. The accuracy of the coefficient and pseudo-spectral approaches is almost identical. The value of error measures Ξ_q are much higher than Ξ_u which is similar to the steady-state case and consequently the same conclusions can be drawn. Figures 3.20 - 3.24 show that the differences between the solutions for different time integration schemes are evident, in the case of temperature they are insignificant, while in the case of heat flux they are very significant in some cases. Differences in the evolution of heat fluxes are especially visible in the cases where the Dirichlet boundary condition was used and are manifested in a strong but declining oscillation of the heat flux. Evolutions show a characteristic feature of hyperbolic models of heat flow, i.e. the delay of temperature and heat flux. It is worth noting an interesting fact that the solutions obtained with the Houbolt scheme show lower damping than those obtained with the Euler scheme. This is manifested by the fact that in the case of the Houbolt scheme the amplitude of the temperature and heat flux oscillations are significantly greater and the rate of convergence to the steady state is lower than in the case of the Euler scheme. It is interesting because the cases described so far in the literature showed the opposite conclusions, namely increased algorithmic damping instead of the decreased one [71, 33, 34]. Explaining this difference is not an easy task, however, it is worth paying attention to one issue that may be an explanation. In the mentioned research, the Houbolt time integration scheme was used in conjunction with finite element method for which the main matrix is sparse, banded and symmetric. The main matrix in the Kansa method does not have these features. It is hypothesized that when the main matrix does not have these features, the numerical dissipation is reduced due to spurious eigenmodes.

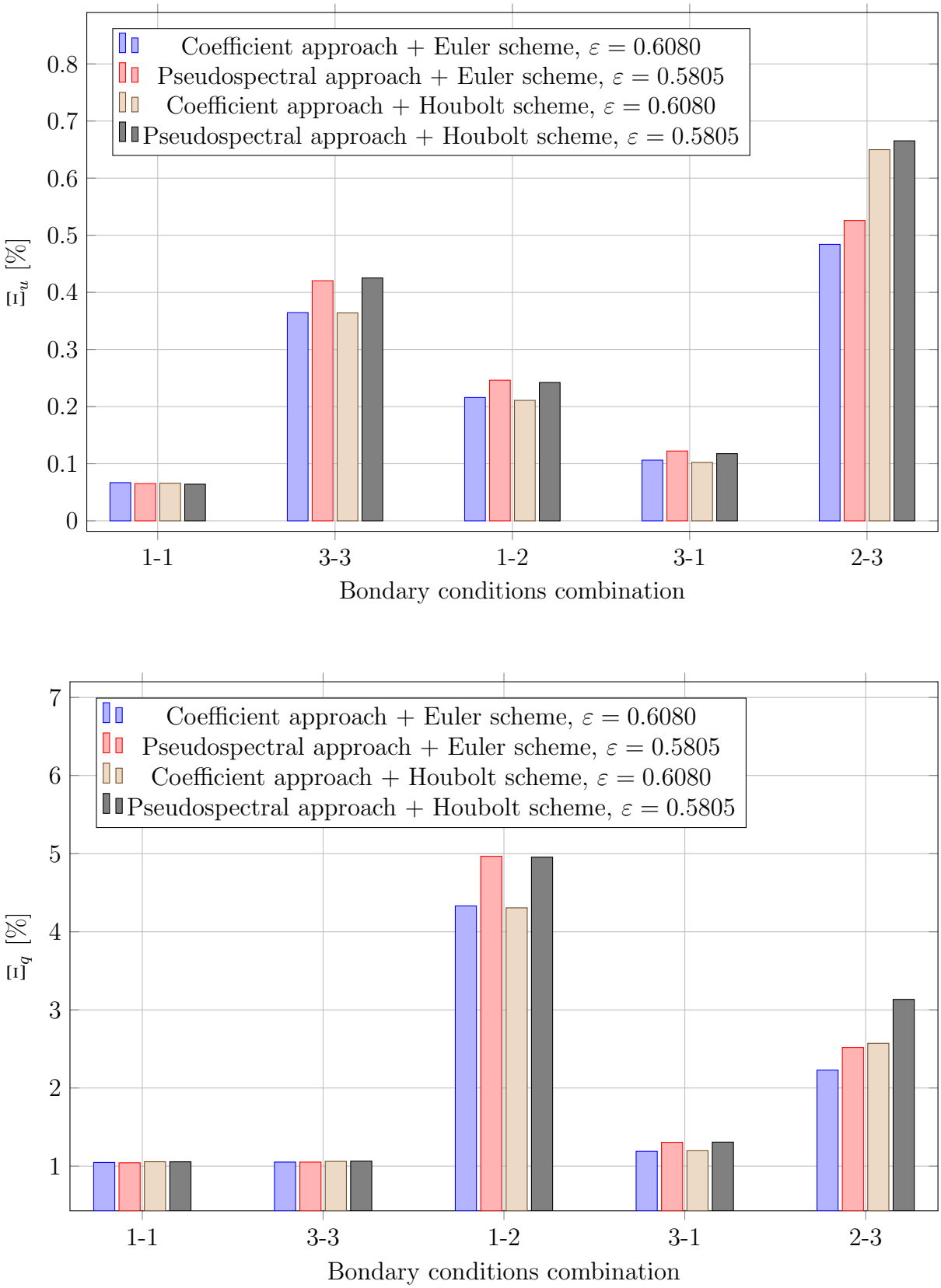

Figure 3.19: Error measures Ξ_u and Ξ_q for the one-dimensional hyperbolic problem obtained using various approaches and combinations of boundary conditions and time integration schemes

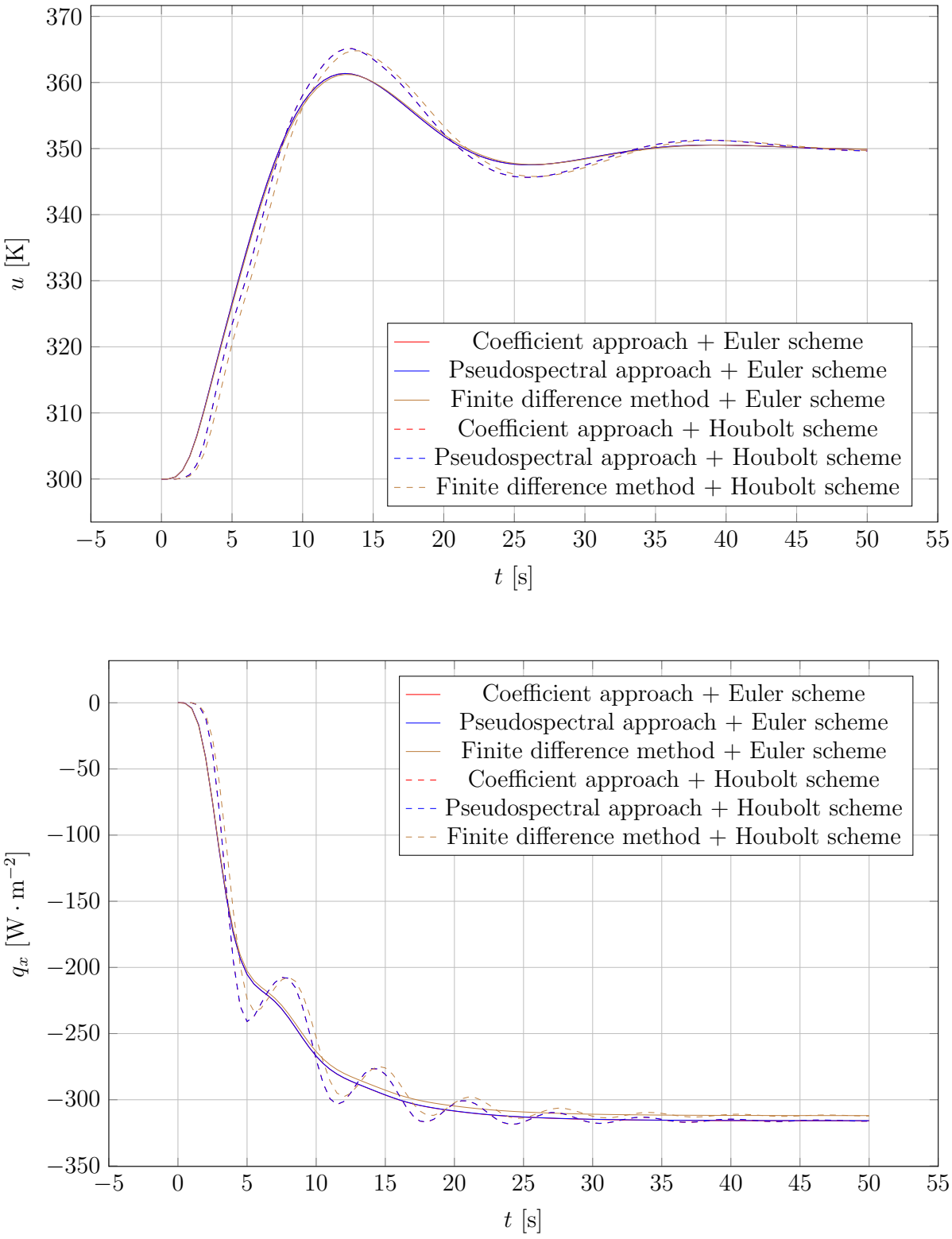

Figure 3.20: The evolution of temperature and heat flux for the one-dimensional hyperbolic problem at the point $x = 0$ obtained using the Dirichlet-Dirichlet boundary conditions

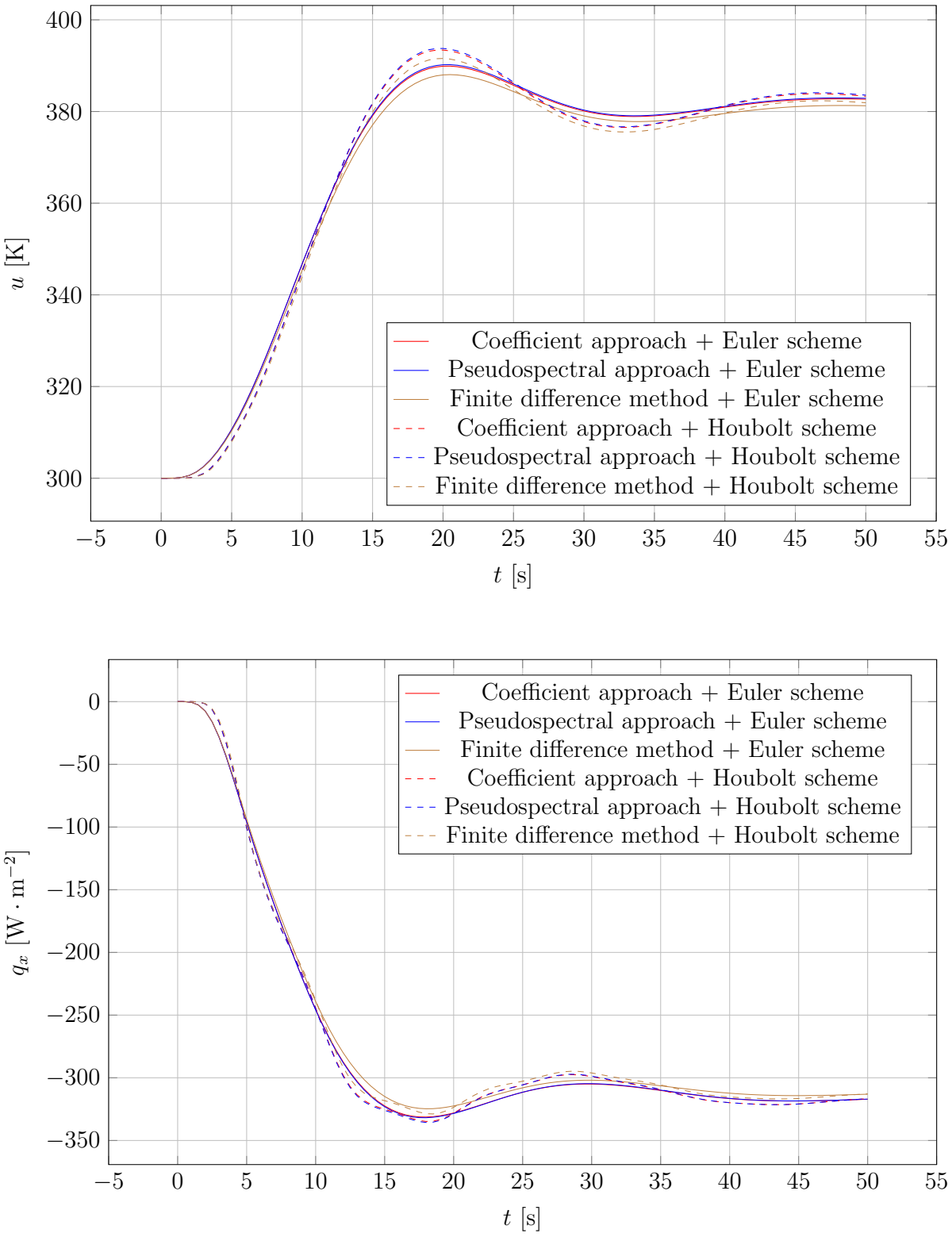

Figure 3.21: The evolution of temperature and heat flux for the one-dimensional hyperbolic problem at the point $x = 0$ obtained using the Robin-Robin boundary conditions

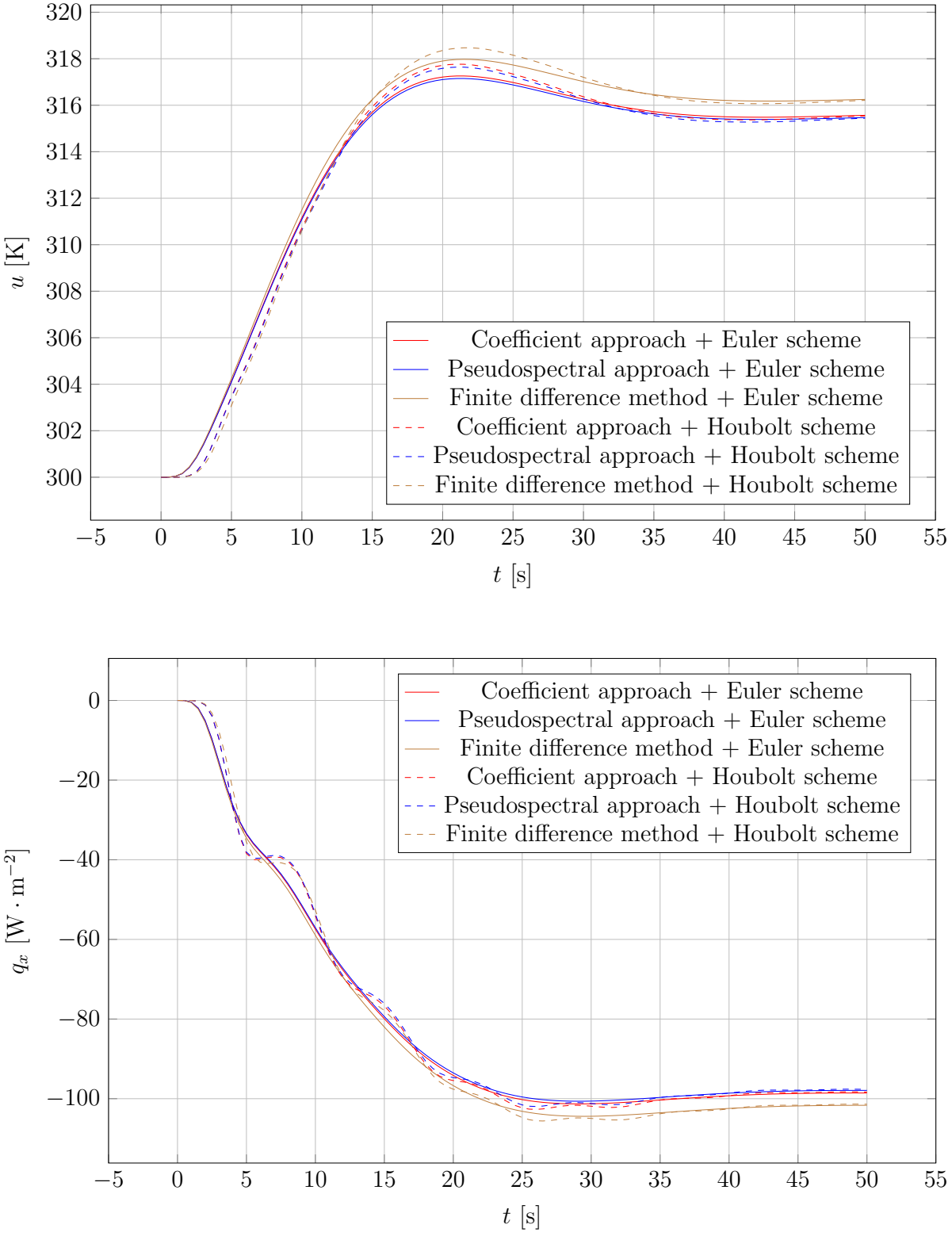

Figure 3.22: The evolution of temperature and heat flux for the one-dimensional hyperbolic problem at the point $x = 0$ obtained using the Dirichlet-Neumann boundary conditions

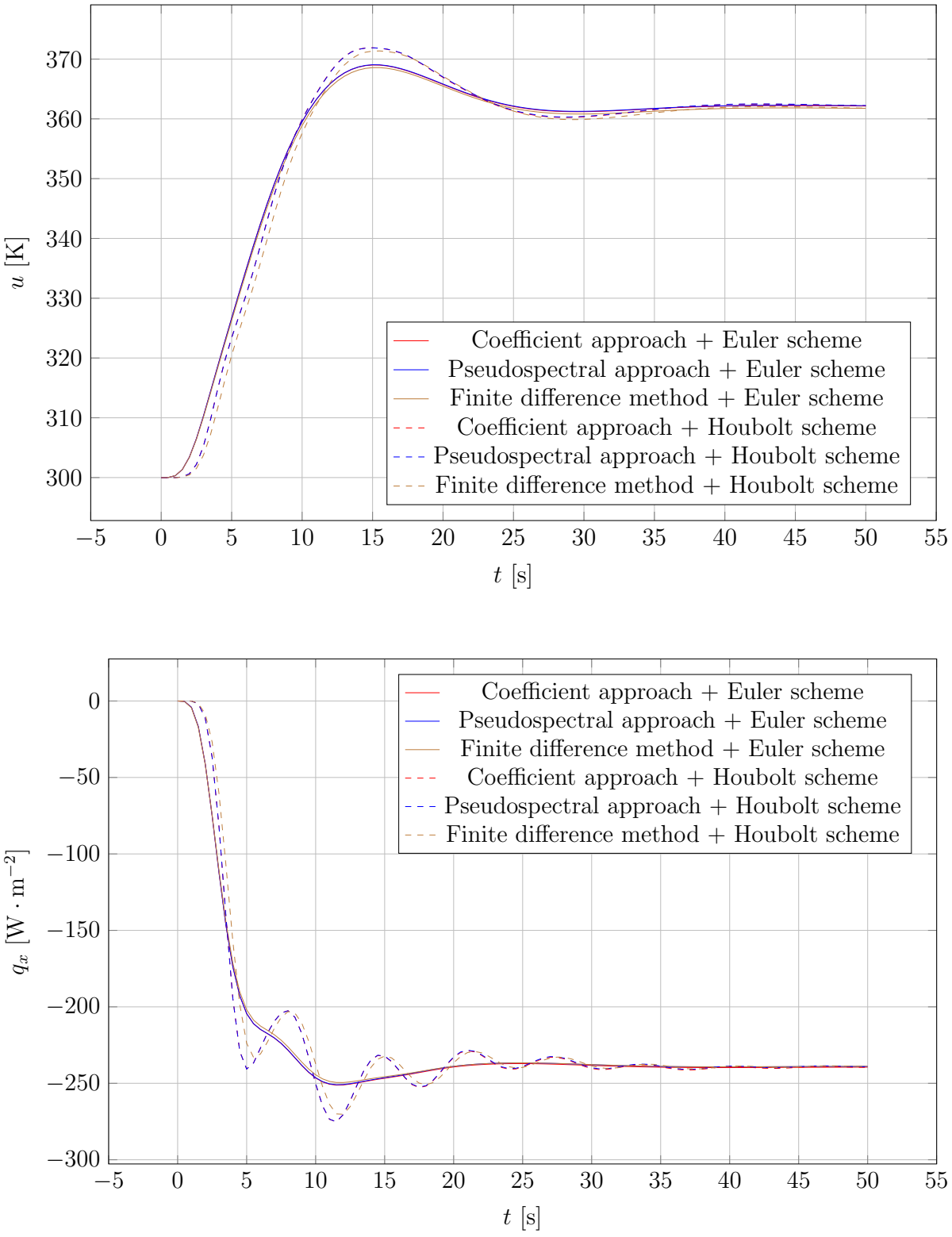

Figure 3.23: The evolution of temperature and heat flux for the one-dimensional hyperbolic problem at the point $x = 0$ obtained using the Robin-Dirichlet boundary conditions

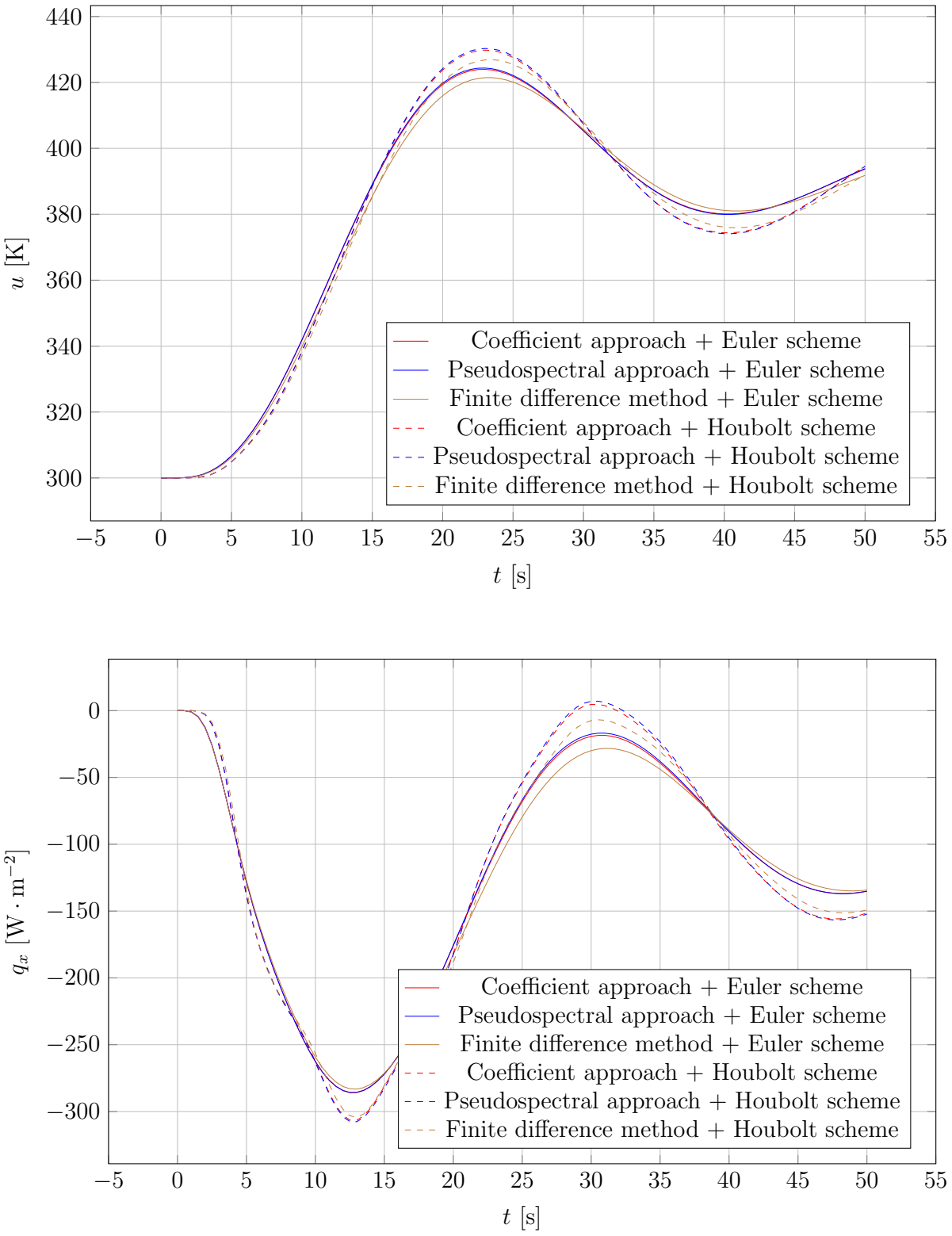

Figure 3.24: The evolution of temperature and heat flux for the one-dimensional hyperbolic problem at the point $x = 0$ obtained using the Neumann-Robin boundary conditions

However, this requires further analyses and is certainly an interesting direction for further research.

3.3.3.2 Spacetime approach

In the second step, the spacetime approach was examined. In the course of simulations performed as part of the research, many simulations of hyperbolic problems were performed using the spacetime approach. However, the results of these studies turned out to be unsatisfactory and the solutions were highly inaccurate. Therefore, in this subsection only an example of such inaccurate solution will be presented. It has been decided to present the example with the most numerically favorable boundary conditions, i.e. Dirichlet boundary conditions on both boundaries. It was decided not to use any algorithm for finding a value of the shape parameter value, but to use the brute force method due to the fact that the analytical solution of the considered problem is known. As part of it, a series of simulations was performed for the shape parameter values in the range from 10^{-4} to 1. For each simulation, the value of the error measure Ξ_u was calculated. Figure 3.25 shows the values of the error measure Ξ_u versus the value of shape parameter ε obtained using coefficient and pseudospectral approaches for the Dirichlet-Dirichlet boundary conditions.

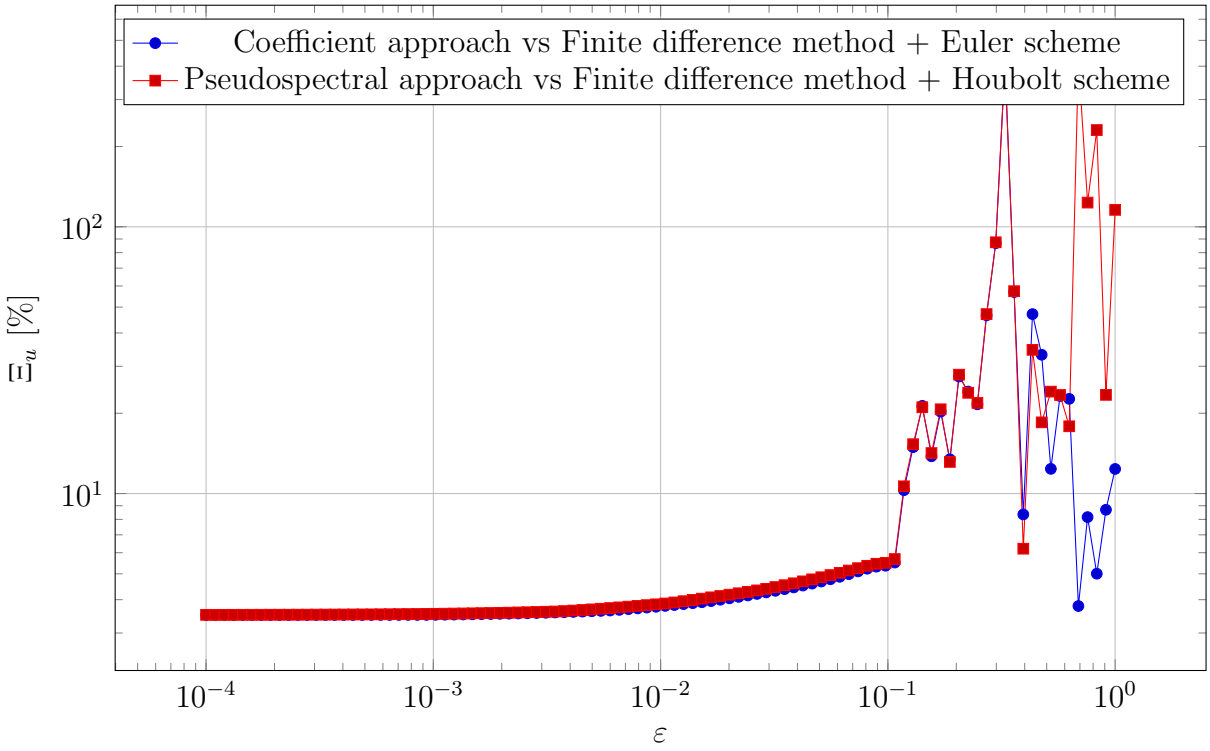

Figure 3.25: Error measure Ξ_u versus the value of shape parameter ε for the one-dimensional hyperbolic problem obtained using the spacetime approach in conjunction with the Dirichlet-Dirichlet boundary conditions

Figure 3.25 shows that in the studied range the smallest value of the error measure Ξ_u occurs for the shape parameter value equal to 10^{-4}. For values lower than 10^{-4} the function is flat and the solutions for these values of the shape parameter do not differ from that for 10^{-4}. Therefore, the solution for this value was closely examined. Figure 3.26 shows the evolution of temperature at the point $x = 0$ obtained using spacetime Kansa method in conjunction with coefficient and pseudospectral approaches as well as the finite

difference method with Euler and Houbolt time integration schemes for Dirichlet-Dirichlet boundary conditions.

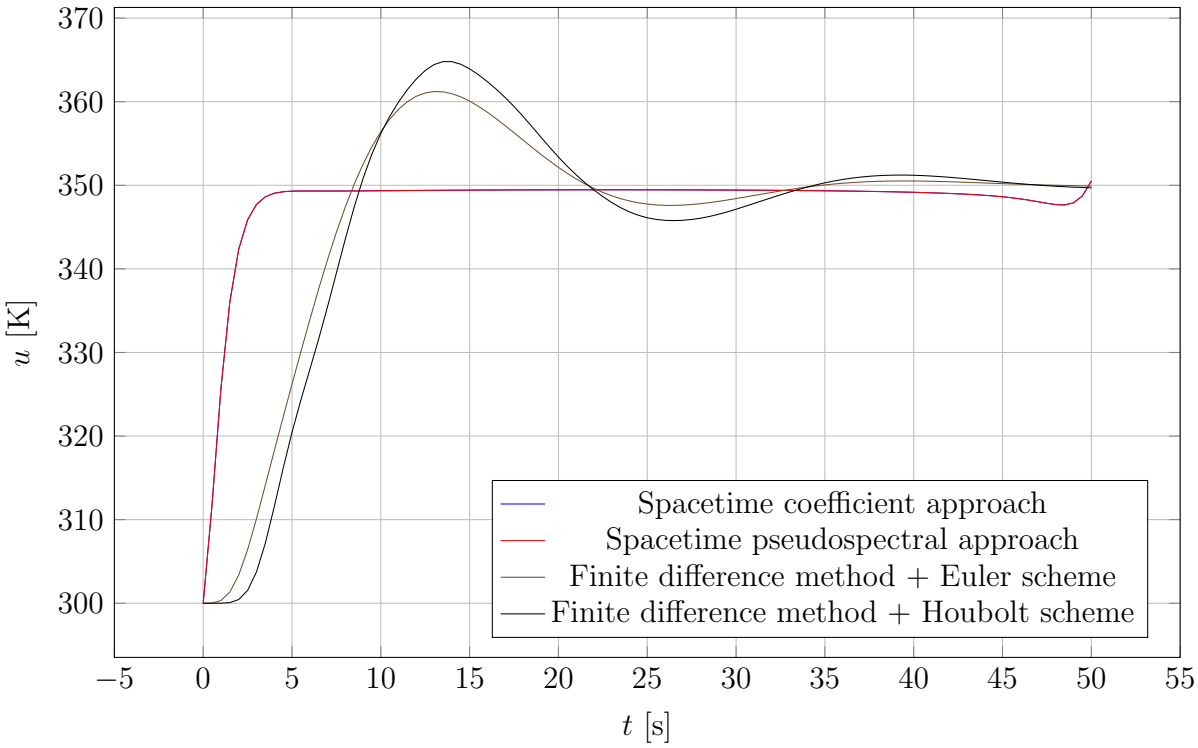

Figure 3.26: The evolution of temperature and heat flux for the one-dimensional hyperbolic problem at the point $x = 0$ obtained using the spacetime approach in conjunction with the Dirichlet-Dirichlet boundary conditions

The results presented in Figure 3.26 show that the solution obtained using the Kansa method is significantly different from the solution obtained using the finite difference method. It means that the spacetime Kansa method with this numeric setup is not suitable for solving the considered initial-boundary value problem. However, it is worth pointing out the noteworthy elements in the numerical setup, the modifications of which could make the method effective, namely the spacetime scaling parameter β, which has a huge impact on the quality of the interpolation in the spacetime Kansa method. Finding a formula to calculate its optimal or quasi-optimal value would probably overcome the encountered difficulties. It is worth pointing to this area as important for further research.

3.4 Two-dimensional problems

If the problem is two-dimensional, the Cattaneo-Vernotte Equation 2.9 simplifies to the two-dimensional Cattaneo-Vernotte equation in the form of:

$$\gamma(\boldsymbol{x})\,\rho(\boldsymbol{x})\,(\tau\ddot{u}+\dot{u}) = \kappa_{,x}(\boldsymbol{x})\,u_{,x} + \kappa_{,y}(\boldsymbol{x})\,u_{,y} + \kappa(\boldsymbol{x})\,(u_{,xx}+u_{,yy})\,. \tag{3.18}$$

In the case of the two-dimensional problems, two computational domains were used, one for the problems governed by the elliptic and parabolic heat equations and one for the problems governed by the hyperbolic Cattaneo-Vernotte equation. The computational

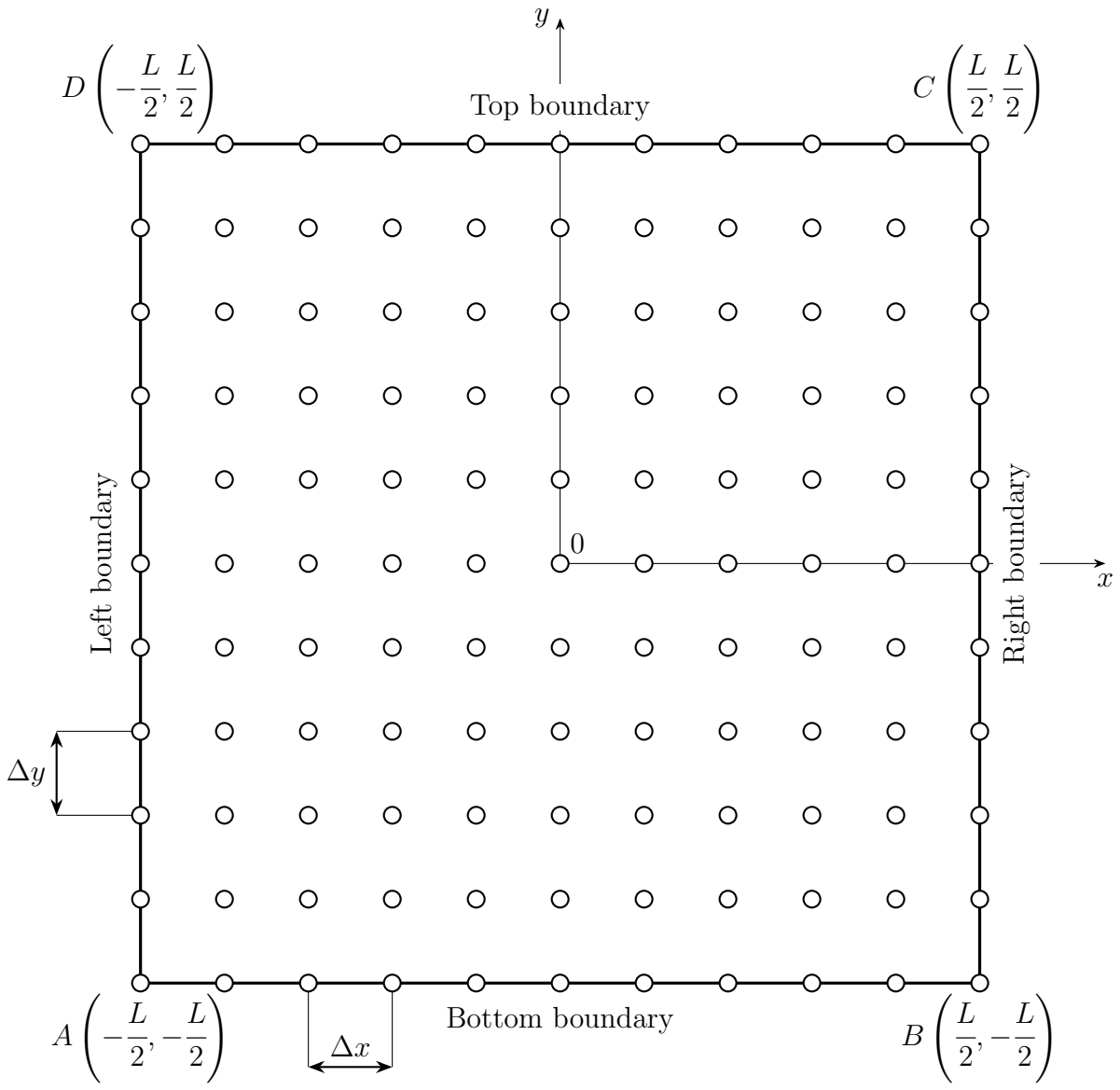

Figure 3.27: The two-dimensional computational domain used for the problems governed by elliptic and parabolic heat equations

domain used in the problems governed by the elliptic and parabolic heat equations is a rectangular domain which a simplified sketch is shown in Figure 3.27.

The number of points in the horizontal direction is n_x, while the number in the vertical direction is n_y, the consequence is:

$$\Delta x\,(n_x - 1) = \Delta y\,(n_y - 1) = L. \tag{3.19}$$

Two sets of distributions of thermophysical parameters were used for this domain. The first set was the same as that for the one-dimensional case and is described by Equations 3.6, 3.7, and 3.8. In simulations where these parameters were used, the adiabatic boundary conditions $q_b = 0$ were imposed on the bottom and top boundary. Such a formulation of the problem results in the fact that there is an analytical solution for it, which is the same as for a one-dimensional problem and is described by Equation 3.12. For this reason, problems with this setup are called 1.5-dimensional problems in the thesis. The boundary conditions imposed on the left and right boundaries and the associated parameter values

were the same as for the one-dimensional case. This set was used for some of the elliptic steady-state problems. The second set of distributions is given by the following harmonic functions:

$$\kappa\left(x,y\right)=\frac{\kappa_{\max}+\kappa_{\min}}{2}+\frac{\kappa_{\max}-\kappa_{\min}}{4}\left(\cos\left(\omega\pi\frac{x}{L}\right)+\cos\left(\omega\pi\frac{y}{L}\right)\right), \tag{3.20}$$

$$\rho\left(x,y\right)=\frac{\rho_{\max}+\rho_{\min}}{2}+\frac{\rho_{\max}-\rho_{\min}}{4}\left(\cos\left(\omega\pi\frac{x}{L}\right)+\cos\left(\omega\pi\frac{y}{L}\right)\right), \tag{3.21}$$

$$\gamma\left(x,y\right)=\frac{\gamma_{\max}+\gamma_{\min}}{2}+\frac{\gamma_{\max}-\gamma_{\min}}{4}\left(\cos\left(\omega\pi\frac{x}{L}\right)+\cos\left(\omega\pi\frac{y}{L}\right)\right), \tag{3.22}$$

where:

- $\kappa_{\min}=1\,\mathrm{W}\cdot\mathrm{m}^{-1}\cdot\mathrm{K}^{-1}$,
- $\kappa_{\max}=10\,\mathrm{W}\cdot\mathrm{m}^{-1}\cdot\mathrm{K}^{-1}$,
- $\rho_{\min}=1\,\mathrm{kg}\cdot\mathrm{m}^{-3}$,
- $\rho_{\max}=10\,\mathrm{kg}\cdot\mathrm{m}^{-3}$,
- $\gamma_{\min}=1\,\mathrm{J}\cdot\mathrm{kg}^{-1}\cdot\mathrm{K}^{-1}$,
- $\gamma_{\max}=10\,\mathrm{J}\cdot\mathrm{kg}^{-1}\cdot\mathrm{K}^{-1}$,
- $\omega=2$.

This set was used for some of the elliptic steady-state problems and for the parabolic unsteady-state problems. The computational domain used in the hyperbolic problems is different from the one shown. For consistency, it will be presented later in the paper where the hyperbolic problems will be analyzed.

3.4.1 Steady-state elliptic problem

If the problem is steady, the two-dimensional Cattaneo-Vernotte Equation 3.18 simplifies to the two-dimensional steady-state elliptic heat equation:

$$\kappa_{,x}\left(\boldsymbol{x}\right)u_{,x}+\kappa_{,y}\left(\boldsymbol{x}\right)u_{,y}+\kappa\left(\boldsymbol{x}\right)\left(u_{,xx}+u_{,yy}\right)=0. \tag{3.23}$$

Two problems governed by the above equation were considered.

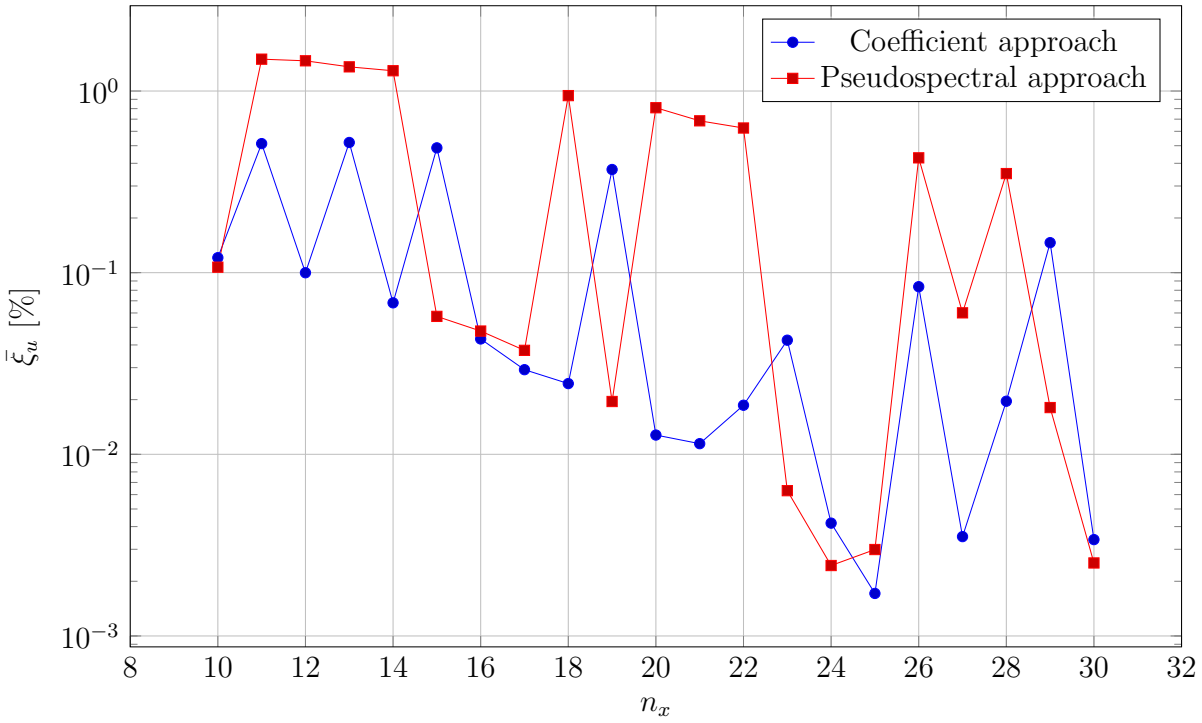

Figure 3.28: Error measure $\bar{\xi}_u$ versus the number of collocation points obtained during two-dimensional convergence study for the Dirichlet-Dirichlet boundary conditions

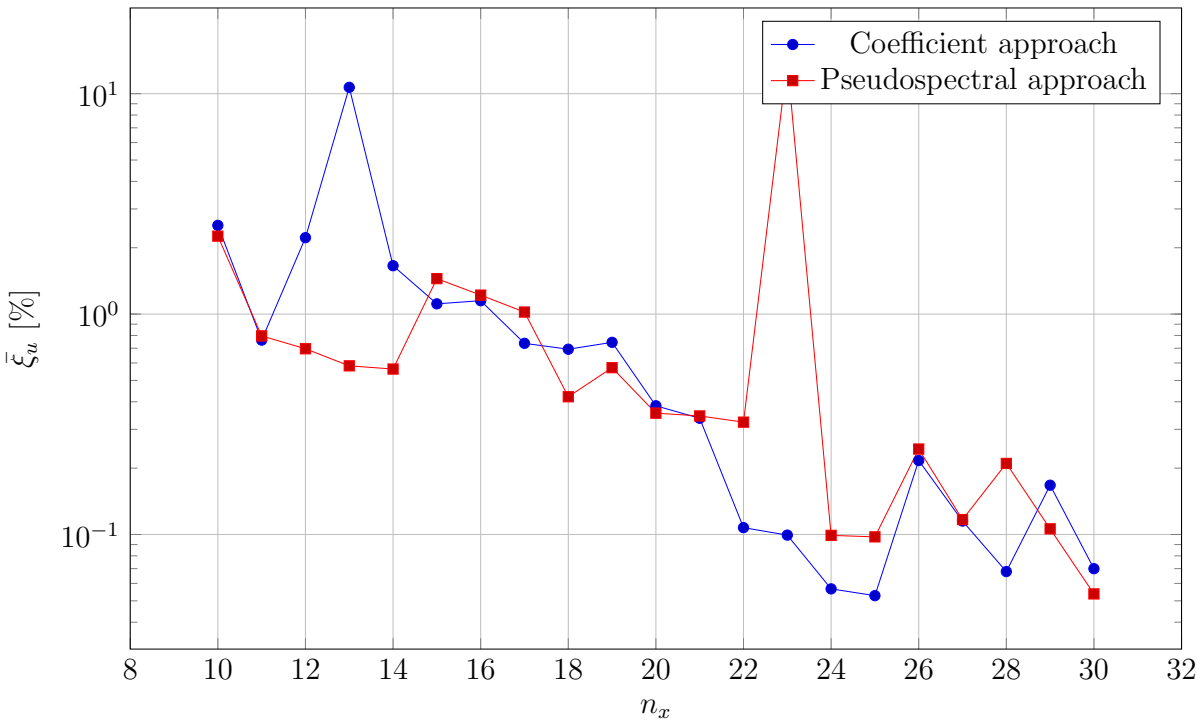

Figure 3.29: Error measure $\bar{\xi}_u$ versus the number of collocation points obtained during two-dimensional convergence study for the Robin-Robin boundary conditions

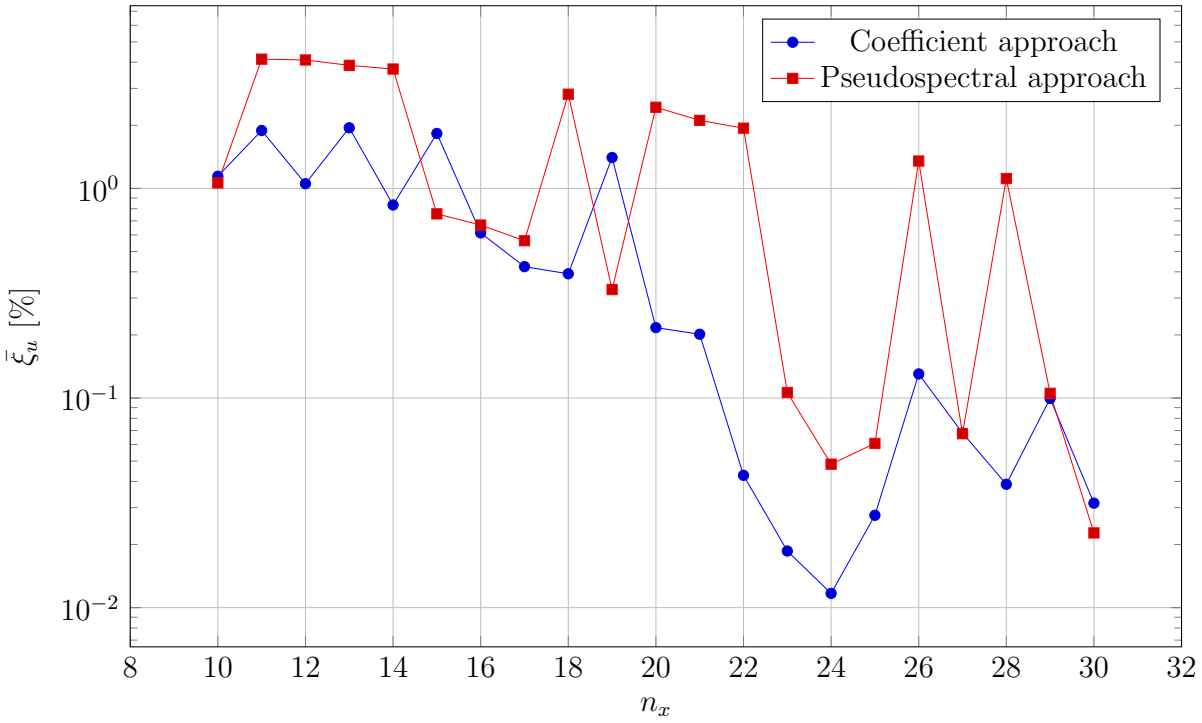

Figure 3.30: Error measure $\bar{\xi}_u$ versus the number of collocation points obtained during two-dimensional convergence study for the Dirichlet-Neumann boundary conditions

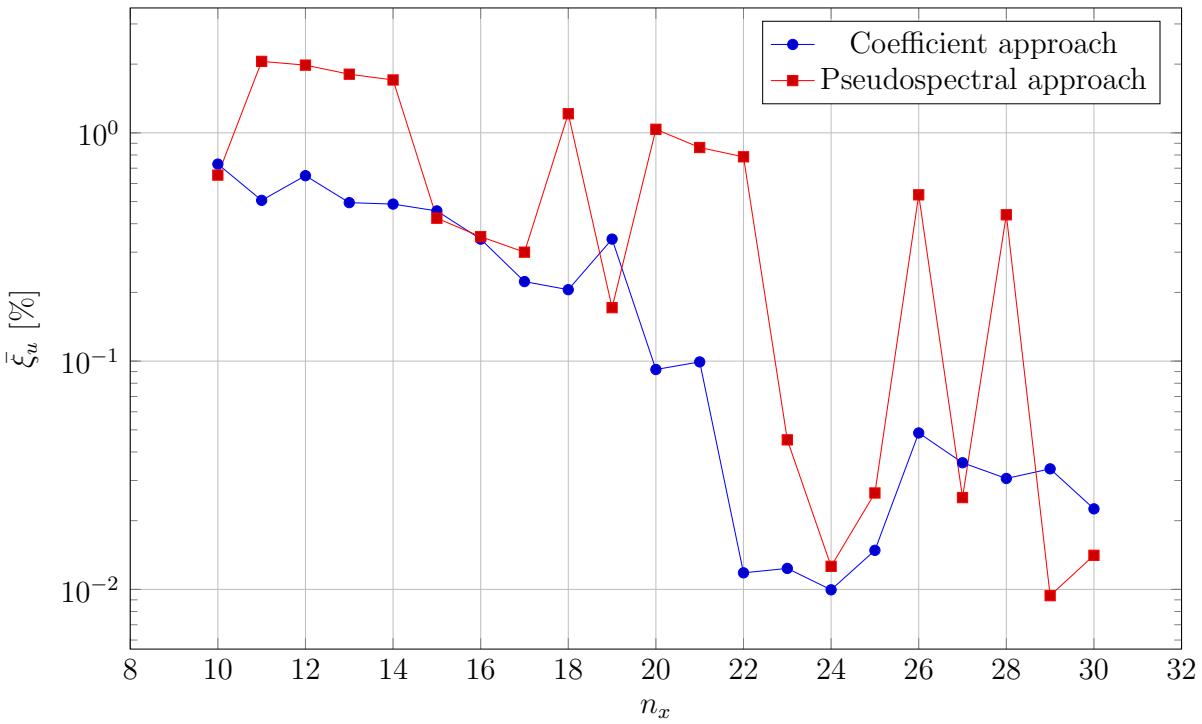

Figure 3.31: Error measure $\bar{\xi}_u$ versus the number of collocation points obtained during two-dimensional convergence study for the Robin-Dirichlet boundary conditions

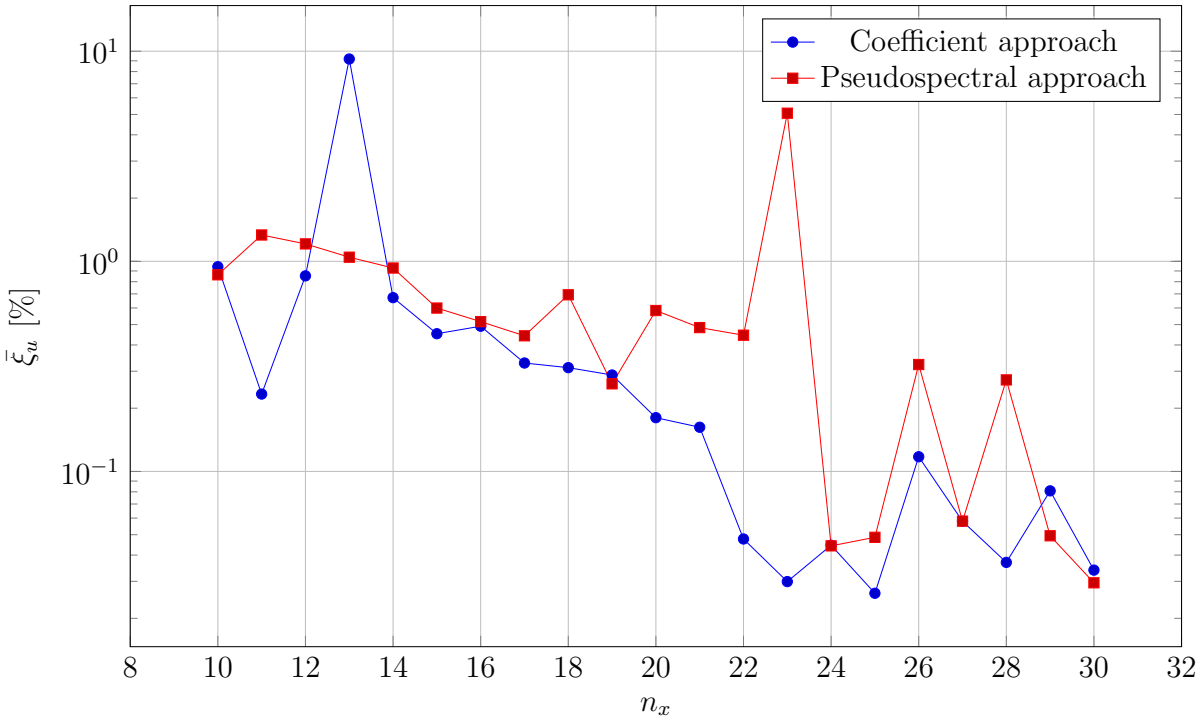

Figure 3.32: Error measure $\bar{\xi}_u$ versus the number of collocation points obtained during two-dimensional convergence study for the Neumann-Robin boundary conditions

3.4.1.1 Convergence study

After defining the numerical setups, it is possible to proceed to the convergence study in which the 1.5-dimensional setup was used. As part of it, a series of simulations was performed for $n = n_x \times n_y$ collocation points where n_x was in the range from 10 to 30. For each simulation, the good value of the shape parameter was individually selected. After each simulation, the value of the error measure $\bar{\xi}_u$ was calculated with respect to the analytical solution. The simulations were carried out for the coefficient and pseudospectral approach for various combinations of boundary conditions. Figures 3.28 - 3.32 show the values of error measure $\bar{\xi}_u$ versus the number of collocation points $n_x = n_y$ calculated with respect to the analytical solution for various approaches and combinations of the boundary conditions.

The results presented in the Figures 3.28 - 3.32 leads to conclusions similar to those for the one-dimensional cases. The advantages of the high-order multiquadric scheme are once again being proven. Even for $n_x = n_y = 10$ satisfactory values of $\bar{\xi}_u$ lower than 1% are achieved. It was decided that the number of collocation points $n_x = n_y = 25$ would be used for the next simulations because of the fact that for such a value the values of $\bar{\xi}_u$ are even lower than 10^{-2} %. When it comes to comparing the accuracy between the coefficient and pseudospectral approaches, the results are very similar. As in the one-dimensional case, it can be seen that the resulting distributions are oscillatory and have peaks.The reasons for their occurrence are the same as in the one-dimensional case. The nature of the solution results from the fact that for each simulation the shape parameter value was individually selected with the use of the condition algorithm.

3.4.1.2 Two-dimensional elliptic problem no. 1

After performing the convergence study, it is possible to more closely examine the accuracy of the method for the 1.5-dimensional problem using the cloud selected in the convergence study. A series of simulations for different approaches and combinations of boundary conditions were performed and the error measures values $\bar{\xi}_u$ and $\bar{\xi}_q$ were calculated with respect to the analytical solution after each simulation. Figure 3.33 shows the values of the error measures $\bar{\xi}_u$ and $\bar{\xi}_q$ calculated for the Kansa method solution with respect to the analytical solution for various approaches and combinations of the boundary conditions. In order to perform a substantive qualitative comparison of the solutions, the intersections of the temperature surfaces with the plane $y = 0$ was used. Figures 3.34 - 3.38 show the comparison between the Kansa method solutions and the analytical solution for points $y = 0$ and various combinations of the boundary conditions.

Low values of error measures $\bar{\xi}_u$ and good agreement of the Kansa method solutions with the reference solutions show that the Kansa method is suitable for solving the considered class of problems and the solver is correctly implemented. The value of error measures $\bar{\xi}_q$ are much higher than $\bar{\xi}_u$ which is similar to the one-dimensional steady-state case and consequently the same conclusions can be drawn. The temperature fields almost do not differ from those for the one-dimensional case, however, the heat flux fields show some visible, but insignificant differences. Finally, it is worth answering the question that probably arises. Why are the two-dimensional temperature fields not shown? The answer is simple, the temperature surfaces are so similar to each other that it is impossible to distinguish them with the naked eye. Therefore, it was decided to show only a two-dimensional temperature field for the case where the Dirichlet boundary conditions were imposed on both boundaries. It is shown in Figure 3.39.

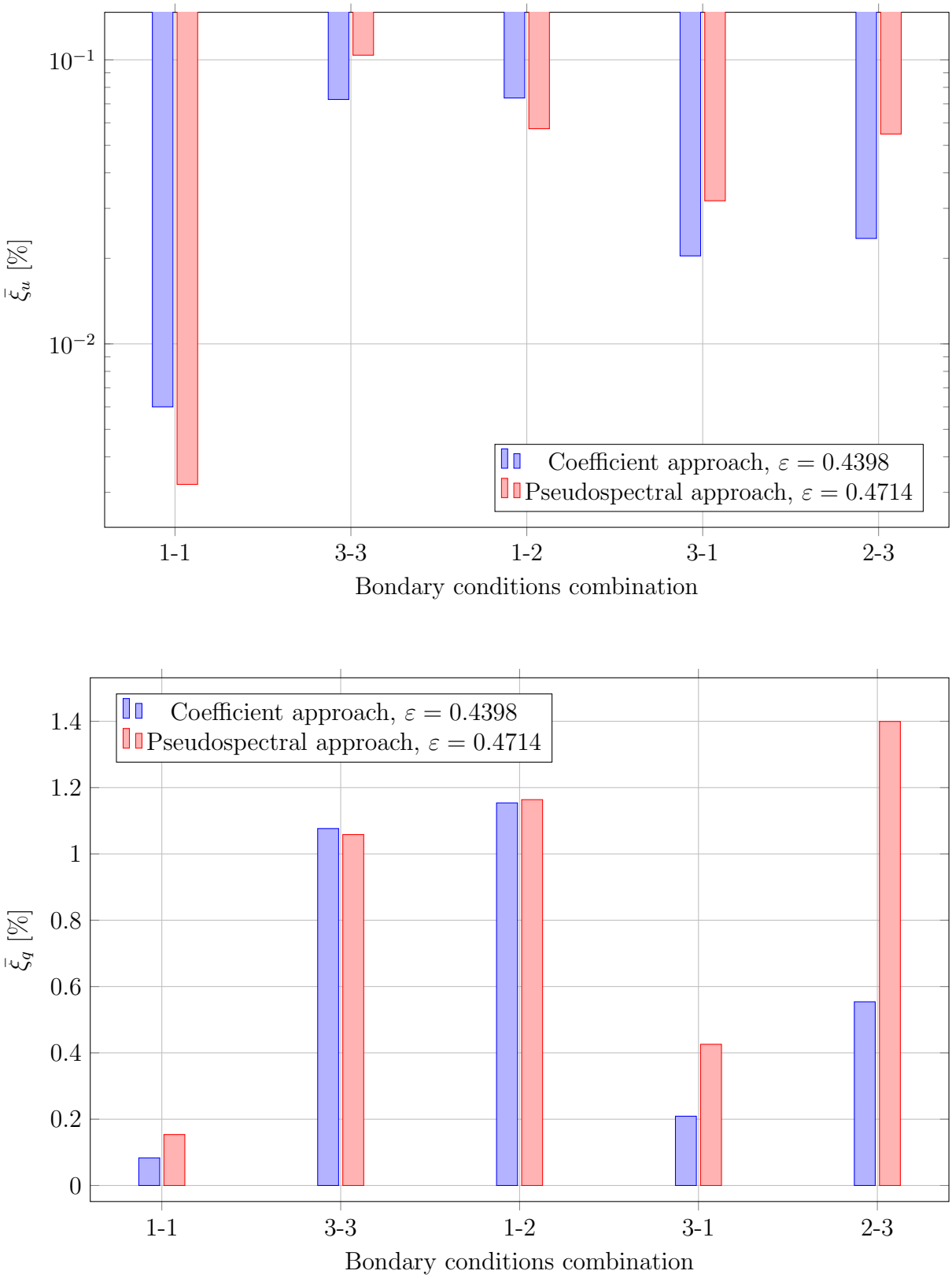

Figure 3.33: Error measures $\bar{\xi}_u$ and $\bar{\xi}_q$ for the two-dimensional elliptic problem no. 1 obtained using various approaches and combinations of boundary conditions

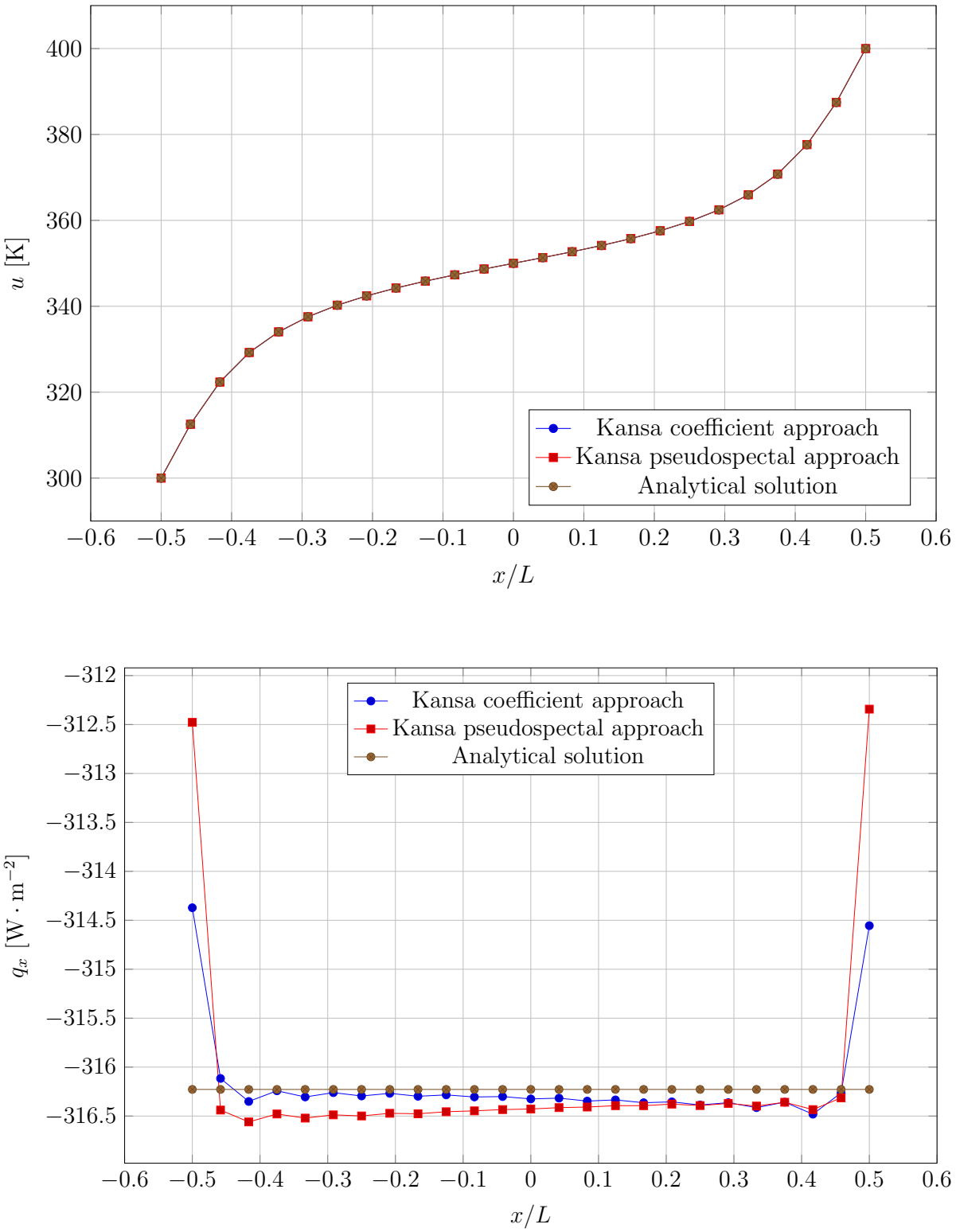

Figure 3.34: Comparison between the Kansa method solutions and the analytical solution for the two-dimensional elliptic problem no. 1 for points $y = 0$ obtained using the Dirichlet-Dirichlet boundary conditions

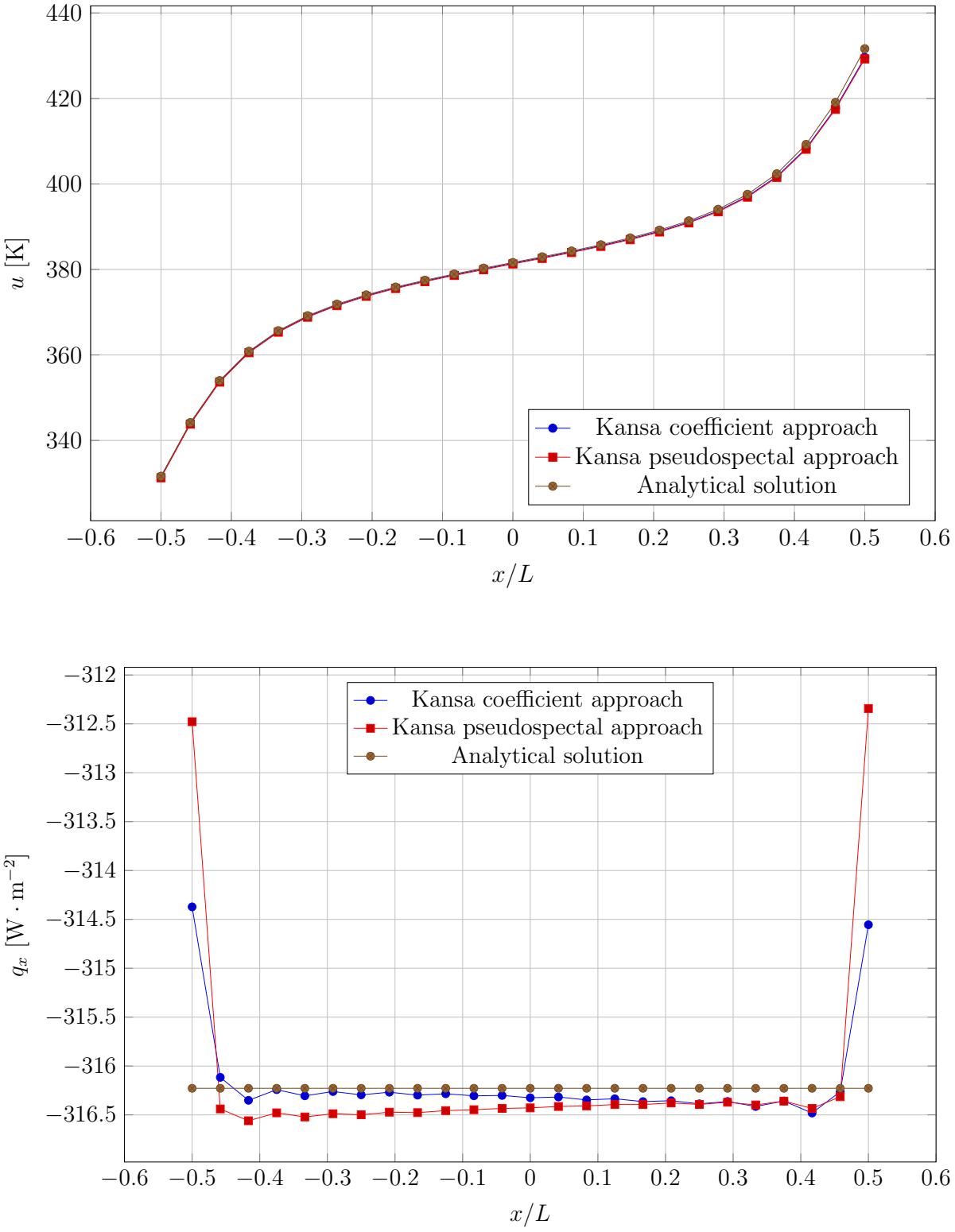

Figure 3.35: Comparison between the Kansa method solutions and the analytical solution for the two-dimensional elliptic problem no. 1 for points $y = 0$ obtained using the Robin-Robin boundary conditions

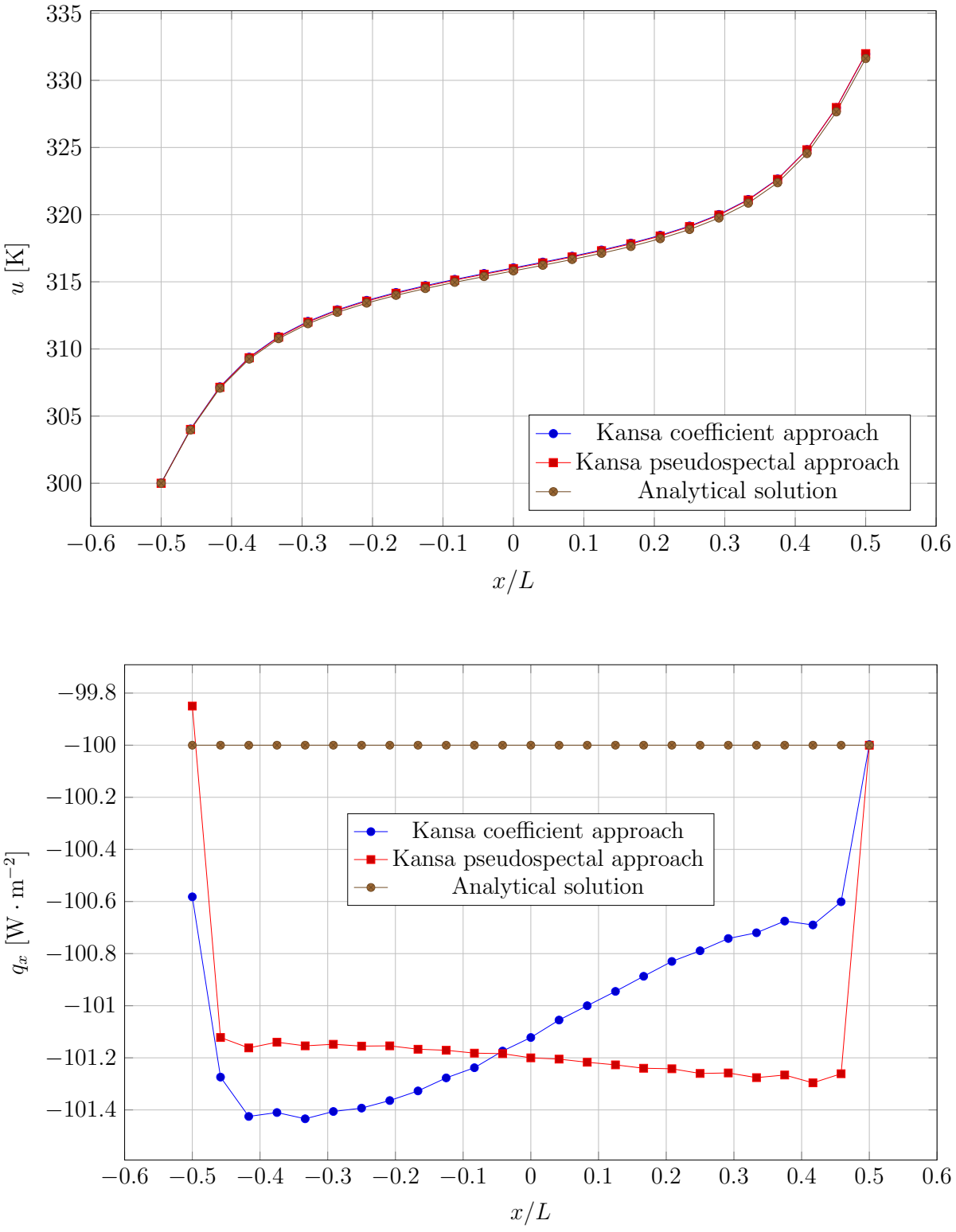

Figure 3.36: Comparison between the Kansa method solutions and the analytical solution for the two-dimensional elliptic problem no. 1 for points $y = 0$ obtained using the Dirichlet-Neumann boundary conditions

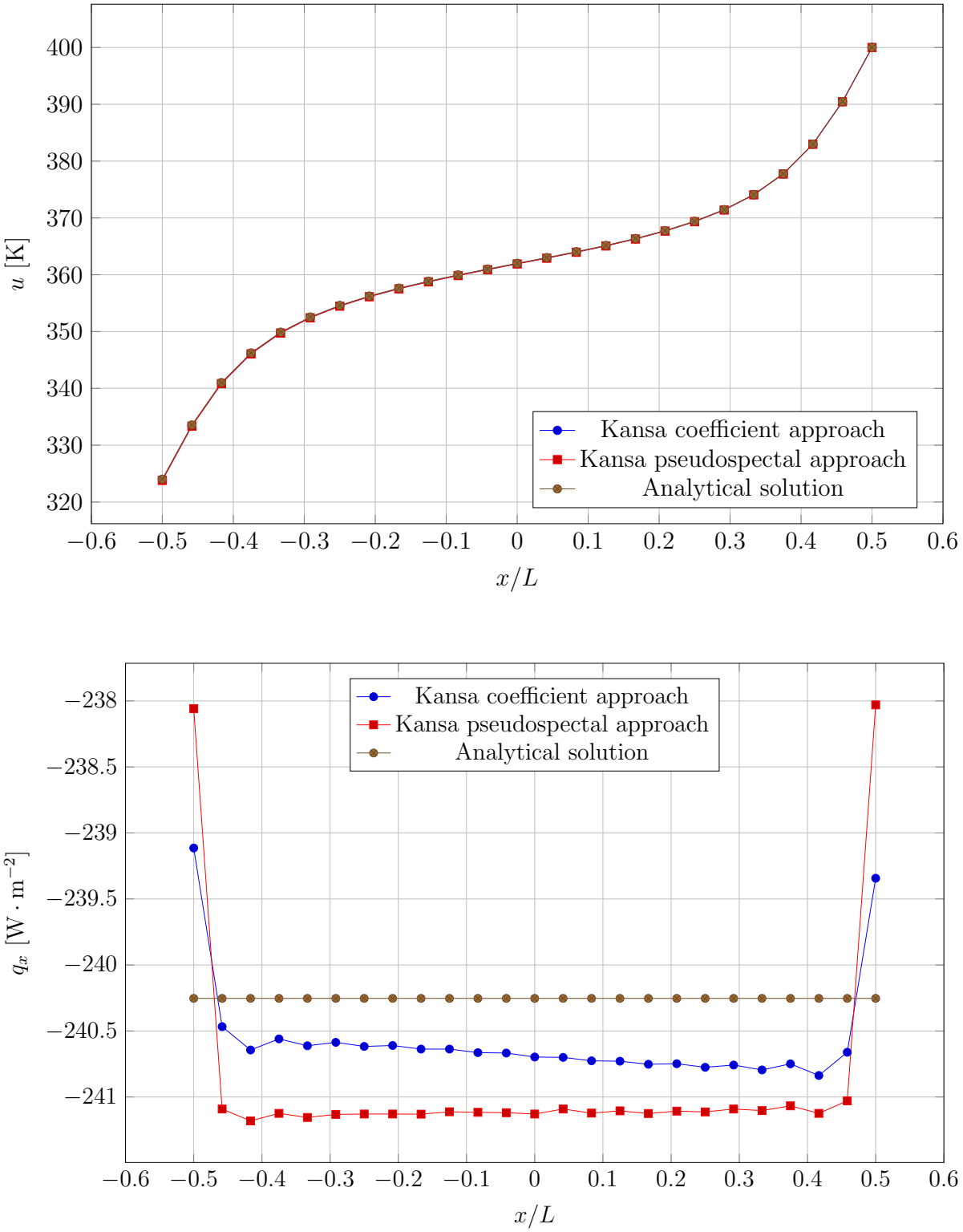

Figure 3.37: Comparison between the Kansa method solutions and the analytical solution for the two-dimensional elliptic problem no. 1 for points $y = 0$ obtained using the Robin-Dirichlet boundary conditions

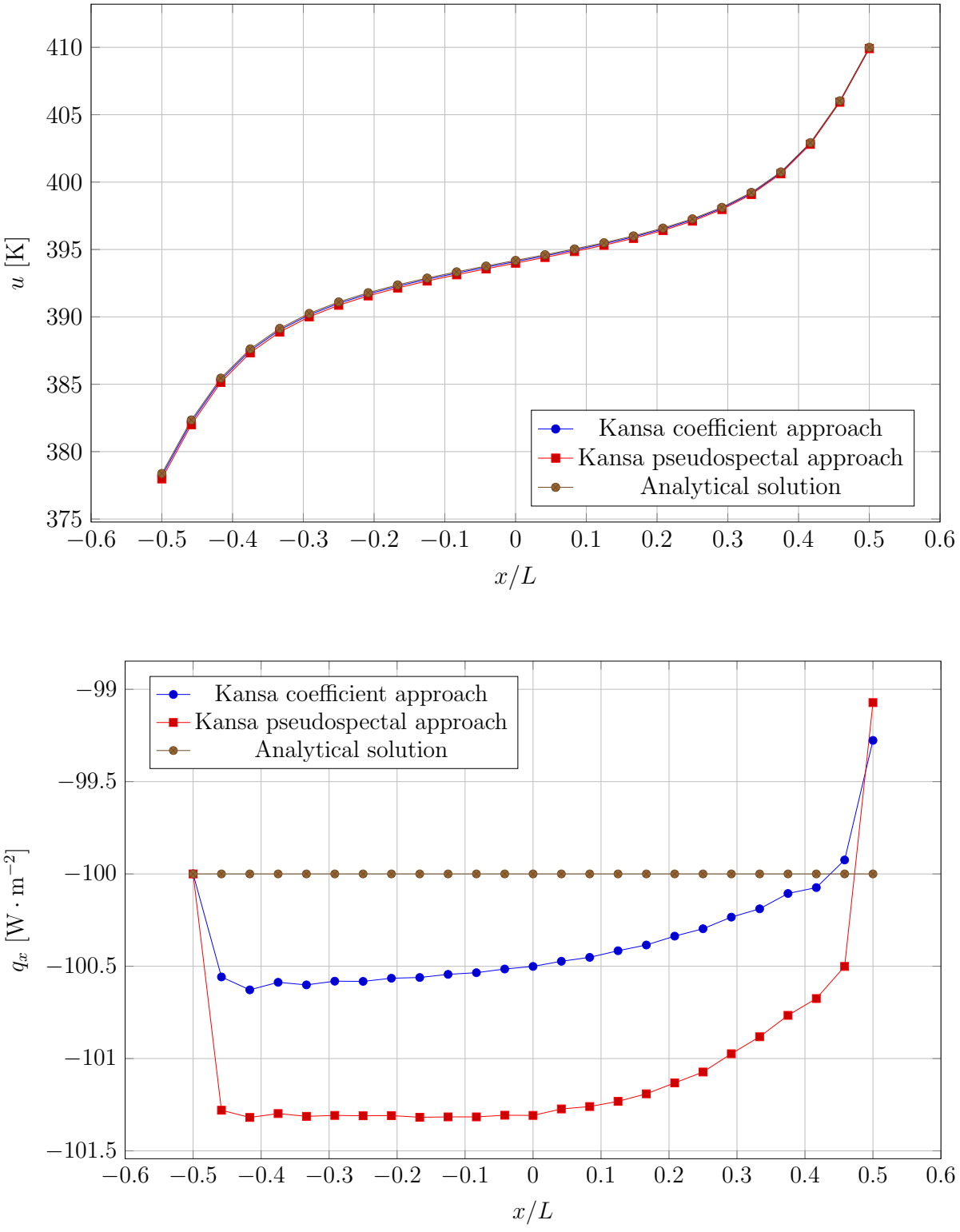

Figure 3.38: Comparison between the Kansa method solutions and the analytical solution for the two-dimensional elliptic problem no. 1 for points $y = 0$ obtained using the Neumann-Robin boundary conditions

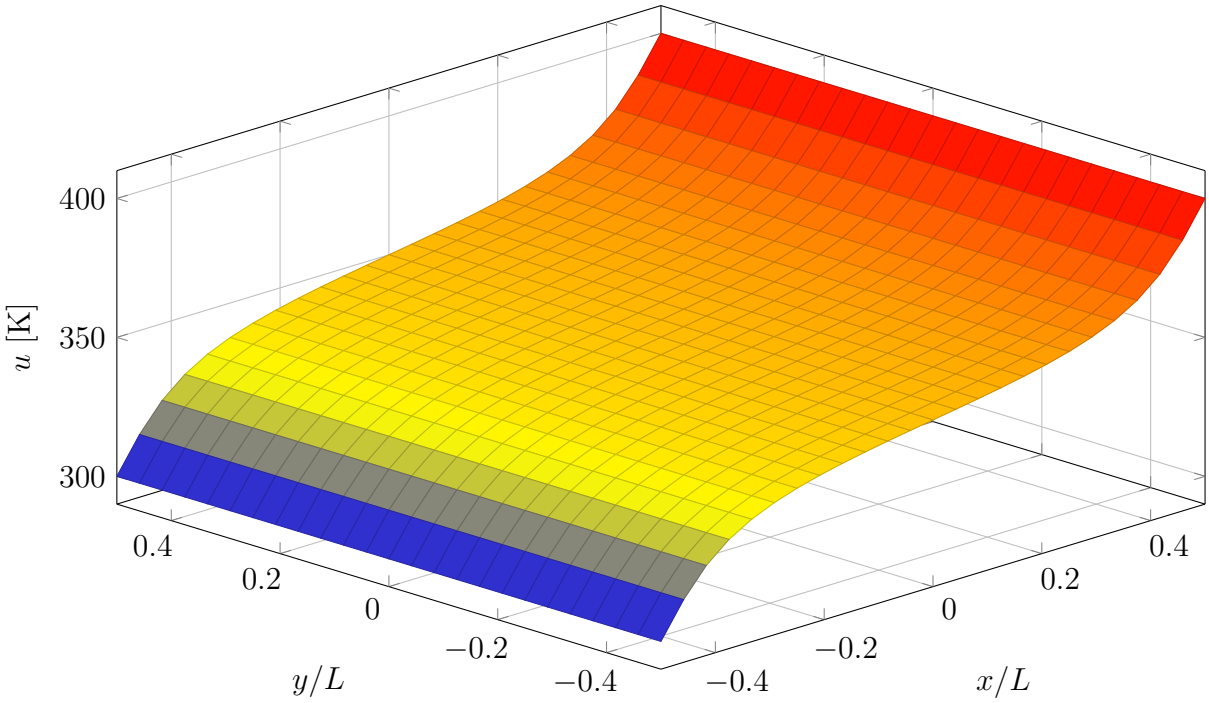

Figure 3.39: Analytical solution temperature field for the two-dimensional elliptic problem no. 1 obtained using the Dirichlet-Dirichlet boundary conditions

3.4.1.3 Two-dimensional elliptic problem no. 2

The second problem was similar in its setup to the first one, however it differed in several aspects:

- the number of collocation points was $n_x \times n_y = 21 \times 21$,
- the distributions of thermophysical parameters were described by Equations 3.20, 3.21, and 3.22,
- Robin boundary condition was imposed on the right boundary, for which the ambient temperature was equal to $u_\infty = 300\,\mathrm{K}$, while the heat transfer coefficient was equal to $\alpha = 10\,\mathrm{W} \cdot \mathrm{m}^{-2} \cdot \mathrm{K}^{-1}$,
- Neumann boundary condition was imposed on the left, bottom and top boundaries for which the heat fluxes were equal to $q_b = 100\,\mathrm{W} \cdot \mathrm{m}^{-2}$, $q_b = -100\,\mathrm{W} \cdot \mathrm{m}^{-2}$ and $q_b = 100\,\mathrm{W} \cdot \mathrm{m}^{-2}$, respectively.

Two reference solutions were used for this problem. The first of the reference solutions is the solution obtained using the finite element method solver implemented in MATLAB [113]. The second of the reference solutions is the finite difference method solution. A series of simulations for different approaches were performed and the error measures values $\bar{\xi}_u$ were calculated with respect to the reference solutions solution after each simulation. The error measure $\bar{\xi}_q$ has not been calculated because the complex pattern of the heat flux causes it to locally reach values close to zero, which in consequence causes the error measure value to reach huge values that are not reliable when it comes to the assessment of the accuracy of the solution. Figure 3.40 shows the values of error measures $\bar{\xi}_u$ calculated for the Kansa method solution with respect to the reference solutions for various approaches.

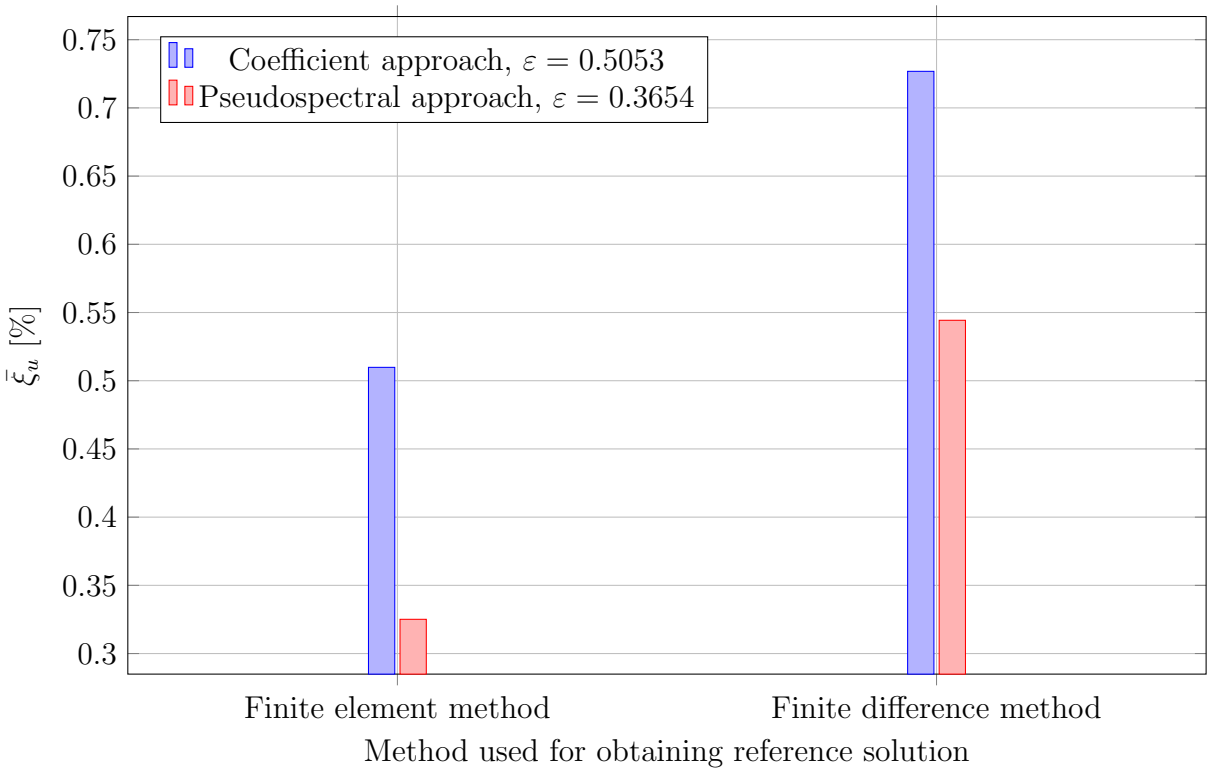

Figure 3.40: Error measure $\bar{\xi}_u$ for elliptic problem no. 2 obtained using various approaches of the Kansa method

Low values of error measures $\bar{\xi}_u$ show that the Kansa method is suitable for solving the considered class of problems and the solver is correctly implemented. It is worth noting that the pseudospectral approach for this class of problems turned out to be more accurate than the coefficient approach. This conclusion is of great importance because problems of this class will be considered in the next chapter. For this reason they will be analysed using the pseudospectral approach. It is worth presenting some Kansa method solutions and compare it with the reference solution. However, similar to the first two-dimensional problem, the temperature surfaces and heat flux vector fields obtained with different methods and approaches indistinguishable to the naked eye and therefore it is not possible to perform a substantive comparison of them in this way. Nevertheless, one example of a solution will be presented to familiarize the reader with the shape of the solution. Figure 3.41 shows the temperature field and the heat flux vector field obtained using the coefficient Kansa method.

In order to perform a substantive qualitative comparison of the solutions, the intersections of the temperature surfaces with the certain planes were used. Due to the fact that the temperature field shown in Figure 3.41 is somewhat similar to the hyperbolic paraboloid, points $y = 0$ and $x = 0$ were chosen. Figures 3.42 and 3.42 show the comparison between the temperature fields and the heat flux field obtained using the Kansa method and using the reference solutions for points $y = 0$ and $x = 0$.

As can be seen in figures Figurs 3.42 and 3.43 the agreement of the temperature fields is very good, while the agreement of the heat flux fields is slightly worse. The reasons for this phenomenon and the ways to remedy it have already been described earlier in the work in the section on one-dimensional elliptic problems.

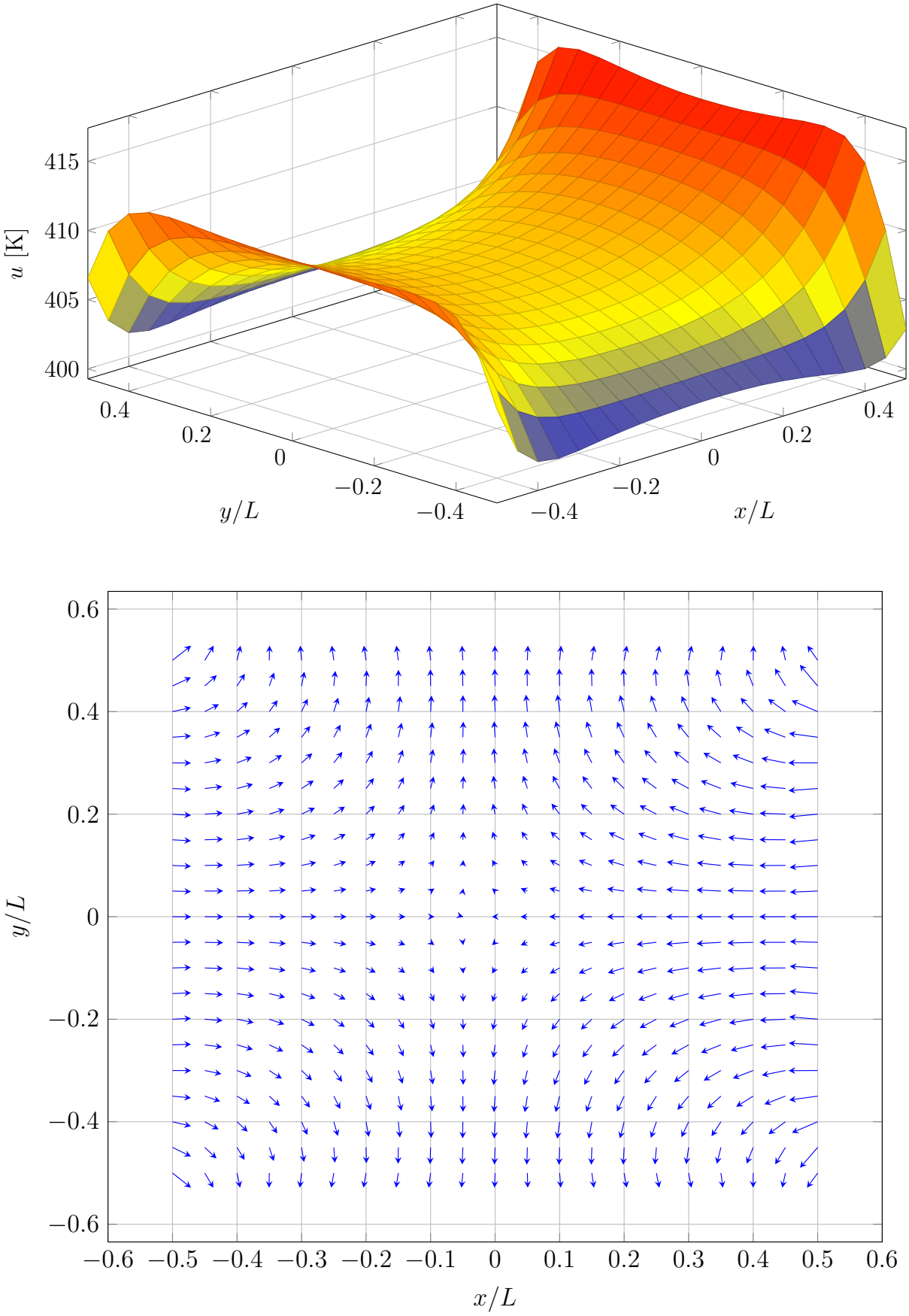

Figure 3.41: Temperature field and heat flux vector field obtained for elliptic problem no. 2 using the coefficient Kansa method

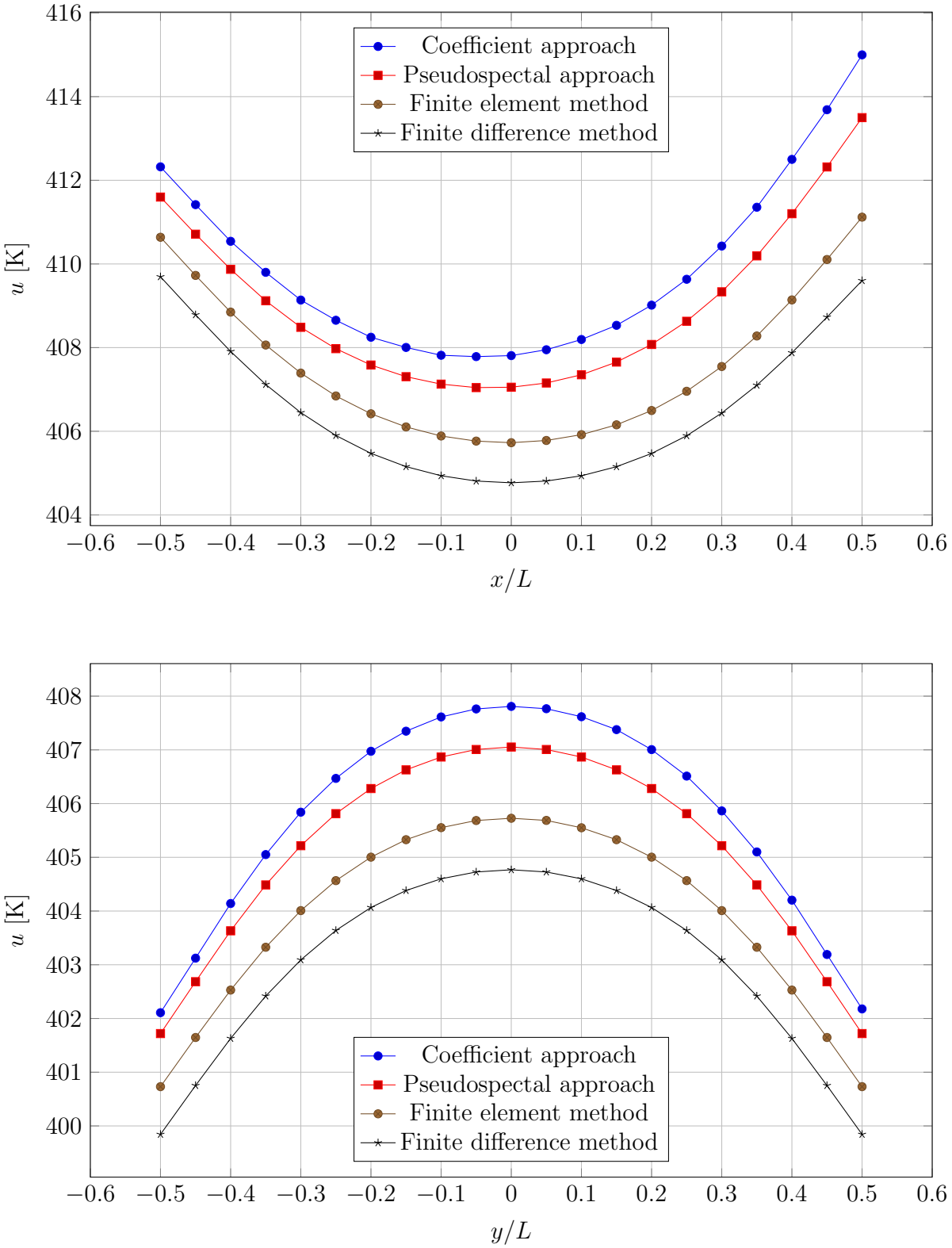

Figure 3.42: Comparison between the temperature fields obtained using the Kansa method solutions and using the reference solutions for points $y = 0$ and $x = 0$

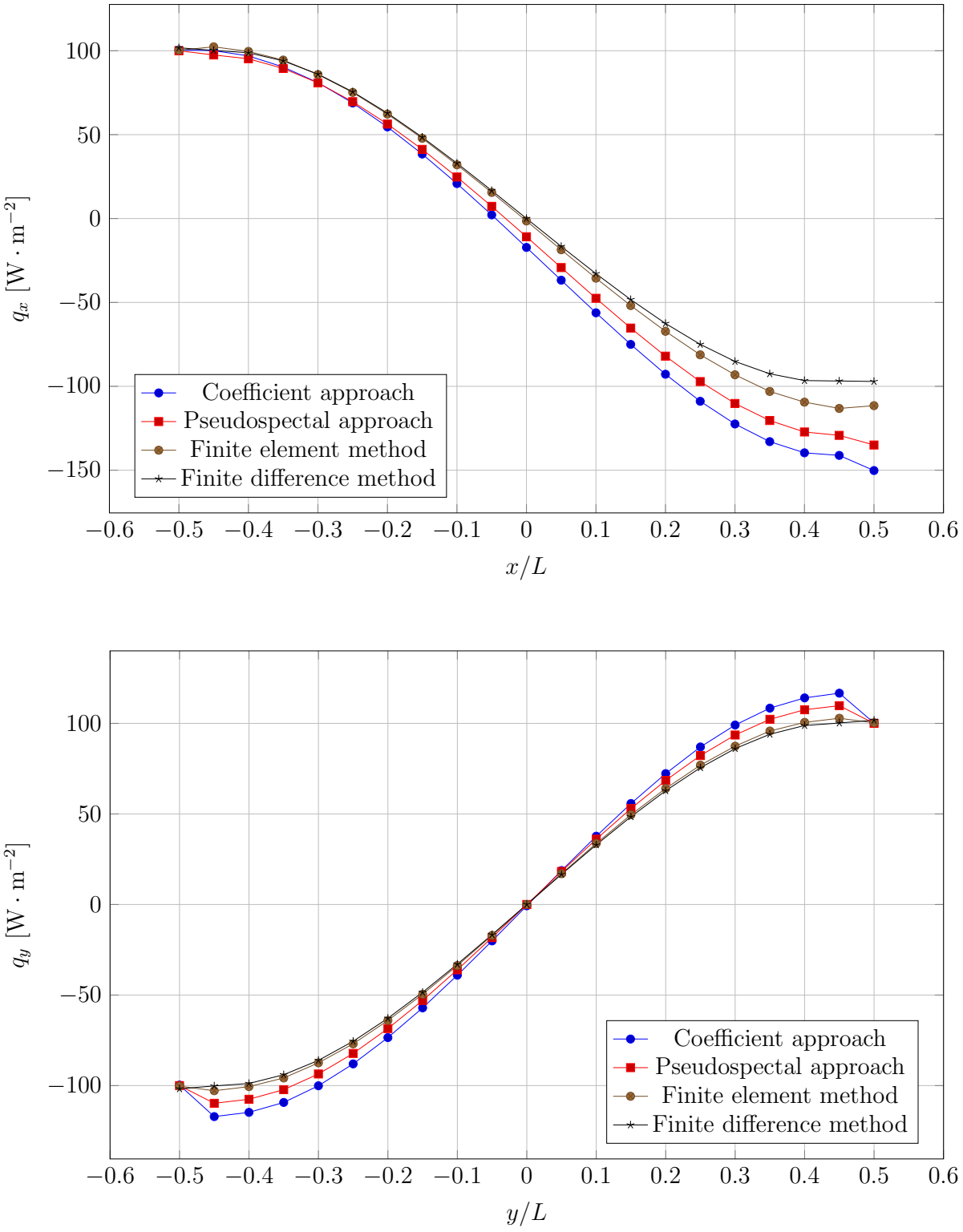

Figure 3.43: Comparison between the heat flux fields obtained using the Kansa method solutions and using the reference solutions for points $y = 0$ and $x = 0$

3.4.2 Unsteady-state parabolic problem

If the relaxation time $\tau = 0$, the two-dimensional Cattaneo-Vernotte Equation 3.18 simplifies to the two-dimensional parabolic heat equation:

$$\gamma(\boldsymbol{x})\,\rho(\boldsymbol{x})\,\dot{u} = \kappa_{,x}(\boldsymbol{x})\,u_{,x} + \kappa_{,y}(\boldsymbol{x})\,u_{,y} + \kappa(\boldsymbol{x})\,(u_{,xx} + u_{,yy})\,. \tag{3.24}$$

The reference solution for this problem was the finite difference method solution. In this case, exactly the same numerical setup as in the elliptic problem no. 2 was used. The only difference was in time advancement, which was not present in the steady-state problem. Time step size was equal to $\Delta t = 0.6\,\mathrm{s}$, while the number of time advancements was equal to 15. A series of simulations for different approaches were performed and the error measure values Ξ_u were calculated with respect to the reference solution after each simulation. The error measure Ξ_q has not been calculated because the complex pattern of the heat flux causes it to locally reach values close to zero, which in consequence causes the error measure value to reach huge values that are not reliable when it comes to the assessment of the accuracy of the solution. Figure 3.44 shows the evolution of the temperature at the point $x = 0$, $y = 0$ obtained using the finite difference method and the Kansa method for various approaches along with the values of the error measure Ξ_u and the selected value of the shape parameter ε.

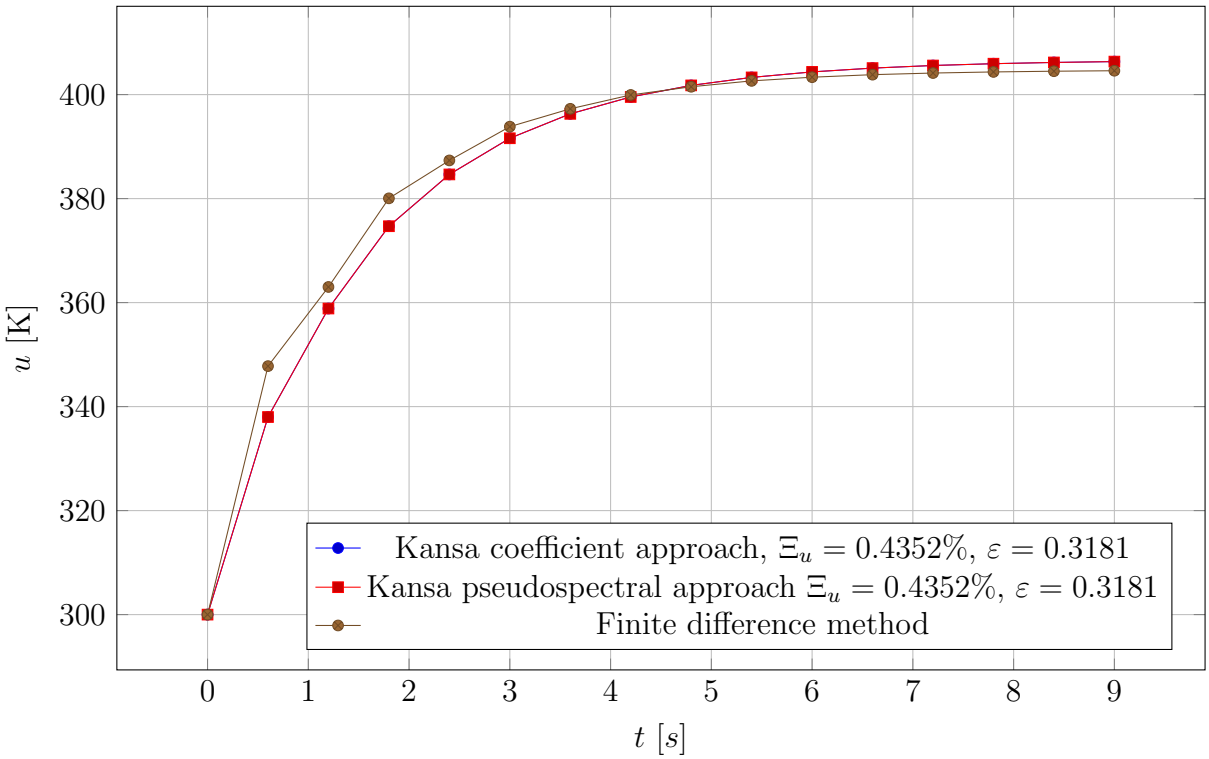

Figure 3.44: The evolution of temperature the two-dimensional parabolic problem at the point $x = 0$, $y = 0$

Low values of error measures Ξ_u and good agreement of the Kansa method solutions with the reference solutions show that the Kansa method is suitable for solving the considered class of problems and the solver is correctly implemented. Additionally, it is worth noting that the obtained shape parameter value turned out to be the same for both approaches - it is a coincidence. The results shown in Figure 3.44 show a good agreement

between the solutions obtained using the Kansa method and the solution obtained using the finite difference method. However, it seems that the Kansa method solution is slightly better due to the fact that the Kansa method solution is smoother in the first three time advancements for which the the finite difference method solution exhibits slight oscillations.

3.4.3 Unsteady-state hyperbolic problem

Let's move on to the most general problem in this section, namely the two-dimensional hyperbolic problem which is described by Equation 3.18:

$$\gamma\left(\boldsymbol{x}\right)\rho\left(\boldsymbol{x}\right)\left(\tau\ddot{u}+\dot{u}\right)=\kappa_{,x}\left(\boldsymbol{x}\right)u_{,x}+\kappa_{,y}\left(\boldsymbol{x}\right)u_{,y}+\kappa\left(\boldsymbol{x}\right)\left(u_{,xx}+u_{,yy}\right).$$

The computational domain used in the problems governed by the hyperbolic Cattaneo-Vernotte equation is the well known in the literature amoeba-like domain [29, 138], the boundary of which is described by the following equation written in the polar coordinate system:

$$r\left(\theta\right)=\exp\left(\sin\theta\right)\sin^{2}2\theta+\exp\left(\cos\theta\right)\cos^{2}2\theta,\quad 0\leq\theta\leq2\pi, \tag{3.25}$$

and presented in Figure 3.45.

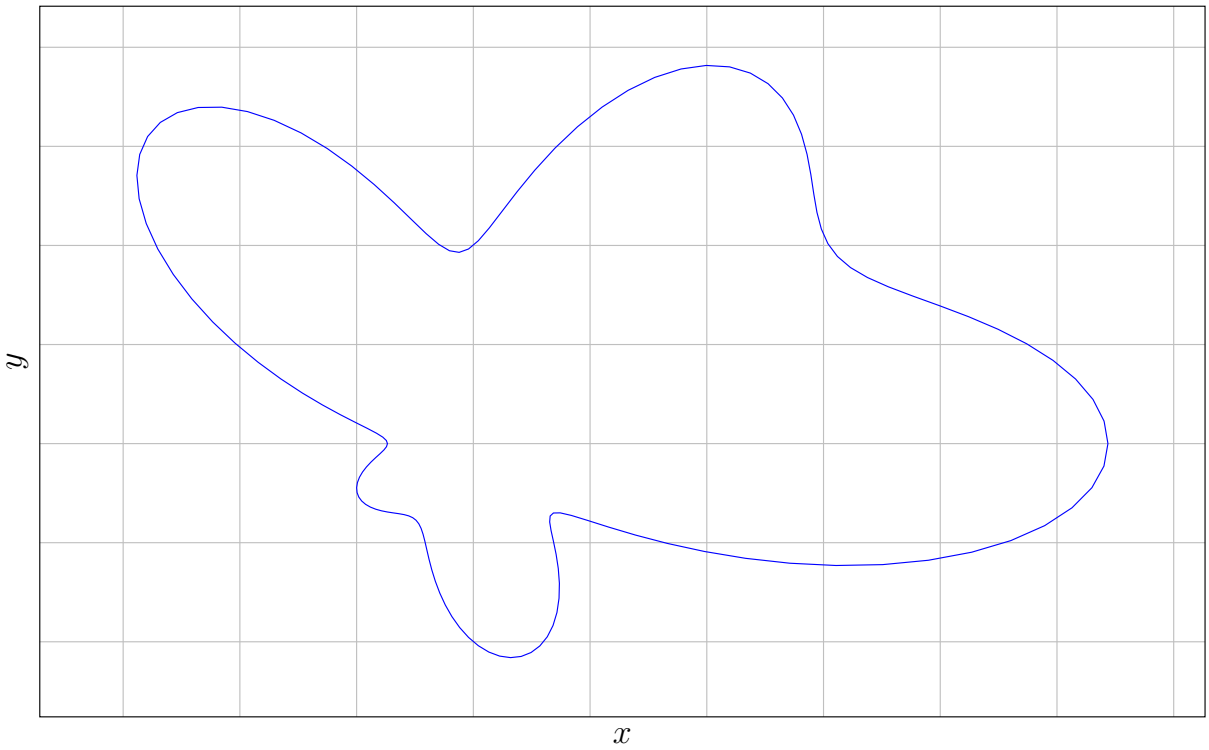

Figure 3.45: Shape of the boundary of the amoeba-like domain

The distributions of thermophysical parameters in the amoeba-like domain are given by the following functions:

$$\kappa\left(x,y\right)=\left(2x+y+2\right)^{2}, \tag{3.26}$$

$$\rho\left(x,y\right)=1, \tag{3.27}$$

$$\gamma\left(x,y\right)=1. \tag{3.28}$$

The Dirichlet boundary condition was applied on the whole boundary in the following form:

$$u\left(x_b,y_b,t\right)=\frac{30y_b^2-30x_b^2-100x_by_b-150}{2x_b+y_b+2}\exp\left(-\frac{t}{5}\right), \tag{3.29}$$

$$\dot{u}\left(x_b,y_b,t\right)=0, \tag{3.30}$$

where x_b, y_b are coordinates of boundary points. The initial conditions were as follows:

$$u\left(x,y,t=0\right)=\frac{30y^2-30x^2-100xy-150}{2x+y+2}. \tag{3.31}$$

The reference solution for this problem was the so-called artificial analytical solution [119], and for the interior of the domain is has the following form:

$$u\left(x,y,t\right)=\frac{30y^2-30x^2-100xy-150}{2x+y+2}\exp\left(-\frac{t}{5}\right), \tag{3.32}$$

$$q_x\left(x,y,t\right)=\left(-300+120x+60x^2+200y+60xy+160y^2\right)\exp\left(-\frac{t}{5}\right), \tag{3.33}$$

$$q_y\left(x,y,t\right)=\left(-150+200x+170x^2-120y-120xy-30y^2\right)\exp\left(-\frac{t}{5}\right). \tag{3.34}$$

The computational domain consisted of 386 collocation points, which consisted of 120 boundary points and 266 interior points. As for the distribution of the collocation points, two approaches were used in the work. The boundary points were regularly distributed, while the interior points were distributed in one of two ways: regular or irregular (random). Figures 3.46 and 3.47 show the examples of amoeba-like domain with regular and irregular distributions of collocation points in the domain interior.

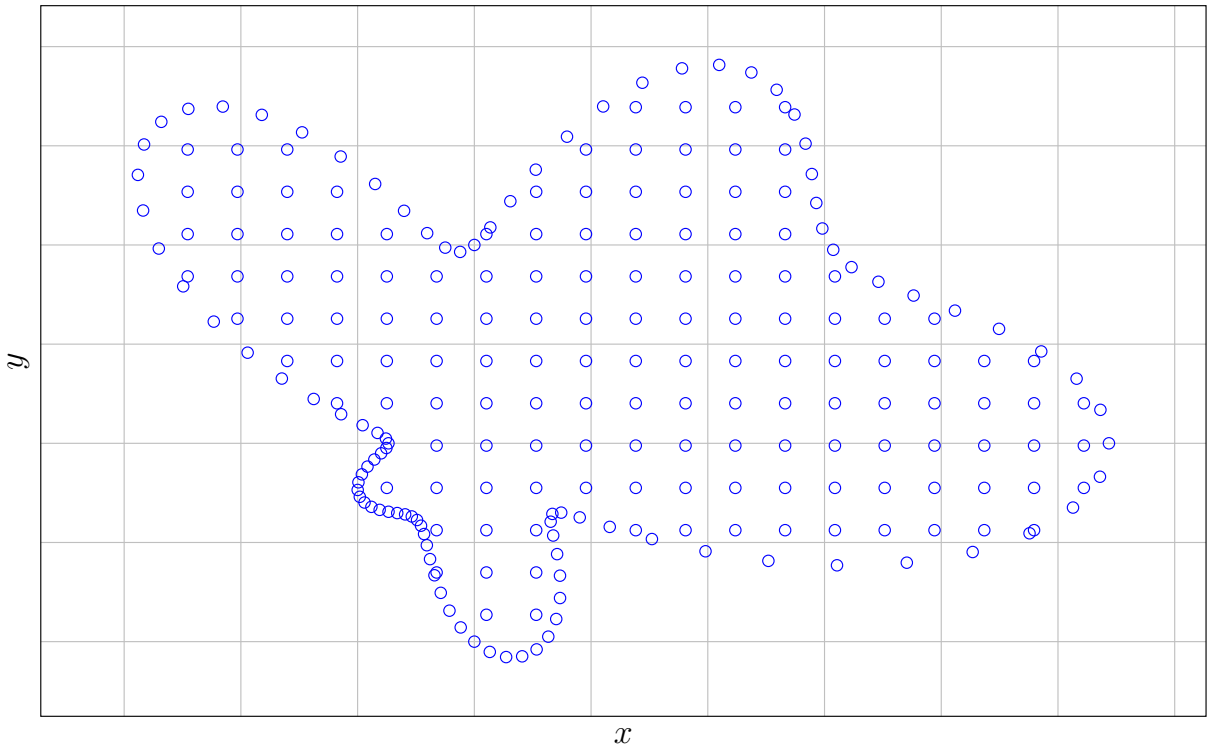

Figure 3.46: An example of the amoeba-like domain with the regular distribution of internal collocation points

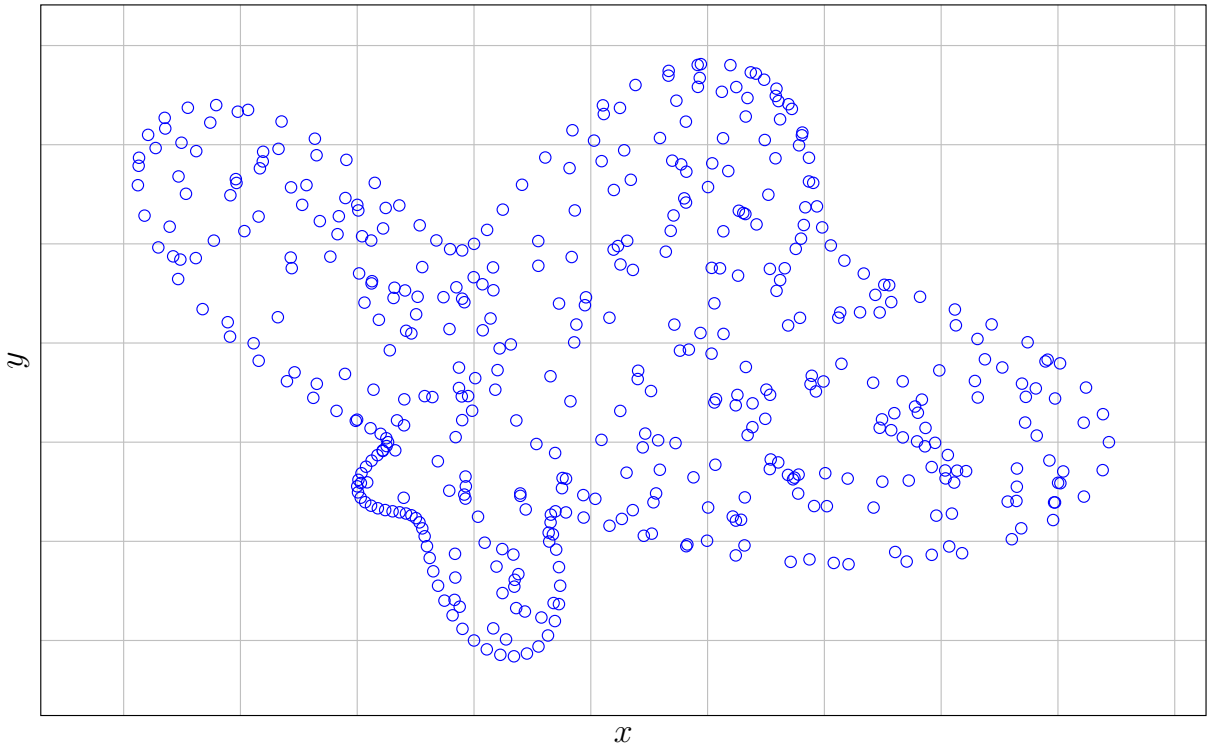

Figure 3.47: An example of the amoeba-like domain with the irregular (random) distribution of internal collocation points

3.4.3.1 Regular distribution of collocation points in the interior

In the case of regular distribution of collocation points in the interior the time step size was equal to $\Delta t = 0.75\,\mathrm{s}$, while the number of time advancements was equal to 20. A series of simulations for different approaches and time integrations schemes were performed and the error measures values Ξ_u were calculated with respect to the reference solution after each simulation. The error measure Ξ_q has not been calculated because the complex pattern of the heat flux causes it to locally reach values close to zero, which in consequence causes the error measure value to reach huge values that are not reliable when it comes to the assessment of the accuracy of the solution. Figure 3.48 shows the values of error measure Ξ_u calculated for the Kansa method solution with respect to the reference solution for various approaches. Figures 3.49 and 3.50 show the evolution of temperature over time at point $x = 1$, $y = 0.5$ obtained using the analytical solution and the Kansa method for various approaches and time integration schemes. This point was chosen because it is one of the farthest points from the boundaries. Due to the fact that Dirichlet boundary conditions are imposed, near boundary, it is easy to achieve a low error. The above causes that the evolution of the solution will be analyzed at the point for which there will be no artificial improvement of the result by the influence of the proximity of the boundary.

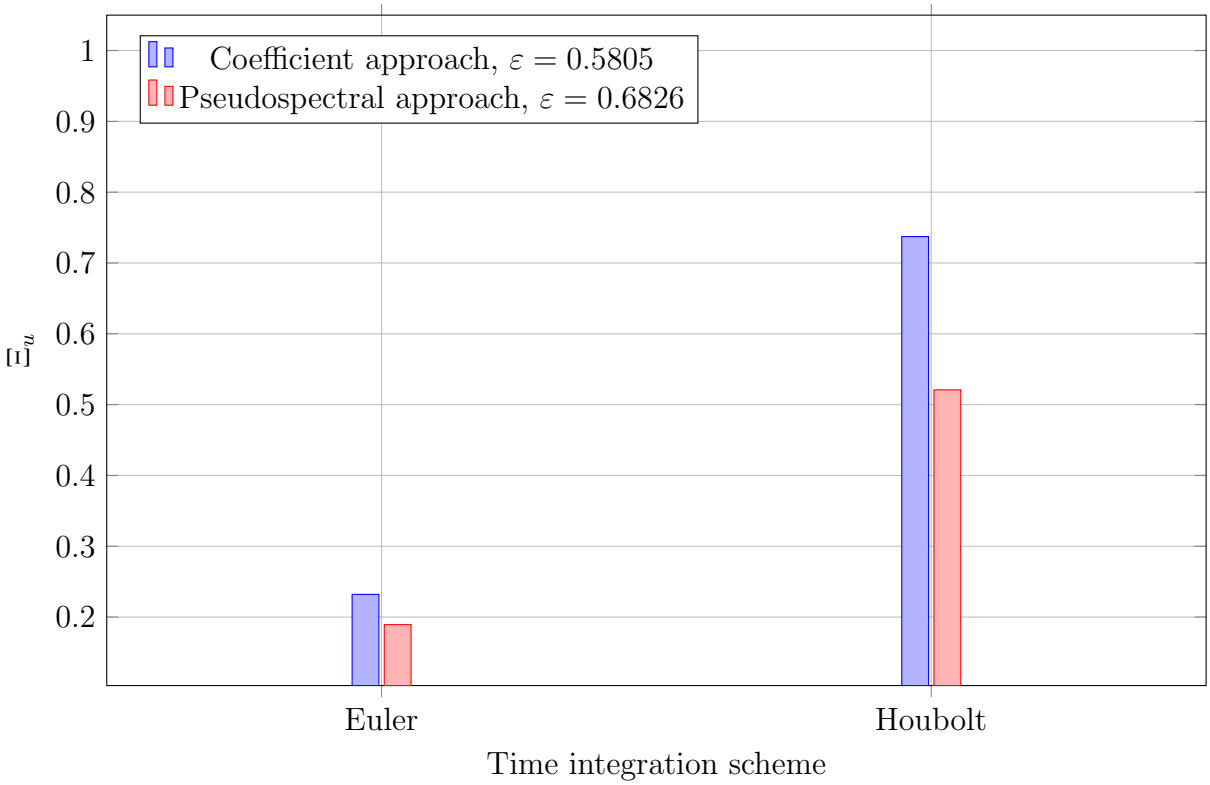

Figure 3.48: Error measure Ξ_u for the two-dimensional hyperbolic problem obtained using various approaches and time integration schemes

Low values of error measures Ξ_u and good agreement of the Kansa method solutions with the reference solutions show that the Kansa method is suitable for solving the considered class of problems and the solver is correctly implemented. As for the agreement of the temperature evolution obtained using the Kansa method and using the analytical method, it is very good, much better than the agreement in the case of the evolution of the heat fluxes. The reasons for this phenomenon and the ways to remedy it have already

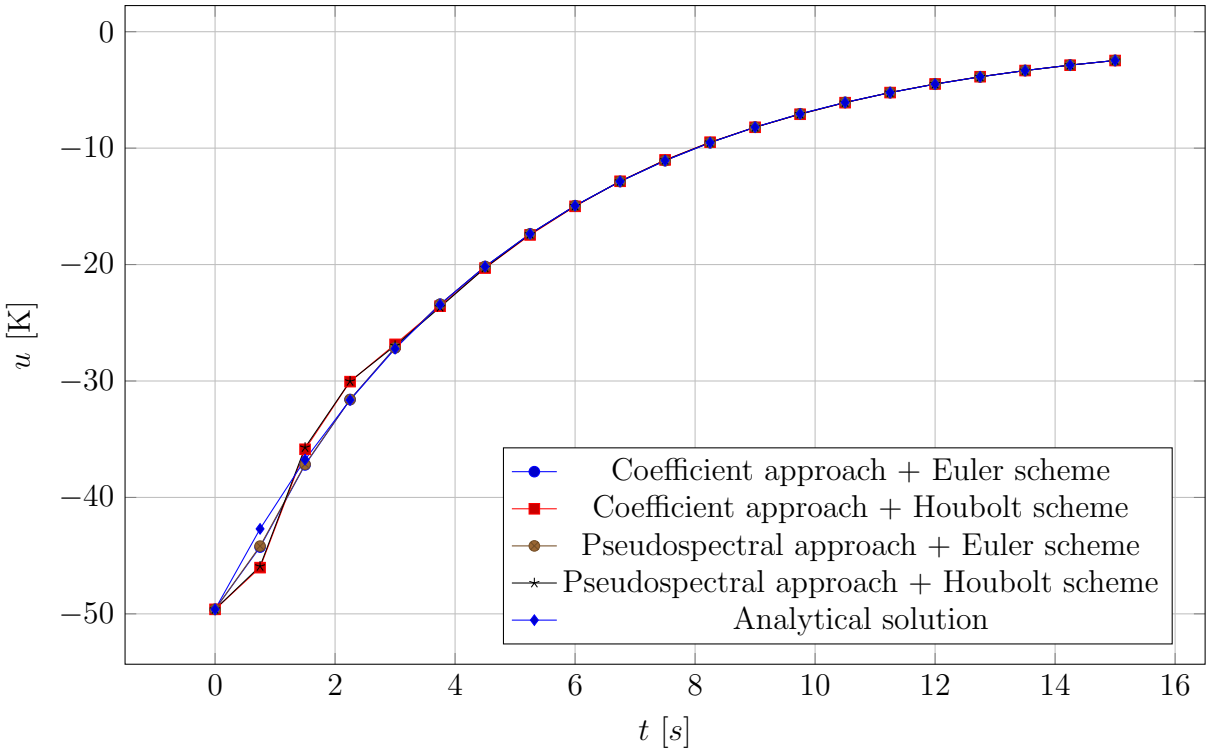

Figure 3.49: The evolution of the temperature for the two-dimensional hyperbolic problem at the point $x = 1$, $y = 0.5$ obtained using various approaches and time integration schemes

been described earlier in the work in the section on one-dimensional elliptic problems. The evolution of temperature and flux obtained with the different approaches and time integration schemes did not differ significantly.

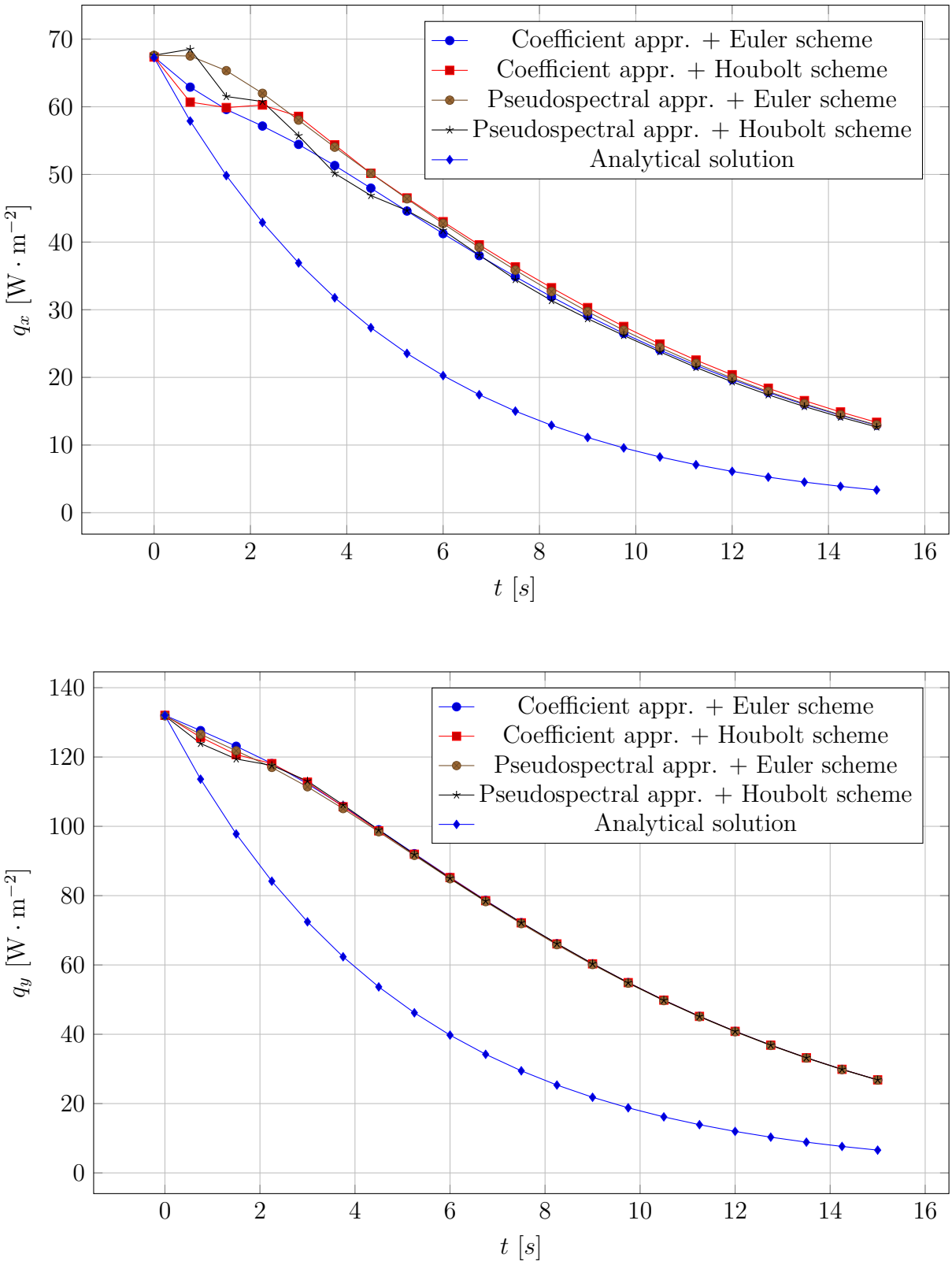

Figure 3.50: The evolution of the heat flux for the two-dimensional hyperbolic problem at the point $x = 1$, $y = 0.5$ obtained using various approaches and time integration schemes

3.4.3.2 Irregular (random) distribution of collocation points in the interior

The simulations using irregular distribution of collocation points in the interior turned out to be a little problematic. Due to the fact that the distributions of collocation points are random, after performing a dozen or so simulations, the results were obtained, in which the accuracy in some cases is comparable with the results for the regular distribution, sometimes it is lower and sometimes the simulation turns out to be completely unstable. In other words, the repeatability and reliability of this approach is limited. For this reason, for the class of problem under consideration, it is not recommended to use irregular distribution of collocation points.

Author's publications More information on the problems discussed so far in thesis can be found in the author's publications that have been published in the course of the research: [128, 129, 126, 131, 132].

3.5 Algorithms for finding good value of shape parameter and examples of application

After positive verification and validation of the formulated variants of the Kansa method and the solver, it is possible to analyse the condition algorithm. For this purpose, two series of steady-state problems simulations were performed using the coefficient Kansa method - one for the one-dimensional case and one for the two-dimensional case. As part of these simulations, the functions $\mathcal{L}(\varepsilon)$ and $E_{\infty}(\varepsilon)$ were examined. For the first one, the place of transition to the oscillatory region was searched according to the condition algorithm, and for the second - the minimum according to Rippa's algorithm. These graphs of the functions were collated with the graph of the error measure function $\bar{\xi}_u(\varepsilon)$. As mentioned in the section on the condition algorithm, this algorithm does not have to be limited to examining the oscillation of the $\mathcal{L}(\varepsilon)$ function. Therefore, the $E_{\infty}(\varepsilon)$, $\left|\left|\bar{\boldsymbol{A}}(\varepsilon)\,\boldsymbol{c}-\bar{\boldsymbol{b}}\right|\right|^2$ and $||\boldsymbol{c}(\varepsilon)||^2$ functions were also examined. The numerical setup for the one-dimensional simulations was the same as for the discussed earlier one-dimensional elliptic problem no. 1 with Robin-Dirichlet boundary conditions. The numerical setup for the two-dimensional simulations was the same as for the discussed earlier two-dimensional elliptic problem no. 1 with Neumann-Robin boundary conditions. The research was carried out for 200 logarithmically distributed values of shape parameter ranging from 10^{-1} to 10^{1}. Figures 3.51 - 3.54 show the graphs of functions $\mathcal{L}(\varepsilon)$, $E_{\infty}(\varepsilon)$, $\left|\left|\bar{\boldsymbol{A}}(\varepsilon)\,\boldsymbol{c}-\bar{\boldsymbol{b}}\right|\right|^2$, $||\boldsymbol{c}(\varepsilon)||^2$ collated with the graph of the error measure function $\bar{\xi}_u(\varepsilon)$ for the one-dimensional case, respectively. Figures 3.55 - 3.58 show the graphs of functions $\mathcal{L}(\varepsilon)$, $E_{\infty}(\varepsilon)$, $\left|\left|\bar{\boldsymbol{A}}(\varepsilon)\,\boldsymbol{c}-\bar{\boldsymbol{b}}\right|\right|^2$, $||\boldsymbol{c}(\varepsilon)||^2$ collated with the graph of the error measure function $\bar{\xi}_u(\varepsilon)$ for the two-dimensional case, respectively.

Figures 3.51 - 3.58 lead to some interesting conclusions. First of all, it is noticeable that not only the condition algorithm, but the whole proposed class of oscillation indicators is effective. This is due to the fact that all the shape parameter values obtained using oscillation algorithms lead to high accuracy results, in all considered cases the error measure did not exceed 1%. Regarding reliability, there are some disadvantages with the oscillation algorithm in conjunction with $\left|\left|\bar{\boldsymbol{A}}(\varepsilon)\,\boldsymbol{c}-\bar{\boldsymbol{b}}\right|\right|^2$ function. The point is that the zone below the strong oscillation threshold, which is smooth for other functions, is slightly oscillating for the $\left|\left|\bar{\boldsymbol{A}}(\varepsilon)\,\boldsymbol{c}-\bar{\boldsymbol{b}}\right|\right|^2$ function, which may lead to an erroneous finding of the

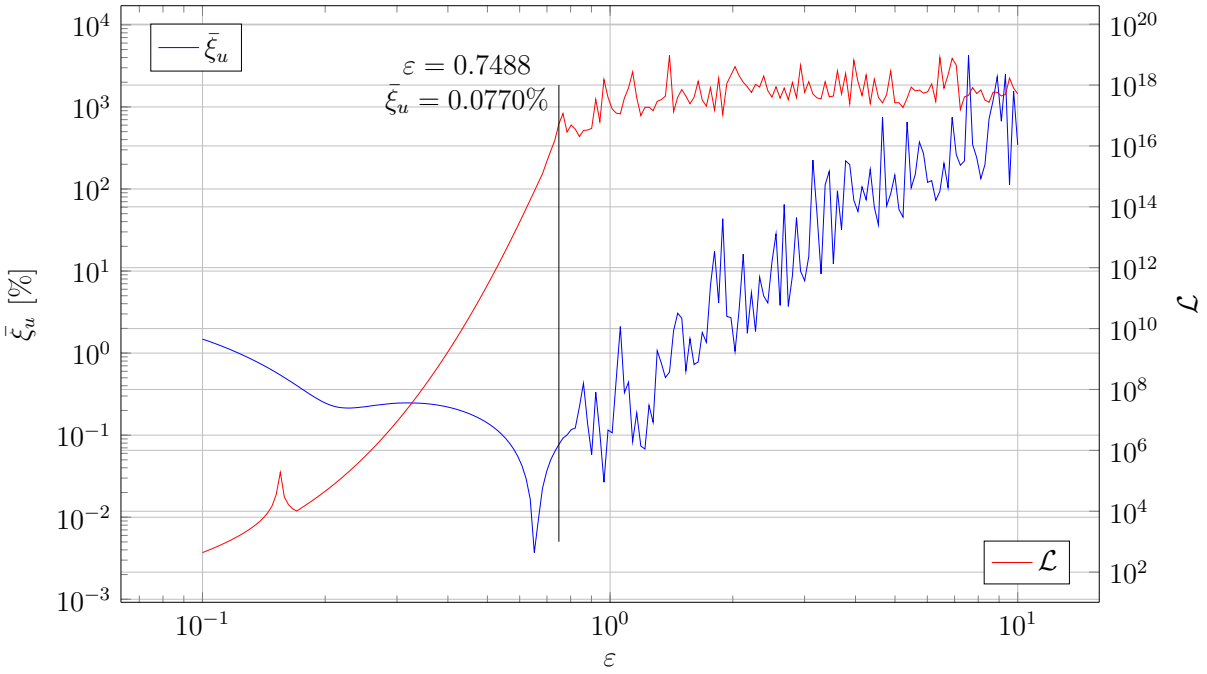

Figure 3.51: Graphs of functions $\mathcal{L}(\varepsilon)$ and $\bar{\xi}_u(\varepsilon)$ for the one-dimensional case

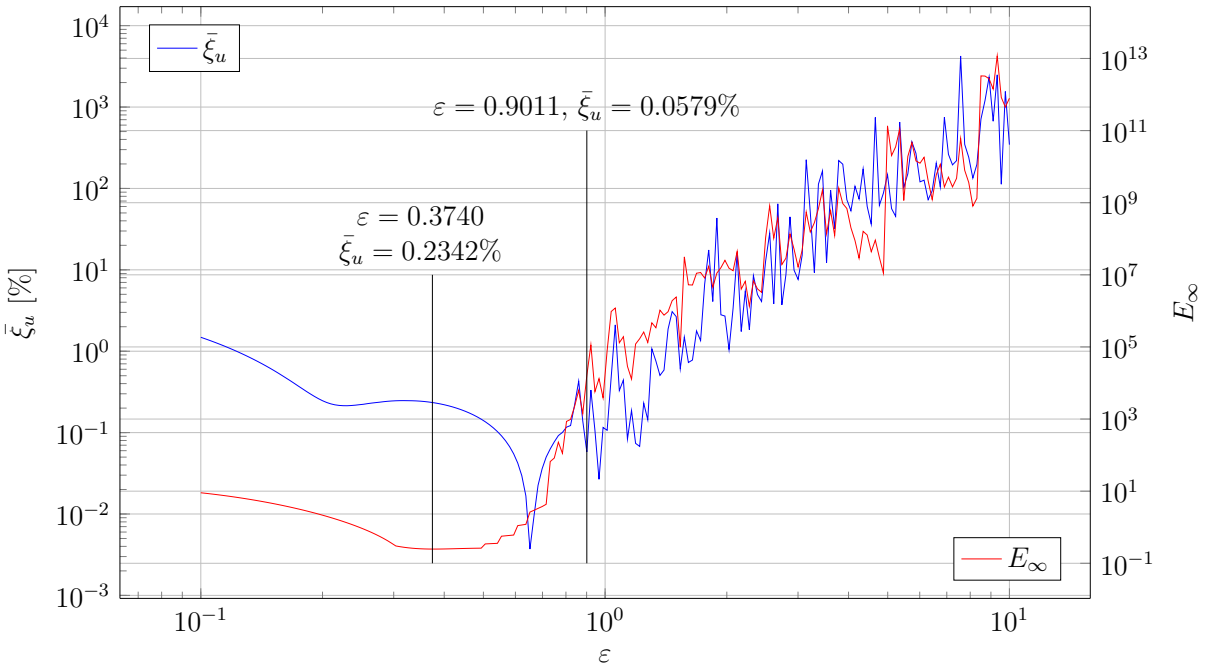

Figure 3.52: Graphs of functions $E_\infty(\varepsilon)$ and $\bar{\xi}_u(\varepsilon)$ for the one-dimensional case. The left value corresponds to Rippa's algorithm and the right value corresponds to the oscillation algorithm

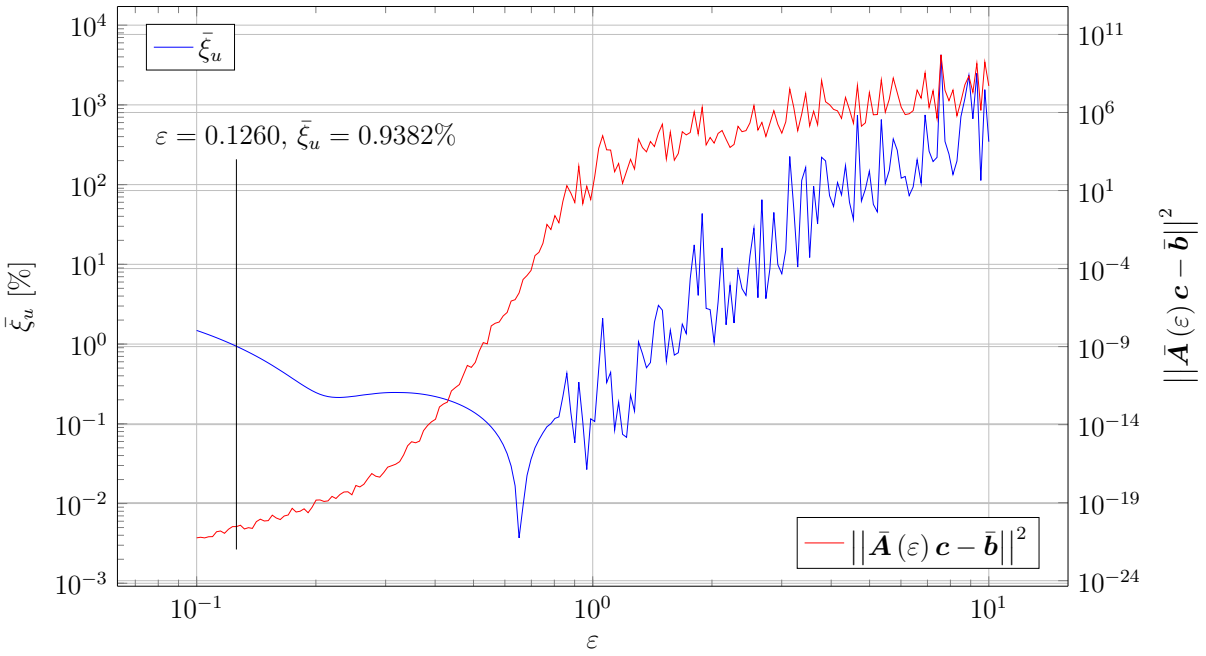

Figure 3.53: Graphs of functions $\left|\left|\bar{\boldsymbol{A}}(\varepsilon)\,\boldsymbol{c} - \bar{\boldsymbol{b}}\right|\right|^2$ and $\bar{\xi}_u(\varepsilon)$ for the one-dimensional case

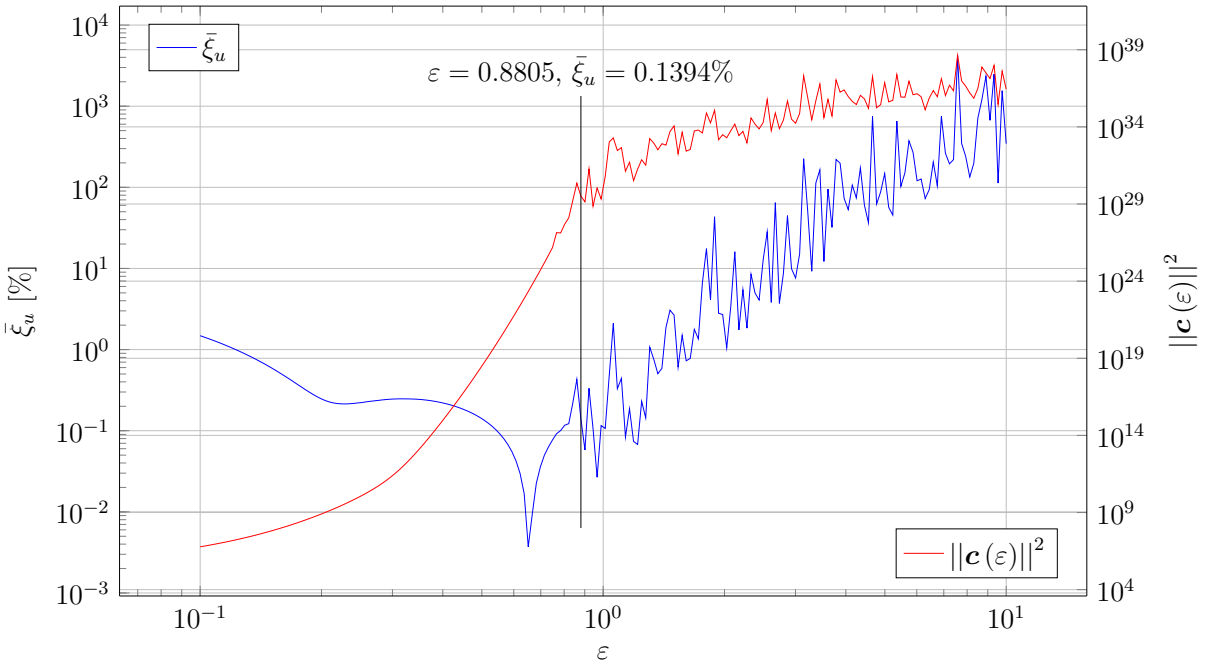

Figure 3.54: Graphs of functions $||\boldsymbol{c}(\varepsilon)||^2$ and $\bar{\xi}_u(\varepsilon)$ for the one-dimensional case

threshold value for the oscillation zone. This is also what happened in the one-dimensional case. As for the accuracy of the results obtained with the oscillation algorithms, in all cases, except for the one mentioned above relating to the function $\left|\left|\bar{\boldsymbol{A}}(\varepsilon)\,\boldsymbol{c} - \bar{\boldsymbol{b}}\right|\right|^2$, more accurate results were obtained than using Rippa's algorithm. Naturally, the algorithm most strongly promoted in the work is the condition algorithm. On the other hand, it happened that other functions from the group of oscillation algorithms gave better results. So why is it this algorithm that deserves special attention? It should be remembered that the condition algorithm, unlike other presented algorithms, does not require solving the

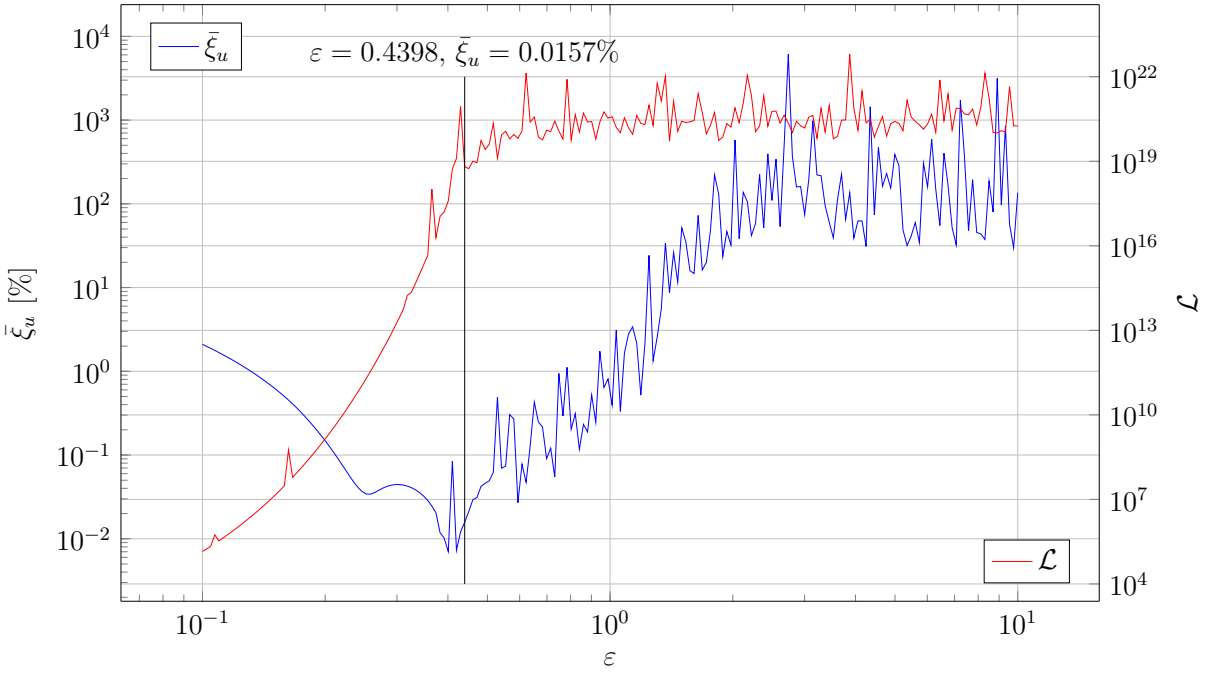

Figure 3.55: Graphs of functions $\mathcal{L}(\varepsilon)$ and $\bar{\xi}_u(\varepsilon)$ for the two-dimensional case

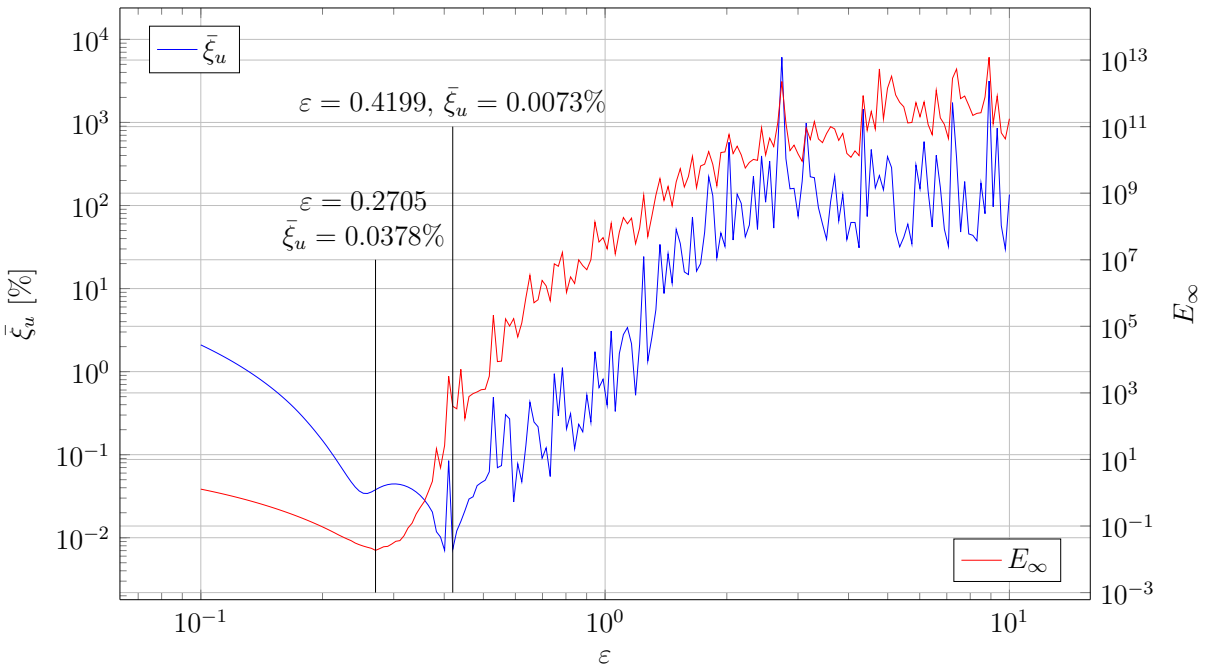

Figure 3.56: Graphs of functions $E_\infty(\varepsilon)$ and $\bar{\xi}_u(\varepsilon)$ for the two-dimensional case. The left value corresponds to Rippa's algorithm and the right value corresponds to the oscillation algorithm

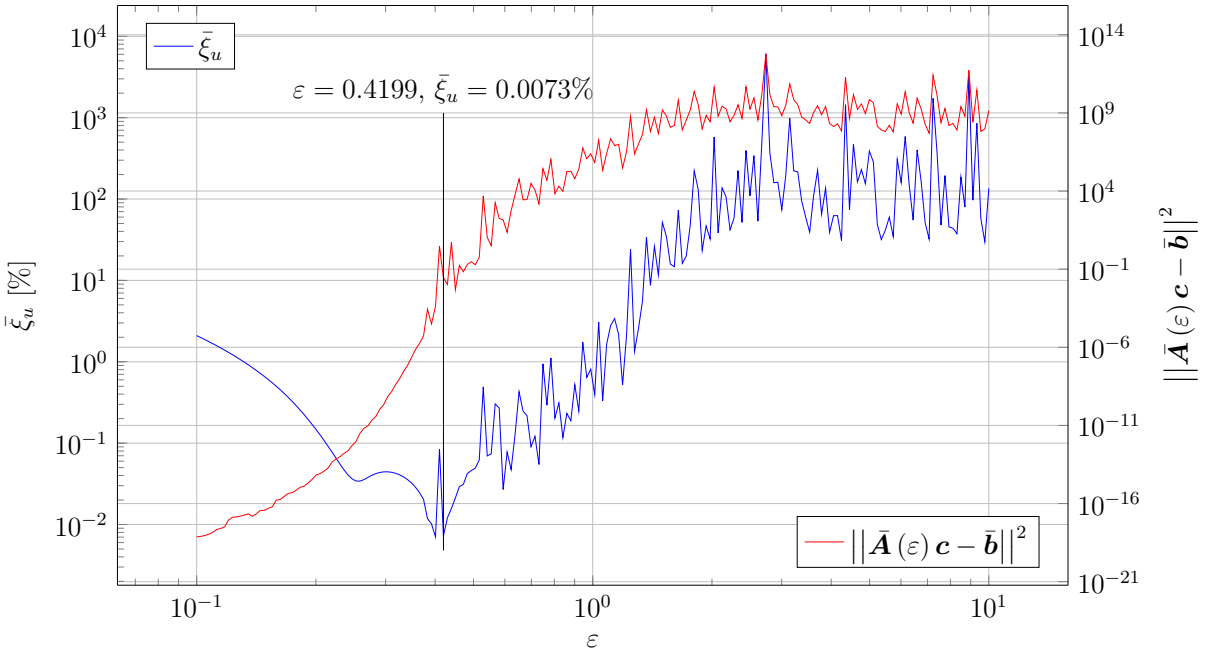

Figure 3.57: Graphs of functions $\left|\left|\bar{\boldsymbol{A}}(\varepsilon)\,\boldsymbol{c} - \bar{\boldsymbol{b}}\right|\right|^2$ and $\bar{\xi}_u(\varepsilon)$ for the two-dimensional case

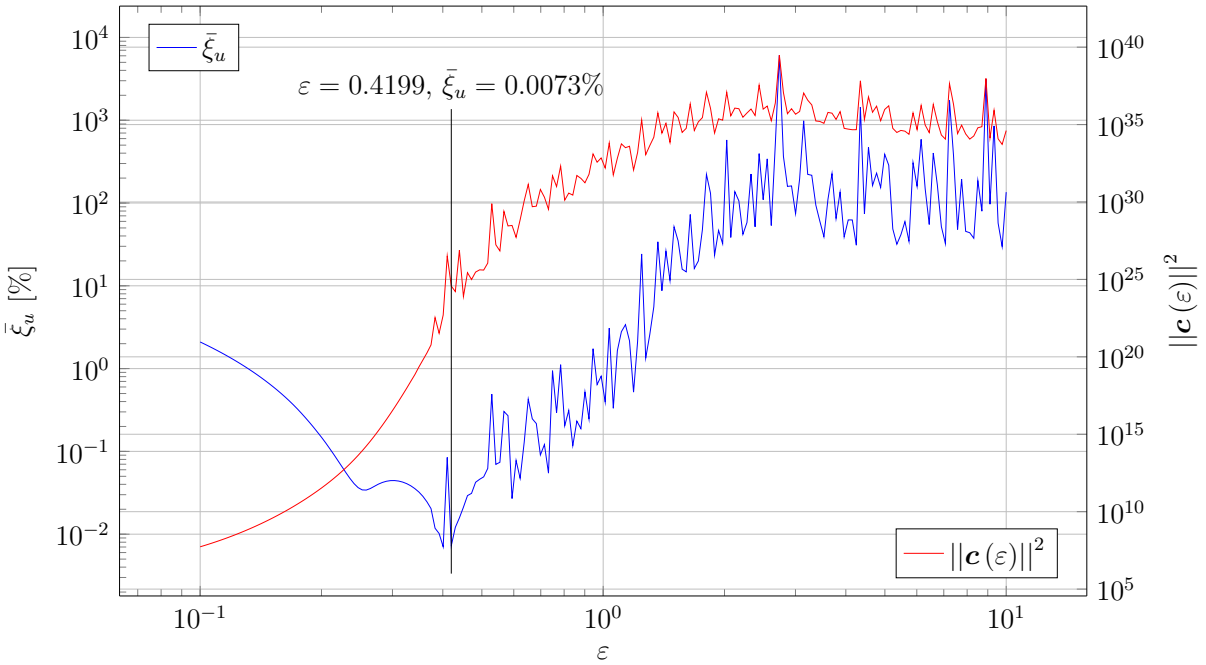

Figure 3.58: Graphs of functions $||\boldsymbol{c}(\varepsilon)||^2$ and $\bar{\xi}_u(\varepsilon)$ for the two-dimensional case

problem, which is a significant saving from the point of view of the numerical budget and, consequently, a very strong advantage. Of course, one can argue that determining the condition number is also numerically expensive. This is true, however, the more collocation points, the weaker this argument is because for computational domains with a large number of collocation points, the cost of solving the problem can be significantly higher than the cost of determining the condition number. Algorithms from the group of oscillation algorithms in the considered examples led to very precise results. One can risk saying that they are extremely promising, however, there are many questions related to

them, for which there is no answer. First of all, it is necessary to consider an alternative method of detecting the oscillations so that they are not detected at the wrong threshold. Potentially, application of Fourier analysis to detect the transition from the smooth region to the oscillating region analysis is an interesting direction for further research. Another important issue is the search for new functions that meet two conditions at the same time: their determination will not be numerically expensive and will give reliable, accurate results. Finally, it is worth emphasizing the fact that was already indicated in the previous chapter, namely that the work considers only the problems in which a good value of the shape parameter is sought for a given problem and a given cloud of collocation points.

Author's publications More information on the algorithms for searching for a good value of the shape parameter can be found in the author's publications that have been published in the course of the research: [133, 130, 127].

Validation and verification conclusions The chapter on validation and verification allows to draw a number of conclusions. The most important one is that the Kansa method is suitable for solving the problems associated with elliptic, parabolic and hyperbolic heat flow equations in a material with spatially variable thermophysical parameters. Additionally, the algorithms for finding a good value of the shape parameter proposed in the thesis turned out to be effective. It can be objected that the cases considered in this chapter were idealized and unrelated to the real systems in which the heat flow is modelled. This is only half true because without the study of these idealized cases, it would be impossible to analyze more complex, real-life cases. Now is the time for that. In the next chapter the problems of design of a thermal metamaterial device for heat flux manipulation will be discussed.

4. Optimal design for the heat flux manipulation device

4.1 Problem formulation

After confirming the suitability of the Kansa method for solving heat flow problems in materials with spatially variable thermophysical parameters and confirming the correctness of the implementation, it is time to consider the practical problems. In the introduction it was mentioned that the work will consider thermal metamaterials, materials enabling the manipulation of the heat flux. Heat flow is a highly diffusive process, which makes it extremely difficult to control the direction of heat flow. However, metamaterials allow to do this. They are characterized by a special spatial variability of thermophysical parameters. The work considers the device, the idea of which was proposed by Narayana's [116], it is presented in Figure 4.1.

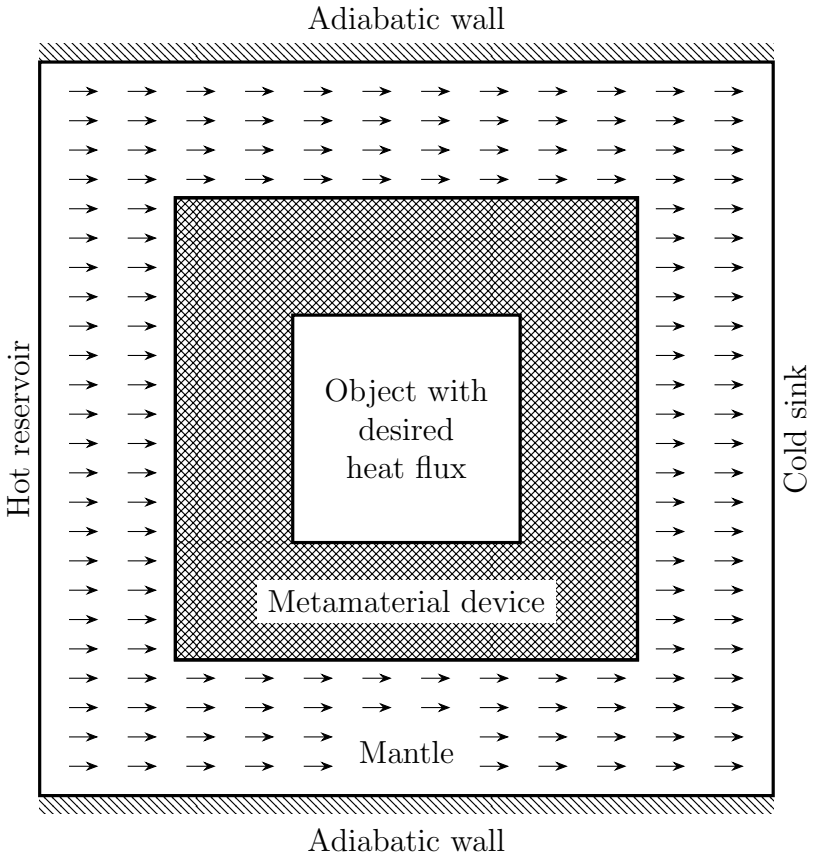

Figure 4.1: Narayana's device for heat flux manipulation

As shown in Figure 4.1, Narayana's device consists of an object surrounded by a device built of thermal metamaterial surrounded by a mantle. The upper and lower edges are insulated with an ideal adiabatic wall, while the left boundary has contact with the hot reservoir and the right one with the cold sink. The temperature difference between the left and right forces the heat to flow uniformly from left to right. The metamaterial insert is designed to create the desired heat flow distribution in the object, which would be very hard to obtain with the use of classic materials. The group of heat flows very hard to achieve with the use of classic materials is very numerous, however, one can distinguish four very important ones with a wide range of applications [116]:

- Cloaking, in which the heat flow in the object has the same intensity and direction as the flow in the mantle,
- Shielding, in which the intensity of the heat flow in the object tends to zero,
- Inversion, in which the heat flow in the object has the same intensity but the opposite direction to the flow in the mantle,
- Concentration, in which the heat flow in the object has the same direction but much greater intensity than the flow in the mantle.

These four ways of heat flux manipulation have a particularly wide application, such as photovoltaics, thermal camouflage, advanced insulation [116]. Figure 4.2 shows these four cases of heat flow in Narayana's device.

Performing a heat flow simulation for known distribution of thermophysical parameters in a metamaterial device is a direct problem. However, the problem is that these distributions are not known and need to be found, which is at the heart of designing thermal metamaterials. This type of problems is much more difficult to solve. The way it will be treated in this study will be presented in this chapter. Narayana's device is not a device with strictly defined parameters, but only a general concept. Therefore, there are many specific implementations of this device. In this study, it was decided to use Fachinotti's device [47] the scheme of which is presented in Figure 4.3.

As can be seen in Figure 4.3, Fachinotti's device, just like Narayana's, consists of an object Ω^{obj}, a device Ω^{dvc} and a mantle Ω^{mnt} for which:

$$\Omega = \Omega^{\mathrm{obj}} \cup \Omega^{\mathrm{dvc}} \cup \Omega^{\mathrm{mnt}}. \tag{4.1}$$

Fachinotti's device parameters are as follows:

- The mantle and the object are made of agar water with a thermal conductivity coefficient of $\kappa_{\mathrm{agar}} = 0.57\,\mathrm{W}\cdot\mathrm{m}^{-1}\cdot\mathrm{K}^{-1}$,
- The temperature of hot reservoir is $u_{\mathrm{hot}} = 321.85\,\mathrm{K}$,
- The temperature of cold sink is $u_{\mathrm{cold}} = 283.15\,\mathrm{K}$,
- The width of the device is $L_x = 9\,\mathrm{cm}$,
- The height of the device is $L_y = 18\,\mathrm{cm}$,
- The diameter of the object is $d_{\mathrm{obj}} = 2\,\mathrm{cm}$,
- The external diameter of the device is $d_{\mathrm{dvc}} = 6.5\,\mathrm{cm}$.

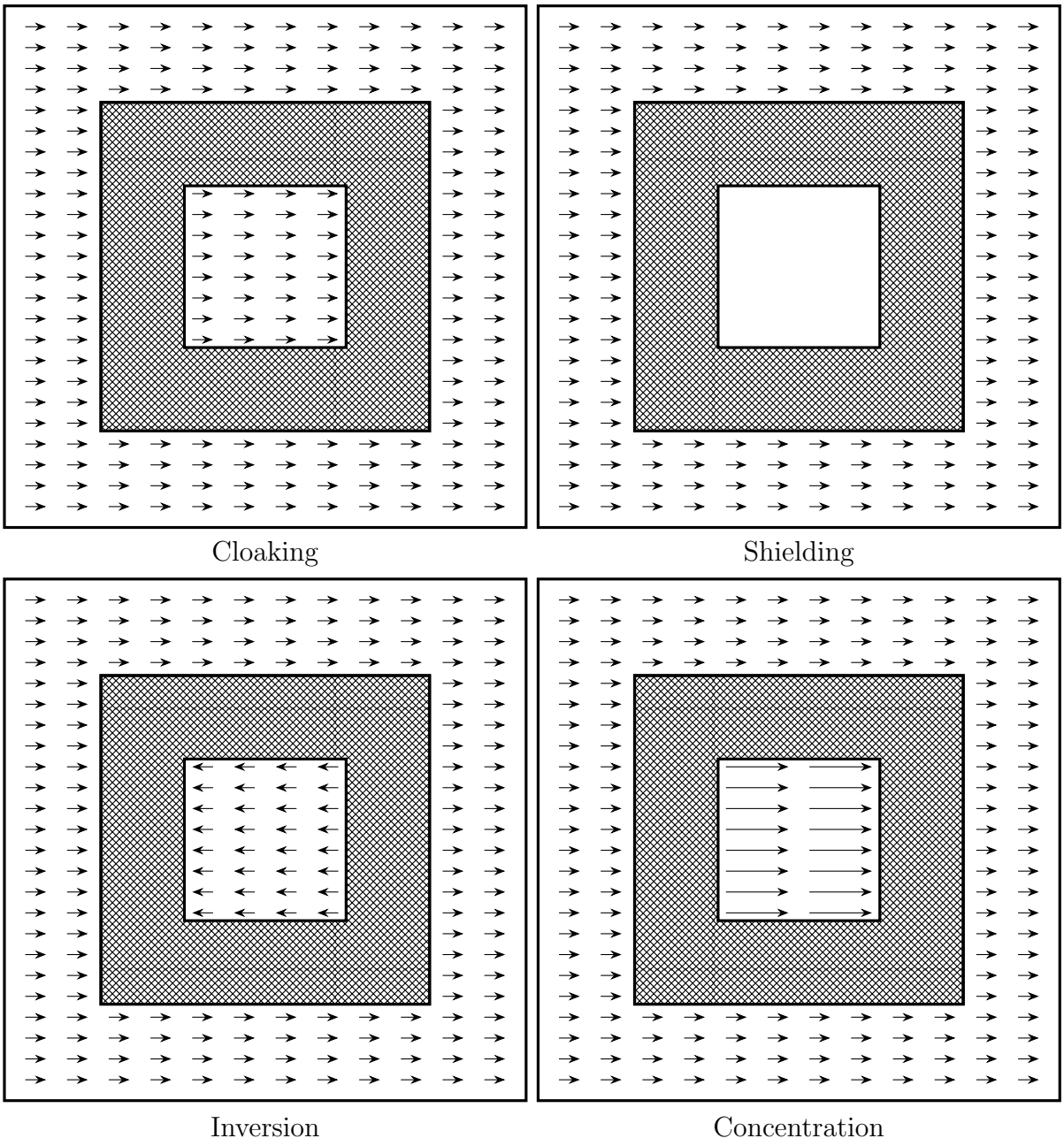

Figure 4.2: Four characteristic cases of heat flow in Narayana's device

Based on the above parameters, it is possible to determine the temperature gradient in the mantle in the absence of a heat flux manipulation device, which is equivalent to a homogeneous mantle:

$$u^0_{,x} = \frac{u_{\text{cold}} - u_{\text{hot}}}{L_x} = -430\,\text{K}\cdot\text{m}^{-1}, \tag{4.2}$$

and the heat flux in the mantle in the absence of a heat flux manipulation device,

$$q^0_x = -\kappa_{\text{agar}} u^0_{,x} = 245.1\,\text{W}\cdot\text{m}^{-2}, \tag{4.3}$$

$$q^0_y = 0 \tag{4.4}$$

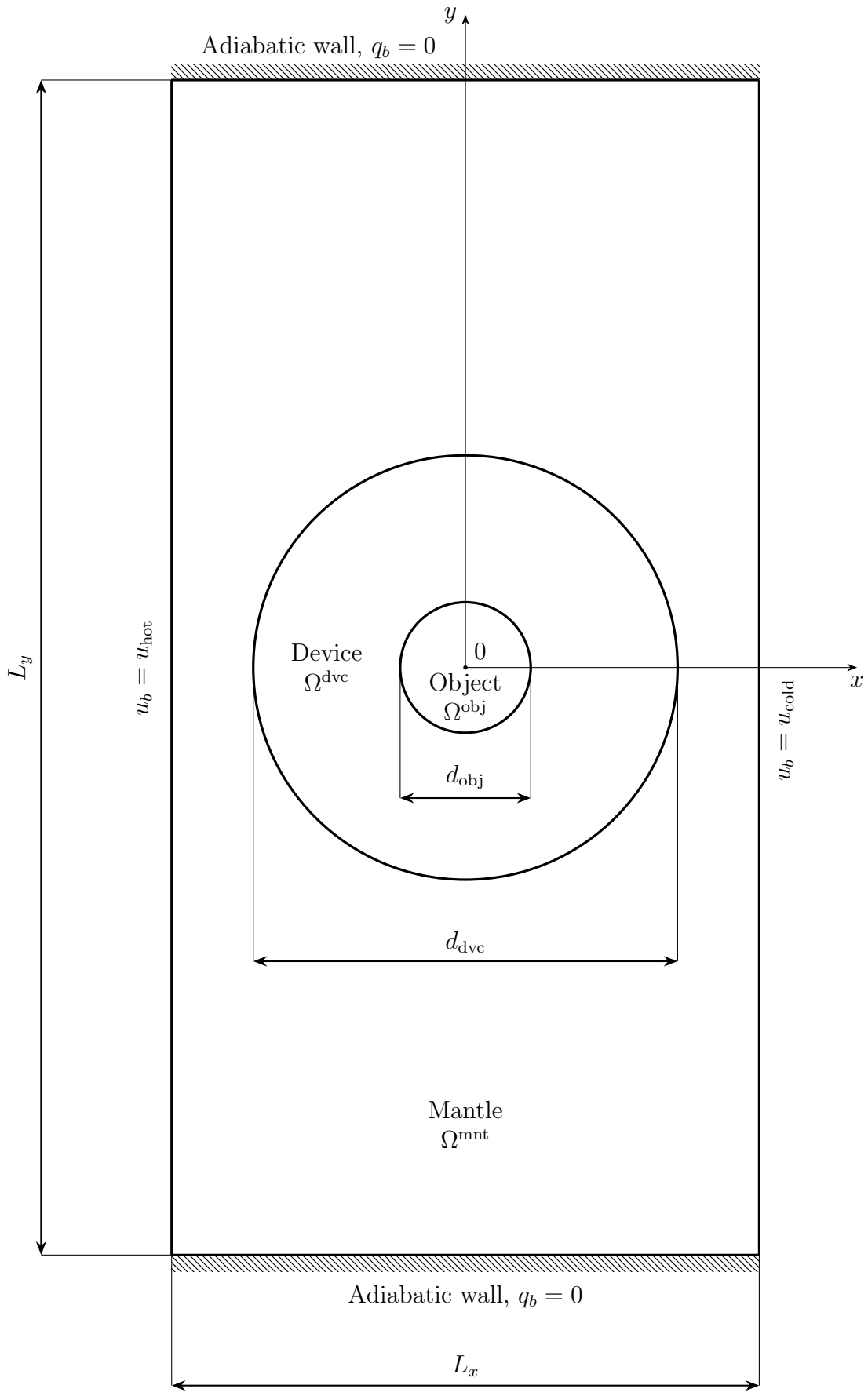

Figure 4.3: Fachinotti's device for heat flux manipulation

4.2 Computational model

4.2.1 Collocation points cloud structure

Numerical calculations using the Kansa method were carried out in the computational domain consisting of a cloud of collocation points, the structure of which together with a sketch of the device is shown in Figure 4.4.

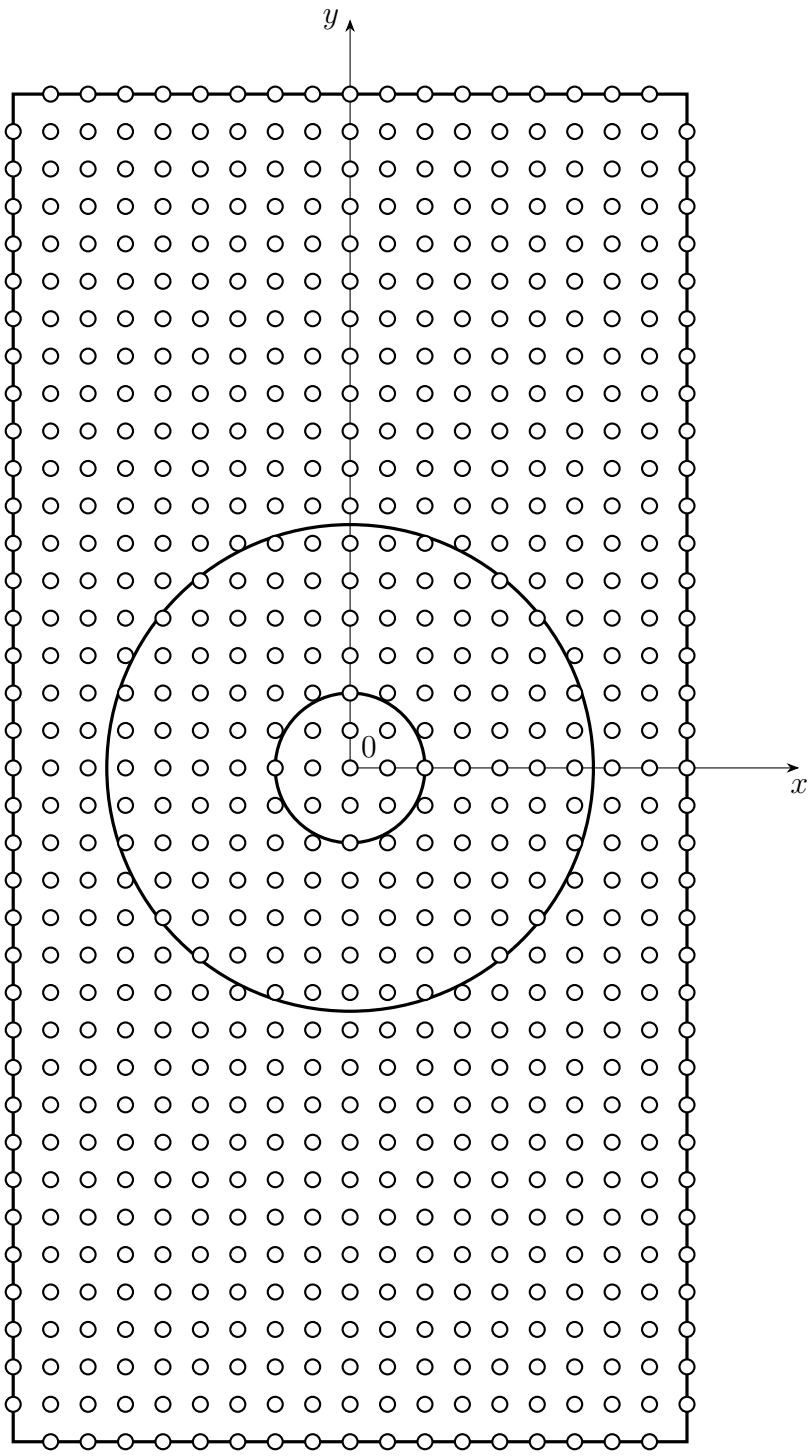

Figure 4.4: The structure of the collocation points cloud used in the optimisation process

As can be seen, the cloud of collocation points shown in Figure 4.4 is regular except that the corner points have been removed to avoid ambiguity in the boundary conditions. The number of collocation points in the cloud n is equal to:

$$n = n_x n_y - 4, \tag{4.5}$$

where n_x and n_y are the numbers of collocation points in each row and column.The total number of collocation points in the cloud has been denoted by n, the number of points in mantle denoted by n^{mnt}, the number of points in the metamaterial device denoted by n^{dvc}, and the number of points in the object denoted by n^{obj}. The numbers of collocation points satisfy:

$$n = n^{\mathrm{mnt}} + n^{\mathrm{dvc}} + n^{\mathrm{obj}}. \tag{4.6}$$

4.2.2 Optimisation problem

After introduction of the Fachinotti's device, it is possible to proceed to the definition of the research problem and the method of its solution. The problem itself is simple to define, one must find such distributions of a thermal conductivity in the metamaterial device to obtain the designed heat flow described earlier. The definition by means of words is very simple, however, is not sufficient to solve the problem and consequently it is necessary to express it in the language of mathematics. The considered problem is the problem of a two-dimensional steady heat flow in a material with spatially variable distributions of thermophysical parameters, given by Equation 3.23:

$$\kappa_{,x} u_{,x} + \kappa_{,y} u_{,y} + \kappa \left(u_{,xx} + u_{,yy} \right) = 0.$$

Equation 3.23 contains derivatives of thermal conductivity which is very undesirable in the approach that was used. Therefore, an equivalent form of Equation 3.23 was used:

$$\left(\kappa u_{,x} \right)_{,x} + \left(\kappa u_{,y} \right)_{,y} = 0. \tag{4.7}$$

After applying the collocation Kansa method, the above equation can be written in a matrix form. It is valid for all collocation points in the considered domain, as in Equation 2.39:

$$\boldsymbol{K}\boldsymbol{u} = \boldsymbol{0}.$$

It was decided to use a pseudospectral approach which allows the stiffness matrix $\boldsymbol{K}$ to be computed using the modified Equation 2.113 for the two-dimensional problem:

$$\boldsymbol{K} = -\left(\boldsymbol{\mathcal{D}}_{,x} \psi\left(\boldsymbol{\kappa}\right) \boldsymbol{\mathcal{D}}_{,x} + \boldsymbol{\mathcal{D}}_{,y} \psi\left(\boldsymbol{\kappa}\right) \boldsymbol{\mathcal{D}}_{,y} \right). \tag{4.8}$$

As can be seen, the difference between Equation 2.113 and Equation 4.8 is the occurrence of the matrix $\psi\left(\boldsymbol{\kappa}\right)$ instead of $\boldsymbol{\kappa}$. Let's discuss these differences more closely. First of all, when considering the heat flux manipulation problem, $\boldsymbol{\kappa}$ denotes a vector containing thermal conductivities at all collocation points:

$$\boldsymbol{\kappa} = \begin{bmatrix} \kappa\left(\boldsymbol{x}_1\right) \\ \kappa\left(\boldsymbol{x}_2\right) \\ \vdots \\ \kappa\left(\boldsymbol{x}_n\right) \end{bmatrix}, \tag{4.9}$$

The operator $\psi(\cdot)$ denotes creation of a diagonal matrix on the basis of the vector of thermal conductivity values in collocation points $\boldsymbol{\kappa}$. This operation is equivalent to the following operation:

$$\psi(\boldsymbol{\kappa}) = \left(\boldsymbol{\kappa}\mathbf{1}^T\right) \circ \boldsymbol{I} \tag{4.10}$$

where:

$$\mathbf{1} = \begin{bmatrix} 1 \\ 1 \\ \vdots \\ 1 \end{bmatrix}, \tag{4.11}$$

and $\circ$ is Hadamard product [75]. The vector $\mathbf{1}$ and the matrix $\boldsymbol{I}$ in this case have a dimension of $n \times 1$ and $n \times n$, respectively. Substituting Equation 4.8 to 2.39 and imposing boundary conditions creates an Equation of state 2.44 of the considered problem:

$$\bar{\boldsymbol{A}}\boldsymbol{u} = \bar{\boldsymbol{b}}.$$

The problem of manipulating the heat flux in the object region Ω^{obj} is equivalent to minimizing the following objective function f, which describes the mean squared error of the deviation between the obtained heat flux vector and the heat flux vector assumed in the design process:

$$f = \sqrt{\left(\boldsymbol{q}_x^{\text{obj}} - \boldsymbol{q}_x^0\right)^T \boldsymbol{W} \left(\boldsymbol{q}_x^{\text{obj}} - \boldsymbol{q}_x^0\right) + \left(\boldsymbol{q}_y^{\text{obj}} - \boldsymbol{q}_y^0\right)^T \boldsymbol{W} \left(\boldsymbol{q}_y^{\text{obj}} - \boldsymbol{q}_y^0\right)}, \tag{4.12}$$

where $\boldsymbol{q}_x^{\text{obj}}$, $\boldsymbol{q}_y^{\text{obj}}$ are vectors containing heat flux components in the x and y direction for the collocation points belonging to the object region Ω^{obj}, while $\boldsymbol{q}_x^0$, $\boldsymbol{q}_y^0$ are vectors containing desired heat flux components in the x and y direction for the collocation points belonging to the object region Ω^{obj}, the values of which were assumed in the design process. It was assumed in the work that:

$$\boldsymbol{q}_x^0 = \zeta q_x^0 \mathbf{1}, \tag{4.13}$$

$$\boldsymbol{q}_y^0 = \mathbf{0}, \tag{4.14}$$

where ζ is the heat flux manipulation parameter that takes a value depending on the considered heat flow problem:

- $\zeta = -1$ for inversion,
- $\zeta = 0$ for shielding,
- $\zeta = 1$ for cloaking,
- $\zeta > 1$ for concentration,

and $\boldsymbol{W}$ is the $n^{\mathrm{obj}} \times n^{\mathrm{obj}}$ diagonal weight matrix:

$$\boldsymbol{W} = \frac{1}{n^{\mathrm{obj}}}\boldsymbol{I}. \tag{4.15}$$

The vector $\mathbf{1}$ and the matrix $\boldsymbol{I}$ in this case have a dimension of $n^{\mathrm{obj}} \times 1$ and $n^{\mathrm{obj}} \times n^{\mathrm{obj}}$, respectively, which is different than dimension of the vector $\mathbf{1}$ in Equation 4.10. If the design variable is the value of thermal conductivity in the device region Ω^{dvc}, it can be parametrized using the so-called artificial density ϱ that ranges from 0 to 1 [47]:

$$\forall \boldsymbol{x}_i \in \Omega^{\mathrm{dvc}} : \kappa_i = \kappa_{\min} + (\varrho_i)^g \left(\kappa_{\max} - \kappa_{\min}\right), \tag{4.16}$$

where $i = 1, ..., n^{\mathrm{dvc}}$. Why was it decided to parametrize the thermal conductivity? Without the application of appropriate constraints, the values of thermal conductivity at the collocation points could reach any values, even those that are non-physical and not represented by any existing material. To avoid this, a limitation is placed on the value of the thermal conductivity so that at any point of the device it is not lower than a certain minimum value $\kappa_{\min}$ and not greater than a certain maximum value $\kappa_{\max}$. By choosing $g \geq 3$ [47], ϱ is compelled to tend to either 0 or 1, i.e., the material at the device is forced to be either that of conductivity $\kappa_{\min}$ or that of conductivity $\kappa_{\max}$, respectively, instead of a mixture of them. This is of great importance because the resulting distribution of thermal conductivity in the device can be well approximated with a composition of only two materials and thus the actual device can be created using only two materials. The device will be fabricated using copper and polymethyl methacrylate, having conductivities $\kappa_{\max} = 403\,\mathrm{W} \cdot \mathrm{m}^{-1} \cdot \mathrm{K}^{-1}$ and $\kappa_{\min} = 0.22\,\mathrm{W} \cdot \mathrm{m}^{-1} \cdot \mathrm{K}^{-1}$, respectively [47]. The parameterization described by Equation 4.16 is an example of an approach called Solid Isotropic Material with Penalization used in the topological optimisation [13]. After defining the objective function f, the following optimisation problem with equality constraints in the form of Equation of state 2.44 can be posed:

$$\begin{aligned} &\boldsymbol{\varrho}^{\mathrm{opt}} = \arg \min_{\boldsymbol{\varrho} \in \mathbb{R}^{n^{\mathrm{dvc}}}} f(\boldsymbol{\varrho}) \\ &\text{s.t.} \begin{cases} \bar{\boldsymbol{A}}(\boldsymbol{\varrho})\,\boldsymbol{u}(\boldsymbol{\varrho}) = \bar{\boldsymbol{b}} \\ \forall i \in 1, ..., n^{\mathrm{dvc}} : 0 \leq \varrho_i \leq 1 \end{cases} \end{aligned} \tag{4.17}$$

Using the Lagrange method for the conditional extreme problem [74], the constrained problem described by Equation 4.17 can be transformed to an unconstrained optimisation problem in the following form:

$$\begin{aligned} &\boldsymbol{\varrho}^{\mathrm{opt}} = \min_{\boldsymbol{\varrho} \in \mathbb{R}^{n^{\mathrm{dvc}}}} \ell(\boldsymbol{\varrho}) \\ &\text{s.t. } \forall i \in 1, ..., n^{\mathrm{dvc}} : 0 \leq \varrho_i \leq 1, \end{aligned} \tag{4.18}$$

where only box constrains are given. The Lagrangian $\ell(\boldsymbol{\varrho})$ has the following form:

$$\ell(\boldsymbol{\varrho}) = f(\boldsymbol{\varrho}) - \boldsymbol{\lambda}^T \left(\bar{\boldsymbol{A}}(\boldsymbol{\varrho})\,\boldsymbol{u}(\boldsymbol{\varrho}) - \bar{\boldsymbol{b}}\right), \tag{4.19}$$

where $\boldsymbol{\lambda}$ is the Lagrange multipliers vector. Due to the fact that $n^{\mathrm{dvc}} \gg 1$, which means that the number of design variables is large, it was decided to solve the problem described by Equation 4.18 using the gradient optimisation method. For this purpose, the gradient of the objective function was analytically calculated using the adjoint state method [86].

The derivative of Lagrangian 4.19 with respect to the component of design variables vector is as follows:

$$\frac{\partial \ell}{\partial \varrho_i} = \left.\frac{\partial f}{\partial \varrho_i}\right|_{\boldsymbol{u}=\text{const}} + \frac{\partial f}{\partial \boldsymbol{u}}\frac{\partial \boldsymbol{u}}{\partial \varrho_i} - \boldsymbol{\lambda}^T\left(\frac{\partial \bar{\boldsymbol{A}}}{\partial \varrho_i}\boldsymbol{u} + \bar{\boldsymbol{A}}\frac{\partial \boldsymbol{u}}{\partial \varrho_i}\right). \tag{4.20}$$

In Equation 4.20, the rules of matrix calculus [110] were used, which gives the appropriate sizes of matrix derivatives and vectors with respect to the vector components of design variables. For example, matrix $\frac{\partial f}{\partial \boldsymbol{u}}$ is $1 \times n$ and $\frac{\partial \boldsymbol{u}}{\partial \varrho_i}$ is $n \times 1$. Rearranging Equation 4.20 leads to:

$$\frac{\partial \ell}{\partial \varrho_i} = \left.\frac{\partial f}{\partial \varrho_i}\right|_{\boldsymbol{u}=\text{const}} + \left(\frac{\partial f}{\partial \boldsymbol{u}} - \boldsymbol{\lambda}^T\bar{\boldsymbol{A}}\right)\frac{\partial \boldsymbol{u}}{\partial \varrho_i} - \boldsymbol{\lambda}^T\frac{\partial \bar{\boldsymbol{A}}}{\partial \varrho_i}\boldsymbol{u}. \tag{4.21}$$

Computing the derivatives of the temperature field vector with respect to the components of the design variables vector $\frac{\partial \boldsymbol{u}}{\partial \varrho_i}$ is an extremely computationally expensive operation. This problem can be solved by assuming that the following term is equal to 0:

$$\frac{\partial f}{\partial \boldsymbol{u}} - \boldsymbol{\lambda}^T\bar{\boldsymbol{A}} = \boldsymbol{0}^T. \tag{4.22}$$

Solving Equation 4.22 for $\boldsymbol{\lambda}$ leads to:

$$\boldsymbol{\lambda} = \bar{\boldsymbol{A}}^{-T}\left(\frac{\partial f}{\partial \boldsymbol{u}}\right)^T. \tag{4.23}$$

Finally, Equation 4.21 simplifies to:

$$\frac{\partial \ell}{\partial \varrho_i} = \left.\frac{\partial f}{\partial \varrho_i}\right|_{\boldsymbol{u}=\text{const}} - \boldsymbol{\lambda}^T\frac{\partial \bar{\boldsymbol{A}}}{\partial \varrho_i}\boldsymbol{u}. \tag{4.24}$$

The calculation of the Lagrangian derivative described by Equation 4.24 requires the calculation of three derivatives: $\left.\frac{\partial f}{\partial \varrho_i}\right|_{\boldsymbol{u}=\text{const}}$, $\frac{\partial f}{\partial \boldsymbol{u}}$, and $\frac{\partial \bar{\boldsymbol{A}}}{\partial \varrho_i}$. In order to provide a recipe for their calculation, one should use the fact that in the Kansa method in the pseudospectral formulation, the components of the heat flux vector for the collocation points in the object can be calculated as:

$$\boldsymbol{q}_x^{\text{obj}}(\boldsymbol{\varrho}) = -\boldsymbol{Y}\psi(\boldsymbol{\kappa}(\boldsymbol{\varrho}))\boldsymbol{\mathcal{D}}_{,x}\boldsymbol{u}(\boldsymbol{\varrho}) \tag{4.25}$$

$$\boldsymbol{q}_y^{\text{obj}}(\boldsymbol{\varrho}) = -\boldsymbol{Y}\psi(\boldsymbol{\kappa}(\boldsymbol{\varrho}))\boldsymbol{\mathcal{D}}_{,y}\boldsymbol{u}(\boldsymbol{\varrho}) \tag{4.26}$$

where $\boldsymbol{Y}$ is $n^{\text{obj}} \times n$ output matrix composed of the rows of the $n \times n$ identity matrix, which corresponds to the collocation points in the object region Ω^{obj}. Consequently, $\left.\frac{\partial f}{\partial \varrho_i}\right|_{\boldsymbol{u}=\text{const}}$

can be computed as follows:

$$\left.\frac{\partial f}{\partial \varrho_i}\right|_{\boldsymbol{u}=\text{const}} = -\frac{1}{f}\left(\boldsymbol{q}_x^{\text{obj}}(\boldsymbol{\varrho}) - \boldsymbol{q}_x^0\right)^T \boldsymbol{W}\boldsymbol{Y}\psi\left(\frac{\partial \boldsymbol{\kappa}(\boldsymbol{\varrho})}{\partial \varrho_i}\right)\boldsymbol{\mathcal{D}}_{,x}\boldsymbol{u} + \\ -\frac{1}{f}\left(\boldsymbol{q}_y^{\text{obj}}(\boldsymbol{\varrho}) - \boldsymbol{q}_y^0\right)^T \boldsymbol{W}\boldsymbol{Y}\psi\left(\frac{\partial \boldsymbol{\kappa}(\boldsymbol{\varrho})}{\partial \varrho_i}\right)\boldsymbol{\mathcal{D}}_{,y}\boldsymbol{u} \tag{4.27}$$

where:

$$\frac{\partial \boldsymbol{\kappa}(\boldsymbol{\varrho})}{\partial \varrho_i} = \begin{cases} g(\varrho_i)^{g-1}(\kappa_{\max} - \kappa_{\min}) & \text{if } \boldsymbol{x}_i \in \Omega^{\text{dvc}} \\ 0 & \text{otherwise} \end{cases}. \tag{4.28}$$

$\dfrac{\partial f}{\partial \boldsymbol{u}}$ can be computed as follows:

$$\frac{\partial f}{\partial \boldsymbol{u}} = -\frac{1}{f}\left(\boldsymbol{q}_x^{\text{obj}}(\boldsymbol{\varrho}) - \boldsymbol{q}_x^0\right)^T \boldsymbol{W}\boldsymbol{Y}\psi(\boldsymbol{\kappa}(\boldsymbol{\varrho}))\boldsymbol{\mathcal{D}}_{,x} + \\ -\frac{1}{f}\left(\boldsymbol{q}_y^{\text{obj}}(\boldsymbol{\varrho}) - \boldsymbol{q}_y^0\right)^T \boldsymbol{W}\boldsymbol{Y}\psi(\boldsymbol{\kappa}(\boldsymbol{\varrho}))\boldsymbol{\mathcal{D}}_{,y} \tag{4.29}$$

while $\dfrac{\partial \bar{\boldsymbol{A}}}{\partial \varrho_i}$ as follows:

$$\frac{\partial \bar{\boldsymbol{A}}}{\partial \varrho_i} = \boldsymbol{\mathcal{D}}_{,x}\psi\left(\frac{\partial \boldsymbol{\kappa}(\boldsymbol{\varrho})}{\partial \varrho_i}\right)\boldsymbol{\mathcal{D}}_{,x} + \boldsymbol{\mathcal{D}}_{,y}\psi\left(\frac{\partial \boldsymbol{\kappa}(\boldsymbol{\varrho})}{\partial \varrho_i}\right)\boldsymbol{\mathcal{D}}_{,y}. \tag{4.30}$$

When performing the operation of calculating $\dfrac{\partial \bar{\boldsymbol{A}}}{\partial \varrho_i}$, it must be remembered that the rows of this matrix corresponding to the boundary points on which the boundary conditions are imposed are zero-rows. To ensure a stable optimisation process and to avoid checkerboard solutions, two different types of filtration have been used [124]:

- spatial filtration of the design variable, i.e. the artificial density vector $\boldsymbol{\varrho}$,
- spatial filtration of the objective function gradient with respect to the vector of design variables $\dfrac{\partial \ell}{\partial \boldsymbol{\varrho}}$.

A linear filter was used as the artificial density filter, so that the filtering operation is given by a linear transform of the form $\bar{\boldsymbol{\varrho}} = \boldsymbol{\varrho}\boldsymbol{H}$ where $\bar{\boldsymbol{\varrho}}$ is the artificial density row vector after filtration. The filter matrix $\boldsymbol{H}$ has the following form:

$$H_{e,j} = \frac{\max(0, r - \delta_{e,j})}{\sum_{i=1}^{n^{\text{dvc}}} \max(0, r - \delta_{e,i})}, \quad e, j \in \{1, 2 \ldots n^{\text{dvc}}\} \tag{4.31}$$

where $\delta_{e,i}$ is the Euclidean distance between the collocation points in the device region Ω^{dvc}:

$$\delta_{e,i} = ||\boldsymbol{x}_e - \boldsymbol{x}_i||, \tag{4.32}$$

and r is the filter radius:

$$r = mr_{\min}, \tag{4.33}$$

where m is a real number and $r_{\min}$ is the minimum distance between collocation points in the device region Ω^{dvc}. The boundary problem is solved in an approximate manner for the artificial density after the filtration process, hence the gradient of the objective function with respect to the original variable is calculated as follows:

$$\frac{\partial \bar{\ell}\left(\boldsymbol{\varrho}\right)}{\partial \boldsymbol{\varrho}} = \frac{\partial \ell\left(\bar{\boldsymbol{\varrho}}\right)}{\partial \bar{\boldsymbol{\varrho}}} \boldsymbol{H}. \tag{4.34}$$

Filtering the gradient vector described by Equation 4.34 is performed using a new filter:

$$\frac{\partial \breve{\ell}\left(\boldsymbol{\varrho}\right)}{\partial \boldsymbol{\varrho}} = \left(\bar{\boldsymbol{\varrho}} \circ \frac{\partial \bar{\ell}\left(\boldsymbol{\varrho}\right)}{\partial \boldsymbol{\varrho}}\right) \boldsymbol{H} \bar{\boldsymbol{W}}, \tag{4.35}$$

where weight matrix $\bar{\boldsymbol{W}}$ has the following form:

$$\bar{\boldsymbol{W}} = \left[\psi\left(\max\left(s, \bar{\boldsymbol{\varrho}}\right)\right)\right]^{-1}. \tag{4.36}$$

$s = 0.001$ is regularization constant [154]. The interior-point method was used in the optimisation process [167].

4.3 Results and discussion

4.3.1 Convergence study

After presenting the fundamental concepts of heat flux manipulation devices and optimisation problems related to them, it is possible to go on to the simulations. Naturally, the first step was a convergence study. The study was carried out for the cloaking test case for which the heat flux manipulation parameter is $\zeta = 1$. The parameters of the collocation point clouds and the corresponding good value of the shape parameters $\varepsilon_{\text{good}}$ are summarized in Table 4.1.

Number of collocation points n	n_{device}	n_{object}	n_{mantle}	$\varepsilon_{\text{good}}$
388	68	4	316	0.023
574	96	12	466	0.021
796	136	16	644	0.0193
964	168	16	780	0.015
1148	192	24	932	0.0147

Table 4.1: Collocation point clouds parameters and shape parameter values used in the convergence study

The results obtained using the above clouds may have insufficient spatial resolution to perform visual qualitative analysis. Therefore, the obtained optimal artificial density, temperature and heat flux fields were interpolated to higher resolutions. It should be emphasized that the interpolated data was used only for visualization and not for further

calculations. The grid on which the artificial density fields were interpolated is a cylindrical grid consisting of $125 \times 20 = 2500$ points. The grid on which the temperature and heat flux fields were interpolated is a Cartesian grid consisting of $35 \times 70 = 2450$ points. The starting density distribution in the iterative optimisation process is a uniform distribution and the value at each collocation point in the device region Ω^{dvc} is $\varrho_i = 0.5$. The value of the spatial filter multiplier m is 2.

Objective function It seems that the most obvious measure to be investigated in the convergence study is the objective function f and the number of he number of iterations in the optimisation process. Figure 4.5 shows the optimal value of the objective function f and the number of iterations in the optimisation process as a functions of the number of collocation points.

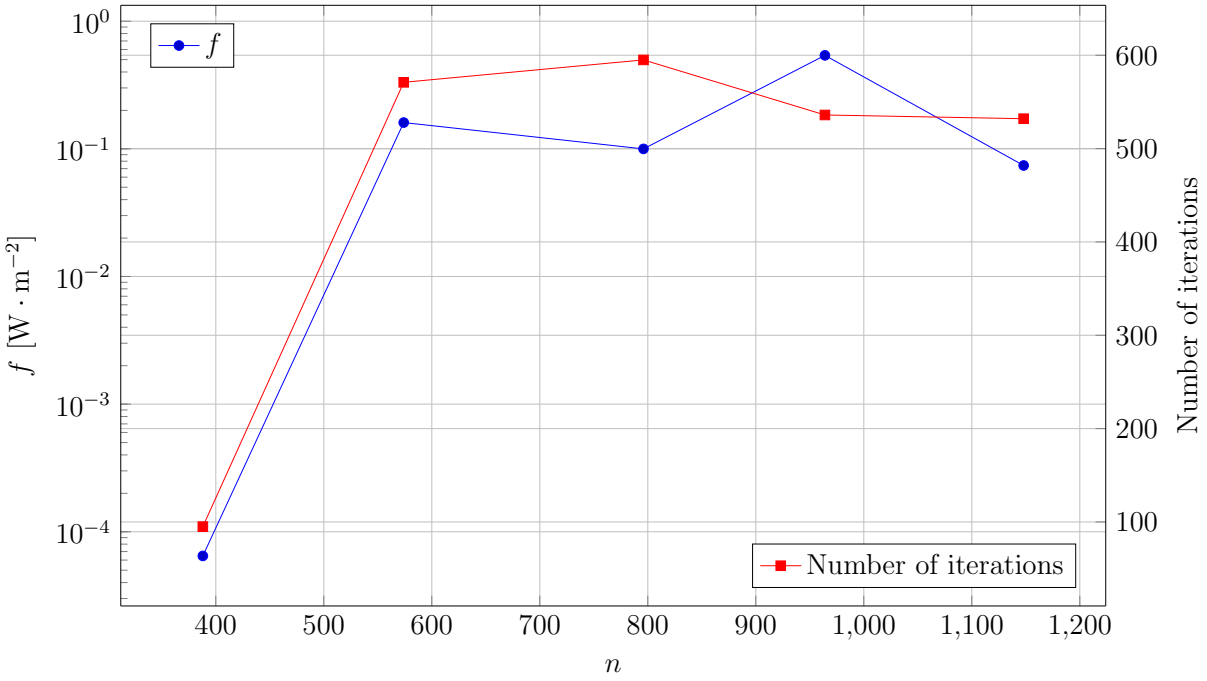

Figure 4.5: The optimal value of the objective function f and the number of iterations as a function of the number of collocation points n

The results presented in Figure 4.5 should be interpreted with great caution. By examining only the objective function and the number of iterations, it can be concluded that the best results are obtained for the simulation with the lowest number of collocation points for which the lowest value of the objective function and the smallest number of iterations are obtained. However, such a situation seems to be incorrect. The reason for this is probably that the low number of collocation points makes the problem numerically easier because the number of design variables and points at which the objective function is calculated is smaller as well as the strong gradients of the temperature field are not well simulated. Consequently, getting a low value for the objective function and small number of iterations is relatively easy. On the other hand, the consequence of this may be the low quality of the solution in the computational domain as a whole and not just in the object. In order to investigate this problem in more detail, it is necessary to examine the artificial density, temperature and heat flux fields.

Artificial density fields Artificial density fields were analysed first. Figures 4.8 - 4.10 show the optimal artificial density fields in the device for the clouds consisting of 388, 574, 796, 964, and 1148 collocation points, respectively.

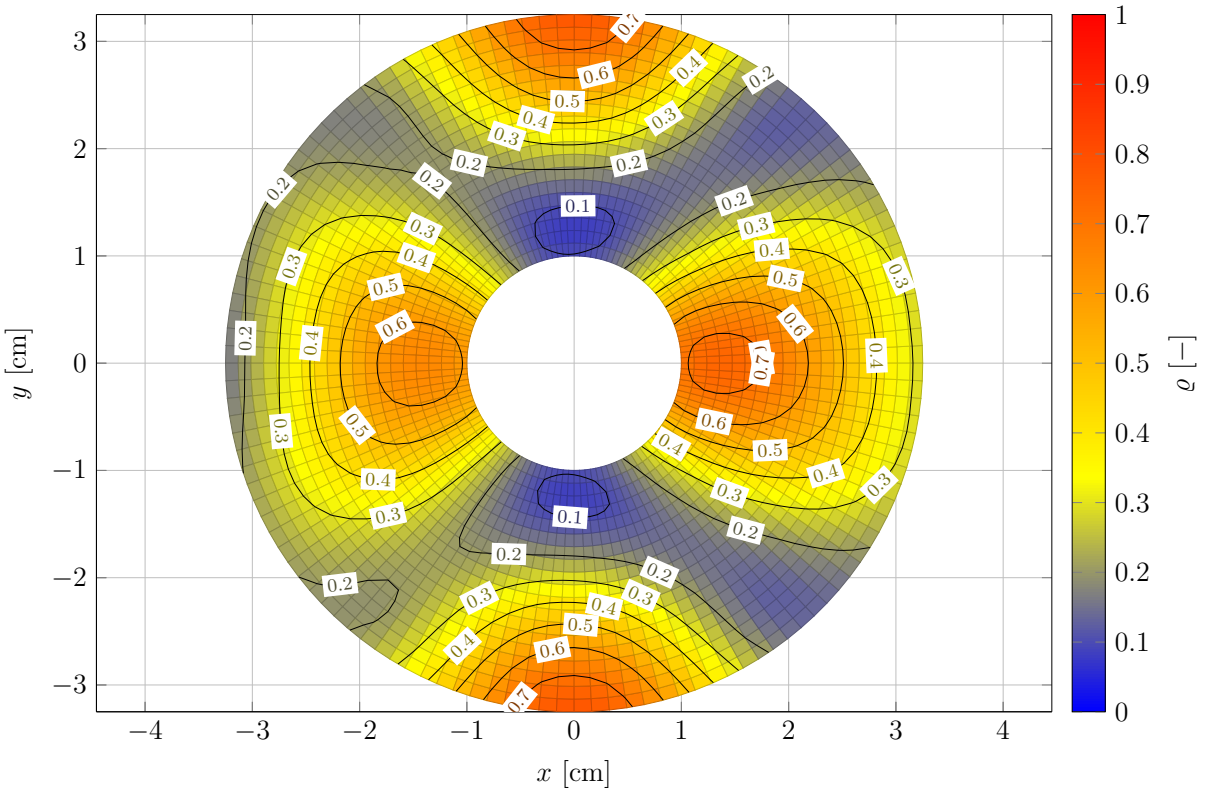

Figure 4.6: The optimal artificial density field for 388 collocation points

Figures 4.6 - 4.10 leads to the following conclusions. First of all, it is visible that all distributions are very symmetrical about the horizontal axis. It is also clearly visible that as the cloud density increases, symmetry appears along the vertical axis. This symmetry appears for 964 collocation points, but for 1148 collocation points it is already very clear. In the reference studies [47], the obtained artificial density distributions were symmetrical, therefore it is assumed that the symmetry is an extremely important parameter indicating the quality of the solution. Therefore, it can be preliminary concluded that cloud consisting of 1148 collocation points is appropriately dense to be used in further simulations. However, to confirm this preliminary conclusion, it is necessary to study the temperature and heat flux fields.

Temperature and heat flux fields Figures 4.11 - 4.15 show the optimal temperature and heat flux fields in the entire device for the clouds consisting of 388, 574, 796, 964, and 1148 collocation points, respectively.

It is clearly visible that only the clouds consisting of 964 and 1148 collocation points gave relatively smooth and regular isotherms as well as an orderly, non-chaotic distribution of the heat flux in the entire device. It is also worth noting that for the two coarsest clouds, a clear deviation of the heat flux is visible in the vicinity of the boundary between the object and the device. From the point of view of temperature field and heat flux analysis, the two most promising clouds are those consting od 964 and 1148 collocation points.

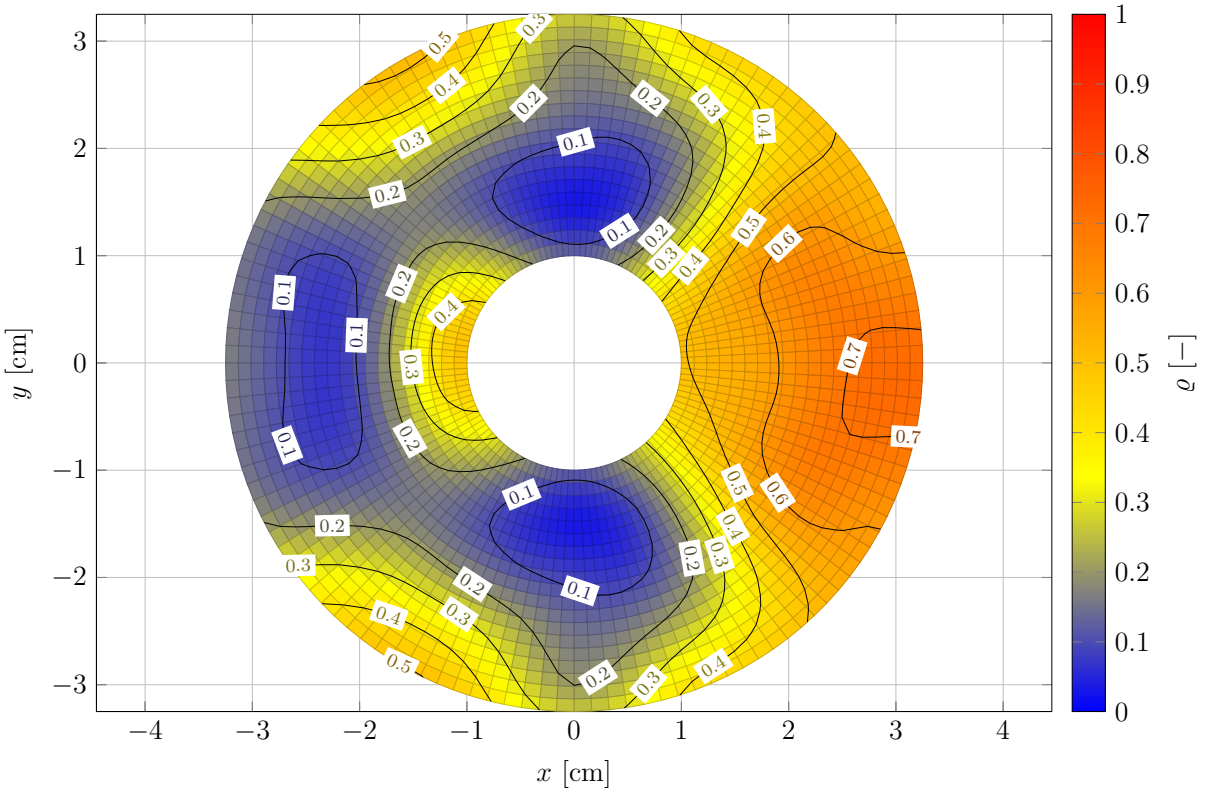

Figure 4.7: The optimal artificial density field for 574 collocation points

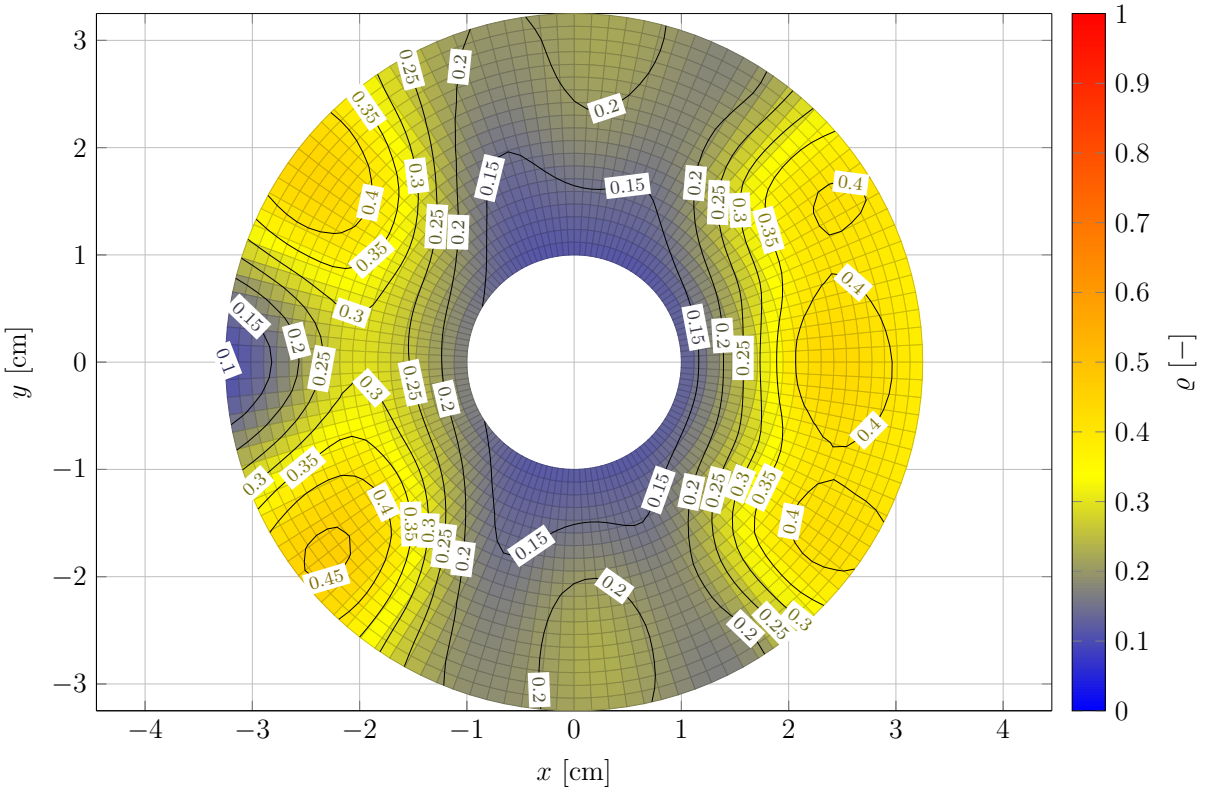

Figure 4.8: The optimal artificial density field for 796 collocation points

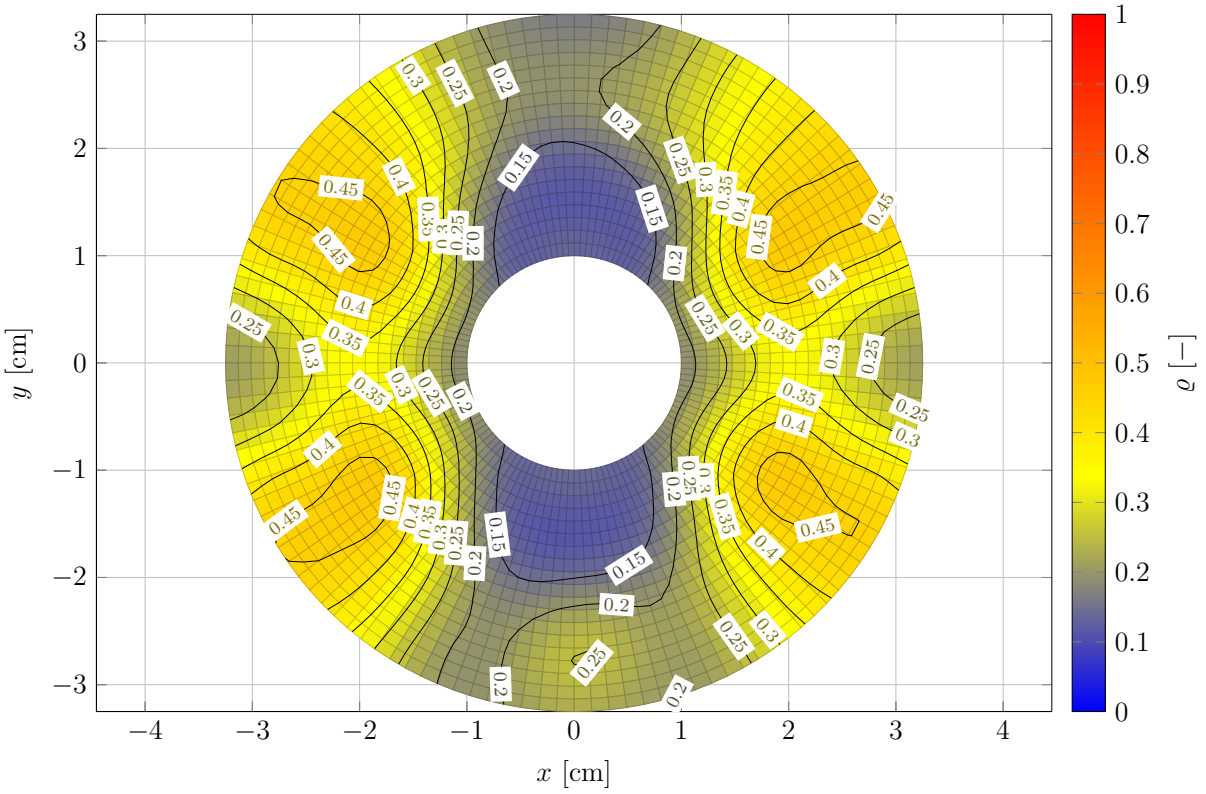

Figure 4.9: The optimal artificial density field for 964 collocation points

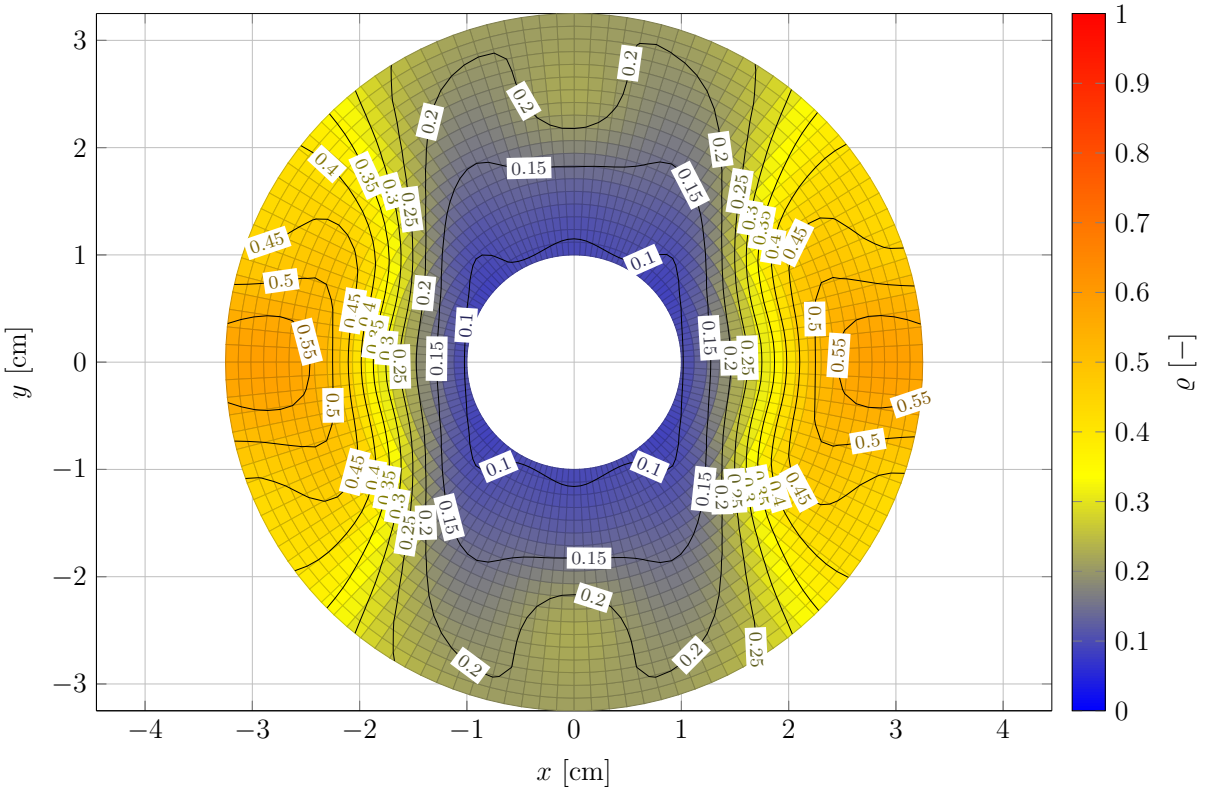

Figure 4.10: The optimal artificial density field for 1148 collocation points

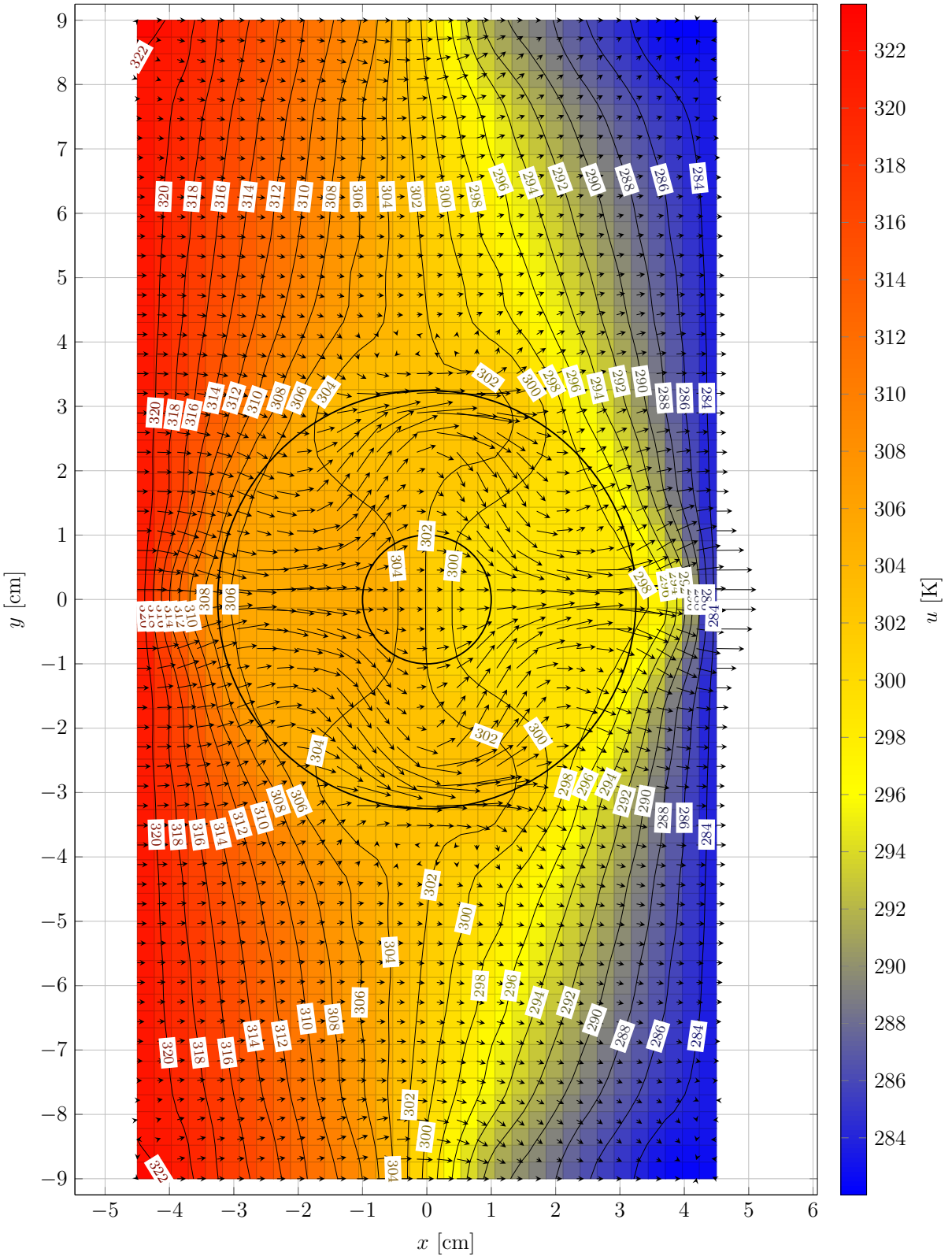

Figure 4.11: The optimal temperature and heat flux fields for 388 collocation points

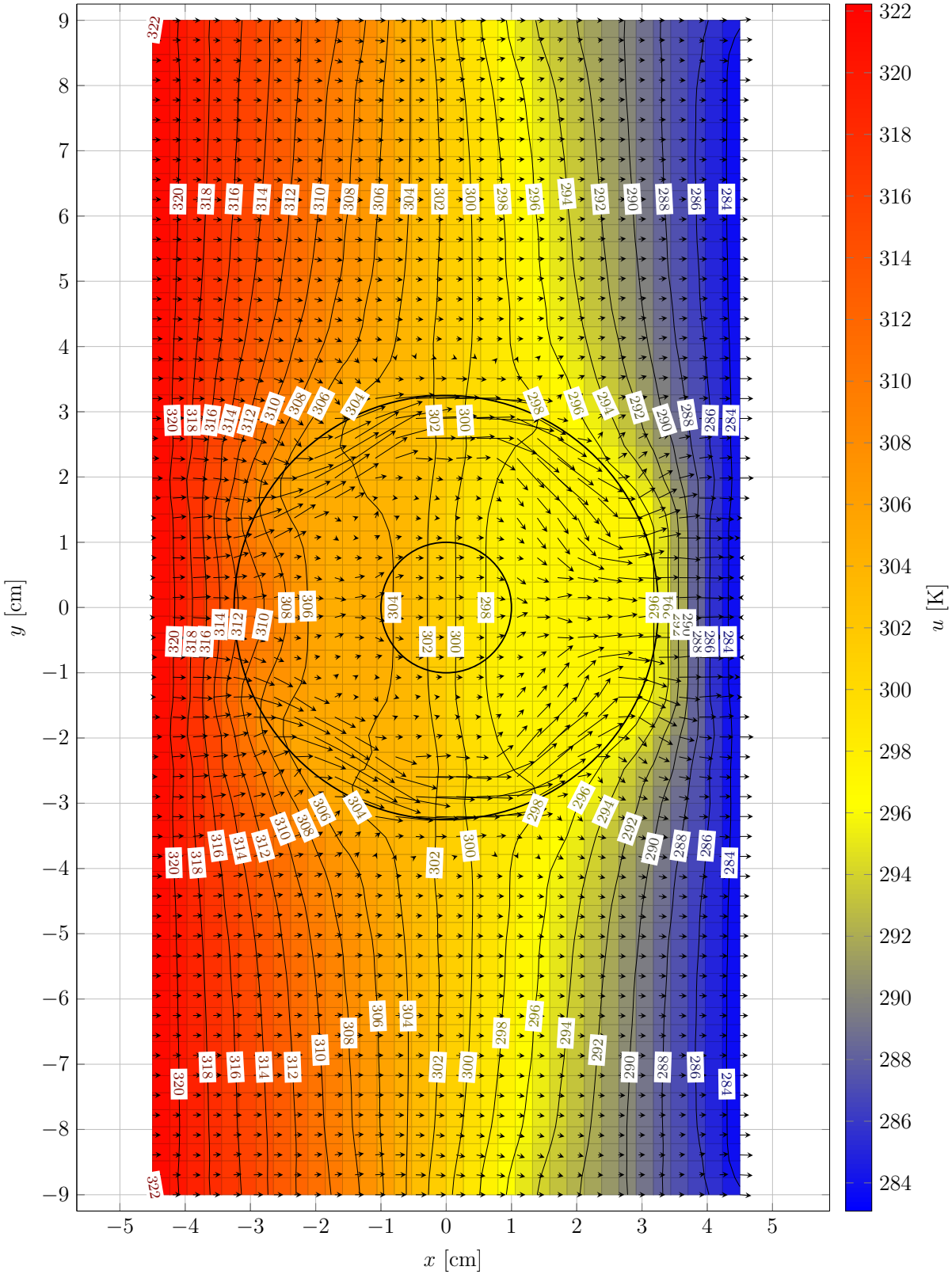

Figure 4.12: The optimal temperature and heat flux fields for 574 collocation points

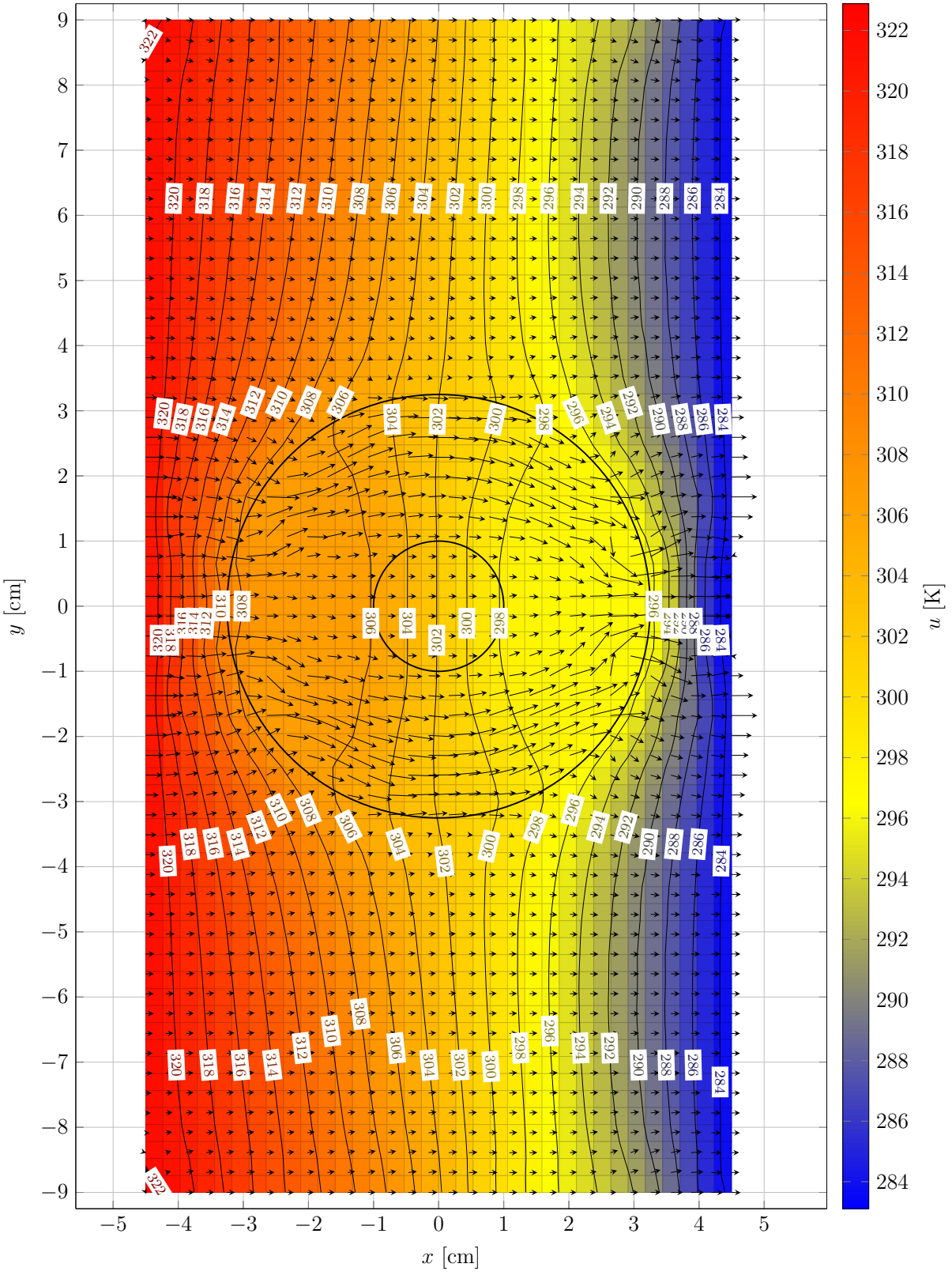

Figure 4.13: The optimal temperature and heat flux fields for 796 collocation points

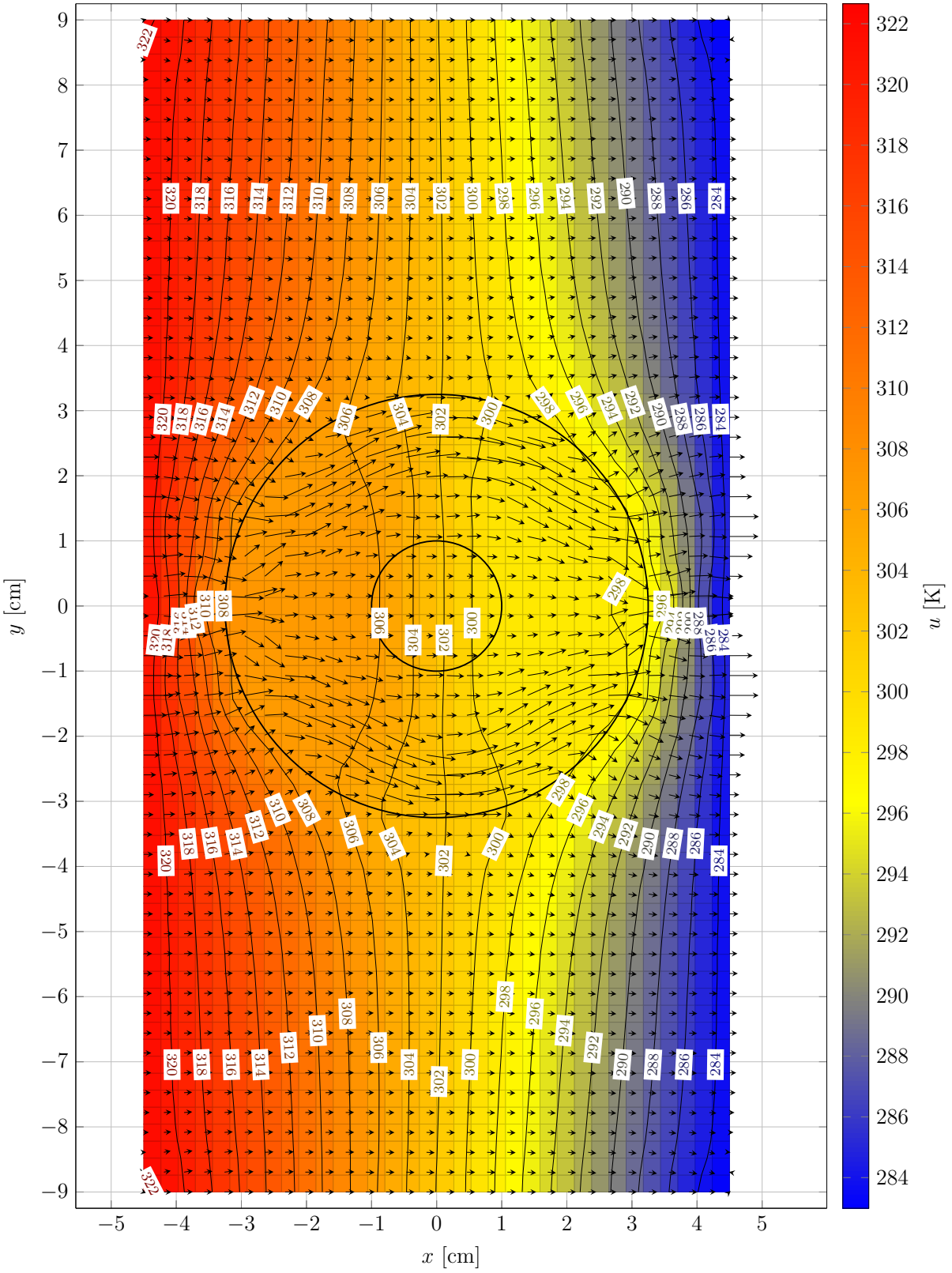

Figure 4.14: The optimal temperature and heat flux fields for 964 collocation points

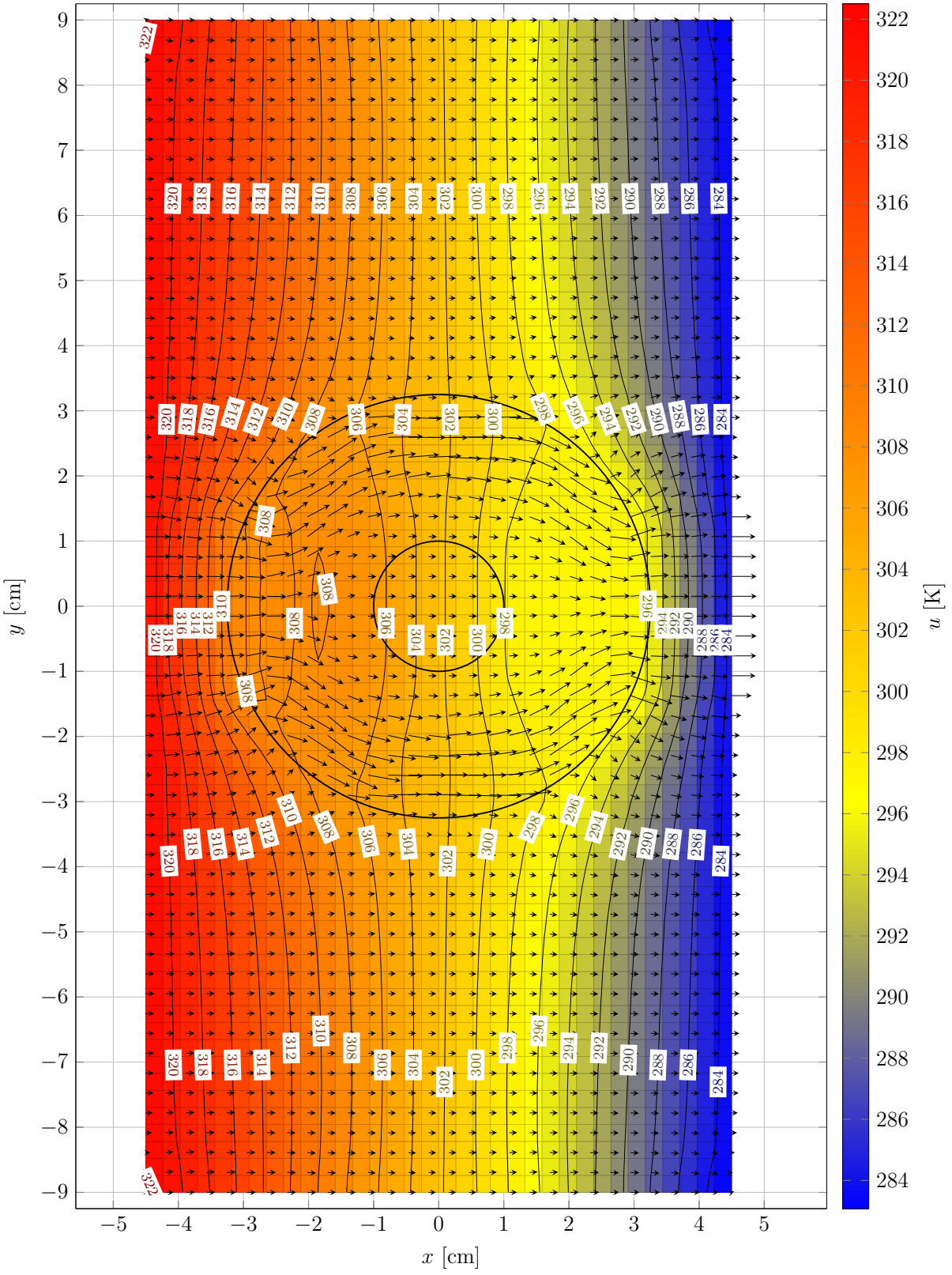

Figure 4.15: The optimal temperature and heat flux fields for 1148 collocation points

Conclusions By collecting together the conclusions drawn on the basis of all three subanalysis, namely the value of the objective function, the optimal distribution of the artificial density as well as temperature and heat flux fields, it was decided that the cloud used in further simulations would be cloud consisting of 1148 collocation points.

4.3.2 Influence of spatial filter multiplier

A study almost as important as the convergence is that of the spatial filter multiplier m. In the convergence study, the value of $m = 2$ was used, but it was an empirical choice, now it will be examined whether it was right. As part of this study, a series of simulations using the cloud consisting of 1148 collocation points were performed for different multiplier m values. The initial density distribution in the iterative optimisation process is an uniform distribution and the value at each collocation point in the device is $\varrho_i = 0.5$.

Objective function Figure 4.16 shows the optimal value of the objective function and the number of iterations for the value of the spatial filter multiplier m equal to 1, 2, 3 and 4.

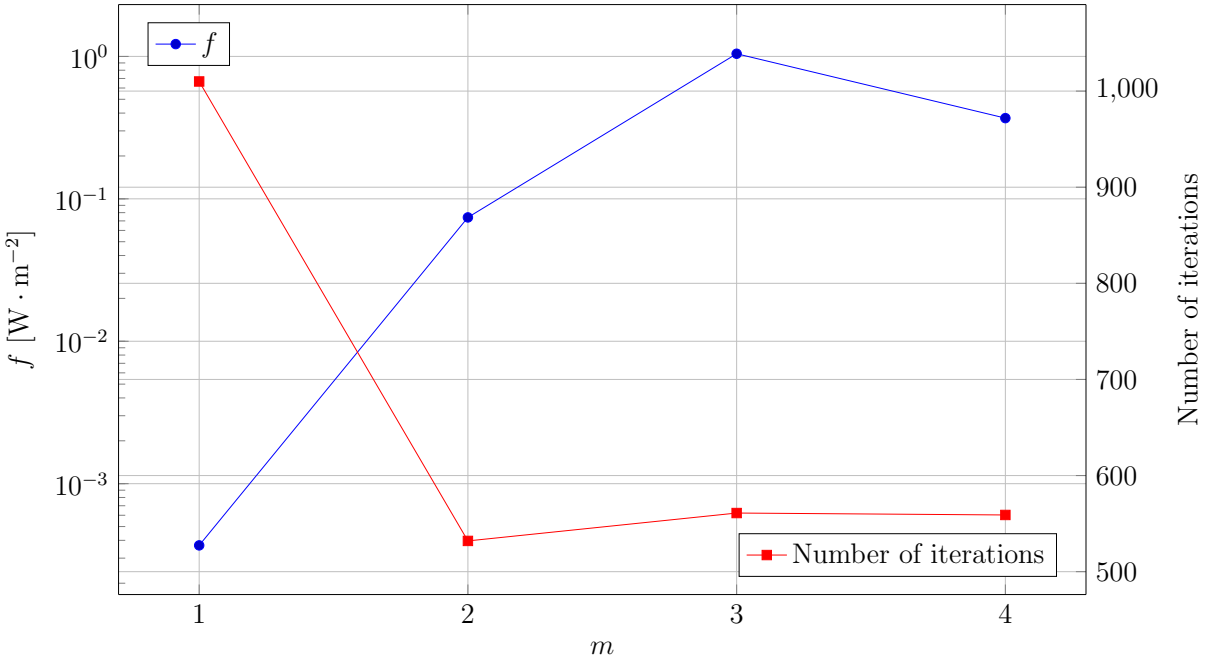

Figure 4.16: The optimal value of the objective function f and the number of iterations as a function of the spatial filter multiplier m

The results presented in Figure 4.16 should be interpreted, as in the convergence study, with great caution. By examining only the objective function values, it can be concluded that the best results are obtained using spatial filter multiplier m equal to 1. It is worth noting that low spatial filter multiplier m values may result in a checkerboard solution. Therefore, it is necessary to study artificial density fields. As for the number of iterations for the multiplier value $m > 1$, the iteration number is similar and is equal to around 500, while for the value $m = 1$ it is over 1000.

Artificial density fields Figures 4.17 - 4.20 show the optimal artificial density fields in the device obtained for the value of the spatial filter multiplier m: 1,2, 3, and 4,

respectively.

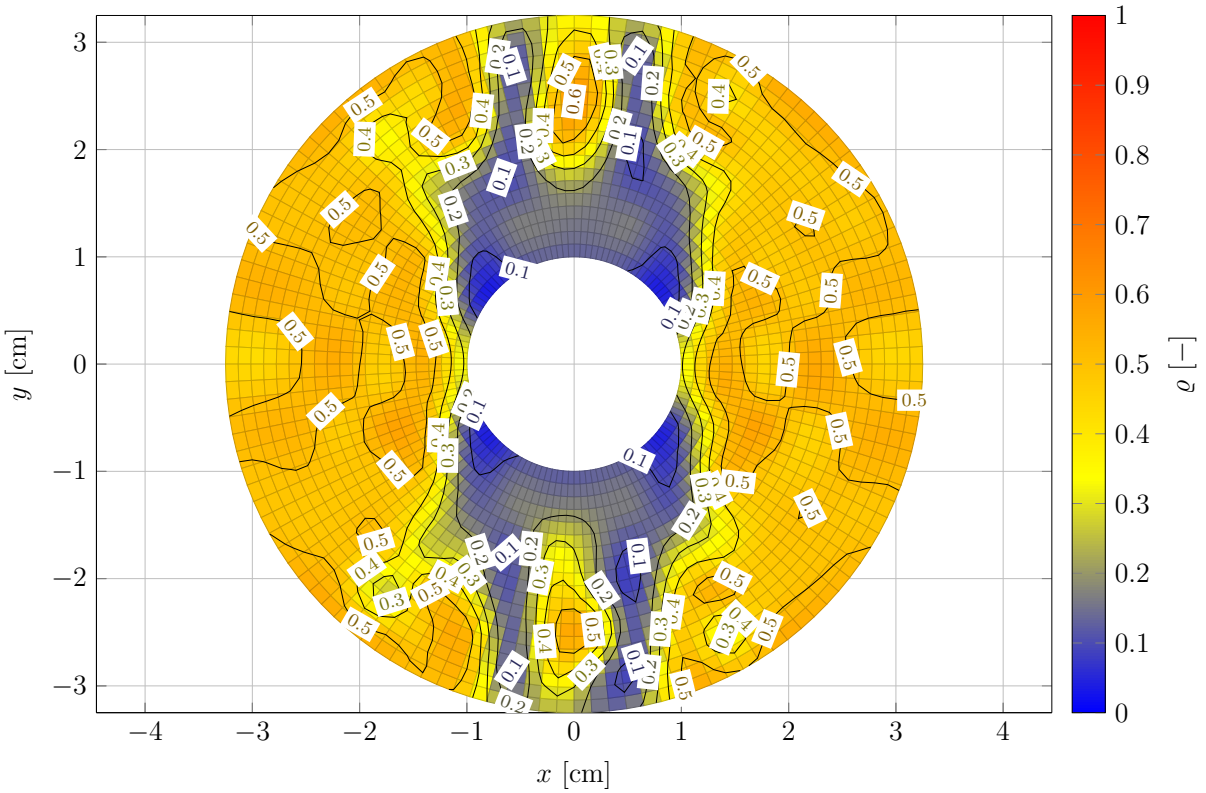

Figure 4.17: The optimal artificial density field obtained for $m = 1$

In line with the concerns presented above, the distribution for $m = 1$ clearly shows the checkerboard phenomenon. It confirms that the use of low value of spatial filter multiplier may be disadvantageous because a device with a thermal conductivity distribution resulting from such a distribution of artificial density may be very impractical and expensive to produce. As for the distributions for $m = 4$, the results indicate an extremely interesting problem. It is worth starting the discussion about it by pointing out that the cloaking problem for Fachinotti's device has a trivial solution. It is a solution in which the thermal conductivity of the device is equal to the thermal conductivity of the object and the mantle. As a consequence, the material becomes homogeneous and for this problem it is possible to determine the analytical solution using Equation 3.11. The value of the artificial density corresponding to this situation can be obtained by substituting the value of the agar's thermal conductivity κ_{agar} to the Equation 4.16 and solving it for the artificial density ϱ:

$$\varrho = \sqrt[3]{\frac{\kappa_{\text{agar}} - \kappa_{\text{min}}}{\kappa_{\text{max}} - \kappa_{\text{min}}}} \approx 0.0954. \tag{4.37}$$

The above value is very close to the values obtained for $m = 4$ which are in the range $0.1 - 0.16$. This leads to the conclusion that for the cloaking problem, too high value of spatial filter multiplier leads to a trivial solution. On the other hand, the very fact that there is a trivial solution to the cloaking problem is an inconvenience. Therefore, it is suggested to modify Fachinotti's device so that the thermal conductivity of the mantle and the object would be different, which would eliminate the existence of a trivial solution.

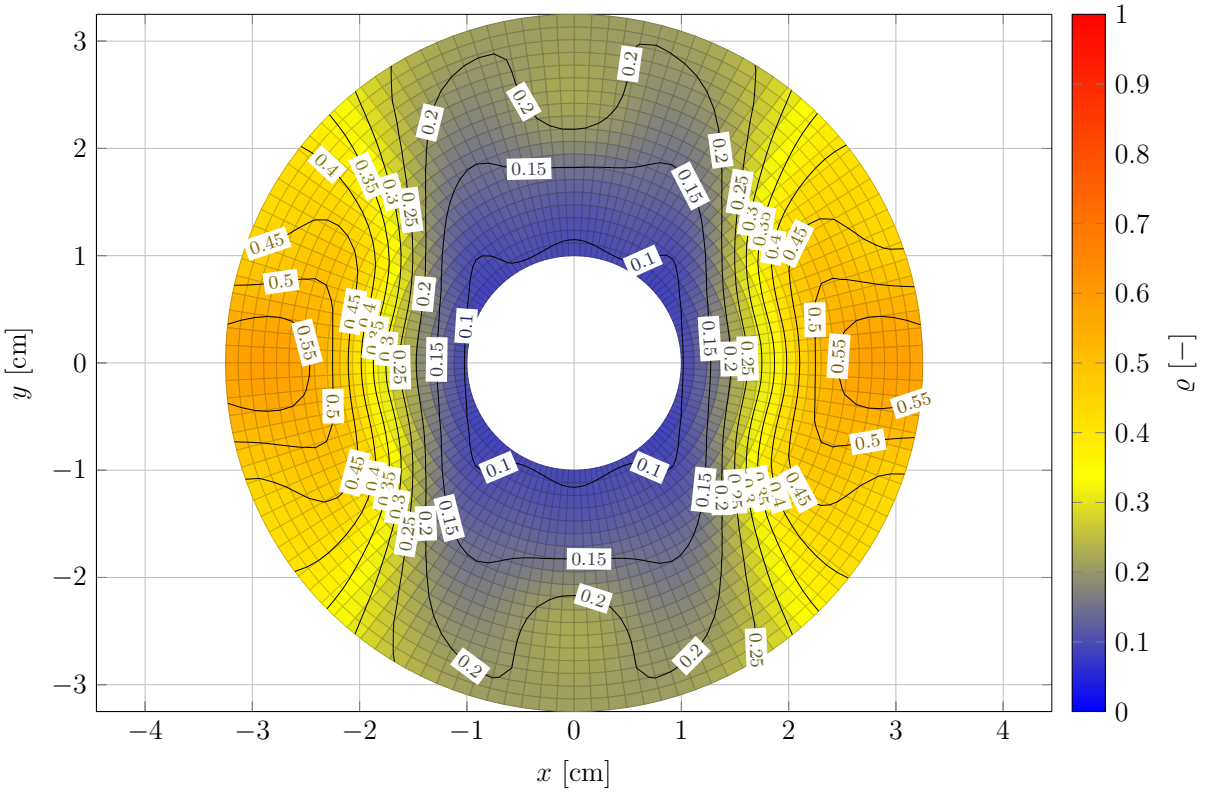

Figure 4.18: The optimal artificial density field obtained for $m = 2$

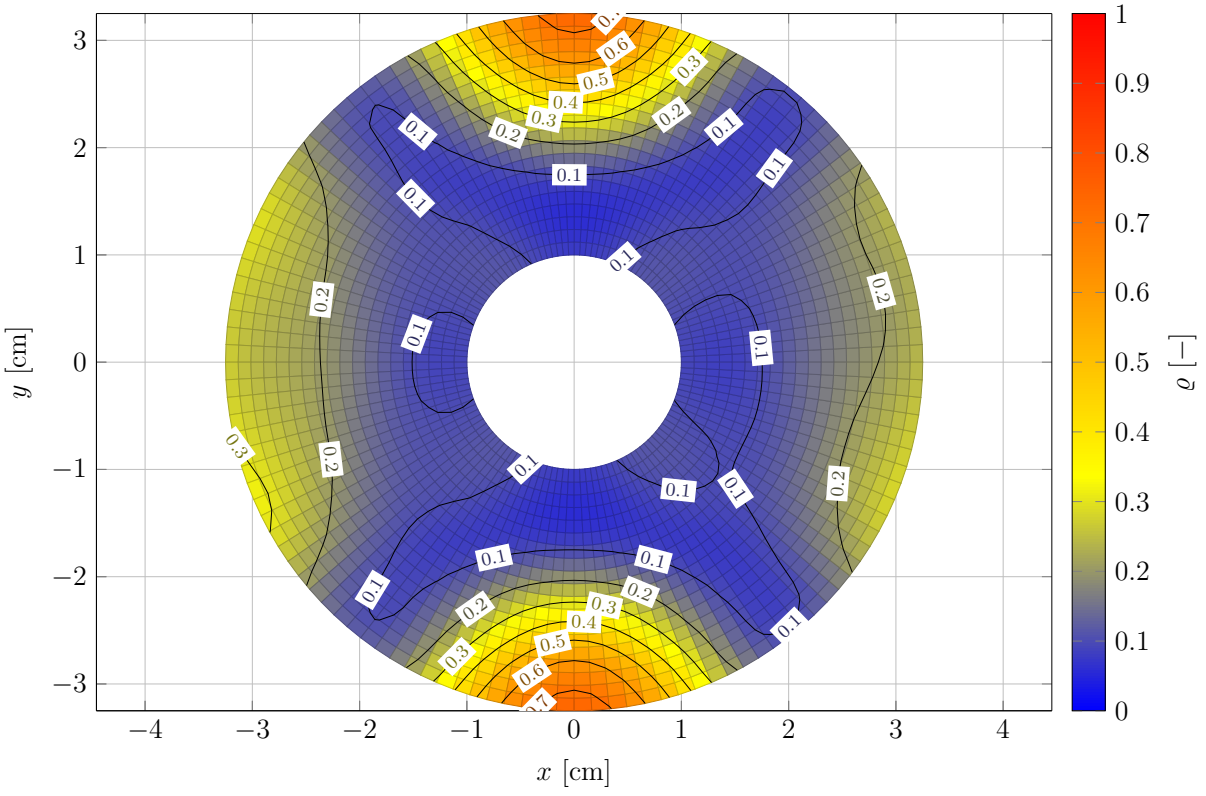

Figure 4.19: The optimal artificial density field obtained for $m = 3$

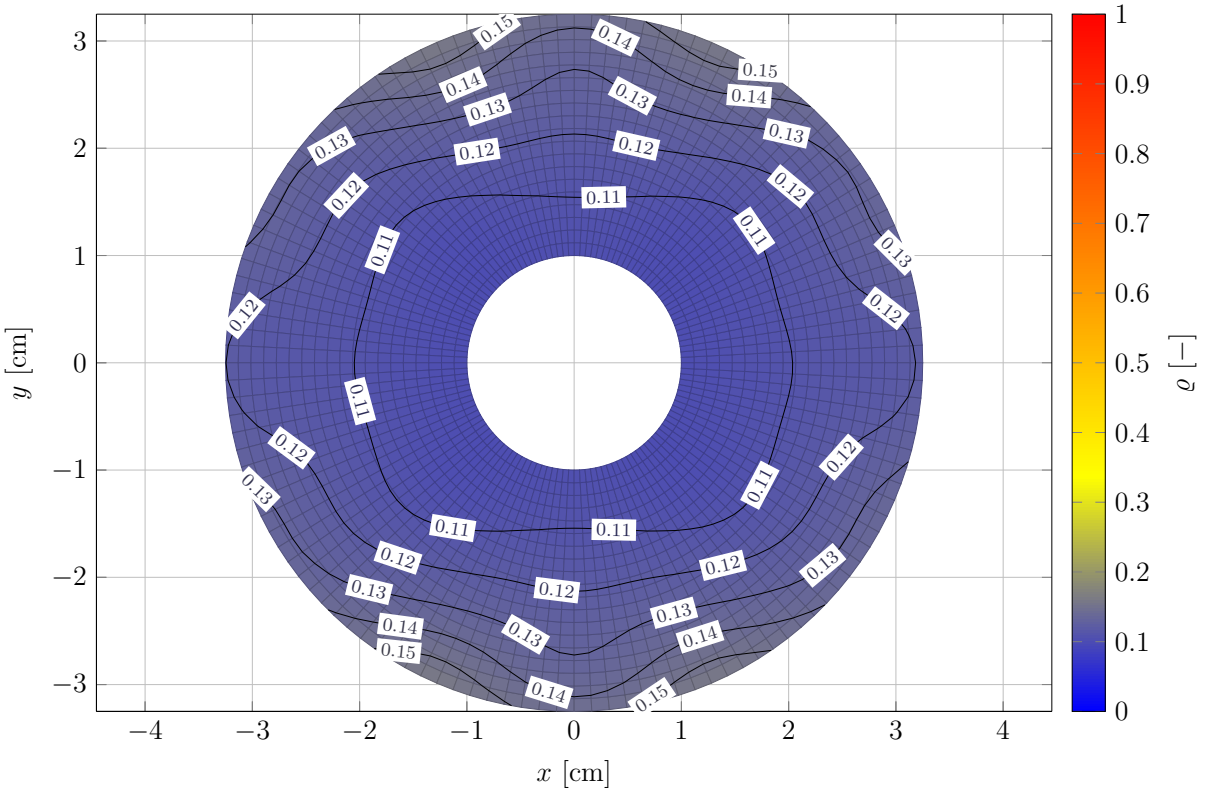

Figure 4.20: The optimal artificial density field obtained for $m = 4$

Such a modification will not be considered in the paper, however, it is an interesting direction for further research. As for the results for the other two values of m, i.e. 2 and 3, the artificial density fields seem correct, however, for $m = 2$, the field shows clearly better symmetry in the vertical and horizontal axis. The final assessment can be made only after examining the temperature fields and the heat flux.

Temperature and heat flux fields Figures 4.21 - 4.24 show the optimal temperature and heat flux fields in the device obtained for the value of the spatial filter multiplier m: 1, 2, 3, and 4, respectively.

The smoothest solution was obtained for $m = 4$, however, as it was shown earlier, it is a trivial solution. The flux field for $m = 1$ is extremely varying in the device region, which results from the checkerboard phenomenon, while for $m = 3$ it is characterized by a significant gradient in the upper and lower region of the device. By using the elimination process, it is concluded that the temperature and flux fields for $m = 2$ seem to be the best from the point of view of the smoothness of the solution.

Conclusions By collecting together the conclusions drawn on the basis of all three subanalysis: the optimal value of the objective function, the distribution of the optimal artificial density as well as temperature and heat flux fields in the optimal case, it was concluded that the most appropriate value of the spatial filter multiplier m is 2, for the considered collocation points set.

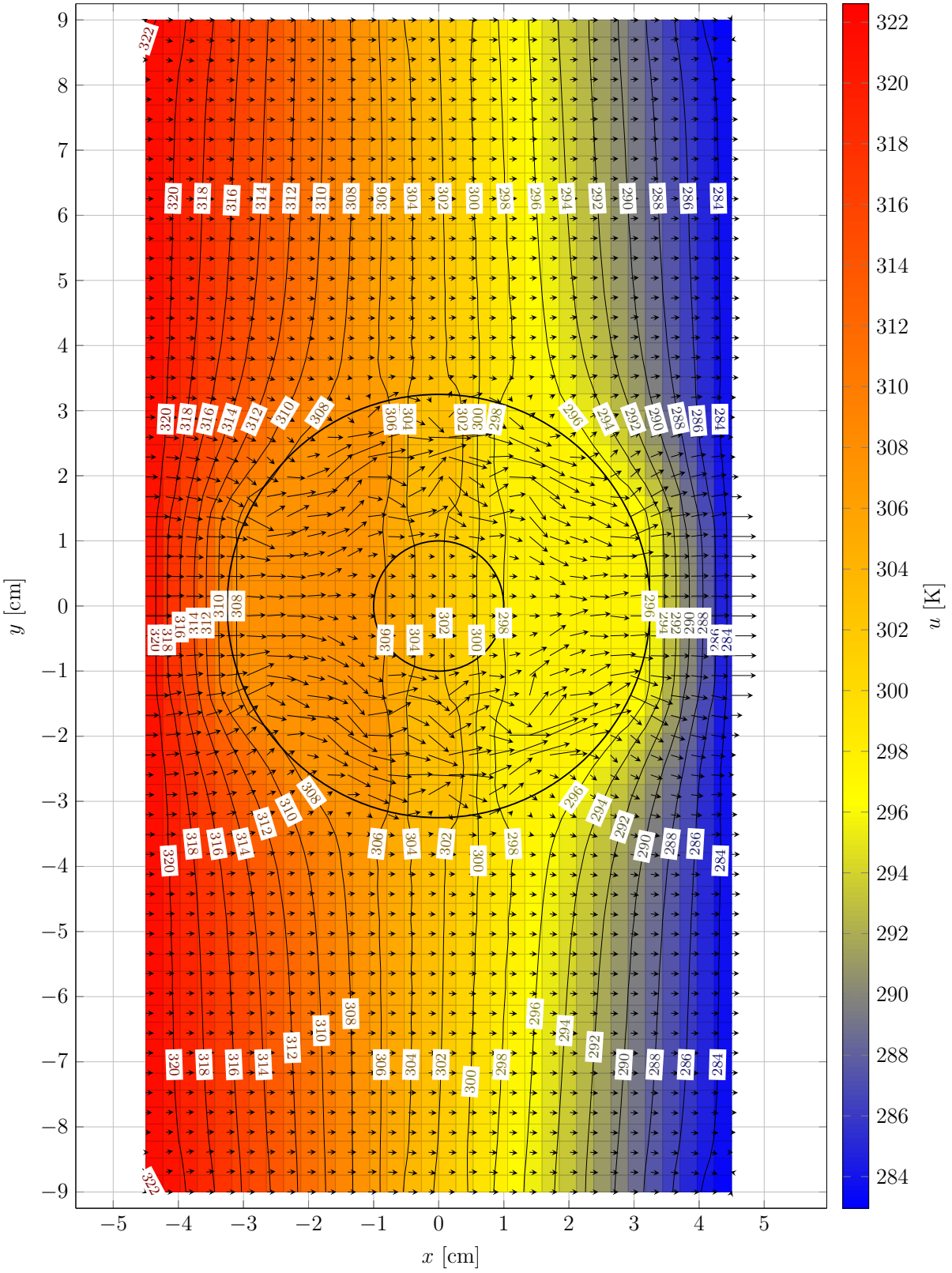

Figure 4.21: The optimal temperature and heat flux fields obtained for $m = 1$

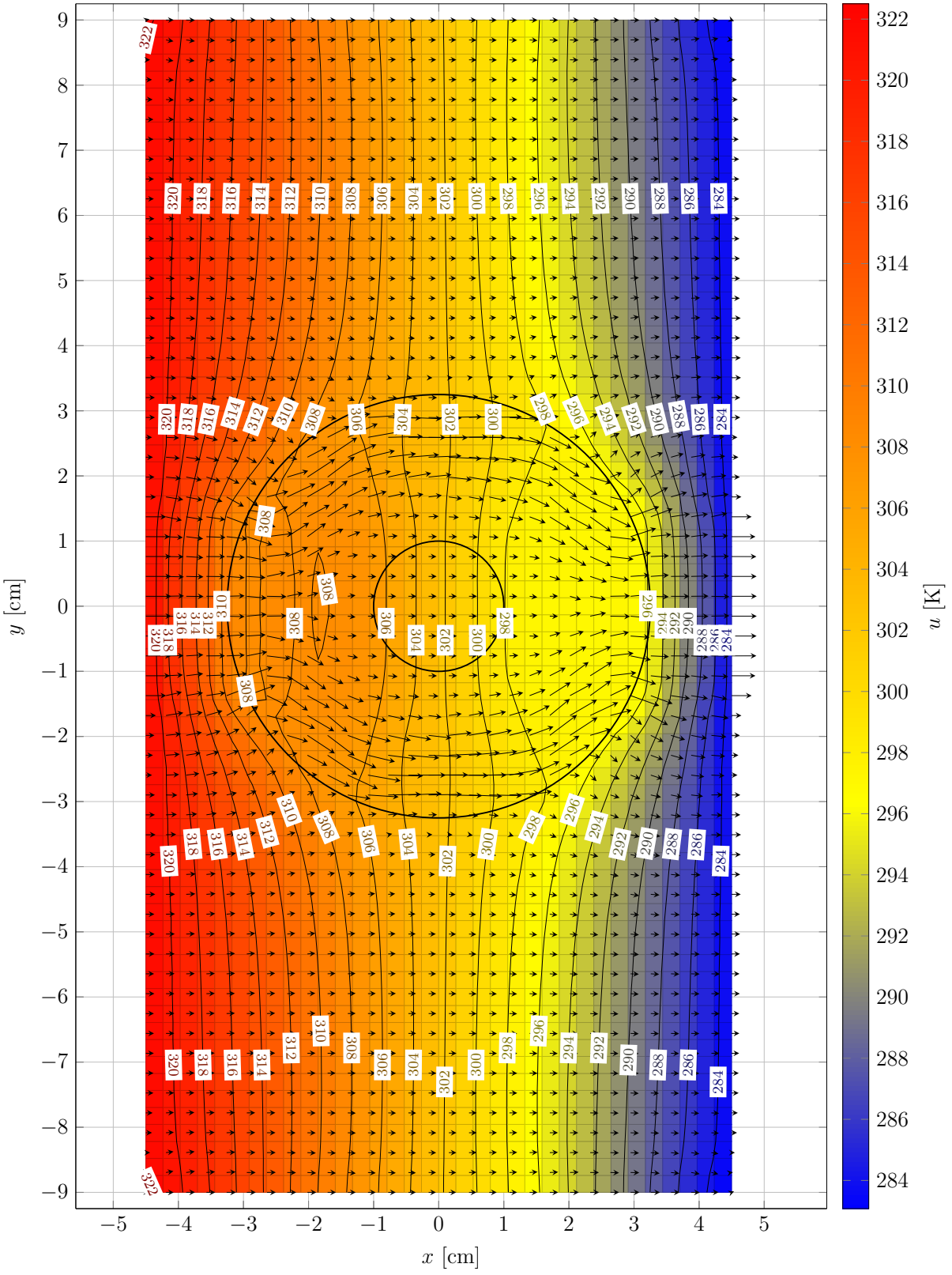

Figure 4.22: The optimal temperature and heat flux fields obtained for $m = 2$

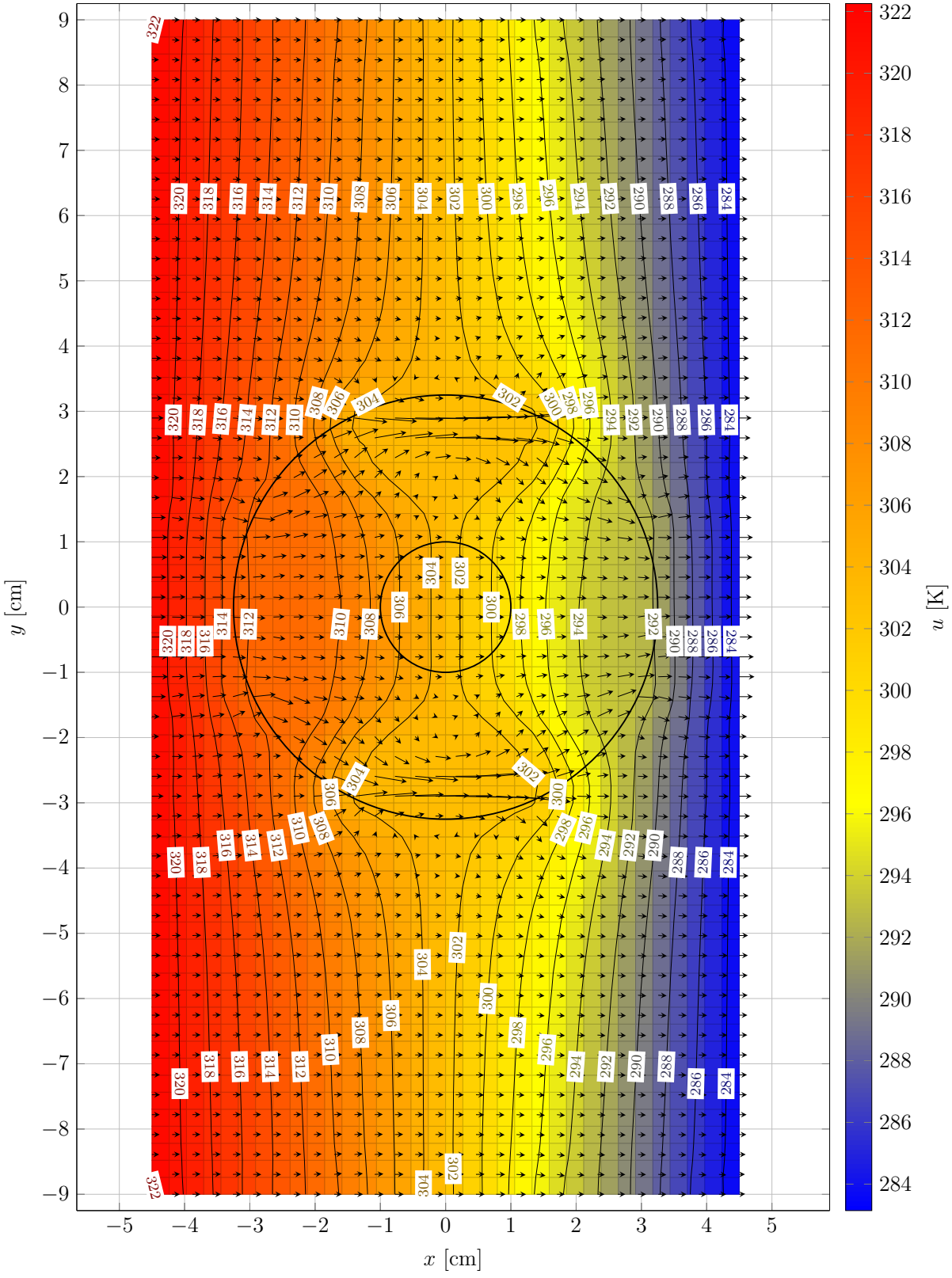

Figure 4.23: The optimal temperature and heat flux fields obtained for $m = 3$

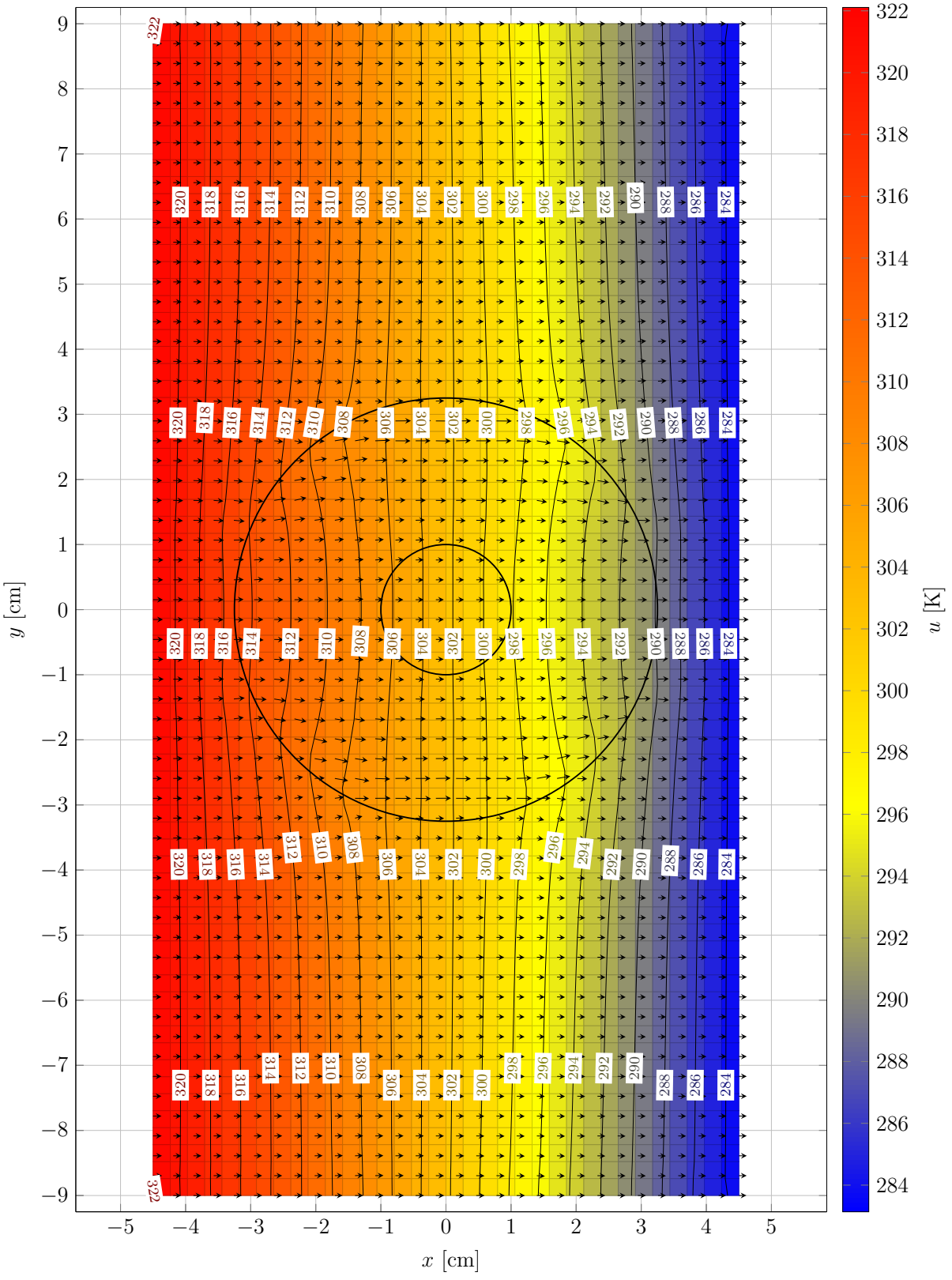

Figure 4.24: The optimal temperature and heat flux fields obtained for $m = 4$

4.3.3 Influence of starting artificial density distribution

There is one more important issue that needs to be investigated - the starting distribution of the artificial density in the iterative optimisation process. All previous simulations were performed for an uniform, deterministic distribution in which the artificial density was constant $\varrho_i = 0.5$. As part of this study, a series of 10 simulations were carried out in which the initial distribution of artificial density was a random distribution in the range of $[0\,,1]$. In the simulations, a cloud consisting of 1148 collocation points and the spatial filter multiplier $m = 2$ were used. It turned out that the simulation results are very similar to each other, so it was decided to present only one results for which the optimal value of the objective function reached value $f = 0.1057\,\mathrm{W}\cdot\mathrm{m}^{-2}$. Figures 4.25 and 4.26 show the optimal artificial density field in the device as well as temperature and heat flux fields in the entire device obtained for random starting distribution of artificial density in the iterative optimisation process. The number of iterations was 582.

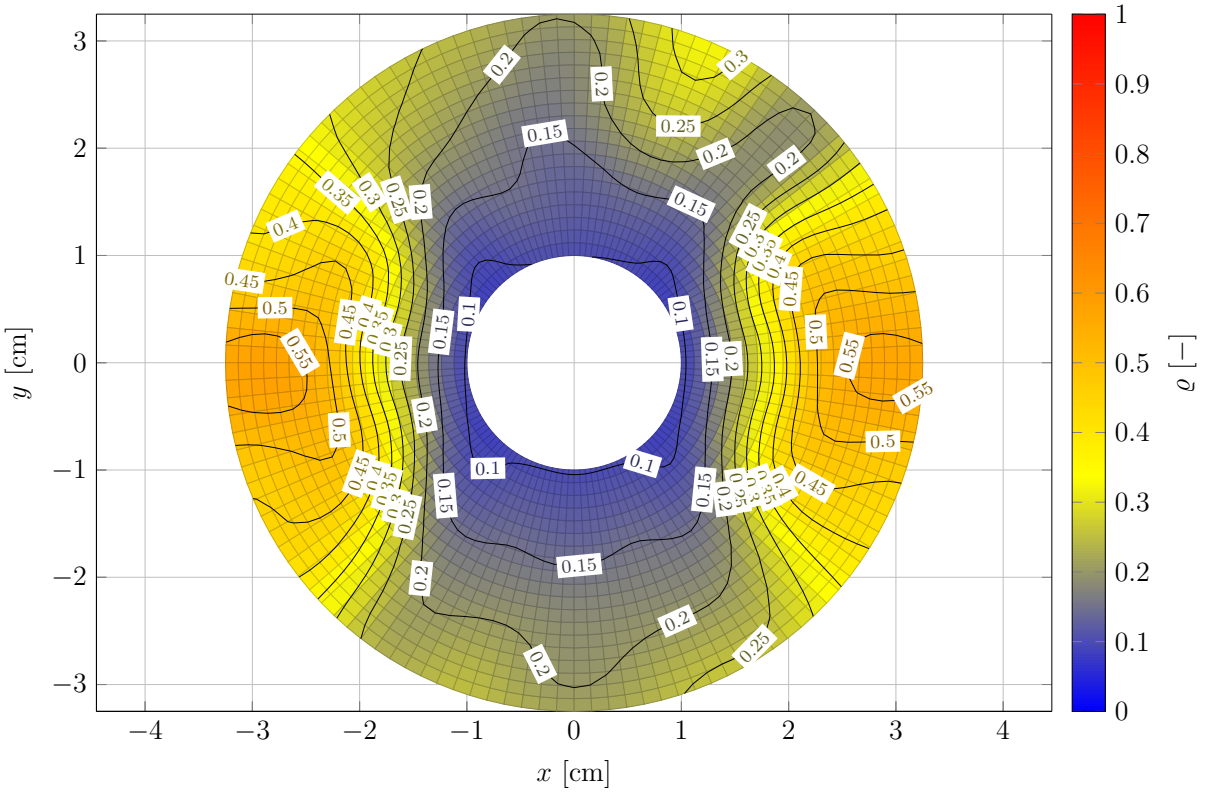

Figure 4.25: The optimal artificial density field obtained for random starting distribution of artificial density

As can be seen in Figures 4.25 and 4.26, the results obtained using random starting distribution are very similar to the results obtained using the deterministic starting distribution, as seen, for example in Figures 4.18 and 4.22. In conclusion, for the considered problems, the starting artificial density distribution does not seem to have a fundamental impact on the optimisation process results when using the interior-point gradient algorithm.

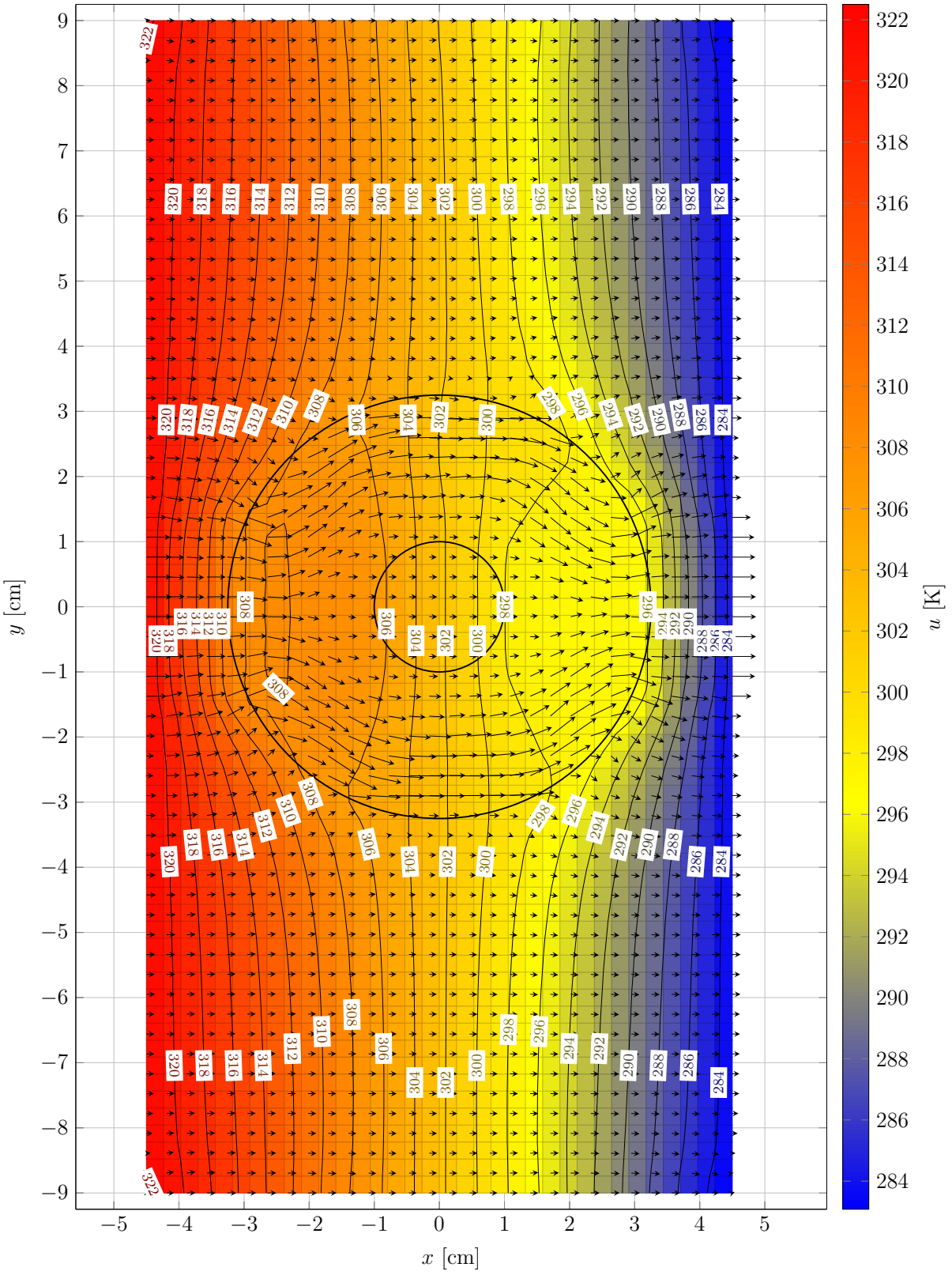

Figure 4.26: The optimal temperature and heat flux fields obtained for random starting distribution of artificial density

4.3.4 Shielding

After a thorough examination of the cloaking case and carrying out several studies, it is possible to proceed to the next case - shielding for which the heat flux manipulation parameter is $\zeta = 0$. The most important simulation parameters remained unchanged: cloud consisting of 1148 collocation points was used, the spatial filter multiplier m was equal to 2, while the starting density distribution in the iterative optimisation process was uniform and $\varrho_i = 0.5$. As a result of the optimisation process, the objective function has reached the value of $f = 1.883\,\mathrm{W}\cdot\mathrm{m}^{-2}$. Figures 4.27 and 4.28 show the optimal artificial density field in the device as well as temperature and heat flux fields in the entire device for shielding test case. The number of iterations was 616.

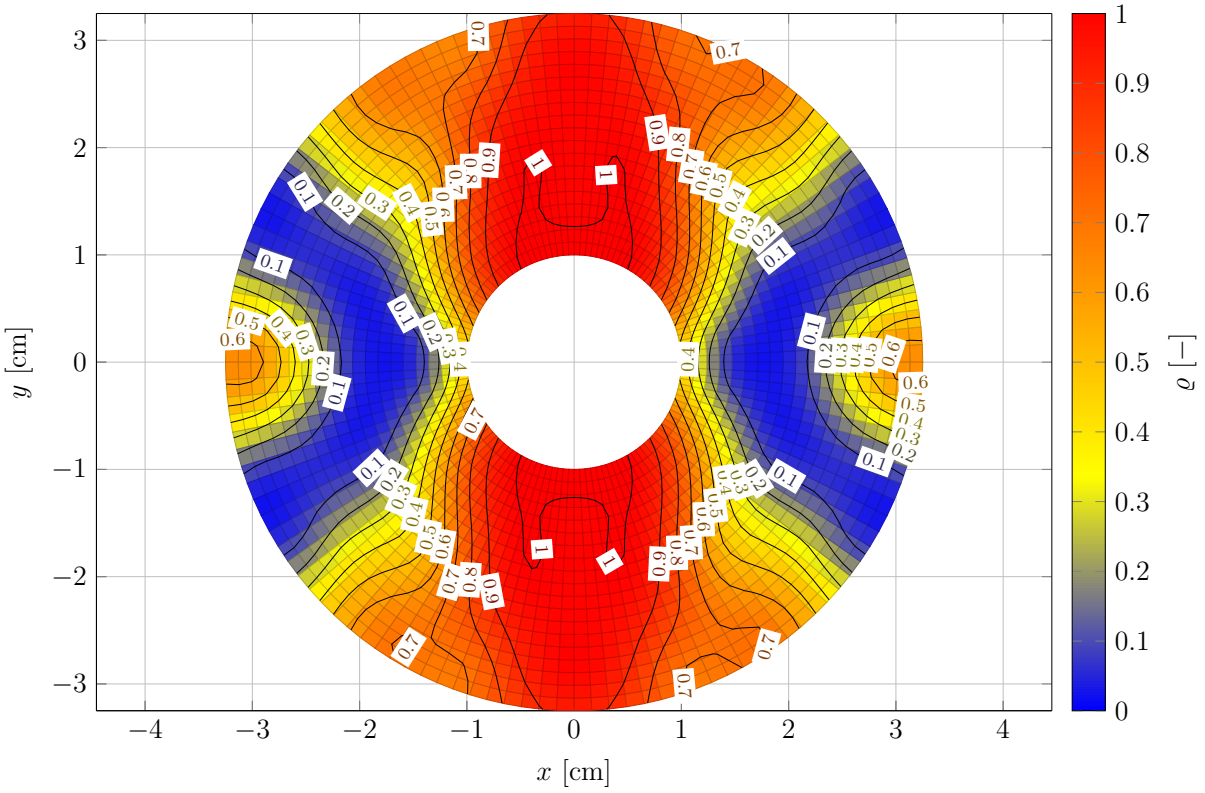

Figure 4.27: The optimal artificial density field obtained for the shielding test case

As can be seen, the distribution of artificial density is clearly symmetrical in both the vertical and horizontal axis, which is in line with the expectations [47]. On the other hand, the visual analysis of the heat flux field shows that the flux values in the device are very small. Quantitatively, the average value of the heat flux in the object was $1.7702\,\mathrm{W}\cdot\mathrm{m}^{-2}$, which is 0.7222 % of the heat flux in the mantle which is $245.1\,\mathrm{W}\cdot\mathrm{m}^{-2}$. Overall, the shielding test case simulation gave very satisfying results.

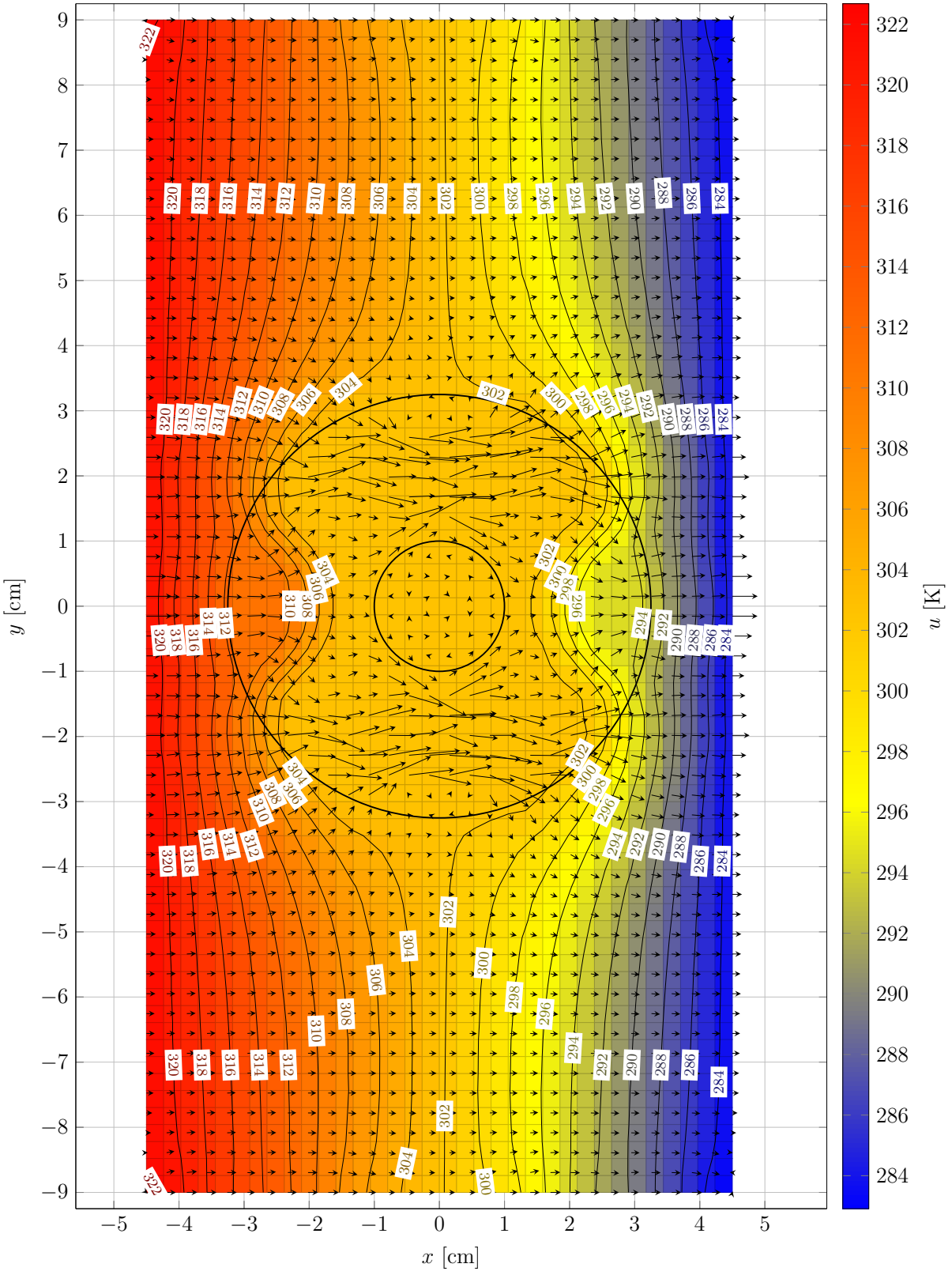

Figure 4.28: The optimal temperature and heat flux fields obtained for shielding test case

4.3.5 Concentration

The next analysed test case is concentration for which the heat flux manipulation parameter is $\zeta = 3.125$. The most important simulation parameters remained unchanged: cloud consisting of 1148 collocation points was used, the spatial filter multiplier m was equal to 2, while the starting density distribution in the iterative optimisation process was uniform and $\varrho_i = 0.5$. As a result of the optimisation process, the objective function has reached the value of $f = 234.27\,\mathrm{W}\cdot\mathrm{m}^{-2}$. Analysing the optimal value of the objective function, at first glance it seems that this value indicates a complete failure and a highly incorrect solution. Before the final judgement is issued, it is worth taking a look at the optimal artificial density, temperature and heat flux fields. Figures 4.29 and 4.30 show the optimal artificial density field in the device as well as temperature and heat flux fields in the entire device for the concentration test case with the heat flux manipulation parameter equal to $\zeta = 3.125$

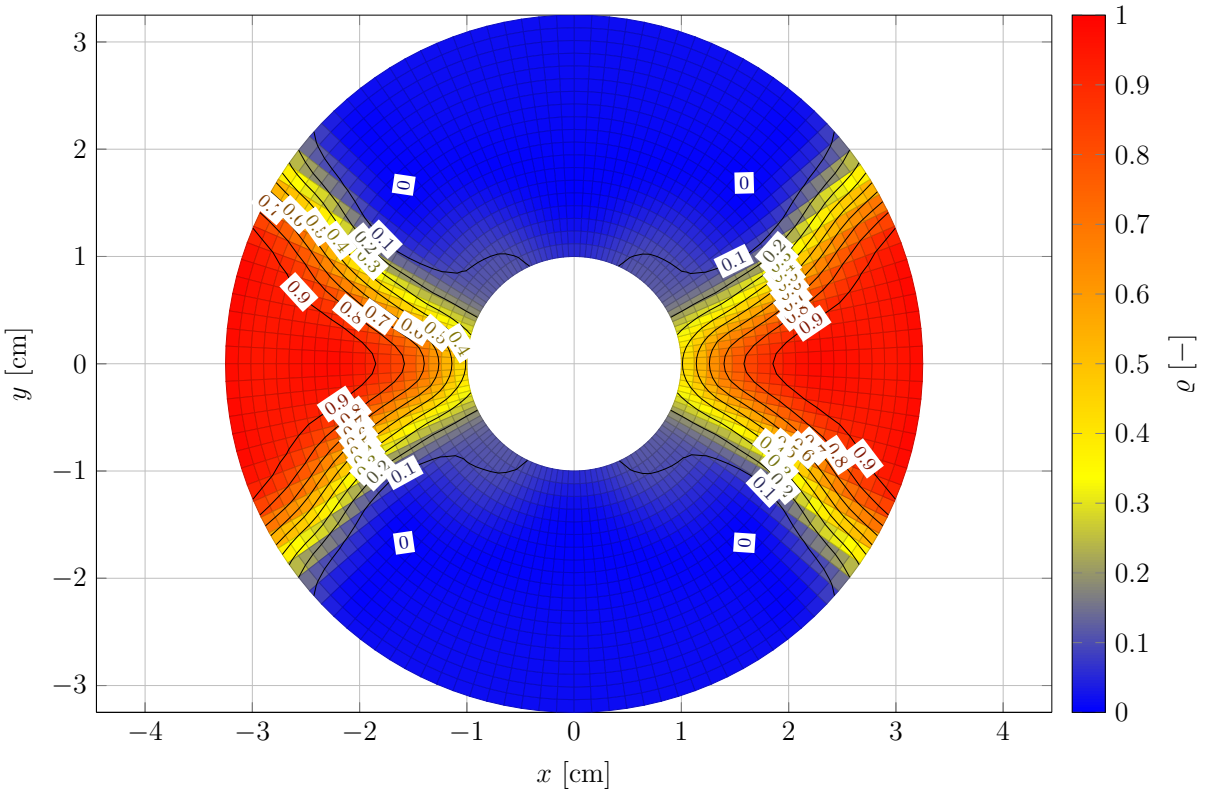

Figure 4.29: The optimal artificial density field obtained for the concentration test case with the heat flux manipulation parameter equal to $\zeta = 3.125$

What is striking is the fact that the distribution of the optimal artificial density is very similar to that obtained by Fachinotti [47]. So why is the objective function so high? The answer to this question lies in the heat flux field. As can be seen, the object shows a significant amplification of the heat flux in relation to the heat flux in the mantle, which is exactly what was supposed to be achieved. However, has an amplification of 3.125 been achieved? The average value of the heat flux in the object was $543.37\,\mathrm{W}\cdot\mathrm{m}^{-2}$, which is 2.217 time higher that the heat flux in the mantle which is $245.1\,\mathrm{W}\cdot\mathrm{m}^{-2}$. It means that the assumed concentration was not achieved, however, a slightly lower concentration was achieved. It is possible that a denser cloud of collocation points is necessary to

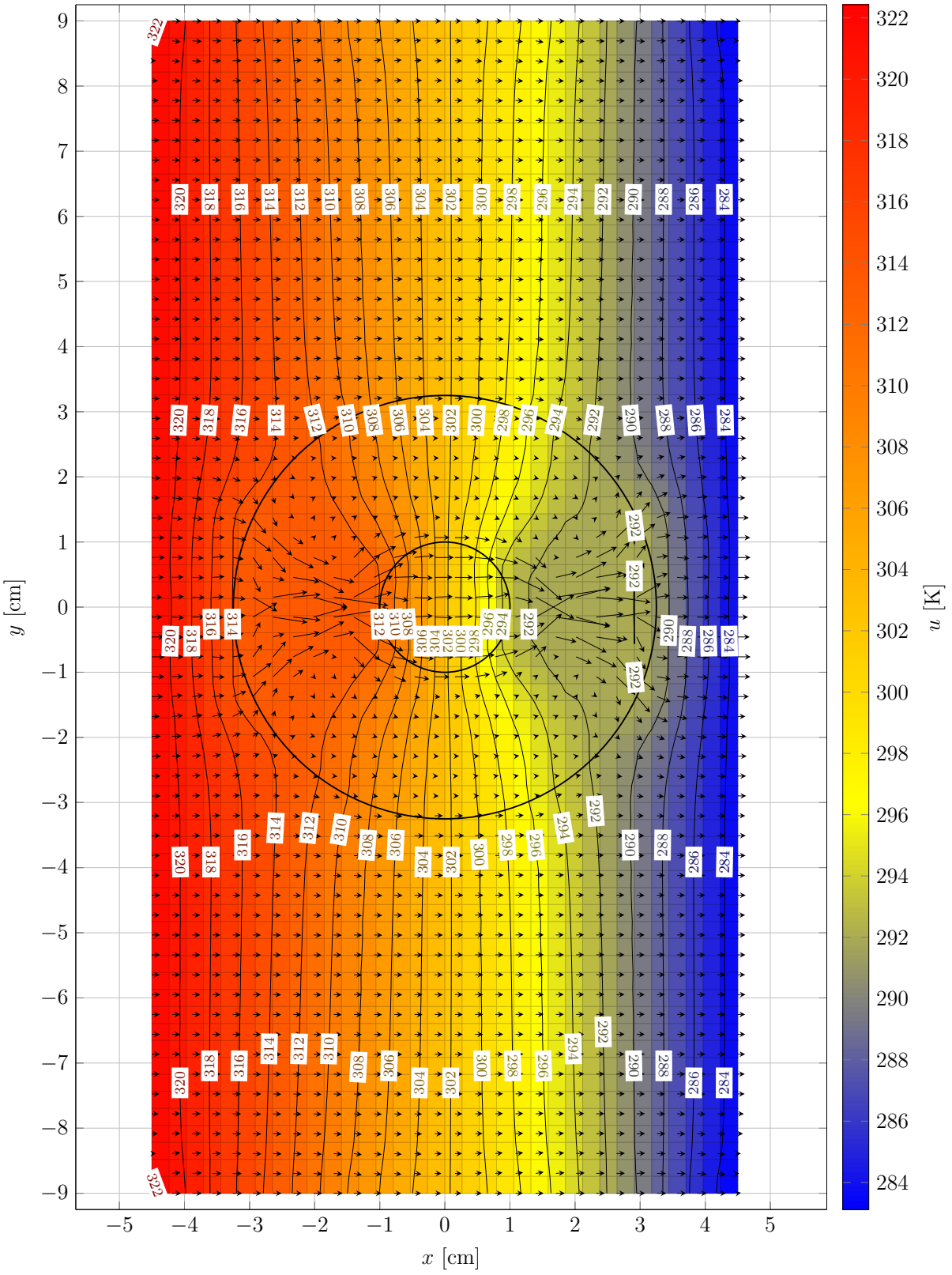

Figure 4.30: The optimal temperature and heat flux fields obtained for the concentration test case with the heat flux manipulation parameter equal to $\zeta = 3.125$

achieve desired amplification. However, since the concentration with a gain of 2.2 has been achieved, it is worth trying to perform the optimisation process for the heat flux manipulation parameter equal to $\zeta = 2$. So it was done, other parameters remained unchanged. This time, as a result of the optimisation process, the objective function has reached the value of $f = 0.5783\,\mathrm{W}\cdot\mathrm{m}^{-2}$ Figures 4.31 and 4.32 show the optimal artificial density field in the device as well as the optimal temperature and heat flux fields in the entire device for the concentration test case with the heat flux manipulation parameter equal to $\zeta = 2$.

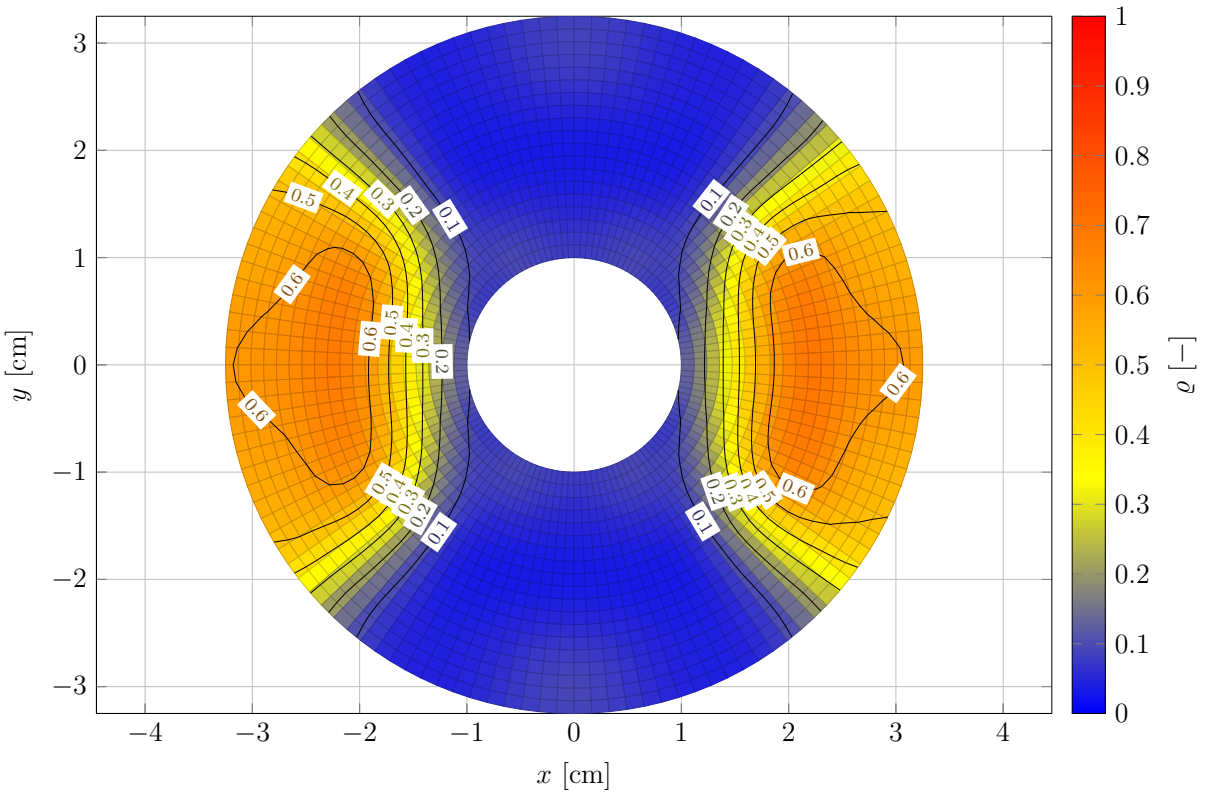

Figure 4.31: The optimal artificial density field obtained for the concentration test case with the heat flux manipulation parameter equal to $\zeta = 2$

It can be seen that the optimal artificial density field is slightly different than that obtained for the concentration device with the amplification 3.125, but the general character is very similar - there are areas of "tunneling" the heat flux on the left and right side of the device. When it comes to temperature and heat flux fields, there is a clear amplification of the heat flux in the object. The heat flow is regular and symmetrical without any sudden changes in the entire device. Overall, the concentration test case has been a half success. The amplification of magnitude 2 was obtained, but not 3.125 as in the reference case.

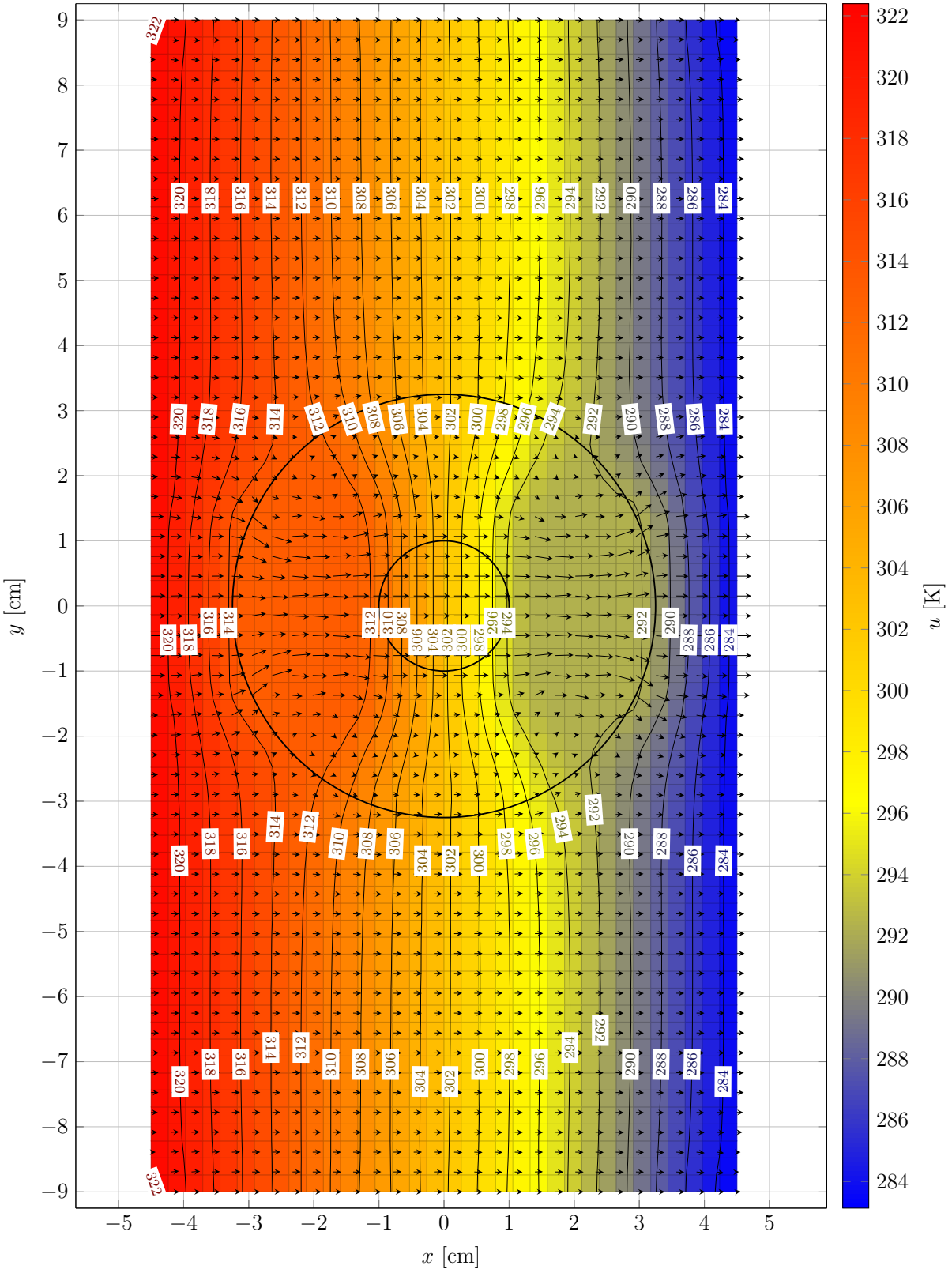

Figure 4.32: The optimal temperature and heat flux fields obtained for the concentration test case with the heat flux manipulation parameter equal to $\zeta = 2$

4.3.6 Inversion

The last of the considered cases is an inversion problem. It is analysed as the last for a reason, it is suspected that it is the most demanding numerically. After all, the inversion of the heat flux is an apparent contradiction to Fourier's law (which of course is always locally satisfied), it would be surprising if its realisation were easy. The suspicions turned out to be correct. Dozens of simulations of this test case were carried out for various combinations of collocation point clouds, spatial filter multiplier values, and starting distributions of the artificial density. The finest cloud consisted of 2044 collocation points. The simulations were even carried out for the value of the heat flux manipulation parameter $\zeta = -0.5$, which theoretically should be a much easier case. Unfortunately, each of the analysed cases gave unsatisfactory results. Summing up, it is possible to draw a conclusion that the considered numerical setup did not allow solving this test case. However, it is suspected that it is possible to solve it using a cloud with a large number of collocation points, which, however, would be computationally expensive. However, it was decided to show some sample results of a failed simulation. The cloud consisting of 2044 collocation points was used in this simulation. Out of 2044 points, 360 were device points and 32 were object points. The spatial filter multiplier was equal to $m = 1$, the heat flux manipulation parameter was equal to $\zeta = -1$, the starting distribution of the artificial density in the iterative optimisation process was random. Why was it decided to show the results obtained using spatial filter multiplier equal to $m = 1$, and random starting distribution? This is because the promising results obtained by Fachinotti [47] indicate that the field of artificial density for the inversion case is very complex and irregular. The random starting distribution of the artificial density and the low value of the spatial filter multiplier m are intended to help achieve good results. On the other hand, as mentioned before, it's worth remembering that a low value for the spatial filter multiplier m parameter can lead to the checkerboard solution. Figures 4.33 and 4.34 show the optimal artificial density field in the device as well as the optimal temperature and heat flux fields in the entire device for inversion test case.

Results presented in Figures 4.33 and 4.34 show the failure of the simulation. The artificial density field shows a very strong checkerboard phenomenon, while the heat flux field shows complete irregularity and chaos, especially in the device region. The only success that can be seen in the results of this simulation is the fact that some of the heat flux vectors in the object are turned to the left, i.e. there has been an inversion, but the values of these inverted fluxes are very small.

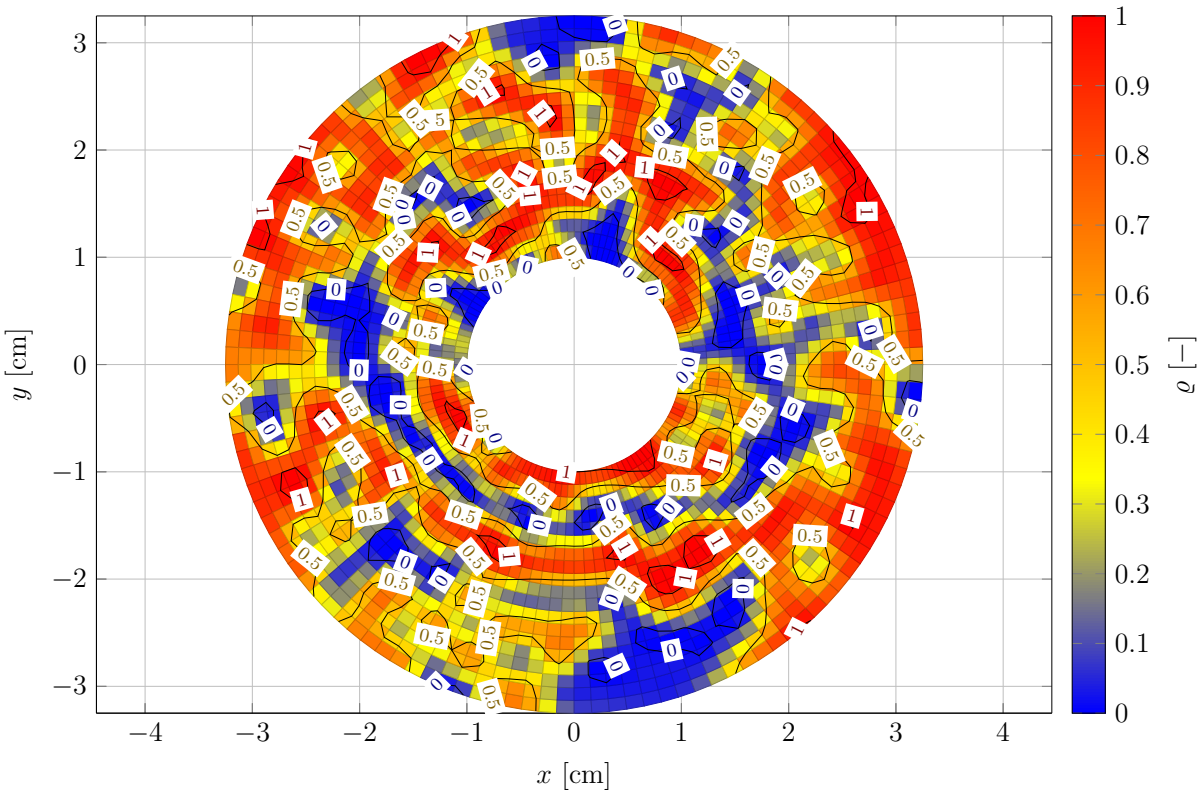

Figure 4.33: The optimal artificial density field obtained for the inversion test case

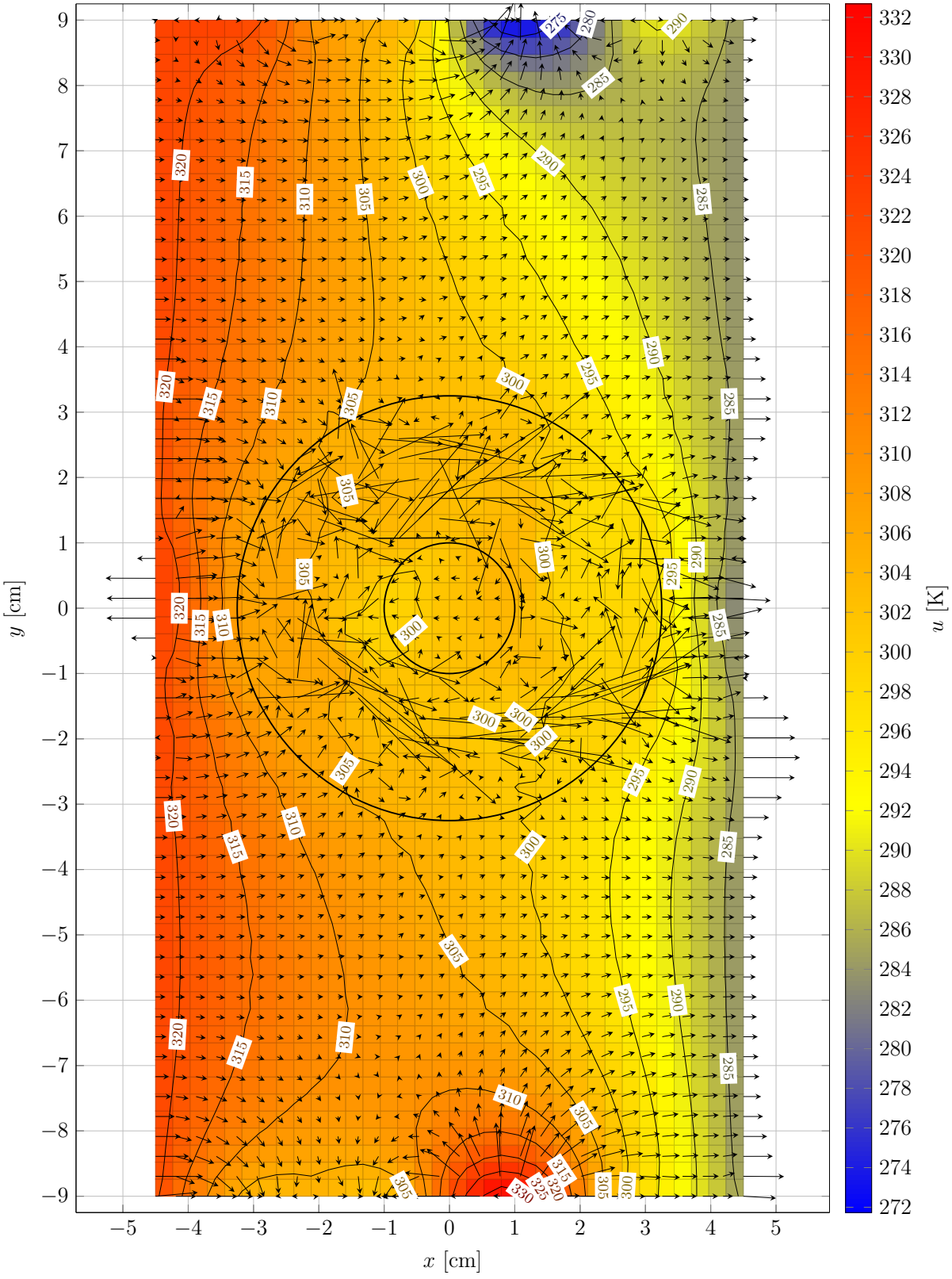

Figure 4.34: The optimal temperature and heat flux fields obtained for the inversion test case

5. Conclusions

Conclusions The research carried out as part of the work has led to a number of very interesting conclusions, the most important of which are as follows:

1. The Kansa method in its classical formulation is a method that has proven to be remarkably good for solving a wide variety of heat flow problems with spatially variable distributions of thermophysical properties: steady and unsteady, one-dimensional and two-dimensional, elliptic, parabolic and hyperbolic for various combinations of Dirichlet, Neumann, and Robin boundary conditions.

2. The problems of heat flow in a material with spatially variable thermophysical parameters are much more difficult than the problems of heat flow in homogeneous materials. Despite this, the Kansa method has proved to be appropriate for this class of problems.

3. The Kansa method in the spacetime formulation has proved to be moderately effective. The only problem in which it turned out to be accurate was the one-dimensional parabolic heat flow problem. It is suspected that these problems result from inadequate selection of the spacetime scaling parameter β value. Unfortunately, to the best of the authors' knowledge, there is no work on the selection of its value for the spacetime of the Kansa method. In the case of hyperbolic problems, the quality of the solution could have been influenced by the method of imposing of the initial condition related to the temperature derivative, which was imposed thorough ghost collocation points.

4. The differences in accuracy between the coefficient and pseudospectral approaches are negligible. The decision to choose between the two approaches is rather related to practical issues. The pseudospectral approach is slightly easier to implement because it does not require an intermediate step of determining the linear combination coefficients. Another issue is the fact that operating on the field of the searched variable rather than on the linear combination coefficients facilitates certain operations, for example calculating the derivative of the field of the searched variable. On the other hand, the indisputable advantage of the coefficient approach is the fact that by obtaining linear combination coefficients as a solution, it is possible to quickly, easily and computationally cheaply find a solution between the collocation points.

5. Due to the fact that the multiquadric scheme is a high-order scheme, for the considered problems, the Kansa method allows to obtain a high-accuracy solution using even relatively coarse clouds of collocation points.

6. As part of the work on this thesis, a very important advantage of the Kansa method was confirmed - the ease of implementation for problems with complex geometry.

The problem of heat flow for the amoeba-like domain considered in the paper can be written in MATLAB using about 100 lines of code. Solving this problem using, for example, an own code of the finite element method would probably be several times more time-consuming due to the need to write an unstructured mesher.

7. The applied approach of using mass, damping and stiffness matrices known from structural mechanics has a number of advantages: its implementation is very simple, allows for very easy use of time integration schemes and greatly improves the readability of the code. This approach was also used in the case of the finite difference method, where it tremendously facilitates the imposition of boundary conditions.

8. In the considered cases, the results obtained when using the Houbolt time integration scheme showed lower algorithmic damping than in the case of the Euler time integration scheme. It is interesting because the cases described so far in the literature showed the opposite conclusions, namely increased algorithmic damping instead of the decreased one [71, 33, 34]. Explaining this difference is not an easy task, however, it is worth paying attention to one issue that may be an explanation. In the mentioned research, the Houbolt time integration scheme was used in conjunction with finite element method for which the main matrix is sparse, banded and symmetric. The main matrix in the Kansa method does not have these features. It is hypothesized that that when the main matrix does not have these features, the numerical dissipation is reduced.

9. The values of error measures related to heat flux fields were significantly greater than the values of error measures related to temperature fields. It seems that they should be similar because the heat flux field is calculated from the temperature field after the simulation is finished. However, this is probably what causes such a significant difference because the heat flux field is computed from the temperature field using the differentiation operator. This operation is burdened with a numerical error, which in this case is strongly amplified because the interpolation matrices are characterized by very high conditon number values. This problem can be probably minimized using regularization.

10. For the problems considered in the paper, higher accuracy of calculations was achieved when using regular collocation point distributions in the domain interiors than when using clouds with random point distributions in the domain interiors.

11. The interpolation matrix created using the multiquadric radial basis function is full and non-symmetric. This is a significant problem because it increases the computational complexity of the Kansa method and makes it less competitive with, for example, the finite element method. A potential solution could be to use the symmetric Kansa method or the local formulation [51].

12. The algorithm for finding a good shape parameter value proposed by Zhang [175], which is based on the condition number study of the interpolation matrix, is an algorithm with great potential and, on the other hand, very little interest in the scientific community [67]. In this paper, an extensive study of it has been made and shows that it gives accurate results and can easily compete with such well-established algorithms as Rippa's algorithm. Additionally, it was proposed to extend this algorithm to the whole group of algorithms examining the oscillation of certain

simulation parameters. The work proposes several such alternative parameters and shows that they also lead to satisfactory results.

13. The manipulation of the heat flux considered in the paper as the optimisation problem and the related search for the distribution of the artificial density led to good results. The cloaking and shielding cases yielded very good results while the concentration test case results achieved an amplification of 2.2 which is lower than 3.125 in the reference work. Optimisation for the inversion problem turned out to be a failure, which probably resulted from an insufficient number of collocation points. The distribution of collocation points itself also requires special attention in this case.

14. The study on the influence of simulation parameters on the result of the optimisation process for the cloaking test case showed that the effect of the number of collocation points and the spatial filter multiplier is fundamental, while influence of the starting distribution of the artificial density in the iterative optimisation process is moderate.

15. The interior-point gradient optimisation method has proven to be an effective way to solve the optimisation problem. It is worth noting that in the considered case the gradient of the objective function was determined analytically.

Further research recommendations During the research, many problems were encountered which, due to time constraints, were not thoroughly investigated. These problems open up interesting options for future research. The most important of them are:

1. Further research of the group of algorithms proposed in the work to search for a good value of the shape parameter. In particular, finding new functions for the study of oscillations, such that can be determined without performing the simulation process. An interesting issue is also the development of methods to identify the transition point from smooth to oscillatory region.

2. Research on the influence of the radial basis function parameters other than shape parameter (exponent p for multiquadric radial basis function) on the accuracy of the simulation and proposing an algorithm for selecting their values.

3. Investigation of the heat flow problems considered in the work with the use of radial basis function other than multiquadric.

4. Research on the influence of the spacetime scaling parameter β on the accuracy of the simulation and proposing an algorithm for selecting this value.

5. Regularization of heat flow problems solutions, so that the obtained heat flux fields were more accurate than obtained in the work.

6. Research on the algorithmic dissipation of the Houbolt time integration scheme and application of other time integration schemes for the hyperbolic heat flow problems.

7. Further research on the heat flux problems manipulation using the Kansa method, and in particular further research on the heat flow inversion with special emphasis on: conducting simulations with denser clouds of collocation points, using the collocation point clouds optimised for the considered problem, reducing the order

of the model using the proper orthogonal decomposition or parameterization of the artificial density surface.

8. Analysis of the spacetime approach as an ill-posed Cauchy problem.
9. Application of the Laplace transform method for evolution equations.
10. Optimal control of heat flow with reduced dynamic models.
11. Application of delay systems model for thermal wave phenomena.

It is worth emphasizing that the conclusions and recommendations presented above do not fully cover the conclusions that can be drawn from the work and the recommendations that can be formulated.

Bibliography

[1] C. Ackerman, B. Bertman, H. A. Fairbank, and R. Guyer. Second sound in solid helium. *Physical Review Letters*, 16(18):789, 1966.

[2] C. Ackerman and R. Guyer. Temperature pulses in dielectric solids. *Annals of Physics*, 50(1):128–185, 1968.

[3] F. Afiatdoust and M. Esmaeilbeigi. Optimal variable shape parameters using genetic algorithm for radial basis function approximation. *Ain Shams Engineering Journal*, 6(2):639–647, 2015.

[4] I. Ahmadi. A truly meshless method formulation for analysis of non-fourier heat conduction in solids. *Journal of Computational & Applied Research in Mechanical Engineering (JCARME)*, 6(1):75–89, 2016.

[5] A. Alù and N. Engheta. Achieving transparency with plasmonic and metamaterial coatings. *Physical Review E*, 72(1):016623, 2005.

[6] A. Alù and N. Engheta. Multifrequency optical invisibility cloak with layered plasmonic shells. *Physical review letters*, 100(11):113901, 2008.

[7] J. Andkjær, N. Asger Mortensen, and O. Sigmund. Towards all-dielectric, polarization-independent optical cloaks. *Applied Physics Letters*, 100(10):101106, 2012.

[8] J. Andkjær and O. Sigmund. Topology optimized low-contrast all-dielectric optical cloak. *Applied Physics Letters*, 98(2):021112, 2011.

[9] W.-T. Ang. A boundary element and radial basis function method for the cattaneo–vernotte equation in anisotropic media with spatially varying and temperature dependent properties. *Partial Differential Equations in Applied Mathematics*, 4:100138, 2021.

[10] C. Bai and A. Lavine. On hyperbolic heat conduction and the second law of thermodynamics. *Journal of Heat Transfer*, 117:256–263, 1995.

[11] V. Bayona, M. Moscoso, and M. Kindelan. Optimal constant shape parameter for multiquadric based rbf-fd method. *Journal of Computational Physics*, 230(19):7384–7399, 2011.

[12] D. A. Belsley, E. Kuh, and R. E. Welsch. The condition number. *Regression Diagnostics: Identifying Influential Data and Sources of Collinearity*, 100:104, 1980.

[13] M. P. Bendsøe. Optimal shape design as a material distribution problem. *Structural optimization*, 1(4):193–202, 1989.

[14] M. Bisoffi, B. Hjelle, D. Brown, D. Branch, T. Edwards, S. Brozik, V. Bondu-Hawkins, and R. Larson. Detection of viral bioagents using a shear horizontal surface acoustic wave biosensor. *Biosensors and Bioelectronics*, 23(9):1397–1403, 2008.

[15] J. P. Boyd and K. W. Gildersleeve. Numerical experiments on the condition number of the interpolation matrices for radial basis functions. *Applied Numerical Mathematics*, 61(4):443–459, 2011.

[16] M. Brun, S. Guenneau, and A. B. Movchan. Achieving control of in-plane elastic waves. *Applied physics letters*, 94(6):061903, 2009.

[17] T. Bückmann, M. Thiel, M. Kadic, R. Schittny, and M. Wegener. An elasto-mechanical unfeelability cloak made of pentamode metamaterials. *Nature communications*, 5(1):1–6, 2014.

[18] J. C. Butcher. *Numerical methods for ordinary differential equations*. John Wiley & Sons, 2016.

[19] W. Cai, U. K. Chettiar, A. V. Kildishev, and V. M. Shalaev. Optical cloaking with metamaterials. *Nature photonics*, 1(4):224–227, 2007.

[20] C. Cattaneo. Sulla conduzione del calore. *Atti Sem. Mat. Fis. Univ. Modena*, 3:83–101, 1948.

[21] Y. Cengel and J. Cimbala. *Fluid Mechanics: Fundamentals and Applications*. New York: McGraw-Hill Education, 2018.

[22] Y. A. Cengel and A. J. Ghajar. *Heat and mass transfer: fundamentals and applications*. McGraw-Hill Higher Education, 2019.

[23] S. Chantasiriwan. Error and variance of solution to the stochastic heat conduction problem by multiquadric collocation method. *International communications in heat and mass transfer*, 33(3):342–349, 2006.

[24] H. Chen and C. Chan. Acoustic cloaking in three dimensions using acoustic metamaterials. *Applied physics letters*, 91(18):183518, 2007.

[25] H. Chen and B. Zheng. Broadband polygonal invisibility cloak for visible light. *Scientific reports*, 2(1):1–4, 2012.

[26] H. Chen, B. Zheng, L. Shen, H. Wang, X. Zhang, N. I. Zheludev, and B. Zhang. Ray-optics cloaking devices for large objects in incoherent natural light. *Nature communications*, 4(1):1–6, 2013.

[27] T. Chen, C.-N. Weng, and J.-S. Chen. Cloak for curvilinearly anisotropic media in conduction. *Applied Physics Letters*, 93(11):114103, 2008.

[28] W. Chen, Z.-J. Fu, and C.-S. Chen. *Recent advances in radial basis function collocation methods*. Springer, 2014.

[29] W. Chen, Y. Hong, and J. Lin. The sample solution approach for determination of the optimal shape parameter in the multiquadric function of the kansa method. *Computers & Mathematics with Applications*, 75(8):2942–2954, 2018.

[30] W. Chen, L. Ye, and H. Sun. Fractional diffusion equations by the kansa method. *Computers & Mathematics with Applications*, 59(5):1614–1620, 2010.

[31] X. Chen, Y. Luo, J. Zhang, K. Jiang, J. B. Pendry, and S. Zhang. Macroscopic invisibility cloaking of visible light. *Nature Communications*, 2(1):1–6, 2011.

[32] K. Cheng and T. Fujii. Heat in history isaac newton and heat transfer. *Heat transfer engineering*, 19(4):9–21, 1998.

[33] J. Chung. *Numerically dissipative time integration algorithms for structural dynamics*. PhD thesis, University of Michigan, 1992.

[34] J. Chung and G. M. Hulbert. A family of single-step houbolt time integration algorithms for structural dynamics. *Computer methods in applied mechanics and engineering*, 118(1-2):1–11, 1994.

[35] S. A. Cummer, J. Christensen, and A. Alù. Controlling sound with acoustic metamaterials. *Nature Reviews Materials*, 1(3):1–13, 2016.

[36] O. Davydov and D. T. Oanh. On the optimal shape parameter for gaussian radial basis function finite difference approximation of the poisson equation. *Computers & Mathematics with Applications*, 62(5):2143–2161, 2011.

[37] S. Daxini and J. Prajapati. A review on recent contribution of meshfree methods to structure and fracture mechanics applications. *The Scientific World Journal*, 2014, 2014.

[38] E. M. Dede, P. Schmalenberg, T. Nomura, and M. Ishigaki. Design of anisotropic thermal conductivity in multilayer printed circuit boards. *IEEE Transactions on Components, Packaging and Manufacturing Technology*, 5(12):1763–1774, 2015.

[39] E. M. Dede, P. Schmalenberg, C.-M. Wang, F. Zhou, and T. Nomura. Collection of low-grade waste heat for enhanced energy harvesting. *AIP Advances*, 6(5):055113, 2016.

[40] M. Dehghan and M. Shirzadi. Numerical solution of stochastic elliptic partial differential equations using the meshless method of radial basis functions. *Engineering Analysis with Boundary Elements*, 50:291–303, 2015.

[41] A. Doicu, T. Trautmann, and F. Schreier. *Numerical regularization for atmospheric inverse problems*. Springer Science & Business Media, 2010.

[42] C. Dong, S. Lo, and Y. Cheung. Numerical solution for elastic inclusion problems by domain integral equation with integration by means of radial basis functions. *Engineering Analysis with Boundary Elements*, 28(6):623–632, 2004.

[43] M. Dubal, S. Oliveira, and R. Matzner. Solution of elliptic equations in numerical relativity using multiquadrics. *Approaches to Numerical Relativity*, pages 265–280, 1992.

[44] B. Edwards, A. Alù, M. G. Silveirinha, and N. Engheta. Experimental verification of plasmonic cloaking at microwave frequencies with metamaterials. *Physical review letters*, 103(15):153901, 2009.

[45] T. Ergin, N. Stenger, P. Brenner, J. B. Pendry, and M. Wegener. Three-dimensional invisibility cloak at optical wavelengths. *science*, 328(5976):337–339, 2010.

[46] M. Esmaeilbeigi and M. Hosseini. A new approach based on the genetic algorithm for finding a good shape parameter in solving partial differential equations by kansa's method. *Applied Mathematics and Computation*, 249:419–428, 2014.

[47] V. D. Fachinotti, Á. A. Ciarbonetti, I. Peralta, and I. Rintoul. Optimization-based design of easy-to-make devices for heat flux manipulation. *International Journal of Thermal Sciences*, 128:38–48, 2018.

[48] A. Fallah, E. Jabbari, and R. Babaee. Development of the kansa method for solving seepage problems using a new algorithm for the shape parameter optimization. *Computers & Mathematics with Applications*, 77(3):815–829, 2019.

[49] C. Fan, Y. Gao, and J. Huang. Shaped graded materials with an apparent negative thermal conductivity. *Applied Physics Letters*, 92(25):251907, 2008.

[50] N. Fang and X. Zhang. Imaging properties of a metamaterial superlens. In *Proceedings of the 2nd IEEE Conference on Nanotechnology*, pages 225–228. IEEE, 2002.

[51] G. E. Fasshauer. *Meshfree approximation methods with MATLAB*, volume 6. World Scientific, 2007.

[52] G. E. Fasshauer and J. G. Zhang. On choosing "optimal" shape parameters for rbf approximation. *Numerical Algorithms*, 45(1-4):345–368, 2007.

[53] A. Ferreira, G. Fasshauer, R. Batra, and J. Rodrigues. Static deformations and vibration analysis of composite and sandwich plates using a layerwise theory and rbf-ps discretizations with optimal shape parameter. *Composite Structures*, 86(4):328–343, 2008.

[54] B. Fornberg and J. Zuev. The runge phenomenon and spatially variable shape parameters in rbf interpolation. *Computers & Mathematics with Applications*, 54(3):379–398, 2007.

[55] J. B. J. Fourier. *Théorie analytique de la chaleur*. F. Didot, 1822.

[56] C. Franke and R. Schaback. Solving partial differential equations by collocation using radial basis functions. *Applied Mathematics and Computation*, 93(1):73–82, 1998.

[57] R. Franke. Scattered data interpolation: tests of some methods. *Mathematics of computation*, 38(157):181–200, 1982.

[58] L. H. Gabrielli, J. Cardenas, C. B. Poitras, and M. Lipson. Silicon nanostructure cloak operating at optical frequencies. *Nature photonics*, 3(8):461–463, 2009.

[59] M. Gherlone, L. Iurlaro, and M. Di Sciuva. A novel algorithm for shape parameter selection in radial basis functions collocation method. *Composite Structures*, 94(2):453–461, 2012.

[60] F. Gömöry, M. Solovyov, J. Šouc, C. Navau, J. Prat-Camps, and A. Sanchez. Experimental realization of a magnetic cloak. *Science*, 335(6075):1466–1468, 2012.

[61] S. Guenneau and C. Amra. Anisotropic conductivity rotates heat fluxes in transient regimes. *Optics express*, 21(5):6578–6583, 2013.

[62] S. Guenneau, C. Amra, and D. Veynante. Transformation thermodynamics: cloaking and concentrating heat flux. *Optics Express*, 20(7):8207–8218, 2012.

[63] T. Han, X. Bai, D. Gao, J. T. Thong, B. Li, and C.-W. Qiu. Experimental demonstration of a bilayer thermal cloak. *Physical review letters*, 112(5):054302, 2014.

[64] T. Han, X. Bai, J. T. Thong, B. Li, and C.-W. Qiu. Full control and manipulation of heat signatures: cloaking, camouflage and thermal metamaterials. *Advanced Materials*, 26(11):1731–1734, 2014.

[65] T. Han, H. Ye, Y. Luo, S. P. Yeo, J. Teng, S. Zhang, and C.-W. Qiu. Manipulating dc currents with bilayer bulk natural materials. *Advanced Materials*, 26(21):3478–3483, 2014.

[66] T. Han, T. Yuan, B. Li, and C.-W. Qiu. Homogeneous thermal cloak with constant conductivity and tunable heat localization. *Scientific reports*, 3(1):1–5, 2013.

[67] S. Haq and M. Hussain. Selection of shape parameter in radial basis functions for solution of time-fractional black–scholes models. *Applied Mathematics and Computation*, 335:248–263, 2018.

[68] S. Haq and M. Hussain. The meshless kansa method for time-fractional higher order partial differential equations with constant and variable coefficients. *Revista de la Real Academia de Ciencias Exactas, Físicas y Naturales. Serie A. Matemáticas*, 113(3):1935–1954, 2019.

[69] R. L. Hardy. Multiquadric equations of topography and other irregular surfaces. *Journal of geophysical research*, 76(8):1905–1915, 1971.

[70] X. He and L. Wu. Illusion thermodynamics: A camouflage technique changing an object into another one with arbitrary cross section. *Applied Physics Letters*, 105(22):221904, 2014.

[71] H. M. Hilber and T. J. Hughes. Collocation, dissipation and [overshoot] for time integration schemes in structural dynamics. *Earthquake Engineering & Structural Dynamics*, 6(1):99–117, 1978.

[72] K. M. Ho, Z. Yang, X. Zhang, and P. Sheng. Measurements of sound transmission through panels of locally resonant materials between impedance tubes. *Applied acoustics*, 66(7):751–765, 2005.

[73] K. A. Hoffman and S. T. Chiang. *Computational fluid dynamics*. Engineering Education System, 2000.

[74] L. D. Hoffmann, G. L. Bradley, and K. H. Rosen. *Calculus for business, economics, and the social and life sciences*. McGraw-Hill, 1989.

[75] R. A. Horn and C. R. Johnson. *Matrix analysis*. Cambridge university press, 2012.

[76] J. C. Houbolt. A recurrence matrix solution for the dynamic response of elastic aircraft. *Journal of the Aeronautical Sciences*, 17(9):540–550, 1950.

[77] R. Hu and B. Cao. Study on thermal wave based on the thermal mass theory. *Science in China Series E: Technological Sciences*, 52(6):1786–1792, 2009.

[78] R. Hu, X. Wei, J. Hu, and X. Luo. Local heating realization by reverse thermal cloak. *Scientific reports*, 4(1):1–6, 2014.

[79] C.-S. Huang, C.-F. Lee, and A.-D. Cheng. Error estimate, optimal shape factor, and high precision computation of multiquadric collocation method. *Engineering Analysis with Boundary Elements*, 31(7):614–623, 2007.

[80] C.-S. Huang, H.-D. Yen, and A.-D. Cheng. On the increasingly flat radial basis function and optimal shape parameter for the solution of elliptic pdes. *Engineering analysis with boundary elements*, 34(9):802–809, 2010.

[81] S. E. Huber and M. R. Trummer. Radial basis functions for solving differential equations: Ill-conditioned matrices and numerical stability. *Computers & Mathematics with Applications*, 71(1):319–327, 2016.

[82] L. Iurlaro, M. Gherlone, and M. Di Sciuva. Energy based approach for shape parameter selection in radial basis functions collocation method. *Composite Structures*, 107:70–78, 2014.

[83] H. E. Jackson and C. T. Walker. Thermal conductivity, second sound, and phonon-phonon interactions in naf. *Physical Review B*, 3(4):1428, 1971.

[84] M. A. Jankowska and A. Karageorghis. Variable shape parameter kansa rbf method for the solution of nonlinear boundary value problems. *Engineering Analysis with Boundary Elements*, 103:32–40, 2019.

[85] D. D. Joseph and L. Preziosi. Heat waves. *Reviews of Modern Physics*, 61(1):41, 1989.

[86] N. Jüngling and J. Niessner. Adjoint-based topology optimization of filter structures for gas–particle systems. *AIP Advances*, 11(6):065008, 2021.

[87] M. Kadic, T. Bückmann, R. Schittny, P. Gumbsch, and M. Wegener. Pentamode metamaterials with independently tailored bulk modulus and mass density. *Physical Review Applied*, 2(5):054007, 2014.

[88] E. J. Kansa. Multiquadrics—a scattered data approximation scheme with applications to computational fluid-dynamics—i surface approximations and partial derivative estimates. *Computers & Mathematics with applications*, 19(8-9):127–145, 1990.

[89] E. J. Kansa. Multiquadrics—a scattered data approximation scheme with applications to computational fluid-dynamics—ii solutions to parabolic, hyperbolic and elliptic partial differential equations. *Computers & mathematics with applications*, 19(8-9):147–161, 1990.

[90] J. T. Katsikadelis. *The boundary element method for engineers and scientists: theory and applications*. Academic Press, 2016.

[91] J. A. Kołodziej and A. Zielinski. *Boundary collocation techniques and their application in engineering*. WIT Press, 2009.

[92] C. Körner and H. Bergmann. The physical defects of the hyperbolic heat conduction equation. *Applied Physics A*, 67(4):397–401, 1998.

[93] T. Koschny, C. M. Soukoulis, and M. Wegener. Metamaterials in microwaves, optics, mechanics, thermodynamics, and transport. *Journal of Optics*, 19(8):084005, 2017.

[94] J. A. Koupaei, M. Firouznia, and S. M. M. Hosseini. Finding a good shape parameter of rbf to solve pdes based on the particle swarm optimization algorithm. *Alexandria engineering journal*, 57(4):3641–3652, 2018.

[95] R. Kumar, M. Kumar, J. S. Chohan, and S. Kumar. Overview on metamaterial: History, types and applications. *Materials Today: Proceedings*, 2021.

[96] D.-H. Kwon and D. H. Werner. Transformation optical designs for wave collimators, flat lenses and right-angle bends. *New Journal of Physics*, 10(11):115023, 2008.

[97] N. Landy and D. R. Smith. A full-parameter unidirectional metamaterial cloak for microwaves. *Nature materials*, 12(1):25–28, 2013.

[98] U. Langer and O. Steinbach. *Space-Time Methods: Applications to Partial Differential Equations*, volume 25. Walter de Gruyter GmbH & Co KG, 2019.

[99] E. Larsson and B. Fornberg. A numerical study of some radial basis function based solution methods for elliptic pdes. *Computers & Mathematics with Applications*, 46(5-6):891–902, 2003.

[100] E. Larsson and B. Fornberg. Theoretical and computational aspects of multivariate interpolation with increasingly flat radial basis functions. *Computers & Mathematics with Applications*, 49(1):103–130, 2005.

[101] U. Leonhardt. Optical conformal mapping. *science*, 312(5781):1777–1780, 2006.

[102] U. Leonhardt and T. Tyc. Broadband invisibility by non-euclidean cloaking. *Science*, 323(5910):110–112, 2009.

[103] J. Li, Y. Gao, and J. Huang. A bifunctional cloak using transformation media. *Journal of Applied Physics*, 108(7):074504, 2010.

[104] J. Li and J. B. Pendry. Hiding under the carpet: a new strategy for cloaking. *Physical review letters*, 101(20):203901, 2008.

[105] Q. Li and J. S. Vipperman. Two-dimensional acoustic cloaks of arbitrary shape with layered structure based on transformation acoustics. *Applied Physics Letters*, 105(10):101906, 2014.

[106] Z.-C. Li, T.-T. Lu, H.-Y. Hu, and A. H. Cheng. *Trefftz and collocation methods*. WIT press, 2008.

[107] J. Lin, H. Yu, S. Reutskiy, and Y. Wang. A meshless radial basis function based method for modeling dual-phase-lag heat transfer in irregular domains. *Computers & Mathematics with Applications*, 85:1–17, 2021.

[108] C.-S. Liu and C.-W. Chang. An energy regularization of the mq-rbf method for solving the cauchy problems of diffusion-convection-reaction equations. *Communications in Nonlinear Science and Numerical Simulation*, 67:375–390, 2019.

[109] R. Liu, C. Ji, J. Mock, J. Chin, T. Cui, and D. Smith. Broadband ground-plane cloak. *Science*, 323(5912):366–369, 2009.

[110] J. R. Magnus and H. Neudecker. *Matrix differential calculus with applications in statistics and econometrics*. John Wiley & Sons, 2019.

[111] D. Maillet. A review of the models using the cattaneo and vernotte hyperbolic heat equation and their experimental validation. *International Journal of Thermal Sciences*, 139:424–432, 2019.

[112] E. Majchrzak and B. Mochnacki. Dual-phase lag equation. stability conditions of a numerical algorithm based on the explicit scheme of the finite difference method. *Journal of Applied Mathematics and Computational Mechanics*, 15(3):89–96, 2016.

[113] MathWorks. *MATLAB Documentation*. MathWorks.

[114] G. Moridis and E. Kansa. The laplace transform multiquadrics method: a highly accurate scheme for the numerical solution of linear partial differential equations. *Journal of Applied Science and Computation*, 1(2):375–407, 1994.

[115] P. M. Morse and H. Feshbach. Methods of theoretical physics. *American Journal of Physics*, 22(6):410–413, 1954.

[116] S. Narayana and Y. Sato. Heat flux manipulation with engineered thermal materials. *Physical review letters*, 108(21):214303, 2012.

[117] V. Narayanamurti and R. Dynes. Observation of second sound in bismuth. *Physical Review Letters*, 28(22):1461, 1972.

[118] I. Newton. Scala graduum caloris. calorum descriptiones and signa. *Philosophical Transactions of the Royal Society*, 22(271):540–550, 1701.

[119] W. L. Oberkampf and C. J. Roy. *Verification and validation in scientific computing*. Cambridge University Press, 2010.

[120] M. Oudich, M. B. Assouar, and Z. Hou. Propagation of acoustic waves and waveguiding in a two-dimensional locally resonant phononic crystal plate. *Applied Physics Letters*, 97(19):193503, 2010.

[121] M. Ozisik and D. Tzou. On the wave theory in heat conduction. *Journal of Heat Transfer*, 116(3):526–535, 1994.

[122] G. Palai, S. Kisan, and A. Das. A proposal for bio-medical device to measure gus in human blood using metamaterial. *Optik*, 164:138–142, 2018.

[123] G. Pang, W. Chen, and Z. Fu. Space-fractional advection–dispersion equations by the kansa method. *Journal of Computational Physics*, 293:280–296, 2015.

[124] C. G. Pedersen, J. J. Lund, L. Damkilde, and A. S. A. Kristensen. Topology optimization-improved checker-board filtering with sharp contours. In *Proceedings of the 19th Nordic Seminar on Computational Mechanics*, pages 182–185. Lund University, 2006.

[125] J. B. Pendry, D. Schurig, and D. R. Smith. Controlling electromagnetic fields. *science*, 312(5781):1780–1782, 2006.

[126] O. Popczyk and G. Dziatkiewicz. Analysis of a one-dimensional steady heat flow in a variable thermal conductivity metamaterial using kansa method and analytical approximation of the heaviside function. In *Proceedings of 24th International Conference MECHANIKA 2019*, pages 122–125. Kaunas University of Technology, 2019.

[127] O. Popczyk and G. Dziatkiewicz. Examination of the fasshauer's algorithm usability for solving unsteady heat flow in a medium with spatially variable thermal parameters using the kansa method. In *Proceedings of 26th International Conference Engineering Mechanics 2020*, pages 416–419. Brno University of Technology, 2020.

[128] O. Popczyk and G. Dziatkiewicz. Kansa's method for analysis of one-dimensional heat flow in thermal metamaterials. In *AIP Conference Proceedings*, volume 2239, page 020043. AIP Publishing LLC, 2020.

[129] O. Popczyk and G. Dziatkiewicz. Modelling of unsteady heat flow in 1d metamaterial by fourier and c-v equations and the kansa method. In *Proceedings of Studencka Konferencja Naukowa Metody Komputerowe - 2020*, pages 109–112. Silesian University of Technology, 2020.

[130] O. Popczyk and G. Dziatkiewicz. Kansa method for unsteady heat flow in nonhomogenous material with a new proposal of finding the good value of rbf's shape parameter. *Materials*, 14(15):4178, 2021.

[131] O. Popczyk and G. Dziatkiewicz. Modelling of two-dimensional heat flow in nonhomogenous thermal metamaterial using the kansa method. In *Proceedings of Studencka Konferencja Naukowa Metody Komputerowe - 2021*, pages 105–108. Silesian University of Technology, 2021.

[132] O. Popczyk and G. Dziatkiewicz. Kansa method for solving initial-value problem of hyperbolic heat conduction in nonhomogeneous medium. *International Journal of Heat and Mass Transfer*, 183:122088, 2022.

[133] O. Popczyk and G. Dziatkiewicz. On certain relation between main matrix condition number and multiquadric shape parameter in non-symmetric kansa method. In *Proceedings of 45th International Conference on Boundary Elements and other Mesh Reduction Methods*. Wessex Institute, 2022.

[134] M. Qiu, W. Yan, and M. Yan. Designing near-perfect invisibility cloaks. *SPIE Newsroom*, pages 1–3, 2008.

[135] T. J. Rainsford, S. P. Mickan, and D. Abbott. T-ray sensing applications: review of global developments. In *Smart Structures, Devices, and Systems II*, volume 5649, pages 826–838. International Society for Optics and Photonics, 2005.

[136] N. Rajak, N. Chattoraj, and R. Mark. Metamaterial cell inspired high gain multi-band antenna for wireless applications. *AEU-International Journal of Electronics and Communications*, 109:23–30, 2019.

[137] S. Reutskiy. A meshless radial basis function method for 2d steady-state heat conduction problems in anisotropic and inhomogeneous media. *Engineering Analysis with Boundary Elements*, 66:1–11, 2016.

[138] S. Reutskiy and J. Lin. A meshless radial basis function method for steady-state advection-diffusion-reaction equation in arbitrary 2d domains. *Engineering Analysis with Boundary Elements*, 79:49–61, 2017.

[139] S. Rippa. An algorithm for selecting a good value for the parameter c in radial basis function interpolation. *Advances in Computational Mathematics*, 11(2):193–210, 1999.

[140] S. Rogers. Transport of heat and approach to second sound in some isotopically pure alkali-halide crystals. *Physical Review B*, 3(4):1440, 1971.

[141] Y. Sanyasiraju and C. Satyanarayana. On optimization of the rbf shape parameter in a grid-free local scheme for convection dominated problems over non-uniform centers. *Applied Mathematical Modelling*, 37(12-13):7245–7272, 2013.

[142] S. A. Sarra. A numerical study of the accuracy and stability of symmetric and asymmetric rbf collocation methods for hyperbolic pdes. *Numerical Methods for Partial Differential Equations: An International Journal*, 24(2):670–686, 2008.

[143] S. A. Sarra. Radial basis function approximation methods with extended precision floating point arithmetic. *Engineering Analysis with Boundary Elements*, 35(1):68–76, 2011.

[144] S. A. Sarra and S. Cogar. An examination of evaluation algorithms for the rbf method. *Engineering Analysis with Boundary Elements*, 75:36–45, 2017.

[145] S. A. Sarra and E. J. Kansa. Multiquadric radial basis function approximation methods for the numerical solution of partial differential equations. *Advances in Computational Mechanics*, 2(2), 2009.

[146] W. E. Schiesser and G. W. Griffiths. *A compendium of partial differential equation models: method of lines analysis with Matlab*. Cambridge University Press, 2009.

[147] R. Schittny, M. Kadic, S. Guenneau, and M. Wegener. Experiments on transformation thermodynamics: molding the flow of heat. *Physical review letters*, 110(19):195901, 2013.

[148] D. Schurig, J. J. Mock, B. Justice, S. A. Cummer, J. B. Pendry, A. F. Starr, and D. R. Smith. Metamaterial electromagnetic cloak at microwave frequencies. *Science*, 314(5801):977–980, 2006.

[149] R. Shamey and X. Zhao. *Modelling, simulation and control of the dyeing process*. Elsevier, 2014.

[150] M. Sharan, E. Kansa, and S. Gupta. Application of the multiquadric method for numerical solution of elliptic partial differential equations. *Applied Mathematics and Computation*, 84(2-3):275–302, 1997.

[151] R. A. Shelby, D. R. Smith, and S. Schultz. Experimental verification of a negative index of refraction. *science*, 292(5514):77–79, 2001.

[152] S. Simonenko, V. Bayona, and M. Kindelan. Optimal shape parameter for the solution of elastostatic problems with the rbf method. *Journal of Engineering Mathematics*, 85(1):115–129, 2014.

[153] S. Sobolev. On hyperbolic heat-mass transfer equation. *International Journal of Heat and Mass Transfer*, 122:629–630, 2018.

[154] M. Sotola, P. Marsalek, D. Rybansky, M. Fusek, and D. Gabriel. Sensitivity analysis of key formulations of topology optimization on an example of cantilever bending beam. *Symmetry*, 13(4):712, 2021.

[155] G. Strang. *Introduction to linear algebra*, volume 3. Wellesley-Cambridge Press Wellesley, MA, 1993.

[156] J. R. Tillerson and J. A. Stricklin. Numerical methods of integration applied in the nonlinear dynamic analysis of shells of revolution. Master's thesis, Texas A&M University., 1970.

[157] C. J. Trahan and R. E. Wyatt. Radial basis function interpolation in the quantum trajectory method: optimization of the multi-quadric shape parameter. *Journal of Computational Physics*, 185(1):27–49, 2003.

[158] L. N. Trefethen and D. Bau III. *Numerical linear algebra*, volume 50. Siam, 1997.

[159] C. Tsai, J. Kolibal, and M. Li. The golden section search algorithm for finding a good shape parameter for meshless collocation methods. *Engineering Analysis with Boundary Elements*, 34(8):738–746, 2010.

[160] D. Y. Tzou. The generalized lagging response in small-scale and high-rate heating. *International Journal of Heat and Mass Transfer*, 38(17):3231–3240, 1995.

[161] M. Uddin. On the selection of a good value of shape parameter in solving time-dependent partial differential equations using rbf approximation method. *Applied Mathematical Modelling*, 38(1):135–144, 2014.

[162] J. Valentine, J. Li, T. Zentgraf, G. Bartal, and X. Zhang. An optical cloak made of dielectrics. *Nature materials*, 8(7):568–571, 2009.

[163] K. P. Vemuri, F. Canbazoglu, and P. R. Bandaru. Guiding conductive heat flux through thermal metamaterials. *Applied Physics Letters*, 105(19):193904, 2014.

[164] R. Verma and S. Kumar. Computational study on constant and sinusoidal heating of skin tissue using radial basis functions. *Computers in Biology and Medicine*, page 103808, 2020.

[165] P. Vernotte. Paradoxes in the continuous theory of the heat equation. *CR Acad. Sci*, 246(3):154–3, 1958.

[166] H. K. Versteeg and W. Malalasekera. *An introduction to computational fluid dynamics: the finite volume method*. Pearson education, 2007.

[167] A. Wächter and L. T. Biegler. On the implementation of an interior-point filter line-search algorithm for large-scale nonlinear programming. *Mathematical programming*, 106(1):25–57, 2006.

[168] J. Wang and G. Liu. On the optimal shape parameters of radial basis functions used for 2-d meshless methods. *Computer methods in applied mechanics and engineering*, 191(23-24):2611–2630, 2002.

[169] J. Wertz, E. J. Kansa, and L. Ling. The role of the multiquadric shape parameters in solving elliptic partial differential equations. *Computers & Mathematics with Applications*, 51(8):1335–1348, 2006.

[170] S. Xiang, K.-m. Wang, Y.-t. Ai, Y.-d. Sha, and H. Shi. Trigonometric variable shape parameter and exponent strategy for generalized multiquadric radial basis function approximation. *Applied Mathematical Modelling*, 36(5):1931–1938, 2012.

[171] H. Xu, X. Shi, F. Gao, H. Sun, and B. Zhang. Ultrathin three-dimensional thermal cloak. *Physical Review Letters*, 112(5):054301, 2014.

[172] M. Zerroukat, K. Djidjeli, and A. Charafi. Explicit and implicit meshless methods for linear advection–diffusion-type partial differential equations. *International Journal for Numerical Methods in Engineering*, 48(1):19–35, 2000.

[173] M. Zerroukat, H. Power, and C. Chen. A numerical method for heat transfer problems using collocation and radial basis functions. *International Journal for numerical methods in Engineering*, 42(7):1263–1278, 1998.

[174] B. Zhang, Y. Luo, X. Liu, and G. Barbastathis. Macroscopic invisibility cloak for visible light. *Physical Review Letters*, 106(3):033901, 2011.

[175] H. Zhang, C. Guo, X. Su, and L. Chen. Shape parameter selection for multiquadrics function method in solving electromagnetic boundary value problems. *The International Journal for Computation and Mathematics in Electrical and Electronic Engineering*, 2016.

[176] S. Zhang, C. Xia, and N. Fang. Broadband acoustic cloak for ultrasound waves. *Physical review letters*, 106(2):024301, 2011.

[177] Z. Zheng and W. Li. Numerical stabilities and boundary conditions in time-domain eulerian simulations of acoustic wave propagations with and without background flow. *Applied Mathematics and Computation*, 202(1):146–161, 2008.

[178] R. Zhu, X. Liu, G. Hu, C. Sun, and G. Huang. A chiral elastic metamaterial beam for broadband vibration suppression. *Journal of Sound and Vibration*, 333(10):2759–2773, 2014.

[179] O. C. Zienkiewicz, R. L. Taylor, and J. Z. Zhu. *The finite element method: its basis and fundamentals*. Elsevier, 2005.

[180] L. Zigoneanu, B.-I. Popa, and S. A. Cummer. Three-dimensional broadband omnidirectional acoustic ground cloak. *Nature materials*, 13(4):352–355, 2014.

Appendix

Finite difference method for the hyperbolic Cattaneo-Vernotte equation In the work, the finite difference method solution was the reference solution for many simulated problems. They were problems of various kinds, one- and two-dimensional, steady and unsteady, elliptic, parabolic and hyperbolic. In order to compactly describe the method of solving them using the finite differences, it was decided to describe only the most general case, i.e. the two-dimensional hyperbolic case described by the Cattaneo-Vernotte equation. From this general case it is easy to derive specific cases. If the problem is two-dimensional, the Cattaneo-Vernotte Equation 2.9 simplifies to the two-dimensional Cattaneo-Vernotte Equation 3.18:

$$\gamma\left(\boldsymbol{x}\right)\rho\left(\boldsymbol{x}\right)\left(\tau\ddot{u}+\dot{u}\right)=\kappa_{,x}\left(\boldsymbol{x}\right)u_{,x}+\kappa_{,y}\left(\boldsymbol{x}\right)u_{,y}+\kappa\left(\boldsymbol{x}\right)\left(u_{,xx}+u_{,yy}\right).$$

In the finite difference method, similarly to the Kansa method, the matrix approach described by Equation 2.36 was used:

$$\boldsymbol{M}\ddot{\boldsymbol{u}}+\boldsymbol{D}\dot{\boldsymbol{u}}+\boldsymbol{K}\boldsymbol{u}=\boldsymbol{0},$$

and the Euler time integration scheme given by Equation 2.135:

$$\boldsymbol{M}\ddot{\boldsymbol{u}}_k+\boldsymbol{D}\dot{\boldsymbol{u}}_k+\boldsymbol{K}\boldsymbol{u}_{k+1}=\boldsymbol{0}.$$

As in the Kansa method, the $\boldsymbol{M}$ and $\boldsymbol{D}$ matrices are easy to compute using Equations 2.106 and 2.107::

$$\boldsymbol{M}=\tau\boldsymbol{\gamma}\boldsymbol{\rho}, \tag{5.1}$$

$$\boldsymbol{D}=\boldsymbol{\gamma}\boldsymbol{\rho}. \tag{5.2}$$

The computation of the thermal stiffness $\boldsymbol{K}$ is a bit more complex. Let's start with the presentation of the computational domain used in the calculations, it is the same regular domain as in the two-dimensional simulations shown in Figure 3.27. The nodes of the finite difference grid are numbered from left to right from bottom to top: $i=1,2\ldots n$. This means that the adjacent points are numbered as shown in Figure 5.1.

Discretization of the right side of Equation 3.18 gives:

$$\begin{aligned}&\kappa_{,x}\left(\boldsymbol{x}\right)u_{,x}+\kappa_{,y}\left(\boldsymbol{x}\right)u_{,y}+\kappa\left(\boldsymbol{x}\right)\left(u_{,xx}+u_{,yy}\right)\approx\\&\kappa_{xi}\frac{u_{i+1}^{k+1}-u_{i-1}^{k+1}}{2\Delta x}+\kappa_{yi}\frac{u_{i+n_x}^{k+1}-u_{i-n_x}^{k+1}}{2\Delta y}+\\&\qquad\kappa_{i,j}\left(\frac{u_{i+1}^{k+1}-2u_i^{k+1}+u_{i-1}^{k+1}}{\left(\Delta x\right)^2}+\frac{u_{i+n_x}^{k+1}-2u_i^{k+1}+u_{i-n_x}^{k+1}}{\left(\Delta y\right)^2}\right).\end{aligned} \tag{5.3}$$

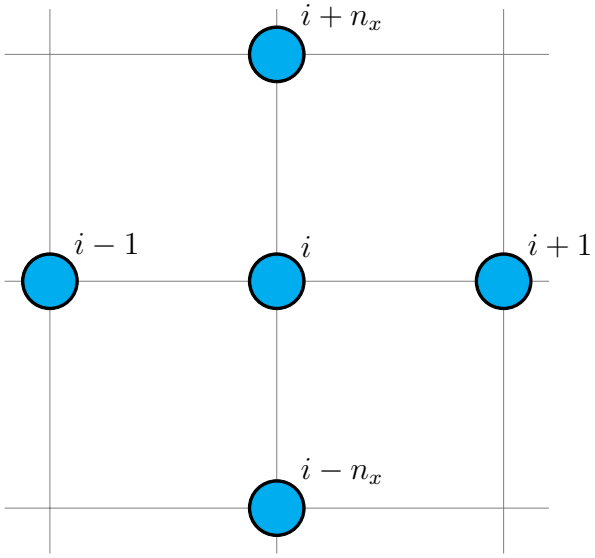

Figure 5.1: Numbering of adjacent points on the finite difference grid

From Equation 5.3 emerges a method of assigning a values to the elements of matrix $\boldsymbol{K}$ which is pentadiagonal:

$$\boldsymbol{K}_{i,i-n_x} = \frac{\kappa_{,y}\left(\boldsymbol{x}_i\right)}{2\Delta y} - \frac{\kappa\left(\boldsymbol{x}_i\right)}{\left(\Delta y\right)^2}, \tag{5.4}$$

$$\boldsymbol{K}_{i,i-1} = \frac{\kappa_{,x}\left(\boldsymbol{x}_i\right)}{2\Delta x} - \frac{\kappa\left(\boldsymbol{x}_i\right)}{\left(\Delta x\right)^2}, \tag{5.5}$$

$$\boldsymbol{K}_{i,i} = \kappa\left(\boldsymbol{x}_i\right)\left(\frac{2}{\left(\Delta x\right)^2} + \frac{2}{\left(\Delta y\right)^2}\right), \tag{5.6}$$

$$\boldsymbol{K}_{i,i+1} = -\frac{\kappa_{,x}\left(\boldsymbol{x}_i\right)}{2\Delta x} - \frac{\kappa\left(\boldsymbol{x}_i\right)}{\left(\Delta x\right)^2}. \tag{5.7}$$

$$\boldsymbol{K}_{i,i+n_x} = -\frac{\kappa_{,y}\left(\boldsymbol{x}_i\right)}{2\Delta y} - \frac{\kappa\left(\boldsymbol{x}_i\right)}{\left(\Delta y\right)^2}. \tag{5.8}$$

Naturally, the initial conditions and time advancement are realized by the above mentioned time integration scheme. After using a time integration scheme, Equation 2.135 is transformed into Equation 2.40:

$$\boldsymbol{A}\boldsymbol{u}_{k+1} = \boldsymbol{b}.$$

The imposition of boundary conditions, as in the case of the Kansa method, is a two stage procedure. First, the rows in matrix $\boldsymbol{A}$ and the elements in vector $\boldsymbol{b}$ corresponding to the boundary points are zeroed. Then, the previously zeroed rows and elements are filled with values depending on the applied boundary conditions. The methods of filling the matrix $\boldsymbol{A}$ and vector $\boldsymbol{b}$ for different boundary conditions are as follows:

- Dirichlet boundary condition:

$$\boldsymbol{A}_{i,i} = 1, \tag{5.9}$$

$$\boldsymbol{b}_i = u_b\left(\boldsymbol{x}_i\right). \tag{5.10}$$

- Neumann boundary condition at the left and right boundary:

$$\boldsymbol{A}_{i,i} = \mp 1, \tag{5.11}$$

$$\boldsymbol{A}_{i,i\pm1} = \pm 1, \tag{5.12}$$

$$\boldsymbol{b}_i = -\Delta x \frac{q_b\left(\boldsymbol{x}_i\right)}{\kappa\left(\boldsymbol{x}_i\right)}. \tag{5.13}$$

- Neumann boundary condition at the bottom and top boundary:

$$\boldsymbol{A}_{i,i} = \mp 1, \tag{5.14}$$

$$\boldsymbol{A}_{i,i\pm n_x} = \pm 1, \tag{5.15}$$

$$\boldsymbol{b}_i = -\Delta y \frac{q_b\left(\boldsymbol{x}_i\right)}{\kappa\left(\boldsymbol{x}_i\right)}. \tag{5.16}$$

- Robin boundary condition at the left and right boundary:

$$\boldsymbol{A}_{i,i} = \pm \frac{\kappa\left(\boldsymbol{x}_i\right)}{\Delta x} + \alpha\left(\boldsymbol{x}_i\right)\left(1 + \frac{\tau}{\Delta t}\right), \tag{5.17}$$

$$\boldsymbol{A}_{i,i\pm1} = \mp \frac{\kappa\left(\boldsymbol{x}_i\right)}{\Delta x}, \tag{5.18}$$

$$\boldsymbol{b}_i = \alpha\left(\boldsymbol{x}_i\right)\left(u_\infty\left(\boldsymbol{x}_i\right) + \frac{\tau}{\Delta t} u_k\left(\boldsymbol{x}_i\right)\right). \tag{5.19}$$

- Robin boundary condition at the bottom and top boundary:

$$\boldsymbol{A}_{i,i} = \pm \frac{\kappa\left(\boldsymbol{x}_i\right)}{\Delta y} + \alpha\left(\boldsymbol{x}_i\right)\left(1 + \frac{\tau}{\Delta t}\right), \tag{5.20}$$

$$\boldsymbol{A}_{i,i\pm n_x} = \mp \frac{\kappa\left(\boldsymbol{x}_i\right)}{\Delta y}, \tag{5.21}$$

$$\boldsymbol{b}_i = \alpha\left(\boldsymbol{x}_i\right)\left(u_\infty\left(\boldsymbol{x}_i\right) + \frac{\tau}{\Delta t} u_k\left(\boldsymbol{x}_i\right)\right). \tag{5.22}$$

The plus or minus signs depend on whether the left, right, bottom or top boundary is being considered. The upper sign is used for the left and bottom boundary, the lower sign is used for the right and top boundary. After imposing the boundary conditions, Equation 2.40 takes the form of Equation 2.43:

$$\bar{\boldsymbol{A}}\boldsymbol{u}_{k+1} = \bar{\boldsymbol{b}}.$$

The procedure of applying boundary conditions is repeated at every time step during time integration.